Étude expérimentale d'écoulements soumis à une transition longitudinale de rugosité en lit simple et en lit composé

Victor Dupuis

N° d'ordre NNT : 2016LYSE1154

THÈSE DE DOCTORAT DE L'UNIVERSITÉ DE LYON
effectuée au sein de
l'Université Claude Bernard Lyon 1

École Doctorale ED162
Mécanique, Énergétique, Génie civil, Acoustique

Discipline : Mécanique des Fluides

Soutenue publiquement le 21/09/2016, par :

Victor DUPUIS

Étude expérimentale d'écoulements soumis à une transition longitudinale de rugosité en lit simple et en lit composé

Devant le jury composé de :

M. Didier BOUSMAR, Professeur, Université Catholique de Louvain, Belgique	Président
M. Laurent DAVID, Professeur des Universités, Université de Poitiers	Rapporteur
M. Mário Jorge FRANCA, Chercheur, EPFL, Suisse	Rapporteur
M. Juan Pedro MARTIN-VÍDE, Professeur, UPC, Espagne	Examinateur
Mme Ivana VINKOVIC, Professeur des Universités, Université de Lyon	Examinatrice
M. André PAQUIER (IGPEF), Directeur d'Unité de Recherche, Irstea	Directeur de thèse
M. Sébastien PROUST, Chercheur (HDR), Irstea	Encadrant de thèse
Mme Céline BERNI, Chargée de Recherche, Irstea	Encadrante de thèse

Préambule

La thèse de doctorat que je présente ici a été préparée au sein de l'Unité de Recherche Hydrologie-Hydraulique du Centre régional de Lyon-Villeurbanne de l'Institut national de Recherche en Sciences et Technologies pour l'Environnement et l'Agriculture (Irstea).

Le doctorat s'est déroulé de janvier 2013 à août 2016. Il a été financé par Irstea (26 mois) et par l'Agence Nationale de la Recherche (18 mois) dans le cadre du projet Flowres (ANR-14-CE03-0010).

Les mesures expérimentales ont été effectuées dans le canal large du Laboratoire d'Hydraulique et d'Hydromorphologie d'Irstea. Le protocole expérimental a été élaboré en partie en fonction des contraintes techniques liées à l'équipement, le canal hydraulique ayant été équipé progressivement tout au long de la thèse (notamment plaine d'inondation, rails de mesure).

Je remercie Laurent David et Mário Franca d'avoir bien voulu être rapporteurs de la thèse, ainsi que Juan Pedro Martin-Víde, Didier Bousmar et Ivana Vinkovic d'avoir accepté la fonction d'examinateur.

Je remercie toutes les personnes qui m'ont accompagné au cours de cette thèse, à commencer par mes deux encadrants, Sébastien Proust et Céline Berni, mon Directeur de thèse, André Paquier, qui ont tout fait pour me transmettre l'esprit de la démarche scientifique et la rigueur associée. Fabien Thollet, Alexis Buffet et l'ensemble de l'équipe technique du Laboratoire d'Hydraulique ont assuré le bon fonctionnement des équipements et du matériel de mesure, participé à la préparation des expériences et assuré la gestion des problèmes techniques. À mentionner également le travail des entreprises impliquées dans la construction du canal hydraulique et de ses équipements et qui ont contribué à faire de cette installation un outil scientifique de grande qualité et agréable à utiliser. Le comité de suivi de thèse (Didier Bousmar, Frédéric Moulin, Alain Recking, Nicolas Rivière) s'est réuni à deux reprises et a permis d'apporter un regard extérieur et critique sur les travaux. L'Unité de Recherche HH et les services généraux du Centre de Lyon-Villeurbanne m'ont accueilli chaleureusement et ont assuré une bonne ambiance de travail. Enfin ma famille m'a soutenu et encouragé.

Victor Dupuis

Étude expérimentale d'écoulements soumis à une transition longitudinale de rugosité en lit simple et en lit composé

Résumé :
Ce travail de thèse s'intéresse à l'effet d'une variation longitudinale de l'occupation du sol de la plaine d'inondation sur l'écoulement d'une rivière en débordement. Nous traitons le cas d'une transition entre une zone de prairie et une zone de forêt, et *vice versa*. Cette variation d'occupation du sol est associée à une transition de rugosité hydraulique entre une rugosité de fond (prairie fortement immergée) et des macro-rugosités émergées (arbres), modélisées respectivement par une moquette plastifiée et par un champ de cylindres. Ces écoulements sont étudiés en laboratoire dans un canal de dimension $18\,\mathrm{m} \times 3\,\mathrm{m}$. Dans un premier temps, nous considérons l'écoulement à travers un champ de cylindres émergents en lit simple, en étudiant l'effet du fond sur le sillage des cylindres et le phénomène de seiche (fortes oscillations de la surface libre). Dans un deuxième temps, nous nous penchons sur le développement vers l'uniformité d'un écoulement en lit composé de rugosité uniforme. La croissance asymétrique de la couche de mélange du lit composé, la propriété d'autosimilarité ainsi que l'organisation tridimensionnelle des structures turbulentes cohérentes associées à la couche de mélange sont analysées. La troisième partie a pour objet la transition longitudinale de rugosité en lit composé, dont l'effet sur la couche de mélange et sur les structures cohérentes est discuté. Nous évaluons également les différentes contributions au transfert latéral de quantité de mouvement entre lit mineur et plaine d'inondation par diffusion turbulente, par échange de masse et par les courants secondaires.

Mots clés : mécanique des fluides, hydraulique fluviale, étude expérimentale, lit composé, turbulence, rugosité hydraulique, écoulement non uniforme, seiche.

Étude expérimentale d'écoulements soumis à une transition longitudinale de rugosité en lit simple et en lit composé

Résumé étendu

L'occupation du sol des plaines d'inondation est très diversifiée : cultures, prairies, zones forestières, constructions, *etc.* Cette hétérogénéité spatiale influence l'écoulement d'une rivière en débordement en créant des non-uniformités hydrodynamiques. Ce travail de thèse s'intéresse à un changement longitudinal d'occupation du sol de la plaine d'inondation, d'une zone de prairie fortement immergée à une zone boisée composée d'arbres émergents, et *vice versa*. Cette variation d'occupation du sol est associée à une transition de rugosité hydraulique entre une rugosité de fond (prairie) modélisée par une moquette plastifiée et des macro-rugosités émergées (arbres) modélisées par un champ de cylindres. Ces écoulements sont étudiés en laboratoire dans un canal vitré de dimension $18\,\mathrm{m} \times 3\,\mathrm{m}$.

L'écoulement débordant, dit en lit composé (lit mineur bordé de plaines d'inondation), génère une couche de mélange tridimensionnelle complexe. De surcroît, un changement longitudinal de rugosité engendre une dynamique d'écoulement également complexe. Cette double complexité nous a conduit à analyser d'abord séparément l'effet du lit composé et l'effet de la transition de rugosité. Ces deux effets ont ensuite été combinés.

Dans un premier temps, les écoulements sont étudiés dans une configuration en lit simple (plaine d'inondation isolée du lit mineur). L'écoulement à travers un champ de cylindres émergents posés sur un fond lisse ou rugueux est d'abord étudié en condition d'uniformité longitudinale. Le profil vertical de vitesse montre : une zone constante dans la partie haute et une couche limite près du fond, dont la hauteur est indépendante de la hauteur d'eau et de la rugosité de fond ; dans l'alignement d'un cylindre, le sommet de cette couche limite est associé à un pic de vitesse qui peut être expliqué par la déstructuration de l'allée tourbillonnaire de von Kármán sous l'effet de la turbulence induite par le fond. Les écoulements à travers le champ de cylindres sont associés à des oscillations cohérentes de la surface libre, appelées seiche. L'amplitude des oscillations dépend de la position longitudinale dans le champ de cylindres, le maximum étant atteint à mi-longueur. Lorsque le rapport entre la hauteur d'eau et la hauteur de couche limite est proche de un, la déstructuration de l'allée tourbillonnaire de von Kármán empêche la formation de la seiche.

Les transitions de rugosité, de prairie à zone boisée et inversement, sont ensuite étudiées en lit simple. Ces transitions induisent une variation de hauteur d'eau uniquement à l'amont de la transition de rugosité. Les profils verticaux normalisés de vitesse et de quantités turbulentes sont autosimilaires à l'amont de la transition et sont identiques aux profils de l'écoulement uniforme. A l'aval du changement de rugosité, les distributions de la vitesse et de la turbulence évoluent sur une distance d'ajustement de l'ordre de 35 à 50 fois la hauteur d'eau. Les écoulements avec changement de rugosité montrent que la seiche est réduite par la non-uniformité de l'écoulement. Le profil en long de hauteur d'eau est modélisé à l'aide d'une équation 1D prenant en compte la force volumique de traînée des cylindres. L'écart moyen de la hauteur d'eau calculée par rapport aux mesures est de $0.9\,\%$. Le calcul des profils de hauteur d'eau montre que celle-ci varie sur une distance d'environ 2600 fois la hauteur d'eau uniforme à l'amont du changement de rugosité. Une résolution analytique de l'équation est proposée lorsque le frottement au fond est négligé.

Dans un deuxième temps, nous étudions l'écoulement en lit composé avec une rugosité

uniforme sur les plaines d'inondation, en nous penchant sur le développement vers l'aval de la couche de mélange. La couche de mélange du lit composé est fortement asymétrique, c'est pourquoi nous distinguons les largeurs de couche de mélange côté plaine d'inondation et côté lit mineur. La présence d'un champ de cylindres (forêt) entraîne une stabilisation beaucoup plus rapide de la largeur de couche de mélange côté plaine d'inondation, par rapport au cas d'une simple rugosité de fond (prairie). Le développement longitudinal de la couche de mélange se caractérise par une autosimilarité des profils transversaux normalisés de vitesse et de turbulence à une altitude donnée. En revanche, sous l'effet du confinement vertical et de la forte tridimensionalité que celui-ci induit, les profils transversaux normalisés ne se superposent pas à différentes altitudes. La présence d'un champ de cylindres dans la plaine d'inondation tend à homogénéiser la couche de mélange sur la verticale. Les structures turbulentes cohérentes associées à la couche de mélange ont été analysées à l'aide de corrélations spatio-temporelles des vitesses. Les structures cohérentes s'étendent sur toute la hauteur d'eau en se déplaçant en bloc. La vitesse de propagation des structures correspond à peu près à la vitesse longitudinale moyennée sur la verticale au niveau de l'interface plaine d'inondation/lit mineur. L'organisation spatiale des fluctuations cohérentes de la vitesse liées aux structures est très différente selon que l'on considère la vitesse longitudinale ou latérale. Notamment, les fluctuations de la vitesse latérale restent corrélées sur des distances latérales beaucoup plus grandes que les fluctuations de la vitesse longitudinale. Le front d'onde des structures cohérentes présente une avance de phase du haut de la colonne d'eau par rapport au bas.

Le travail se termine par l'étude en lit composé de la transition longitudinale de rugosité entre une plaine d'inondation enherbée et une plaine d'inondation boisée, et *vice versa*. Par comparaison au lit simple, la transition de rugosité se caractérise par des variations de hauteur d'eau à la fois en amont et en aval du changement de rugosité, avec une inversion du gradient de hauteur d'eau à la transition. Les largeurs normalisées de la couche de mélange côté lit mineur et côté plaine d'inondation sont spécifiques à chaque rugosité, en étant environ trois fois plus grandes pour la plaine d'inondation enherbée que pour la plaine d'inondation boisée, ce qui est lié à l'effet de blocage du champ de cylindres. En aval du changement de rugosité, la couche de mélange s'adapte à la nouvelle rugosité, soit en s'élargissant, soit en rétrécissant. Le développement longitudinal de la couche de mélange du lit composé soumise à une transition de rugosité ne possède pas la propriété d'autosimilarité. Les transferts latéraux de masse, qui s'opèrent entre lit mineur et plaine d'inondation, sont en partie responsables de cette absence d'équilibre. La dynamique des structures cohérentes est dominée par deux processus physiques différents : à l'amont de la transition, un processus au cours duquel le moment cinétique des structures augmente en allant vers l'aval (fusion de vortex, entraînement de fluide) et à l'aval de la transition, un processus qui conserve le moment cinétique (étirement de vortex). La taille longitudinale des structures cohérentes associées à la couche de mélange varie proportionnellement à la largeur de la couche de mélange. Le transfert de quantité de mouvement entre lit mineur et plaine d'inondation a été analysé à la fois de façon analytique et expérimentale. L'effet dynamique global des transferts latéraux de fluide à l'interface plaine d'inondation/lit mineur est important dans le lit mineur mais quasiment négligeable dans la plaine d'inondation. Dans cette dernière, les deux contributions liées au transfert de masse dans le bilan de quantité de mouvement, à savoir l'effet de contraction d'une part et l'effet de la différence entre vitesse du fluide entrant/sortant et vitesse de la sous-section (lit mineur ou plaine d'inondation) d'autre part, sont de signe opposé. Des courants secondaires (cellule tourbillonnaire à axe longitudinal) de forte intensité sont mesurés dans le lit mineur ; ceux-ci induisent une redistribution importante de la quantité de mouvement à l'intérieur d'une sous-section, et déterminent par là fortement le

tracé des isovitesses, mais n'engendrent pas de transfert de quantité de mouvement entre sous-sections. L'intensité normalisée des courants secondaires dans le lit mineur est plus élevée avec des plaines d'inondation boisées qu'avec des plaine d'inondation enherbées. A l'interface lit mineur/plaine d'inondation, le cisaillement turbulent normalisé est plus important en présence de plaines d'inondation boisées.

Pour conclure, ce travail a d'abord montré qu'en traitant séparément la couche de mélange du lit composé côté plaine d'inondation d'une part et côté lit mineur d'autre part, il était possible d'appliquer la théorie des couches de mélange planes à la couche de mélange asymétrique du lit composé. Ensuite, la comparaison lit simple/lit composé a montré l'importance de prendre en compte l'interaction entre lit mineur et plaine d'inondation dans le bilan de forces du lit composé : non seulement de nouvelles forces apparaissent, mais le poids relatif des différentes forces en présence est également changé. Enfin, la comparaison des écoulements sur plaines d'inondation enherbées et boisées a montré que le type de rugosité des plaines d'inondation influençait fortement la dynamique de l'écoulement, notamment concernant la largeur de la couche de mélange, l'intensité de la turbulence et les courants secondaires.

Experimental investigation of flows subjected to a longitudinal transition in hydraulic roughness in single and compound channels

Abstract: This PhD thesis investigates the effect of a longitudinal change in floodplain land use on an overflooding river flow. We consider a transition between a meadow and a woodland and *vice versa*. This change in land use is associated with a change in hydraulic roughness, between a bed roughness (highly submerged meadow) and emergent macro-roughnesses (trees), respectively modelled by a plastic artificial grass and an array of emergent cylinders. The flows are experimentally investigated in an $18\,\mathrm{m} \times 3\,\mathrm{m}$ laboratory flume. In a first step, we investigate the flow through a cylinder array in a single channel, focusing on the effect of bed roughness on the cylinder wakes and on the seiche phenomenon (strong free surface oscillations). In a second step, we study the development towards flow uniformity of compound channel flows with a uniform hydraulic roughness on the floodplains. The asymmetrical growth of the compound channel mixing layer, the self-similarity property and the three-dimensional organisation of the turbulent coherent structures associated with the mixing layer are analysed. In a third step, we investigate the longitudinal change in roughness in compound channel configuration, which effects on mixing layer and on coherent structures are discussed. We also assess the contributions to lateral transfers of momentum between main channel and floodplain by turbulent diffusion, by mass exchange and by secondary currents.

Key words: fluid dynamics, river hydraulics, laboratory study, compound channel, turbulence, hydraulic roughness, non-uniform flow, seiching.

Notation

Main quantities[1]

Symbol	Unit	Quantity
a	m^{-1}	Frontal area per unit volume
A	m	Seiche amplitude
B	m	Channel width
B_l	m	Subsection width
c_f	-	Bed friction coefficient
C_D	-	Drag coefficient
d	m	Zero plane displacement (logarithmic law)
D	m	Cylinder diameter
D_r	-	Relative flow depth
f	Hz	Frequency
f_{Fi}	N	Form drag force per unit fluid mass (spatial averaging)
f_H	Hz	Seiche frequency
f_{St}	Hz	Strouhal frequency
f_{TW}	Hz	Natural frequency of the transverse waves across the channel
f_V	Hz	Vortex shedding frequency
f_{Vi}	N	Viscous drag force per unit fluid mass (spatial averaging)
Fr	-	Froude number
Fr_l	-	Subsection Froude number
g	$\mathrm{m.s}^{-2}$	Acceleration of gravitation
H	m	Water depth
H_l	m	Subsection water depth
H_{dw}	m	Uniform water depth relative to the downstream roughness
H_{up}	m	Uniform water depth relative to the upstream roughness
I_A	-	Indicator for longitudinal development of quantity A
k_s	m	Equivalent sand grain size
L_{dw}	m	Downstream adjustment length
$L_{ij}^{(k)}$	m	Eulerian integral length scale
L_{SC}	m	Mean distance between two successive coherent structures
L_{up}	m	Upstream adjustment length
M_0	-	Roughness step
n	$\mathrm{s.m}^{-1/3}$	Manning roughness coefficient of plastic grass
n_0	-	Oscillation mode
n_{glass}	$\mathrm{s.m}^{-1/3}$	Manning roughness coefficient of glass wall
N	m^{-2}	Cylinder density
p	Pa	Pressure
P	Pa	Reynolds- or double-averaged pressure
Q	$\mathrm{L.s}^{-1}$	Flow rate
Q_l	$\mathrm{L.s}^{-1}$	Subsection flow rate
Q_{tot}	$\mathrm{L.s}^{-1}$	Total flow rate
$R_{ij}^{(k)}$	-	Two-point space-time correlation function

[1] In this table sub- or superscripts i, j and k refer to spatial directions, $(i, j, k) \in \{1, 2, 3\}^3$, and subscript l refers to the main channel or floodplain subsection, $l \in \{m, f\}$.

$R_{ij,max}^{(k)}$	-	Maximum space-time correlation (over the time lag)
Re	-	Reynolds number based on the wetted perimeter
Re_D	-	Reynolds number based on the cylinder diameter
Re_l	-	Subsection Reynolds number based on wetted perimeter
S	-	Bed friction number (shallow mixing layers)
S_0	$\mathrm{m.m^{-1}}$	Longitudinal bottom slope
S_c	-	Critical bed friction number
St	-	Strouhal number
t	s	Time
u	$\mathrm{m.s^{-1}}$	Instantaneous longitudinal velocity
U	$\mathrm{m.s^{-1}}$	Reynolds- or double-averaged longitudinal velocity
U^*	$\mathrm{m.s^{-1}}$	Friction velocity
U_0	$\mathrm{m.s^{-1}}$	Average of high- and low-speed stream velocity (mixing layer)
U_1	$\mathrm{m.s^{-1}}$	High-speed stream velocity (mixing layer)
U_2	$\mathrm{m.s^{-1}}$	Low-speed stream velocity (mixing layer)
U_l	$\mathrm{m.s^{-1}}$	Subsection-averaged longitudinal velocity
U_{ij}	$\mathrm{m.s^{-1}}$	Phase velocity (coherent structures)
U_Q	$\mathrm{m.s^{-1}}$	Section-averaged longitudinal velocity
v	$\mathrm{m.s^{-1}}$	Instantaneous lateral velocity
V	$\mathrm{m.s^{-1}}$	Reynolds- or double-averaged lateral velocity
w	$\mathrm{m.s^{-1}}$	Instantaneous vertical velocity
w_l	m	Subsection downstream weir level
W	$\mathrm{m.s^{-1}}$	Reynolds- or double-averaged vertical velocity
x	m	Relative longitudinal coordinate
x_a	m	Absolute longitudinal coordinate
x^r	m	Longitudinal position of the reference probe (space-time correlation)
y	m	Lateral coordinate
y_{IP}	m	Lateral position of the mean velocity inflection point
y_{U_0}	m	Lateral position where velocity U_0 is reached
y^r	m	Lateral position of the reference probe (space-time correlation)
z	m	Vertical coordinate
z_0	m	Bed level
z_{BF}	m	Bankfull level
z_f	m	Relative vertical coordinate (reference at bankfull level)
z^r	m	Vertical position of the reference probe (space-time correlation)
z_s	m	Free surface level
$\alpha_{ii}^{(j)}$	-	Inclination of the velocity wave front (coherent structures)
α_l	-	Subsection aspect ratio
β	-	Boussinesq coefficient or Normalised driving pressure gradient
δ	m	Mixing layer width or Boundary layer height
δ_l	m	Mixing layer width in subsection l
δ^*	-	Normalised mixing layer width
δ_l^+	-	Normalised mixing layer width in subsection l
δ_ω	m	Vorticity mixing layer width
δ_{tot}	m	Total mixing layer width
ϵ	-	Relative error
θ	m	Momentum thickness
λ	-	Normalised velocity difference (mixing layer)
λ_l	-	Normalised velocity difference in subsection l (mixing layer)
ν	$\mathrm{m^2s^{-1}}$	Water kinematic viscosity

ξ_i	m	Spatial lag in the i-th direction (space-time correlation)
ρ	kg.m^{-3}	Water density
σ_H	m	Standard deviation of flow depth
τ	s	Time lag (space-time correlation)
τ_b	Pa	Bed shear stress
τ_{ij}	s	Eulerian integral time scale
$\tau_{ij,max}^{(k)}$	s	Maximum correlation time lag
$\tau_{x_i x_j}$	Pa	Total strain tensor
ψ_t	-	Turbulent exchange coefficient

Main subscripts

Symbol	**Meaning**
dw	Downstream
f	Floodplain
int	Main channel/floodplain interface
m	Main channel
max	Maximum value
up	Upstream

Mathematical operators

Symbol	**Operator**
$(-)_d$	Depth-averaging
$\langle - \rangle$	Space-averaging
$\overline{(-)}$	Time-averaging
$(-)'$	Time fluctuation
$\tilde{(-)}$	Space fluctuation
$(-)_w$	Width-averaging

Abbreviations

Symbol	**Meaning**
C	Compound
FP	Floodplain
M	Meadow
MC	Main channel
PSD	Power spectral density
RMS	Root mean square
W	Wood

Contents

Chapter 1

Introduction

Land use of floodplains is diversified: plantation, meadow, woodland, building, *etc.* This spatial heterogeneity influences the flow dynamics of an overflooding river, the flow being subject to non-uniformities. The present work experimentally investigates a longitudinal transition in floodplain land use, from a meadow to a woodland, and *vice versa*.

An overflooding river gives rise to a flow in a compound channel, which is composed of a deep main channel and of adjacent floodplains. The compound channel flow is characterized by a mixing layer developing at the interface between the main channel and the floodplain. The longitudinal change in floodplain land use will affect the mixing layer development and the mass and momentum exchange between main channel and floodplain.

Compound channel non-uniform flows have been investigated for more than 15 years within the Hydrology-Hydraulics research unit at Irstea (France). The effects of variation in floodplain width were investigated by Proust *et al.* (2006) in the case of an abrupt floodplain contraction and by Bousmar *et al.* (2006) in the case of symmetrically enlarging floodplains. Peltier *et al.* (2013) studied the influence of a groyne-like obstacle set on the floodplain perpendicularly to the main flow direction. Proust *et al.* (2013) studied non-uniform straight compound channel flows caused by an imbalance in the upstream discharge distribution between main channel and floodplains. Following the previous studies, the present work investigates the flow non-uniformity caused by a longitudinal transition in hydraulic roughness over the floodplains. The meadow is modelled by a plastic grass and corresponds to a bed roughness and the woodland is modelled by an array of emergent cylinders set on a plastic grass and corresponds to an emergent macro-roughness. These two hydraulic roughness types were chosen for their very different characteristics: the highly submerged bed roughness induces flow resistance through friction on the bed; the cylinder array set on the bed induces a complex interaction between the bed-induced turbulence and the wake turbulence, which is produced over the whole water column.

Owing to the vertical flow confinement and to the two-stage geometry, the compound cross-section generates a complex three-dimensional mixing layer at the interface between main channel and floodplain. On the other hand, a longitudinal change in hydraulic roughness also generates a complex flow development in the longitudinal direction. Therefore we first analyse separately the effects of the compound section and of the roughness transition. Then, these two effects are combined. The study is thus divided into three parts. In the first part, we treat the longitudinal change in hydraulic roughness in single channel (floodplain isolated from the main channel). The distances upstream and downstream of the transition, beyond which the flow can be considered as uniform, are evaluated. Furthermore, the interaction between cylinder wake and bed roughness is investigated, as well as the coherent oscillations of the free-surface due to cylinder wake resonance

(seiching). In the second part, the compound channel flow is investigated with uniformly distributed roughness, i.e. with bed roughness or emergent macro roughness set on bed roughness over the full length of the floodplains. The influence of each floodplain hydraulic roughness on the compound channel flow can thereby be investigated without the effect of a roughness transition. We analyse the flow development towards uniformity, focusing on the mixing layer growth and on the three-dimensional organisation of the associated coherent structures. In the third part, the longitudinal transition in roughness is investigated in compound channel configuration. The effects of the transition on the mixing layer dynamics are analysed, as well as the physical processes involved in the lateral redistribution of momentum (turbulent diffusion, net mass exchange and secondary currents).

The dissertation is organised as follows. The experimental set up, protocol and methodology are presented in Chapter 2. The equations of motion of the different flow configurations investigated are expounded in Chapter 3. The results relative to the single channel experiments are presented in Chapter 4. The development towards uniformity of the compound channel flows with uniform floodplain roughness is analysed in Chapter 5. The compound channel flows subjected to a longitudinal transition in hydraulic roughness are presented in Chapter 6. Conclusions and perspectives for future research are drawn in Chapter 7.

Chapters 4, 5 and 6 are written in the form of journal articles and can therefore be read quite independently of the other chapters. Chapter 4 has already been published (Dupuis *et al.*, 2016).

Chapter 2

Methodology

2.1 Experimental facility

Single and compound channel experiments were performed in an 18 m long and 3 m wide glassed-wall flume, located in the Hydraulics and Hydromorphology Laboratory of Irstea Lyon-Villeurbanne, France. The longitudinal bottom slope is $S_0 = 1.05\,\mathrm{mm.m^{-1}}$.

The single channel experiments were performed in the right third of the flume width, using the full length of 18 m. A vertical Plexiglas wall was used to isolate a 1 m-wide channel. The flume was then rearranged in a compound channel configuration with two symmetric glass floodplains (Fig. 2.1). Due to the floodplain inlet ramps, the channel length was reduced to 17.25 m.

The compound channel cross section was symmetrical and consisted in a central rectangular main channel of width $B_m = 1\,\mathrm{m}$ and in two adjacent floodplains of width $B_f = 1\,\mathrm{m}$ (Fig. 2.2). Both right and left floodplains were covered by a plastic artificial grass. The bankfull level, measured from the main channel bottom to the crest of the grass blades was $z_{BF} = 115\,\mathrm{mm}$.

Tap water was used for the single channel experiments. Reverse osmosis purified water was then used for the compound channel experiments, in order to prevent scale on the flume glass walls. The water was stored in a $130\,\mathrm{m^3}$ underground reservoir and supplied the flume in a closed circuit. The water was pumped up from the reservoir to a constant-water-level tower and flowed down gravitationally towards the inlet tank of each subsection (main channel, right and left floodplains), passing through control valves. The inlet discharge in each subsection was regulated automatically with the control valve

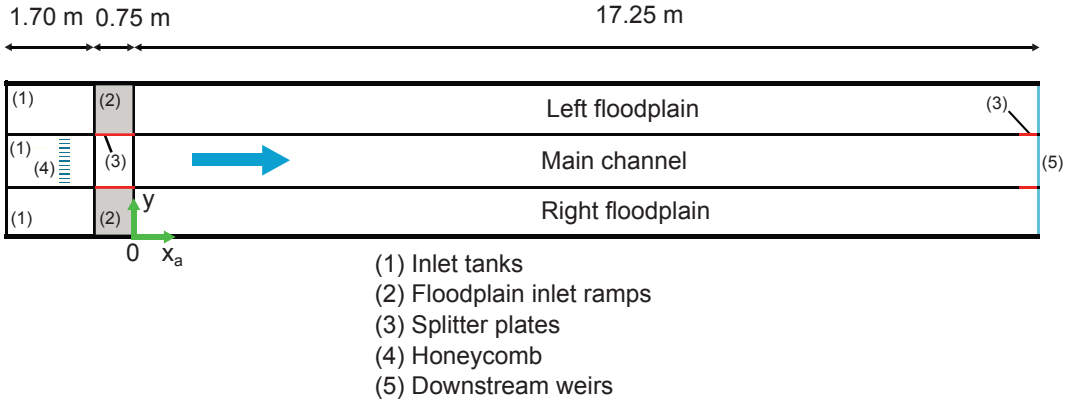

Figure 2.1: Top view of the compound channel flume.

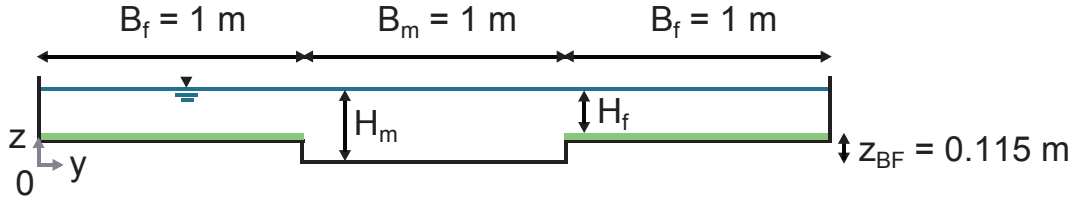

Figure 2.2: Front view of the wide flume.

(Samson 3310 with servomotor PSQ) and measured with an electromagnetic discharge-meter (Krohne Waterflux 3000 IFC100). The standard deviation of the discharge time series was of the order of 1.5 % of the mean discharge value.

After leaving the inlet tank, the flows in the right and left floodplains get over a linear ramp before reaching the bankfull level (see Figs. 2.1 and 2.3a). The flow in each floodplain was separated from the main channel flow by vertical splitter plates until the ramp end. A honeycomb was installed in the inlet tank of the main channel in order to vertically and laterally homogenize the flow (the honeycomb was 100 mm thick and the alveolus size 8 mm). The flow was controlled by three independent weirs, one per subsection, at the flume outlet (see Fig. 2.3b). Downstream splitter plates separated the flow in the three subsections over a distance of 50 cm upstream of the weirs.

A horizontal PVC plate was installed tangentially to the free-surface at the main channel inlet for test case CM (compound channel with meadow-type vegetation only, see Section 2.3, Fig. 2.5), in order to damp the strong waves coming from the inlet tank. This device generated an additional vertical boundary layer that vanished about 3.5 m further downstream. The horizontal PVC plate was not required for the other flow cases because the velocities and therefore the wave generation were smaller, or because the cylinder array in the floodplains dissipated the waves.

As shown in Figs. 2.2 and 2.1, the x-, y- and z-axis refer to the longitudinal, lateral and vertical directions, respectively. The longitudinal axis is defined along the flume bottom, the vertical axis is normal to the bed and the lateral axis is oriented from the right to the left bank. The origin of the absolute longitudinal coordinate (x_a) is defined at the exit of the inlet tank for the single channel experiments and at the trailing edge of the splitter plates for the compound channel experiments. A relative longitudinal coordinate (x) is also used, its origin being located at the change in roughness for the roughness transition test cases. The origin of the lateral axis is located at the side wall of the right floodplain. The origin of the vertical coordinate is defined at the bed level (tip of the blades) for the single channel experiments and at the bottom of the main channel for the compound channel experiments.

The flume was equipped with a motor-driven measuring carriage that moved in the three directions with an accuracy of 0.1 mm. The motor-driven carriage was available for the compound channel experiments only. A hand-driven carriage was used for the single channel experiments.

2.2 Floodplain roughness

Two types of floodplain vegetation were modelled: a meadow-type vegetation and a wood-type vegetation. The meadow-type vegetation was modelled by plastic artificial grass. The rigid grass blades were of uniform length (5 mm) and densely distributed, such that flow velocity within the canopy could be assumed to be negligible. The plastic grass was glued

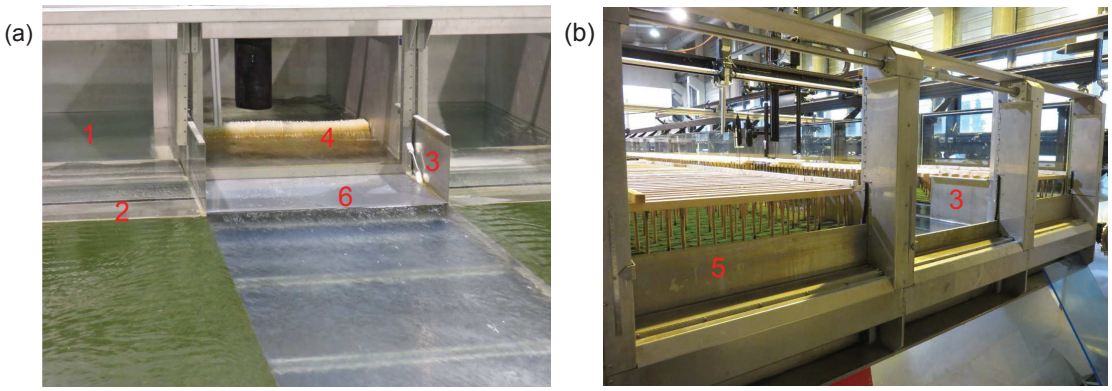

Figure 2.3: Picture of (a) flume inlet for the compound channel configuration with grassed floodplains (configuration CM, see Section 2.3, Fig. 2.5) and (b) flume outlet for the compound channel configuration with wooded floodplains (configuration CW, see Section 2.3, Fig. 2.5). In accordance with Fig. 2.1, the numbers refer to: (1) right floodplain inlet tank, (2) right floodplain inlet ramp, (3) splitter plates, (4) honeycomb, (5) right floodplain downstream weir, (6) horizontal PVC plate.

on PVC plates that in turn were glued on the floodplains. A sketch of the compound channel bank is presented in Fig. 2.4a.

The wood-type vegetation was modelled by circular wooden cylinders uniformly distributed in staggered rows (see Fig. 2.4b). The cylinder diameter was $D = 10\,\text{mm}$ and the cylinder density was $N = 81\,\text{cylinders.m}^{-2}$. These cylinders modelled 1 m diameter trees separated by an average distance of 11.3 m on a 1:100 scale. According to Terrier (2010), this tree distribution stands for a typical riparian forest in the lower reaches of the River Rhône (France). The cylinders were installed on the plastic grass (except for test case W0-Q15 for which a glass bottom was used, see Section 2.3) and were held in place from above by a wooden superstructure. Lateral rows of cylinders were termed even or odd depending on their even or odd number of cylinders. The cylinder array was composed of an elementary $80\,\text{mm} \times 80\,\text{mm}$ pattern, as shown in Fig. 2.4b. The lateral positions of the cylinders across an even row were $y = 100, 260, 420, 580, 740$ and 900 mm on the right floodplain and $y = 2100, 2260, 2420, 2580, 2740$ and 2900 mm on the left floodplain. The lateral positions of the cylinders across an odd row were $y = 20, 180, 340, 500, 660, 820$ and 980 mm on the right floodplain and $y = 2020, 2180, 2340, 2500, 2660, 2820$ and 2980 mm on the left floodplain. The accuracy of the cylinder position was estimated to $\pm 5\,\text{mm}$ in both lateral and longitudinal directions.

2.3 Experimental protocol

The experimental protocol was divided into four steps. Nine flow configurations and 19 flow test cases were investigated. The flow configurations are sketched in Fig. 2.5 and the flow test cases are reported in Table 2.1.

Step 1: The meadow-type vegetation (configuration M) and the wood-type vegetation (configuration W) were investigated in single channel under uniform flow conditions. In order to obtain different degrees of blade submergence, three flow rates were chosen for each roughness type (see Table 2.1). To assess the influence of bed-friction on emergent cylinder drag, a configuration with the cylinder array set on a smooth glass bottom was also studied (configuration W0).

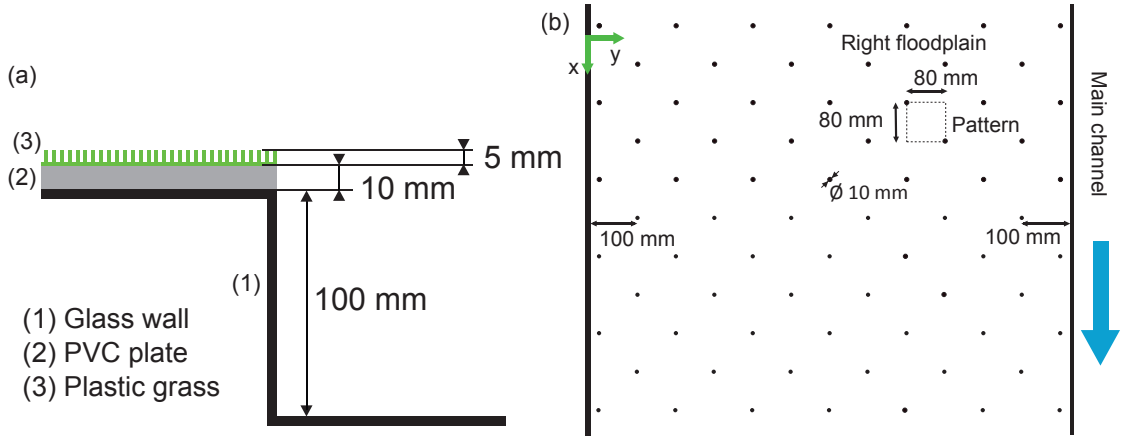

Figure 2.4: (a) Front view of the compound channel bank. (b) Plan view of the cylinder array.

Step 2: The longitudinal transitions in roughness were investigated in single channel, i.e. in a floodplain isolated from the main channel. For each meadow-to-wood (configuration MW, see Fig. 2.7a) and wood-to-meadow (configuration WM) transition, three flow rates were tested, the same as in Step 1 for the roughness downstream of the transition.

Step 3: The meadow-type vegetation (configuration CM, see Fig. 2.7b) and the wood-type vegetation (configuration CW, see Fig. 2.7c) were investigated in compound channel under uniform flow conditions. One test case was investigated for each roughness with the same total flow rate of $Q_{tot} = 162\,\mathrm{L.s^{-1}}$. The total flow rate was chosen such that the floodplain water depth was comparable to that investigated in a test case of Step 1 (test case CM close to test case MQ15 and test case CW close to test case WQ15). The upstream flow rate distribution between main channel and floodplain, together with the levels of the downstream weirs, were set to minimize both the longitudinal variation in flow depth and the lateral net mass exchange between main channel and floodplain.

Step 4: The longitudinal transitions in roughness were investigated in compound channel. The meadow-to-wood transition (configuration CMW) and the wood-to-meadow transition (configuration CWM, see Fig. 2.7d) were studied with the same total flow rate as in Step 3, $Q_{tot} = 162\,\mathrm{L.s^{-1}}$. Two upstream discharge distributions between main channel and floodplain were chosen for each transition. The first distribution generated lateral mass transfers between subsections in the upper channel reach, while these mass transfers were cancelled with the second distribution.

The total flow rate of the compound channel flows was chosen in order to model very high floods, with relative flow depth higher than 0.3.

The levels of the downstream weirs in the main channel w_m and in the floodplains w_f are reported in Table 2.1 for each test case. Level w_m is measured from the bottom of the main channel and level w_f from the crest of the grass blades (in single as in compound channel). For uniform flow cases (M, W, CM, CW), the downstream weirs were set in order to minimize flow depth gradient. Weir levels for the roughness transition experiments were the same as those for the uniform flows over the downstream roughness.

2.4 Free surface and bottom survey

The free surface level z_s is defined from a reference plane inclined with a slope of $S_0 = 1.05\,\mathrm{mm.m^{-1}}$ (channel mean slope), as shown in Fig. 2.7. The bed elevation from the reference plane is denoted z_0. The local water depth is then $H = z_s - z_0$. For the single

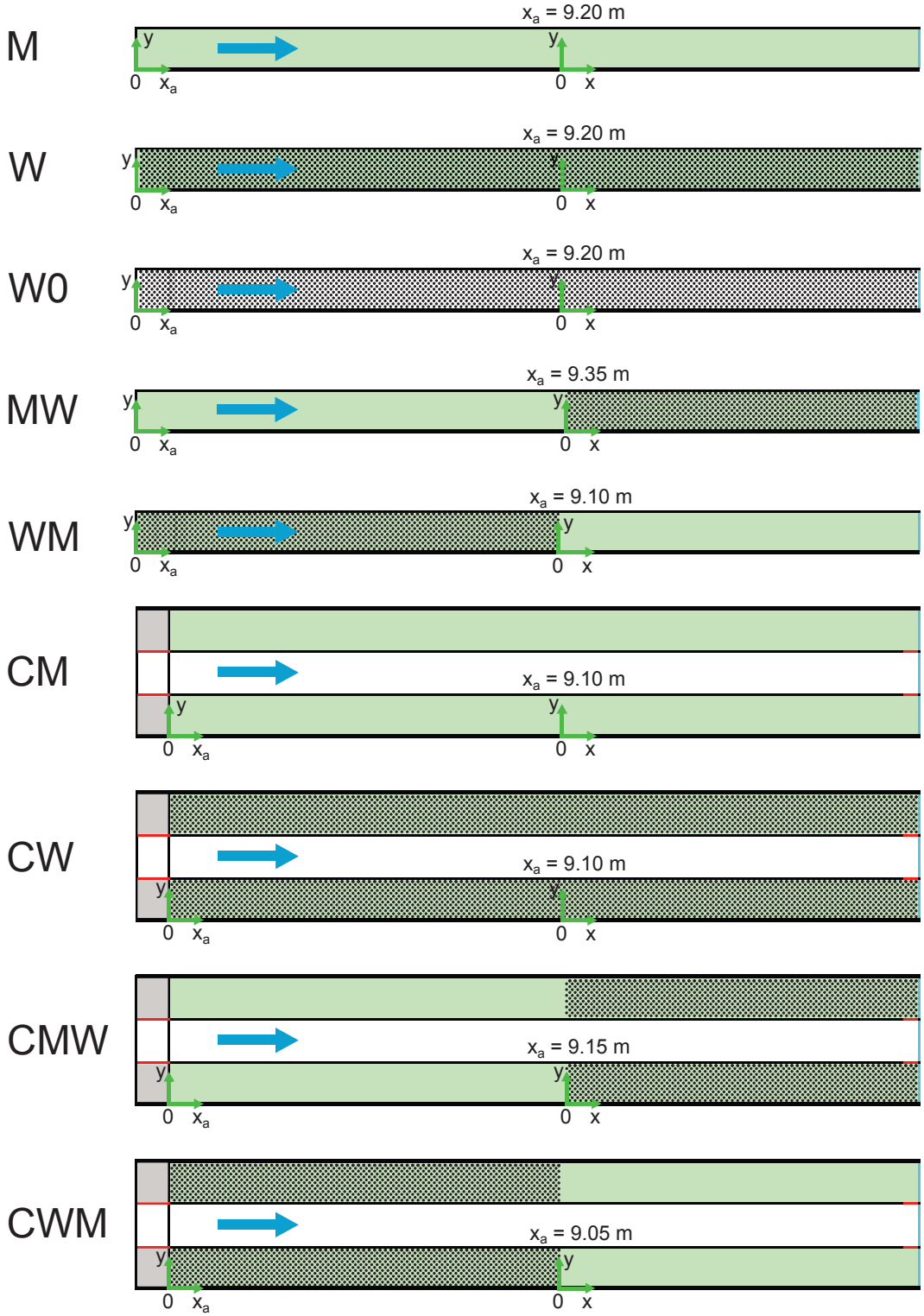

Figure 2.5: Top view of the nine flow configurations investigated. M: meadow; W: wood; C: compound channel; W0: cylinder array on glass bottom.

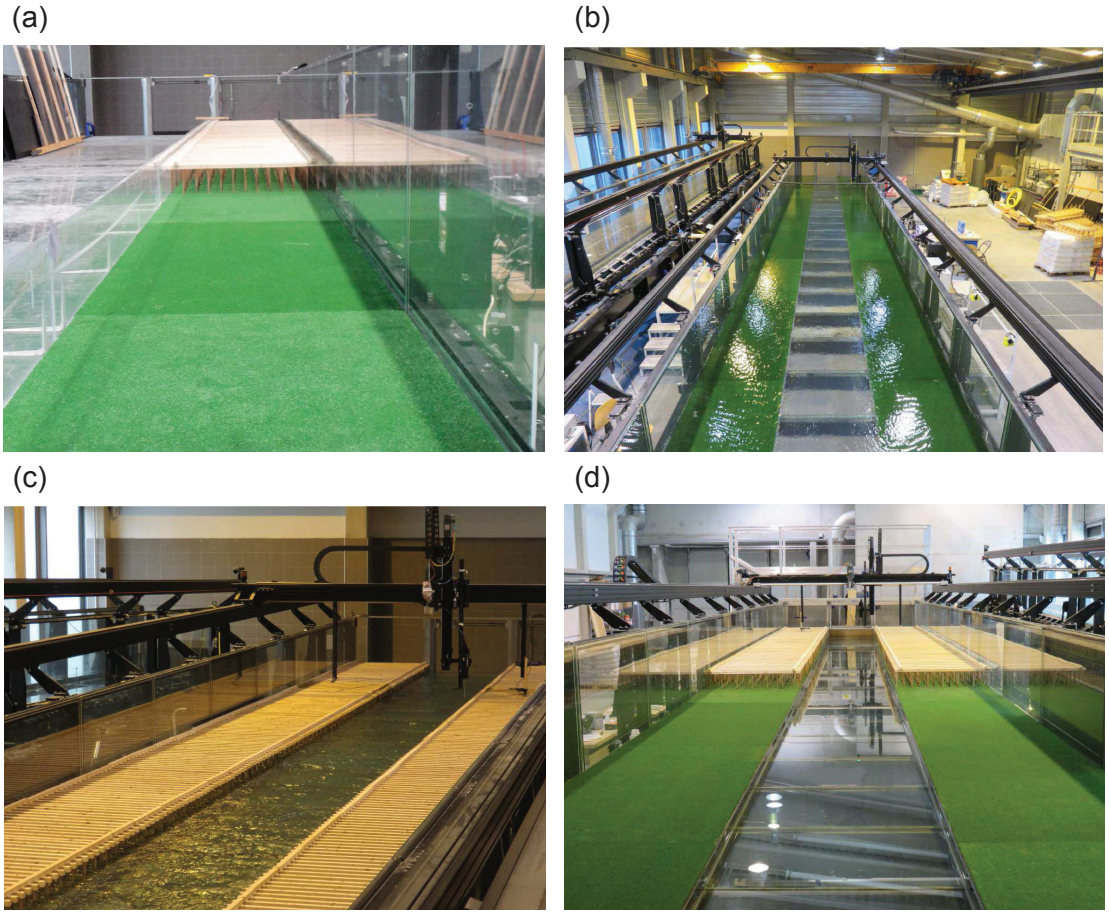

Figure 2.6: Flume viewed from upstream in configurations (a) MW, (b) CM, (c) CW and (d) viewed from downstream in configuration CWM.

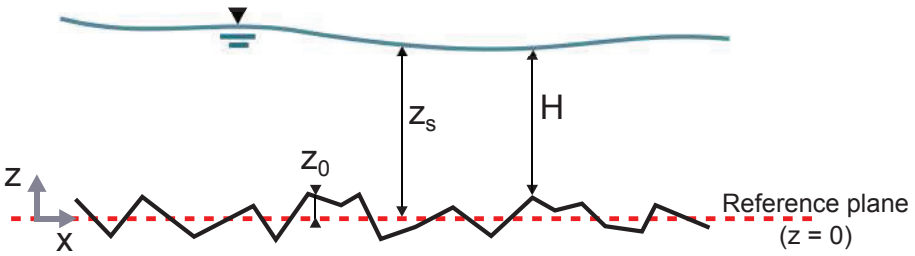

Figure 2.7: Definition of free surface level z_s. Water depth is H and bed elevation z_0.

Table 2.1: Flow conditions of the test cases: inlet main channel discharge $Q_{m,0}$, inlet floodplain discharge $Q_{f,0}$, floodplain water depth H_f, relative flow depth H_r (only for compound channel), downstream weir levels in the main channel w_m and in floodplains w_f. Values H_f and H_r are given at the most upstream measuring station ($x \approx -8\,\mathrm{m}$), at the roughness transition ($x \approx 0\,\mathrm{m}$) and at the most downstream measuring station ($x \approx 7\,\mathrm{m}$).

Test case	Single/ Compound	Floodplain roughness	$Q_{m,0}$ (L.s^{-1})	$Q_{f,0}$ (L.s^{-1})	H_f (mm)			H_r			w_m (mm)	w_f (mm)
					−8 m	0 m	7 m	-8 m	0 m	7 m		
MQ7	S	M		7		35						11
MQ15	S	M		15		55						18
MQ50	S	M		50		116.5						35
WQ7	S	W		7		55						30
WQ15	S	W		15		113						70
WQ21	S	W		21		152						98
W0Q15	S	W†		15		109						67
MWQ7	S	M-W		7	50	56	56					30
MWQ15	S	M-W		15	104	113	114					70
MWQ21	S	M-W		21	143	152	152					98
WMQ7	S	W-M		7	47	35	35					11
WMQ15	S	W-M		15	76	56	57					18
WMQ50	S	W-M		50	168	120	118					35
CM	C	M	126	18		56			0.33		31	12
CW	C	W	134	14		99			0.46		68	45
CMWQ18	C	M-W	126	18	96	105	100	0.45	0.48	0.47	31	12
CMWQ26	C	M-W	110	26	100	107	100	0.47	0.48	0.47	31	12
CWMQ18	C	W-M	126	18	67	51	55	0.37	0.31	0.32	68	45
CWMQ12	C	W-M	138	12	62	50	54	0.35	0.30	0.32	68	45

(†) For test case W0Q15 the cylinder array in installed on the glass bottom (on the plastic grass for all other test cases).

channel experiments an electronic stage gauge (Mitutoyo 570-302) was used for measuring water depth H. For the compound channel experiments ultrasonic sensors (Baumer UNDK20I69) were used for surveying free surface and bed topography. Ultrasonic sensors were also used for investigating the free-surface oscillations (seiching process in single channel, see Chapter 4). The ultrasonic sensor repeatability was ± 0.5 mm. Water depth measurements were time averaged. The convergence of this average against measuring time is presented in Fig. 2.8 for test case CM and at two locations, one in the main channel and one in the floodplain. Measuring time was set systematically to 3 min, for which the signal convergence was satisfactory. The higher measurement scatter in the main channel was due to stronger free surface motions.

Figure 2.9 shows a topographical survey of the bed elevation z_0 at three lateral positions in the main channel ($y = 1200$, 1500, 1800 mm) and at one position ($y = 850$ and 2150 mm) in each grassed floodplain. To survey the floodplains, a 2 mm thick PVC plate was set on the plastic grass, as the ultrasonic sensors were not working on the plastic grass. This PVC plate probably smoothed the topography variations. Figure 2.9 shows that the bottom variations in all subsections are in the range ± 1.5 mm all along the flume.

Figures 2.10 and 2.11 show the longitudinal profiles of water depth (or free surface level) for all uniform flow test cases in single channel (configurations M and W) and in compound channel (configurations CM and CW), respectively. The water depth (or free surface level) variations were in the range ± 1 mm for both the single and compound channel test cases (for the latter the width-averaged profile is considered, see Fig. 2.11).

2.5 Velocimetry

Mean velocity and turbulence fluctuations were recorded using a side-looking micro-ADV probe (Nortek Vectrino Plus) with a sampling rate at 100 Hz. The sampling volume is

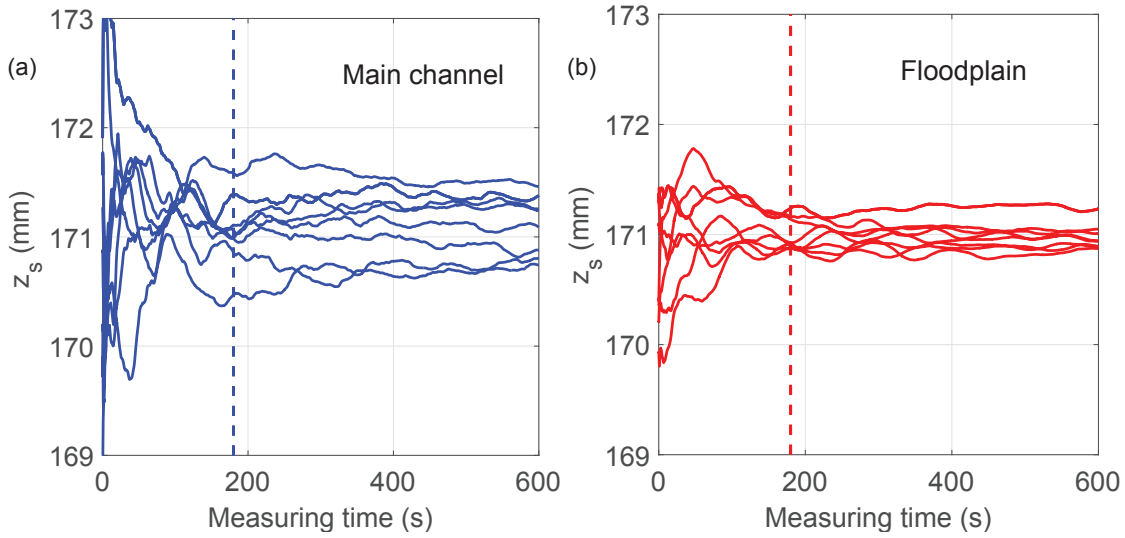

Figure 2.8: Time averaged free surface level as a function of measuring time for test case CM for nine consecutive measurements under the same conditions (a) in the main channel ($y = 1500\,\text{mm}$) and (b) in the floodplain ($y = 500\,\text{mm}$). Longitudinal position: $x = 16.15\,\text{m}$. Dotted lines show the measuring time that was applied thereafter.

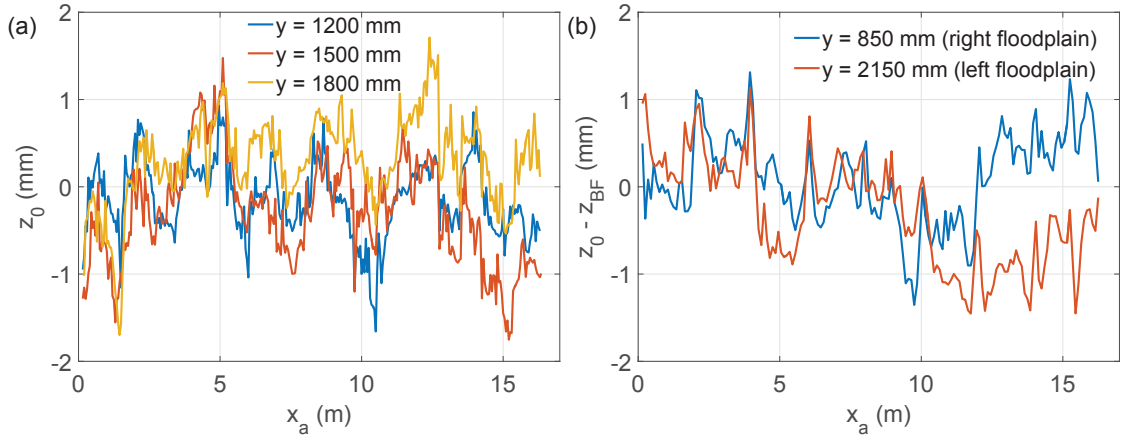

Figure 2.9: Topographical survey of bed elevation z_0 (a) in the main channel and (b) over the grassed floodplains.

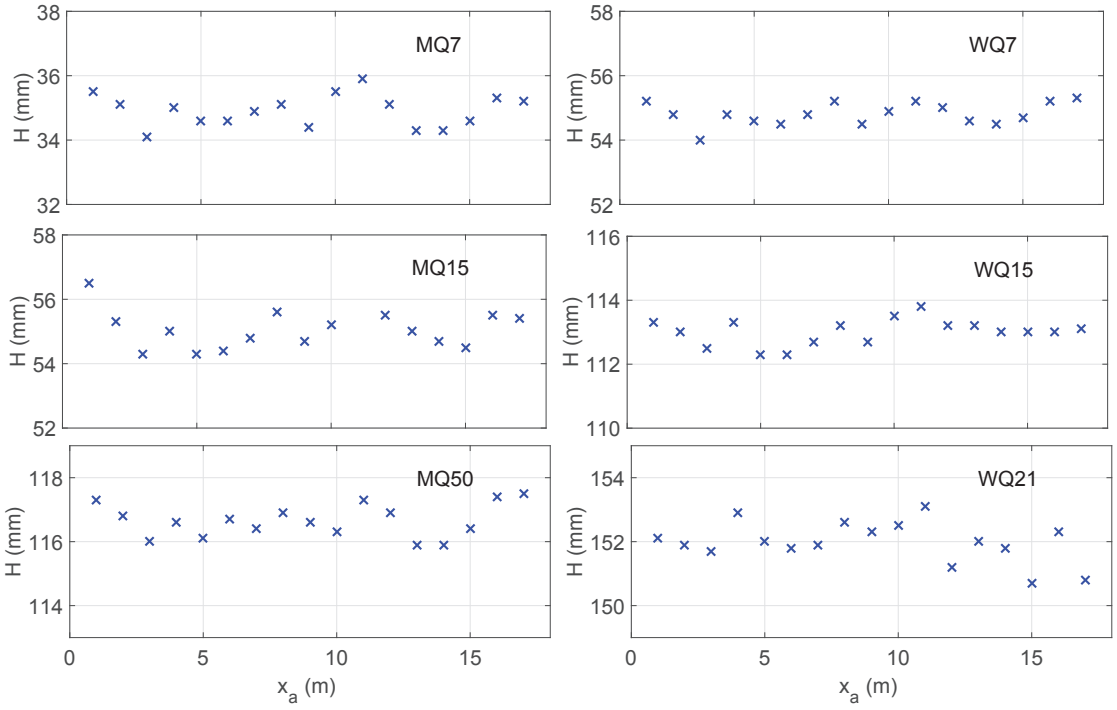

Figure 2.10: Longitudinal profile of water depth for uniform flow configurations M (left panels) and W (right panels) in single channel. Measurement with an electronic stage gauge at lateral position $y = 950\,\text{mm}$.

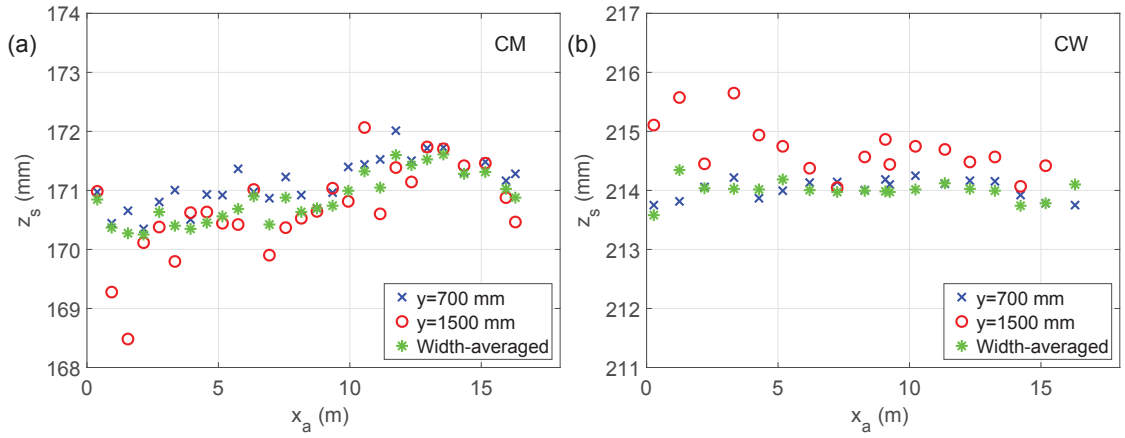

Figure 2.11: Longitudinal profile of free surface level for uniform flow test cases (a) CM and (b) CW. Blue cross and red circle markers are used for measurements at a given lateral position whereas green star markers refer to a width-averaged measurement over seven lateral positions ($y = 300, 700, 1200, 1500, 1800, 2200$ and $2700\,\text{mm}$). Measurement with ultrasonic sensor.

a circular cylinder with diameter 6 mm and length 7 mm. The ADV raw data were filtered using WinADV freeware based on the de-spiking concept developed by Goring and Nikora (2002). Seeding was hydrogen micro-bubbles for the single channel experiments. The micro-bubbles were generated by an iron-wire anode set on the flume bottom approximately 3 m upstream of the measuring point. The micro-bubble diameter was less than 0.1 mm. The associated maximum rising velocity was 5.10^{-6} m.s^{-1}, when calculated with the Stokes law, and was therefore negligible. With the reverse osmosis purified water (compound channel experiments), the micro-bubbles generator could not be used. The flow was seeded by 10 μm hollow glass spheres (Dantec) or by 50 μm polyamid powder (Evonik Vestosint 1164 white). The grain fall velocity was 2.10^{-6} m.s^{-1} and 82.10^{-6} m.s^{-1} respectively, i.e. negligible too.

Convergence tests of the time-averaged ADV signal against measuring time were carried out, as shown in Fig. 2.12 for test case CW. The measuring time was set to 120 s, for which first and second statistical moments were converged.

ADV velocity measurements were carried out across the channel section at various downstream positions. For instance, Fig. 2.13 shows the measuring mesh used for test case CM. This mesh consists in 597 points, with a refined mesh in the region of the right-hand mixing layer ($y = 1000$ mm).

ADV measurements were also carried out with two probes in order to calculate space-time correlations. The mathematical framework of the two-point space-time velocity correlation is exposed in Chapter 5. A reference probe had a constant position, whereas the second probe was moved in one direction (longitudinally, laterally or vertically). The two probes were simultaneously triggered using a LabView program. They were first positioned on either side of the same sampling volume and the moving probe was then moved away. The measuring time was set to a minimum of 600 s for ensuring a good quality of correlation computation. In order to check the influence of one probe on the other, measurements were carried out with (1) only one probe working, the other probe being out of water, (2) only one probe working, the other probe being positioned symmetrically and targeting the same sampling volume but being switched off and (3) the two probes simultaneously measuring the same sampling volume. It was found that one probe did not influence the other probe for measuring the time-averaged velocities and turbulence quantities. Figure 2.14 shows the time series of the longitudinal and lateral velocities when the two probes were measuring the same sampling volume. The lateral velocity was very similar for the two probes (Fig. 2.14b). Larger discrepancies were observed for the longitudinal velocity (Fig. 2.14a). These differences, probably due to interactions (interferences) between the two acoustic signals, led to erroneous correlations between the two measurements. Figure 2.15 shows the maximum correlation $R_{ii,max}^{(1)}$ ($i = 1$ for the longitudinal velocity and $i = 2$ for the lateral velocity) between the time series measured by the two probes when the moving probe was displaced in the longitudinal direction (longitudinal space lag ξ_1). The correlation maximum is theoretically equal to unity for a space lag equal to zero and gradually decreases with increasing space lag. The weak correlations for small spatial lags that are observed in Fig. 2.15 are attributed to the interaction between the two probes. The two probes influenced each other until a longitudinal space lag of 120 mm for the longitudinal velocity and of 60 mm for the lateral velocity. In the two other directions, the influence region of one probe on the other was far more reduced: the two probes were influencing each other for lateral spatial lags of 10-20 mm and vertical spatial lags of 5-10 mm (not shown).

Velocity measurements were also carried out with a PIV system in the single channel experiments. The PIV system is specifically described in Chapter 4.

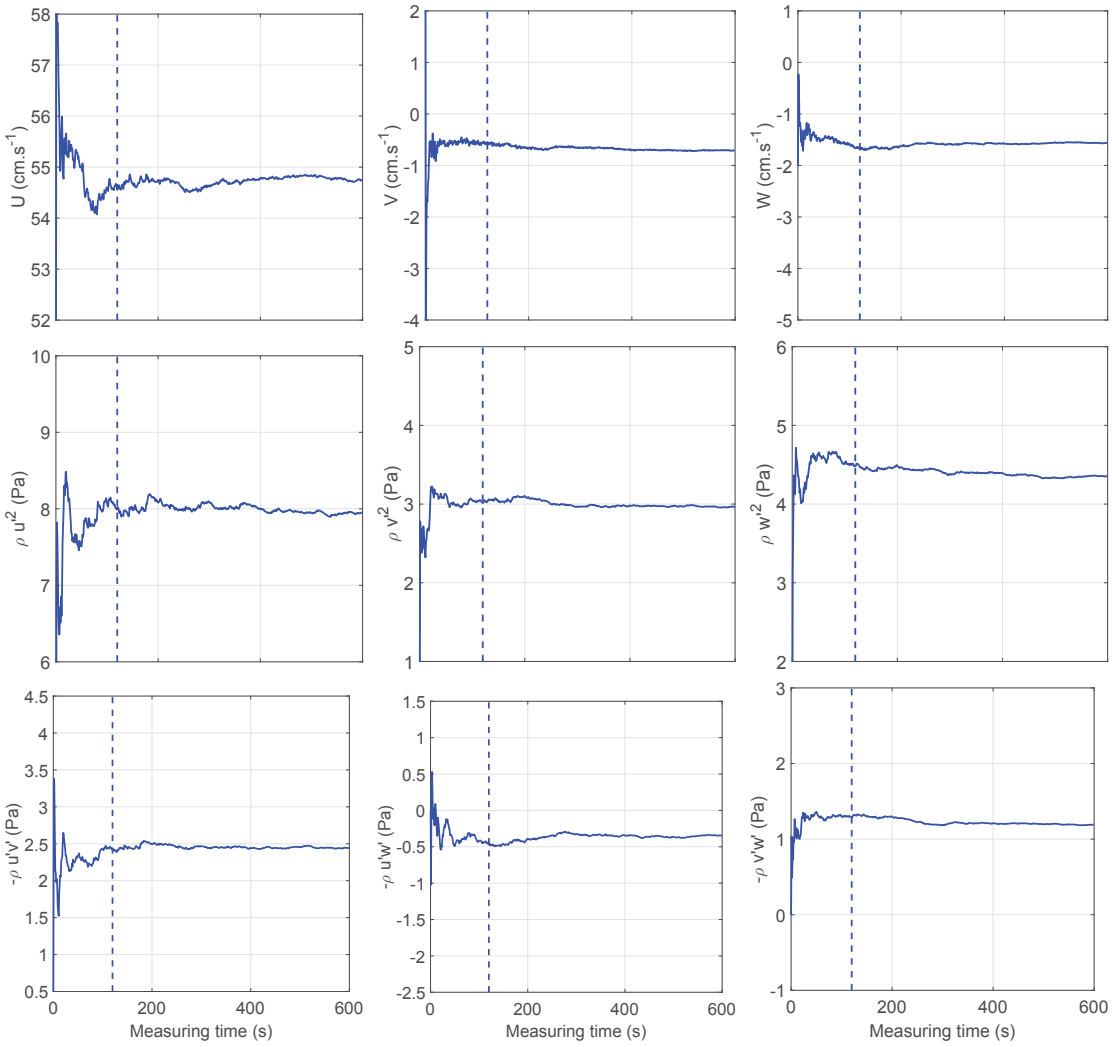

Figure 2.12: Time-averaged velocities and turbulence quantities as a function of measuring time. Test case CW at $x = 9.40\,\mathrm{m}$, $y = 1000\,\mathrm{mm}$ and $z = 143\,\mathrm{mm}$. Dotted lines show the chosen measuring time.

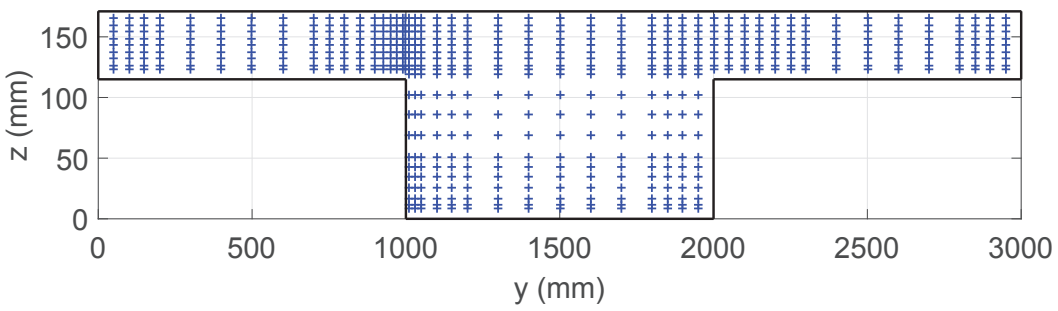

Figure 2.13: Measuring mesh for the total compound channel cross-section for test case CM.

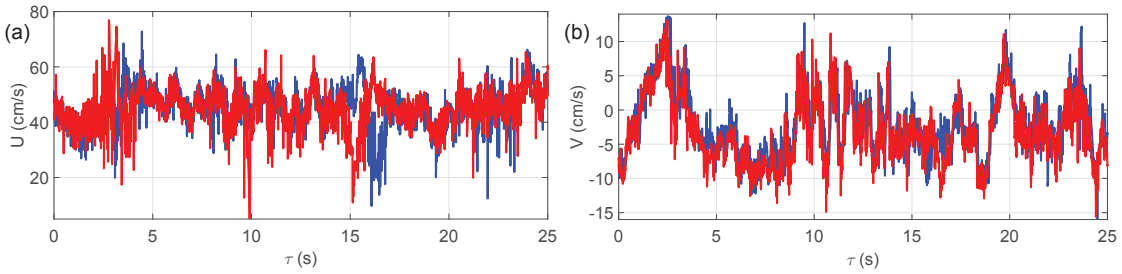

Figure 2.14: Time series of (a) longitudinal and (b) lateral velocities measured by the reference probe (blue line) and the moving probe (red line), when both probes are measuring the same sampling volume. Test case CMWQ18 at $x = 8.57\,\mathrm{m}$, $y = 1000\,\mathrm{mm}$ and $z = 206\,\mathrm{mm}$.

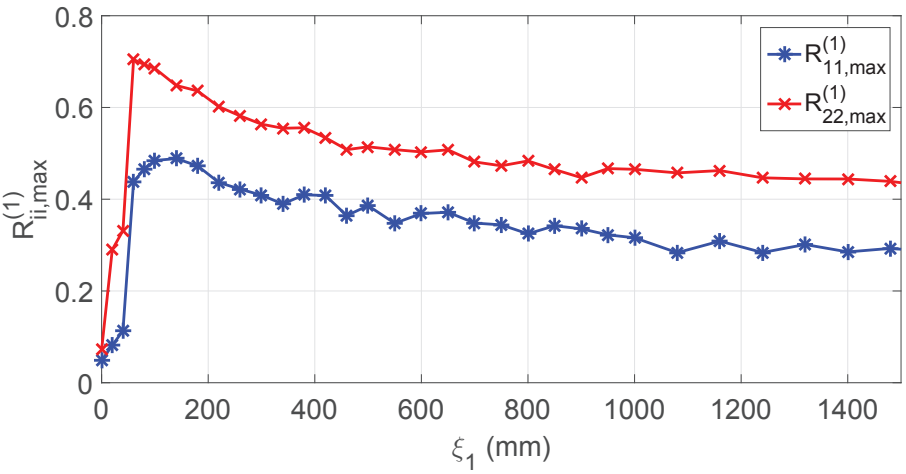

Figure 2.15: Spatial correlation for the longitudinal and lateral velocities $R^{(1)}_{11,max}$ and $R^{(1)}_{22,max}$ as a function of the longitudinal spatial lag ξ_1 between a fixed probe and a moving probe.

Chapter 3

Equations

The objective of the present chapter is to derive the equations of motion related to the different flow configurations presented in Section 2.3. We first consider the fluid dynamics equation at local scale. The equations are then depth-averaged and cross-section-averaged. In the following we note equally (x, y, z) or (x_1, x_2, x_3) the coordinates in longitudinal, lateral and vertical directions and equally (u, v, w) or (u_1, u_2, u_3) the components of the velocity vector.

3.1 Local equations

Consider the flow in the most complex configuration investigated in the present study, i.e. with a longitudinal transition in roughness in compound channel (configuration CMW and CWM). The dynamics of a Newtonian incompressible fluid is governed by the Navier-Stokes equations:

$$\frac{\partial u}{\partial x} + \frac{\partial v}{\partial y} + \frac{\partial w}{\partial z} = 0 \tag{3.1}$$

$$\rho\frac{\partial u}{\partial t} + \rho u\frac{\partial u}{\partial x} + \rho v\frac{\partial u}{\partial y} + \rho w\frac{\partial u}{\partial z} = -\frac{\partial p}{\partial x} + \rho\nu\left(\frac{\partial^2 u}{\partial x^2} + \frac{\partial^2 u}{\partial y^2} + \frac{\partial^2 u}{\partial z^2}\right) + F_{vol,x} \tag{3.2}$$

$$\rho\frac{\partial v}{\partial t} + \rho u\frac{\partial v}{\partial x} + \rho v\frac{\partial v}{\partial y} + \rho w\frac{\partial v}{\partial z} = -\frac{\partial p}{\partial y} + \rho\nu\left(\frac{\partial^2 v}{\partial x^2} + \frac{\partial^2 v}{\partial y^2} + \frac{\partial^2 v}{\partial z^2}\right) + F_{vol,y} \tag{3.3}$$

$$\rho\frac{\partial w}{\partial t} + \rho u\frac{\partial w}{\partial x} + \rho v\frac{\partial w}{\partial y} + \rho w\frac{\partial w}{\partial z} = -\frac{\partial p}{\partial z} + \rho\nu\left(\frac{\partial^2 w}{\partial x^2} + \frac{\partial^2 w}{\partial y^2} + \frac{\partial^2 w}{\partial z^2}\right) + F_{vol,z} \tag{3.4}$$

where ρ is the fluid density, ν is the fluid kinematic viscosity, $F_{vol,x}$, $F_{vol,y}$ and $F_{vol,z}$ are the sums of the volume forces acting along each direction of space. In the present case the only acting volume force is the gravitation force. Assuming that the bottom slope S_0 is small ($S_0 \ll 1$), we can write $\sin(\operatorname{atan} S_0) \approx S_0$ and $\cos S_0 \approx 1$, therefore:

$$F_{vol,x} = \rho g S_0 \tag{3.5}$$

$$F_{vol,y} = 0 \tag{3.6}$$

$$F_{vol,z} = \rho g \tag{3.7}$$

where g is the gravity acceleration.

Consider a flow that is steady in average, i.e. the velocity and pressure fields, averaged over a sufficiently long period of time, are constant with time. Following the Reynolds decomposition, the velocity and pressure fields can be divided into their time-averaged and fluctuating parts. For each flow variable ψ, the time averaged value is denoted $\overline{\psi}$ and the temporal fluctuation ψ', such that $\psi = \overline{\psi} + \psi'$. Introducing the Reynolds decomposition in Eqs. 3.1 to 3.4 and using the notations $U = \overline{u}$, $V = \overline{v}$, $W = \overline{w}$ et $P = \overline{p}$ we obtain the Reynolds Averaged Navier-Stokes equations (RANS):

$$\frac{\partial U}{\partial x} + \frac{\partial V}{\partial y} + \frac{\partial W}{\partial z} = 0 \tag{3.8}$$

$$\begin{aligned}\frac{\partial U^2}{\partial x} + \frac{\partial UV}{\partial y} + \frac{\partial UW}{\partial z} = &-\frac{1}{\rho}\frac{\partial P}{\partial x} + \nu\left(\frac{\partial^2 U}{\partial x^2} + \frac{\partial^2 U}{\partial y^2} + \frac{\partial^2 U}{\partial z^2}\right) \\ &-\frac{\partial \overline{u'u'}}{\partial x} - \frac{\partial \overline{u'v'}}{\partial y} - \frac{\partial \overline{u'w'}}{\partial z} + gS_0\end{aligned} \tag{3.9}$$

$$\begin{aligned}\frac{\partial UV}{\partial x} + \frac{\partial V^2}{\partial y} + \frac{\partial VW}{\partial z} = &-\frac{1}{\rho}\frac{\partial P}{\partial y} + \nu\left(\frac{\partial^2 V}{\partial x^2} + \frac{\partial^2 V}{\partial y^2} + \frac{\partial^2 V}{\partial z^2}\right) \\ &-\frac{\partial \overline{u'v'}}{\partial x} - \frac{\partial \overline{v'v'}}{\partial y} - \frac{\partial \overline{v'w'}}{\partial z}\end{aligned} \tag{3.10}$$

$$\begin{aligned}\frac{\partial UW}{\partial x} + \frac{\partial VW}{\partial y} + \frac{\partial W^2}{\partial z} = &-\frac{1}{\rho}\frac{\partial P}{\partial z} + \nu\left(\frac{\partial^2 W}{\partial x^2} + \frac{\partial^2 W}{\partial y^2} + \frac{\partial^2 W}{\partial z^2}\right) \\ &-\frac{\partial \overline{u'w'}}{\partial x} - \frac{\partial \overline{v'w'}}{\partial y} - \frac{\partial \overline{w'w'}}{\partial z} + g.\end{aligned} \tag{3.11}$$

In these equations the cylinder array is only present indirectly in the boundary conditions. This makes the boundary conditions geometrically very complex. In order to integrate the cylinder array directly in the equation of motion and to get them out of the boundary conditions, a spatial averaging of the equations can be carried out. The equations are thus double-averaged, in time and in space. Historically, the double-averaging concept was firstly introduced for studying flows in porous media (e.g. Gray and Lee, 1977) and was then further developed in several fields, notably by Raupach *et al.* (1991) for atmospheric flows and V. Nikora in river hydraulics (Nikora *et al.*, 2001, 2007, 2013). Double-averaging applies to flows that are spatially invariant at a given length scale but are spatially heterogeneous at a smaller length scale in at least one space direction. To give an example, a flow in a straight channel over a pebble-bed can be spatially invariant in the longitudinal direction at large scale (constant free-surface elevation and bulk velocity) but is spatially heterogeneous in the near-bed region at the pebble scale.

The double-averaging method defines a volume V around the fluid element, in which the time-averaged velocity and pressure fields are spatially averaged. Given a fluid variable ψ, the time-averaged value $\overline{\psi}$ is divided into the spatial-averaged part $\langle\overline{\psi}\rangle$ and the spatial

fluctuation $\tilde{\psi}$, such that $\overline{\psi} = \langle\overline{\psi}\rangle + \tilde{\psi}$. The volume V only extends in the directions where the spatial averaging is aimed to be carried out. In the other directions, the volume is infinitesimally small. In order to cancel the spatial gradients of the double-averaged value $\langle\overline{\psi}\rangle$ in the directions for which spatial averaging is carried out, the volume size has to be chosen at least of one order of magnitude higher than the length scale of the spatial flow heterogeneities. With the example of the pebble-bed channel, the volume V has a longitudinal and lateral size that is about 10-100 times the pebble mean size and has a infinitesimal vertical extension (the flow being intrinsically heterogeneous in the vertical direction, spatial averaging is not relevant in this direction). Note that when measuring velocities (*e.g.* with an ADV probe), spatial averaging is performed inside the sampling volume.

In the present case, we define a volume V of infinitesimal vertical extension and of longitudinal and lateral sizes that are large compared to the mean inter-cylinder spacing. By introducing the space-averaging in Eqs. 3.8 to 3.11 and using the notations $U = \langle\overline{u}\rangle$, $V = \langle\overline{v}\rangle$, $W = \langle\overline{w}\rangle$ et $P = \langle\overline{p}\rangle$, the Double Averaged Navier-Stokes equations (DANS) are obtained:

$$\frac{\partial U}{\partial x} + \frac{\partial V}{\partial y} + \frac{\partial W}{\partial z} = 0 \tag{3.12}$$

$$\begin{aligned} \frac{\partial U^2}{\partial x} + \frac{\partial UV}{\partial y} + \frac{\partial UW}{\partial z} &= -\frac{1}{\rho}\frac{\partial P}{\partial x} + \nu\left(\frac{\partial^2 U}{\partial x^2} + \frac{\partial^2 U}{\partial y^2} + \frac{\partial^2 U}{\partial z^2}\right) \\ -\frac{\partial\langle\overline{u'u'}\rangle}{\partial x} - \frac{\partial\langle\overline{u'v'}\rangle}{\partial y} - \frac{\partial\langle\overline{u'w'}\rangle}{\partial z} - \frac{\partial\langle\tilde{u}\tilde{u}\rangle}{\partial x} - \frac{\partial\langle\tilde{u}\tilde{v}\rangle}{\partial y} - \frac{\partial\langle\tilde{u}\tilde{w}\rangle}{\partial z} &+ f_{Fx} + f_{Vx} + gS_0 \end{aligned} \tag{3.13}$$

$$\begin{aligned} \frac{\partial UV}{\partial x} + \frac{\partial V^2}{\partial y} + \frac{\partial VW}{\partial z} &= -\frac{1}{\rho}\frac{\partial P}{\partial y} + \nu\left(\frac{\partial^2 V}{\partial x^2} + \frac{\partial^2 V}{\partial y^2} + \frac{\partial^2 V}{\partial z^2}\right) \\ -\frac{\partial\langle\overline{u'v'}\rangle}{\partial x} - \frac{\partial\langle\overline{v'v'}\rangle}{\partial y} - \frac{\partial\langle\overline{v'w'}\rangle}{\partial z} - \frac{\partial\langle\tilde{u}\tilde{v}\rangle}{\partial x} - \frac{\partial\langle\tilde{v}\tilde{v}\rangle}{\partial y} - \frac{\partial\langle\tilde{v}\tilde{w}\rangle}{\partial z} &+ f_{Fy} + f_{Vy} \end{aligned} \tag{3.14}$$

$$\begin{aligned} \frac{\partial UW}{\partial x} + \frac{\partial VW}{\partial y} + \frac{\partial W^2}{\partial z} &= -\frac{1}{\rho}\frac{\partial P}{\partial z} + \nu\left(\frac{\partial^2 W}{\partial x^2} + \frac{\partial^2 W}{\partial y^2} + \frac{\partial^2 W}{\partial z^2}\right) \\ &\quad -\frac{\partial\langle\overline{u'w'}\rangle}{\partial x} - \frac{\partial\langle\overline{v'w'}\rangle}{\partial y} - \frac{\partial\langle\overline{w'w'}\rangle}{\partial z} \\ &\quad -\frac{\partial\langle\tilde{u}\tilde{w}\rangle}{\partial x} - \frac{\partial\langle\tilde{v}\tilde{w}\rangle}{\partial y} - \frac{\partial\langle\tilde{w}\tilde{w}\rangle}{\partial z} + f_{Fz} + f_{Vz} + g. \end{aligned} \tag{3.15}$$

Terms f_{Fi} and f_{Vi}, $i \in \{x, y, z\}$ are the form and viscous drag forces per unit fluid mass (Raupach *et al.*, 1991), defined by:

$$f_{Fi} = -\frac{1}{\rho}\left\langle\frac{\partial\tilde{p}}{\partial x_i}\right\rangle \tag{3.16}$$

$$f_{Vi} = \nu\left\langle\frac{\partial^2\tilde{u}_i}{\partial x_j^2}\right\rangle. \tag{3.17}$$

As high Reynolds numbers are associated with the flows investigated in the present study, the viscous drag forces are neglected. The cylinder array induces a form drag force

in the longitudinal direction that can be expressed with the frontal area per unit volume a and the cylinder drag coefficient C_D (Raupach *et al.*, 1991). All other form drag forces, especially those generated by the grass blades, are neglected. Therefore:

$$f_{Fx} = -\frac{1}{2} a C_D U^2 \tag{3.18}$$

$$f_{Fy} = 0, \quad f_{Fz} = 0, \quad f_{Vi} = 0. \tag{3.19}$$

The total strain tensor is defined by:

$$\langle \tau_{x_i x_j} \rangle = \rho \left(-\langle \overline{u_i' u_j'} \rangle - \langle \tilde{u}_i \tilde{u}_j \rangle + \nu \frac{\partial \langle \overline{u_i} \rangle}{\partial x_j} \right). \tag{3.20}$$

The three contributions of the total strain tensor are: the Reynolds stress tensor $\rho \langle \overline{u_i' u_j'} \rangle$, the dissipative (or form-induced) stress tensor $\rho \langle \tilde{u}_i \tilde{u}_j \rangle$ and the viscous stress tensor $\rho \nu \partial \langle \overline{u_i} \rangle / \partial x_j$.

Equations 3.12 to 3.15 then yield:

$$\frac{\partial U}{\partial x} + \frac{\partial V}{\partial y} + \frac{\partial W}{\partial z} = 0 \tag{3.21}$$

$$\begin{aligned} \frac{\partial U^2}{\partial x} + \frac{\partial UV}{\partial y} + \frac{\partial UW}{\partial z} &= -\frac{1}{\rho} \frac{\partial P}{\partial x} \\ + \frac{1}{\rho} \left(\frac{\partial \langle \tau_{xx} \rangle}{\partial x} + \frac{\partial \langle \tau_{xy} \rangle}{\partial y} + \frac{\partial \langle \tau_{xz} \rangle}{\partial z} \right) &- \frac{1}{2} a C_D U^2 + g S_0 \end{aligned} \tag{3.22}$$

$$\frac{\partial UV}{\partial x} + \frac{\partial V^2}{\partial y} + \frac{\partial VW}{\partial z} = -\frac{1}{\rho} \frac{\partial P}{\partial y} + \frac{1}{\rho} \left(\frac{\partial \langle \tau_{xy} \rangle}{\partial x} + \frac{\partial \langle \tau_{yy} \rangle}{\partial y} + \frac{\partial \langle \tau_{yz} \rangle}{\partial z} \right) \tag{3.23}$$

$$\begin{aligned} \frac{\partial UW}{\partial x} + \frac{\partial VW}{\partial y} + \frac{\partial W^2}{\partial z} &= -\frac{1}{\rho} \frac{\partial P}{\partial z} \\ + \frac{1}{\rho} \left(\frac{\partial \langle \tau_{xz} \rangle}{\partial x} + \frac{\partial \langle \tau_{yz} \rangle}{\partial y} + \frac{\partial \langle \tau_{zz} \rangle}{\partial z} \right) &+ g. \end{aligned} \tag{3.24}$$

3.2 Depth-averaged equations

3.2.1 General case

Given a quantity ψ, we define the depth-averaging operator by:

$$\psi_d = \frac{1}{H} \int_{z=z_0}^{z=z_s} \psi(z) \, dz \tag{3.25}$$

where z_0 is the local bed elevation, z_s is the local free surface elevation and $H = z_s - z_0$ is the water depth. Depth-averaging Eqs. 3.21 to 3.24 and multiplying their by H yields:

$$\frac{\partial H U_d}{\partial x} + \frac{\partial H V_d}{\partial y} + [W]_{z=z_0}^{z=z_s} - U_{z=z_s} \frac{\partial H}{\partial x} - V_{z=z_s} \frac{\partial H}{\partial y} + U_{z=z_0} \frac{\partial z_0}{\partial x} + V_{z=z_0} \frac{\partial z_0}{\partial y} = 0 \tag{3.26}$$

$$\begin{aligned}
&\frac{\partial H(U^2)_d}{\partial x}+\frac{\partial H(UV)_d}{\partial y}-(U^2)_{z=z_s}\frac{\partial H}{\partial x}+(U^2)_{z=z_0}\frac{\partial z_0}{\partial x}\\
&-(UV)_{z=z_s}\frac{\partial H}{\partial y}+(UV)_{z=z_0}\frac{\partial z_0}{\partial y}+[UW]_{z=z_0}^{z=z_s}=\\
&-\frac{1}{\rho}\frac{\partial HP_d}{\partial x}+\frac{1}{\rho}P_{z=z_s}\frac{\partial H}{\partial x}-\frac{1}{\rho}P_{z=z_0}\frac{\partial z_0}{\partial x}\\
&+\frac{1}{\rho}\left(\frac{\partial H\langle\tau_{xx}\rangle_d}{\partial x}+\frac{\partial H\langle\tau_{xy}\rangle_d}{\partial y}+[\langle\tau_{xz}\rangle]_{z=z_0}^{z=z_s}\right.\\
&\left.-\langle\tau_{xx}\rangle_{z=z_s}\frac{\partial H}{\partial x}+\langle\tau_{xx}\rangle_{z=z_0}\frac{\partial z_0}{\partial x}-\langle\tau_{xy}\rangle_{z=z_s}\frac{\partial H}{\partial y}+\langle\tau_{xy}\rangle_{z=z_0}\frac{\partial z_0}{\partial y}\right)\\
&-\frac{1}{2}aC_DH(U_d)^2+gS_0H
\end{aligned}\tag{3.27}$$

$$\begin{aligned}
&\frac{\partial H(UV)_d}{\partial x}+\frac{\partial H(V^2)_d}{\partial y}-(UV)_{z=z_s}\frac{\partial H}{\partial x}+(UV)_{z=z_0}\frac{\partial z_0}{\partial x}\\
&-(V^2)_{z=z_s}\frac{\partial H}{\partial y}+(V^2)_{z=z_0}\frac{\partial z_0}{\partial y}+[VW]_{z=z_0}^{z=z_s}=\\
&-\frac{1}{\rho}\frac{\partial HP_d}{\partial y}+\frac{1}{\rho}P_{z=z_s}\frac{\partial H}{\partial y}-\frac{1}{\rho}P_{z=z_0}\frac{\partial z_0}{\partial y}\\
&+\frac{1}{\rho}\left(\frac{\partial H\langle\tau_{xy}\rangle_d}{\partial x}+\frac{\partial H\langle\tau_{yy}\rangle_d}{\partial y}+[\langle\tau_{yz}\rangle]_{z=z_0}^{z=z_s}\right.\\
&\left.-\langle\tau_{xy}\rangle_{z=z_s}\frac{\partial H}{\partial x}+\langle\tau_{xy}\rangle_{z=z_0}\frac{\partial z_0}{\partial x}-\langle\tau_{yy}\rangle_{z=z_s}\frac{\partial H}{\partial y}+\langle\tau_{yy}\rangle_{z=z_0}\frac{\partial z_0}{\partial y}\right)
\end{aligned}\tag{3.28}$$

$$\begin{aligned}
&\frac{\partial H(UW)_d}{\partial x}+\frac{\partial H(VW)_d}{\partial y}-(UW)_{z=z_s}\frac{\partial H}{\partial x}+(UW)_{z=z_0}\frac{\partial z_0}{\partial x}\\
&-(VW)_{z=z_s}\frac{\partial H}{\partial y}+(VW)_{z=z_0}\frac{\partial z_0}{\partial y}+[W^2]_{z=z_0}^{z=z_s}=\\
&-\frac{1}{\rho}[P]_{z=z_0}^{z=z_s}+\frac{1}{\rho}\left(\frac{\partial H\langle\tau_{xz}\rangle_d}{\partial x}+\frac{\partial H\langle\tau_{yz}\rangle_d}{\partial y}+[\langle\tau_{zz}\rangle]_{z=z_0}^{z=z_s}\right.\\
&\left.-\langle\tau_{xz}\rangle_{z=z_s}\frac{\partial H}{\partial x}+\langle\tau_{xz}\rangle_{z=z_0}\frac{\partial z_0}{\partial x}-\langle\tau_{yz}\rangle_{z=z_s}\frac{\partial H}{\partial y}+\langle\tau_{yz}\rangle_{z=z_0}\frac{\partial z_0}{\partial y}\right)+gH.
\end{aligned}\tag{3.29}$$

The Leibniz rule is used for inverting integration and derivation operations. It is responsible for the new terms that are calculated at the boundaries. For a given quantity ψ, the notation $\psi_{x=x_1}=\psi(x=x_1)$ and $[\psi]_{x=x_1}^{x=x_2}=\psi(x=x_2)-\psi(x=x_1)$ are used.

3.2.2 Within a subsection

In single channel or within a subsection in compound channel, bed elevation z_0 is constant, therefore:

$$\frac{\partial z_0}{\partial x}=0,\quad \frac{\partial z_0}{\partial y}=0.\tag{3.30}$$

Furthermore, we assume that the lateral gradient of water depth is equal to zero:

$$\frac{\partial H}{\partial y} = 0. \tag{3.31}$$

The no-slip condition on the bottom yields:

$$U_{z=z_0} = 0, \quad V_{z=z_0} = 0, \quad W_{z=z_0} = 0 \tag{3.32}$$

and the slip condition on the free surface yields:

$$W_{z=z_s} = U_{z=z_s} \frac{\partial H}{\partial x}. \tag{3.33}$$

Equations 3.26 to 3.29 then become:

$$\frac{\partial H U_d}{\partial x} + \frac{\partial H V_d}{\partial y} = 0 \tag{3.34}$$

$$\begin{aligned} \frac{\partial H (U^2)_d}{\partial x} + \frac{\partial H (UV)_d}{\partial y} = -\frac{1}{\rho}\frac{\partial H P_d}{\partial x} + \frac{1}{\rho} P_{z=z_s} \frac{\partial H}{\partial x} \\ + \frac{1}{\rho}\left(\frac{\partial H \langle \tau_{xx} \rangle_d}{\partial x} + \frac{\partial H \langle \tau_{xy} \rangle_d}{\partial y} + [\langle \tau_{xz} \rangle]_{z=z_0}^{z=z_s} - \langle \tau_{xx} \rangle_{z=z_s} \frac{\partial H}{\partial x} \right) \\ - \frac{1}{2} a C_D H (U_d)^2 + g S_0 H \end{aligned} \tag{3.35}$$

$$\begin{aligned} \frac{\partial H (UV)_d}{\partial x} + \frac{\partial H (V^2)_d}{\partial y} - (UV)_{z=z_s} \frac{\partial H}{\partial x} + (VW)_{z=z_s} = -\frac{1}{\rho}\frac{\partial H P_d}{\partial y} \\ + \frac{1}{\rho}\left(\frac{\partial H \langle \tau_{xy} \rangle_d}{\partial x} + \frac{\partial H \langle \tau_{yy} \rangle_d}{\partial y} + [\langle \tau_{yz} \rangle]_{z=z_0}^{z=z_s} - \langle \tau_{xy} \rangle_{z=z_s} \frac{\partial H}{\partial x} \right) \end{aligned} \tag{3.36}$$

$$\begin{aligned} \frac{\partial H (UW)_d}{\partial x} + \frac{\partial H (VW)_d}{\partial y} - (UW)_{z=z_s} \frac{\partial H}{\partial x} + W^2_{z=z_s} = -\frac{1}{\rho}[P]_{z=z_0}^{z=z_s} \\ + \frac{1}{\rho}\left(\frac{\partial H \langle \tau_{xz} \rangle_d}{\partial x} + \frac{\partial H \langle \tau_{yz} \rangle_d}{\partial y} + [\langle \tau_{zz} \rangle]_{z=z_0}^{z=z_s} - \langle \tau_{xz} \rangle_{z=z_s} \frac{\partial H}{\partial x} \right) + gH. \end{aligned} \tag{3.37}$$

3.3 Section-averaged equations

3.3.1 General case

Given a quantity ψ and given two lateral positions y_1 and y_2, the width-averaging operator is defined by:

$$\psi_w = \frac{1}{B} \int_{y=y_1}^{y=y_2} \psi(y)\, dy \tag{3.38}$$

where $B = y_2 - y_1$. After width-averaging Eqs. 3.34 and 3.35 and multiplying them by B we obtain:

$$B \frac{\partial H U_{d,w}}{\partial x} + H [V_d]_{y_1}^{y_2} = 0 \tag{3.39}$$

$$B\frac{\partial H(U^2)_{d,w}}{\partial x} + H[(UV)_d]_{y_1}^{y_2} = -\frac{B}{\rho}\frac{\partial H P_{d,w}}{\partial x} + \frac{1}{\rho}P_{z=z_s,w}\frac{\partial H}{\partial x}B$$
$$+\frac{1}{\rho}\left(B\frac{\partial H\langle\tau_{xx}\rangle_{d,w}}{\partial x} + H[\langle\tau_{xy}\rangle_d]_{y_1}^{y_2} + ([\langle\tau_{xz}\rangle]_{z=z_0}^{z=z_s})_w B - \langle\tau_{xx}\rangle_{z=z_s,w}\frac{\partial H}{\partial x}B\right)$$
$$-\frac{1}{2}aC_D HB(U_{d,w})^2 + gS_0 HB. \qquad (3.40)$$

Since positions y_1 and y_2 are constant, the Leibniz rule does not introduce new terms. In the following we only consider the momentum equation in the longitudinal direction.

The assumption of a hydrostatic mean pressure distribution over the water column yields:

$$P(z) = P_{z=z_s} + \rho g\cos(\operatorname{atan} S_0)(H - z) \approx P_{z=z_s} + \rho g(H - z). \qquad (3.41)$$

Using Eq. 3.41, the first two terms on the right of Eq. 3.40 can be simplified and Eq. 3.40 becomes:

$$B\frac{\partial H(U^2)_{d,w}}{\partial x} + H[(UV)_d]_{y_1}^{y_2} =$$
$$-BHg\frac{\partial H}{\partial x} + \frac{1}{\rho}\left(B\frac{\partial H\langle\tau_{xx}\rangle_{d,w}}{\partial x} + H[\langle\tau_{xy}\rangle_d]_{y_1}^{y_2} + ([\langle\tau_{xz}\rangle]_{z=z_0}^{z=z_s})_w B\right.$$
$$\left.-\langle\tau_{xx}\rangle_{z=z_s,w}\frac{\partial H}{\partial x}B\right) - \frac{1}{2}aC_D HB(U_{d,w})^2 + gS_0 HB. \qquad (3.42)$$

Dividing Eq. 3.42 by gHB and rearranging it yields:

$$S_0 = \frac{1}{gH}\frac{\partial H(U^2)_{d,w}}{\partial x} - \frac{1}{\rho gH}\frac{\partial H\langle\tau_{xx}\rangle_{d,w}}{\partial x} + \frac{1}{gB}[(UV)_d]_{y_1}^{y_2}$$
$$+\frac{\partial H}{\partial x} - \frac{1}{\rho gB}[\langle\tau_{xy}\rangle_d]_{y_1}^{y_2} - \frac{1}{\rho gH}([\langle\tau_{xz}\rangle]_{z=z_0}^{z=z_s})_w$$
$$+\frac{1}{\rho gH}\frac{\partial H}{\partial x}\langle\tau_{xx}\rangle_{z=z_s,w} + \frac{1}{2g}aC_D(U_{d,w})^2. \qquad (3.43)$$

The term on the left of Eq. 3.43 represents the gravitation force. The eight terms on the right stand for, in order of appearance: (1) longitudinal flux of mean flow momentum, (2) longitudinal flux of turbulent momentum, (3) lateral exchange of mean flow momentum, (4) pressure term, (5) lateral turbulent momentum exchange, (6) bed and free surface friction, (7) turbulent pressure on the free surface, (8) cylinder drag forces.

Equation 3.43 is now applied to the different flow configurations presented in Section 2.3.

3.3.2 Configurations M and W

Consider a fully developed uniform flow over the meadow-type or wood-type vegetation in single channel. Equation 3.43 is applied to the total channel cross-section, i.e. width-averaging is carried out between $y_1 = 0$ and $y_2 = 1000\,\text{mm}$.

Due to flow uniformity, the longitudinal gradients of mean quantities are equal to zero (terms 1, 2, 4, and 7 on the right of Eq. 3.43). Furthermore, the secondary currents are equal to zero on the side walls (term 3). The momentum equation becomes:

$$S_0 = -\frac{1}{\rho gB}[\langle\tau_{xy}\rangle_d]_{y=0}^{y=1000} - \frac{1}{\rho gH}([\langle\tau_{xz}\rangle]_{z=z_0}^{z=z_s})_w + \frac{1}{2g}aC_D(U_{d,w})^2. \qquad (3.44)$$

Assuming a negligible friction at the free surface and using flow symmetry, Eq. 3.44 becomes:

$$S_0 = \frac{2}{\rho g B}\langle\tau_{xy}\rangle_{y=0,d} + \frac{1}{\rho g H}\langle\tau_{xz}\rangle_{z=z_0,w} + \frac{1}{2g}aC_D(U_{d,w})^2. \tag{3.45}$$

Since the side walls are of glass and the bottom is a rough bed, and since additionally $2H < B$, friction on the side walls can be neglected compared to bottom friction in first approximation. For flow over the meadow only (configuration M), bed friction can be expressed with the Manning roughness coefficient of the plastic grass n:

$$\langle\tau_{xz}\rangle_{z=z_0,w} = \frac{\rho g n^2 (U_{d,w})^2}{H^{1/3}}. \tag{3.46}$$

The assumption is made that Eq. 3.46 is still valid in first approximation for a flow with a cylinder array. This assumption will be discussed in Chapter 4. We then obtain:

$$S_0 = \frac{1}{\rho g H}\langle\tau_{xz}\rangle_{z=z_0,w} + \frac{1}{2g}aC_D(U_{d,w})^2. \tag{3.47}$$

Note that for configuration M, the second term on the right of Eq. 3.47 vanishes.

3.3.3 Configurations MW and WM

Consider a non-uniform flow over the meadow-type or wood-type vegetation in single channel. Similarly to Section 3.3.2, width-averaging is carried out over the total section, between $y_1 = 0$ and $y_2 = 1000\,\text{mm}$. Secondary currents vanish at the side walls and friction on the free surface and on the glass side walls are neglected compared to the friction on the rough bed, such that Eq. 3.43 becomes:

$$\begin{aligned} S_0 = \frac{1}{gH}\frac{\partial H(U^2)_{d,w}}{\partial x} - \frac{1}{\rho g H}\frac{\partial H\langle\tau_{xx}\rangle_{d,w}}{\partial x} + \frac{\partial H}{\partial x} \\ + \frac{1}{\rho g H}\langle\tau_{xz}\rangle_{z=z_0,w} + \frac{1}{\rho g H}\frac{\partial H}{\partial x}\langle\tau_{xx}\rangle_{z=z_s,w} + \frac{1}{2g}aC_D(U_{d,w})^2. \end{aligned} \tag{3.48}$$

The present experimental measurements show that the longitudinal flux of turbulent momentum (second term on the right of Eq. 3.48) is negligible compared to the longitudinal flux of mean flow momentum (first term). The turbulent pressure on the free surface is also negligible (fifth term). Using a Boussinesq coefficient of $\beta = 1$ we have $(U^2)_{d,w} = \beta U_Q^2 = U_Q^2$, where $U_Q = U_{d,w} = Q/(HB)$ is the section-averaged (or bulk) velocity, with Q the flow rate. As in Section 3.3.2, we assume that bed friction can be calculated with Eq. 3.46, even in the cylinder array. Equation 3.48 then becomes:

$$S_0 = \frac{\partial H}{\partial x}\left(1 - \frac{Q^2}{gBH^3}\right) + \frac{n^2 Q^2}{B^2 H^{10/3}} + \frac{aC_D Q^2}{2gH^2B^2}. \tag{3.49}$$

This equation is numerically solved for all test cases MW and WM in Chapter 4.

3.3.4 Configurations CM and CW

Consider a fully developed uniform compound channel flow with meadow-type or wood-type vegetation over the floodplains. Equation 3.43 is first applied to the main channel, i.e. width-averaging is carried out between $y_1 = 1000$ and $y_2 = 2000\,\text{mm}$

With the uniformity hypothesis, using the flow symmetry and noting that cylinder drag is equal to zero, the momentum equation becomes:

$$S_0 = -\frac{2}{gB_m}(UV)_{y=1000,d} + \frac{2}{\rho g B_m}\langle\tau_{xy}\rangle_{d_{y=1000}} - \frac{1}{\rho g H_m}([\langle\tau_{xz}\rangle]_{z=z_0}^{z=z_s})_w \tag{3.50}$$

with H_m the main channel flow depth and B_m the main channel width.

Equation 3.43 is then applied to the right floodplain, i.e. width-averaging is carried out between $y_1 = 0$ and $y_2 = 1000\,\text{mm}$:

$$S_0 = \frac{1}{gB_f}(UV)_{y=1000,d} - \frac{1}{\rho g B_f}[\langle\tau_{xy}\rangle_d]_{y=1000}^{y=0} - \frac{1}{\rho g H_f}([\langle\tau_{xz}\rangle]_{z=z_0}^{z=z_s})_w + \frac{1}{2g}aC_D(U_{d,w})^2 \tag{3.51}$$

with H_f the floodplain flow depth and B_f the floodplain width.

3.3.5 Configurations CMW and CWM

Consider a non uniform flow over the meadow-type or wood-type vegetation in compound channel configuration. Equation 3.43 is first applied to the main channel ($y_1 = 1000$ and $y_2 = 2000\,\text{mm}$):

$$\begin{aligned} S_0 = \frac{1}{gH_m}\frac{\partial H_m (U^2)_{d,w}}{\partial x} - \frac{1}{\rho g H_m}\frac{\partial H_m \langle\tau_{xx}\rangle_{d,w}}{\partial x} - \frac{2}{gB_m}(UV)_{y=y_{int},d} \\ + \frac{\partial H_m}{\partial x} + \frac{2}{\rho g B_m}\langle\tau_{xy}\rangle_{d_{y=y_{int}}} - \frac{1}{\rho g H_m}([\langle\tau_{xz}\rangle]_{z=z_0}^{z=z_s})_w \\ + \frac{1}{\rho g H_m}\frac{\partial H_m}{\partial x}\langle\tau_{xx}\rangle_{z=z_s,w} \end{aligned} \tag{3.52}$$

where $y_{int} = 1000\,\text{mm}$. According to Eq. 3.52, the gravitational forces (bottom slope) are balanced by (in the order of appearance on the right of the equation): (1) the longitudinal flux of mean flow momentum, (2) the longitudinal flux of turbulent momentum, (3) the mean flow momentum exchange at the interface, (4) the pressure forces, (5) the turbulent momentum exchange at the interface, (6) the bed and free surface frictions, (7) the turbulent pressure forces on the free surface.

For sake of simplicity, following assumptions are made:

1. Free surface friction is neglected.

2. As experimentally measured, the longitudinal flux of turbulent momentum ($-\frac{1}{\rho g H_m}\frac{\partial H_m \langle\tau_{xx}\rangle_{d,w}}{\partial x}$) and the turbulent pressure forces on the free surface ($\frac{1}{\rho g H_m}\frac{\partial H_m}{\partial x}\langle\tau_{xx}\rangle_{z=z_s,w}$) are of the order of 4% and 0.2% of the gravity term, respectively. They are therefore neglected.

3. A Boussinesq coefficient of unity is assumed, i.e. $(U^2)_{d,w} = \beta U_m^2 = U_m^2$.

4. The mean flow momentum exchange at the interface can be rewritten:

$$(UV)_d = U_d V_d - (U(V - V_d))_d \tag{3.53}$$

where the first term on the right represents the lateral exchange due to net lateral flux and the second term represents the lateral exchange due to secondary currents

(Vermaas *et al.*, 2011). The depth-averaged lateral velocity at the interface can be calculated using the longitudinal variation of discharge within the main channel:

$$V_{d,y=y_{int}} = \frac{1}{2H_m}\frac{\partial B_m H_m U_m}{\partial x}. \tag{3.54}$$

As experimentally measured, the exchange due to secondary currents can be neglected (this point will be discussed in Chapter 6). The third term on the right of Eq. 3.52 finally becomes:

$$\frac{-2}{gB_m}(UV)_{y=y_{int},d} = \frac{-U_{d,y=y_{int}}}{gH_m}\frac{\partial H_m U_m}{\partial x}. \tag{3.55}$$

With these assumptions Eq. 3.52 becomes:

$$\begin{aligned} S_0 = \frac{1}{gH_m}\frac{\partial H_m U_m^2}{\partial x} - \frac{U_{d,y=y_{int}}}{gH_m}\frac{\partial H_m U_m}{\partial x} + \frac{\partial H_m}{\partial x} \\ + \frac{2H_f\langle\tau_{xy}\rangle_{y=y_{int},z>z_{BF},d}}{\rho g H_m B_m} + \frac{\langle\tau_{xz}\rangle_{z=0,w}}{\rho g H_m} + \frac{2z_{BF}\langle\tau_{xy}\rangle_{y=y_{int},z<z_{BF},d}}{\rho g H_m B_m}. \end{aligned} \tag{3.56}$$

Equation 3.43 is then applied to the right floodplain, i.e. width-averaging is carried out between $y_1 = 0$ and $y_2 = 1000\,\mathrm{mm}$:

$$\begin{aligned} S_0 = \frac{1}{gH_f}\frac{\partial H_f (U^2)_{d,w}}{\partial x} - \frac{1}{\rho g H_f}\frac{\partial H_f\langle\tau_{xx}\rangle_{d,w}}{\partial x} + \frac{1}{gB_f}(UV)_{y=y_{int},d} \\ + \frac{\partial H_f}{\partial x} - \frac{1}{\rho g B_f}[\langle\tau_{xy}\rangle_d]_{y=0}^{y=y_{int}} - \frac{1}{\rho g H_f}([\langle\tau_{xz}\rangle]_{z=z_0}^{z=z_s})_w \\ + \frac{1}{\rho g H_f}\frac{\partial H_f}{\partial x}\langle\tau_{xx}\rangle_{z=z_s,w} + \frac{1}{2g}aC_D(U_{d,w})^2. \end{aligned} \tag{3.57}$$

Making similar assumptions as those for the main channel equation, Eq. 3.57 can be simplified into:

$$\begin{aligned} S_0 = \frac{1}{gH_f}\frac{\partial H_f U_f^2}{\partial x} - \frac{U_{d,y=y_{int}}}{gH_f}\frac{\partial H_f U_f}{\partial x} + \frac{\partial H_f}{\partial x} \\ - \frac{(\tau_{xy})_{d,y=y_{int},z>z_{BF}}}{\rho g B_f} + \frac{(\tau_{xz})_{w,z=z_0}}{\rho g H_f} + \frac{aC_D U_f^2}{2g}. \end{aligned} \tag{3.58}$$

Chapter 4

Combined effects of bed friction and emergent cylinder drag in open channel flow

Preliminary note

The present chapter corresponds to a journal article published in *Environmental Fluid Mechanics* (Dupuis *et al.*, 2016). Some comments and discussions, that do not appear in the article, are added (small font size), but can be skipped by the reader without hindering the understanding.

4.1 Introduction

Longitudinal transitions in hydraulic roughness often characterise environmental open channel flows, for example, where floodplain vegetation changes along a river. A first common form of transition is a sudden change in bed roughness. This has been experimentally investigated by Robert *et al.* (1992), Chen and Chiew (2003) and Carravetta and Della Morte (2004). There is a second type of roughness transition between bed roughness and emergent elements, for example a longitudinal transition in a floodplain between a deeply flooded meadow and a wood. This laboratory study focuses on the latter type of transition featuring a meadow modelled by plastic grass and trees represented by an array of emergent vertical cylinders.

Longitudinal transitions between two bed roughnesses have been widely investigated in the literature for air flows in wind tunnels (Antonia and Luxton, 1971; Cheng and Castro, 2002; Pendergrass and Arya, 1984) and in air ducts (Siuru and Logan, 1977). The sudden or so-called step change in roughness generates a new layer, which starts at the wall and grows vertically towards the free stream region (or towards the duct axis).

In order to characterize the magnitude of the roughness change, Antonia and Luxton (1971) defined the roughness step as $M_0 = \ln(z_{02}/z_{01})$, where z_{01} and z_{02} are roughness length scales of the downstream and upstream roughness, respectively. For $M_0 = -4.6$, these authors estimated the distance downstream from the transition L_{dw} for the new layer to span the entire boundary layer (junction) at $L_{dw} = 20H$, where H is the boundary layer height at the junction. From the experiments of Cheng and Castro (2002), an adjustment length of $L_{dw} = 24H$ can be evaluated, corresponding to a roughness step change of $M_0 = -2.4$. With air pipes, Siuru and Logan (1977) observed a fully developed boundary layer after 20 pipe radius with a roughness step of about $M_0 = -8.5$. As a result, with air flows the adjustment length downstream from the roughness step L_{dw} appears to be independent of the roughness step value, and of the order of 20 boundary layer heights.

Longitudinal changes in bed roughness for open channel flows have been investigated much less. Chen and Chiew (2003) have shown that velocity profile adjustment to the downstream roughness does not extend gradually from the wall to the free stream region, as it does in air flows, but simultaneously over the entire flow depth. Chen and Chiew (2004) and Carravetta and Della Morte (2004) have indicated that additional effects can appear, such as shear stress overshoot, if the roughness step change is associated with a step change in bed level.

With an estimated roughness step change of $M_0 = -2.4$, Chen and Chiew (2003) observe a fully developed boundary layer after a distance of about 6 water depths. As a result, the response of the mean velocity profile to a roughness step change appears to be faster for open channel flows than for air flows.

Flows through emergent elements, usually vertical cylinder arrays, have been mainly studied under uniform flow conditions (Liu *et al.*, 2008; Martino *et al.*, 2012; Poggi *et al.*, 2004). Flow through an emergent cylinder array is driven by a volume drag force, which generates turbulence throughout the water column. This results in constant mean velocity and turbulence quantities throughout the depth. The physical processes are thus very different to those resulting from a vertical boundary layer on a bed roughness, for which turbulence production is limited to the near-bed region (Raupach *et al.*, 1991). Note that Ricardo *et al.* (2014) analysed experimentally the turbulent kinetic energy budget within a random array of emergent cylinders with the combination of LDA and PIV measurements. Flows through emergent cylinder arrays are also associated with free surface oscillations, namely transverse waves whose amplitude can reach 35 % of the water depth (Zima and Ackermann, 2002).

Zong and Nepf (2010) and Rominger and Nepf (2011) have investigated flows through patches of cylinder arrays occupying only a part of the channel width. Such flows are characterised by a lateral mixing layer developing between the flow through the cylinder array and the free stream. To the author's knowledge, a step change from bed friction to emergent element drag across the entire channel width has not been addressed in the literature. In the present study, we investigate experimentally the transition from (1) bed roughness, typically a fully submerged dense meadow in a river floodplain, to (2) an array of emergent cylinders, typically emergent trees in a wooded floodplain, and *vice versa*. The cylinder array was installed on the bed roughness to more closely represent actual field conditions.

The first objective of this study is to assess the combined effects of bed friction and cylinder drag within the cylinder array. The second objective is to assess the response of flow depth and velocity to longitudinal change from bed friction to emergent cylinder drag. In particular, the distances upstream and downstream of the transition, beyond which the flow can be considered as uniform, need to be evaluated.

The experimental setup is described in Section 4.2 and includes five flow configurations. Each type of roughness (bed roughness and cylinder array) is investigated under uniform flow conditions. Special attention is given to the flow in the near-bed region within the cylinder array and to the free surface oscillation phenomenon (seiching). The results of this part of the study are presented in Section 4.3. The uniform flows are used as references for studying the roughness transitions, which are presented in Section 4.4. The water depth response to the roughness transition is first investigated and a 1D momentum equation is used to predict the water surface profile. The response of velocity and turbulence is then analysed. Finally, Section 4.4 ends with the effect of flow non-uniformity on free surface oscillations.

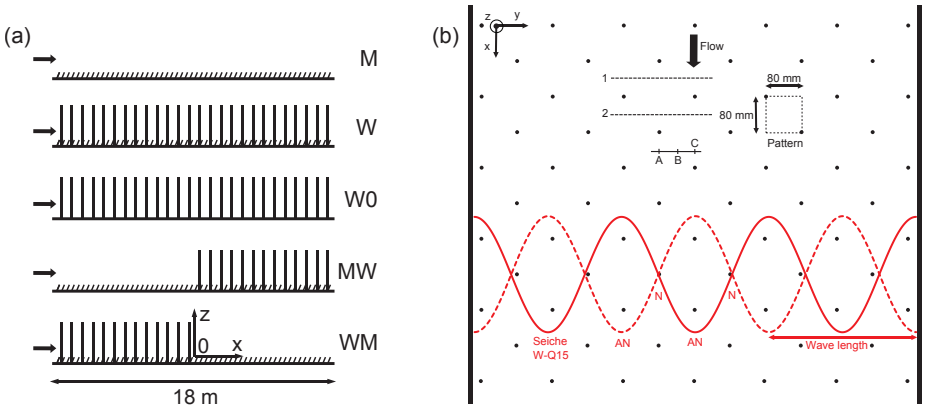

Figure 4.1: (a) Side view of the flow configurations. (b) Plan view of cylinder array. Points A, B and C are velocity measuring positions. Profiles 1 and 2 are measuring positions of water depth for seiching. Red indications relate to seiching in test case W-Q15. Points AN and N are antinodes and nodes respectively.

4.2 Experimental setup and methodology

Experiments were performed in an 18 m long, 1 m wide glass-wall flume in the Hydraulics and Hydromorphology Laboratory at Irstea Lyon-Villeurbanne, France. The longitudinal bottom slope was $S_0 = 1.05\,\mathrm{mm/m}$. Longitudinal, lateral and vertical coordinates were denoted by x, y and z respectively. The channel cross section was rectangular and its width denoted by $B = 1\,\mathrm{m}$.

Four main flow configurations were investigated as outlined in Fig. 4.1a: uniform flows over meadow-type vegetation (M) and over wood-type vegetation (W), transitions from meadow to wood (MW) and from wood to meadow (WM). An additional uniform flow with the wood-type vegetation over a smooth glass bed (W0) was also studied. Table 4.1 reports the 13 flow cases experimented. The notations in the first column of Table 4.1 refer to the different flow configurations. The roughness upstream or downstream of the roughness step change is called the upstream or the downstream roughness respectively.

For the uniform flows, three flow rates were considered for each roughness type. For meadow-type vegetation, the three flow cases correspond to different degrees of blade submergence. For wood-type vegetation, the three flow cases correspond to different bed friction/cylinder drag ratios. In each case, the roughness was uniformly distributed along the whole flume (18 m). The downstream boundary condition (weir level) was adjusted to obtain a constant water depth along the flume (within $\pm 1\,\mathrm{mm}$). Flow rates and weir levels for the roughness transition experiments corresponded to those of uniform flows over the downstream roughness. The roughness step change was located at mid-length of the flume, *i.e.* 9 m downstream of the inlet tank. This location is also the origin of the longitudinal axis ($x = 0$).

Plastic artificial grass was used to model meadow-type vegetation. The blades of grass were 5 mm long and very dense such that the flow velocity and flow rate within the canopy could be assumed to be negligible. The blades of grass were rigid and of uniform length, so the vertical axis origin ($z = 0$) can be accurately defined as the tips of the blades. Wood-type vegetation was modelled using circular wood cylinders uniformly distributed in staggered rows (see Fig. 4.1b). The cylinder diameter was $D = 10\,\mathrm{mm}$ and the cylinder density was $N = 81\,\mathrm{cylinders/m^2}$. On a 1:100 scale, these cylinders modelled 1 m diameter trees separated by a mean distance of 11.3 m. According to Terrier (2010),

Table 4.1: Test case flow conditions: flow rate Q, water depth H, bulk velocity $U_Q = Q/(BH)$, Froude number $Fr = U_Q/\sqrt{gH}$, Reynolds number $Re = 4UH/\nu$, ratio R between bed friction and drag force (see Eq. 4.6), normalized driving pressure gradient β (Eq. 4.15). Variation range between the most upstream measuring point $x = -8\,\mathrm{m}$ and mean value in downstream reach are given for roughness transition flows. R-ratio is only given for the wooded area (undefined for area outside cylinder array) for roughness transition flows.

Test case	Flow configuration	Q (L.s^{-1})	H (mm)	U_Q (cm.s^{-1})	Fr	Re (10^{-3})	R	β
M-Q7	Uniform meadow	7	35	20.6	0.35	29		
M-Q15	Uniform meadow	15	55	27.3	0.37	60		
M-Q50	Uniform meadow	50	116.5	42.9	0.40	200		
W-Q7	Uniform wood	7	55	12.7	0.17	28	0.25	
W-Q15	Uniform wood	15	113	13.3	0.13	60	0.10	
W-Q21	Uniform wood	21	152	13.8	0.11	84	0.06	
W0-Q15	Uniform wood with smooth bed	15	109	13.8	0.13	60	0.04	
MW-Q7	Transition from meadow to wood	7	49-56	14.3-12.5	0.21-0.17	28-28	0.25	-1.10
MW-Q15	Transition from meadow to wood	15	104-113	14.4-13.3	0.14-0.13	60-60	0.10	-0.89
MW-Q21	Transition from meadow to wood	21	143-152	14.7-13.8	0.12-0.11	84-84	0.06	-0.83
WM-Q7	Transition from wood to meadow	7	47-35	14.9-20.0	0.22-0.34	28-28	0.31-0.46	-1.28
WM-Q15	Transition from wood to meadow	15	76-56	19.7-26.8	0.23-0.36	60-60	0.16-0.25	-1.17
WM-Q50	Transition from wood to meadow	50	168-119	29.4-42.7	0.23-0.40	200-200	0.06-0.09	-1.08

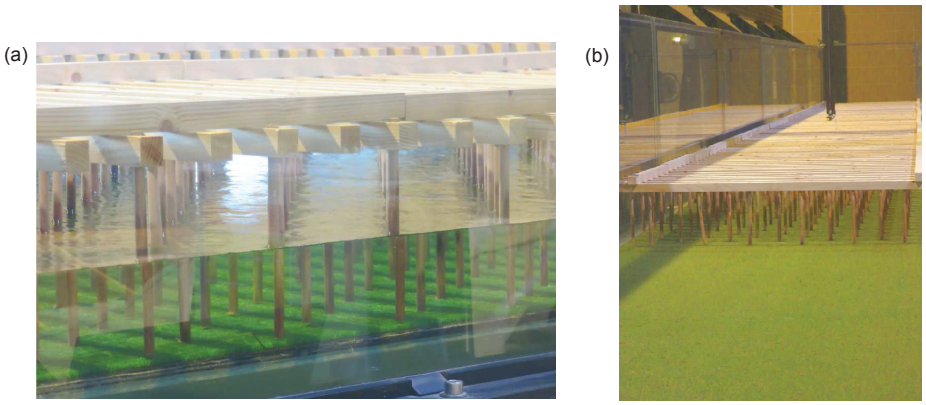

Figure 4.2: (a) Side view of cylinder array over bed roughness. (b) Flume configuration for meadow-to-wood transition (viewed from upstream).

this corresponds to a typical riparian forest in the lower reaches of the River Rhône (France).

The cylinders were installed on the plastic grass (except for test case W0-Q15 for which the bed was smooth glass) and were held in place from above by a wooden superstructure (see Fig. 4.2a). Cylinder lateral rows were termed even or odd depending on their even or odd numbers of cylinders. The array was composed of an elementary $80\,\mathrm{mm} \times 80\,\mathrm{mm}$ pattern as shown in Fig. 4.1b. Points A, B and C are velocity measuring positions. Point A is 4 cm downstream of a cylinder, Point C is 4 cm upstream of a cylinder and Point B is in the free stream between two longitudinal rows of cylinders.

Under uniform flow conditions, thanks to symmetry and periodicity of the flow in the cylinder array, the elementary pattern characterizes the entire flow, except in the side-wall region where the lateral boundary layer plays an additional role.

Water depths were measured using an electronic stage gauge (Mitutoyo 570-302) and free surface oscillations (seiching) were investigated with an ultrasonic sensor (Baumer UNDK20I69) with an accuracy of $\pm 0.5\,\mathrm{mm}$. Mean velocity and turbulence fluctuations

were recorded using a side-looking ADV probe (Nortek Vectrino Plus). The recording time at each point was 180 s and the acquisition rate was 100 Hz. This was found to be sufficient for obtaining converged first and second statistical moments. The ADV raw data were filtered using WinADV freeware based on the de-spiking concept developed by Goring and Nikora (2002). The tracers used for the ADV measurements were hydrogen micro-bubbles, generated by an iron anode (wire) positioned on the flume bottom approximately 3 m upstream of the measuring point. Preliminary measurements showed that this device did not disturb the flow at the measuring location. In addition, the micro-bubble buoyancy was negligible (rising velocity about 5.10^{-6} m.s^{-1}). ADV sensor accuracy was 0.5 % of the measured mean velocity (according to the manufacturer). Some uniform flow velocity profiles were measured using a LaVision 2D PIV laser system. The laser sheet entered the flow from the flume bottom through a narrow slot cut in the plastic grass and illuminated a vertical plane (x, z). ADV probe measurements were used to check that the slot did not influence the local flow field. Each PIV profile presented is a time-based average profile for 150 images taken at 5 Hz and a space-based average over a 100 mm longitudinal distance for flows over bed roughness and over a 30 mm longitudinal distance for flows through the cylinder array. The PIV measuring location is at Point C for flows through the cylinder array (see Fig. 4.1b), *i.e.* 40 mm upstream of a cylinder centre (space averaging between 25 and 65 mm upstream of cylinder centre). Unless otherwise stated, the ADV probe was used for measuring all velocities and turbulence quantities presented herein. The flow rate was automatically regulated by control valves and measured by an electromagnetic flowmeter.

4.3 Uniform flows

This section focuses on uniform flows subjected to (1) bed friction alone (case M in Fig. 4.1a) and (2) combined emergent cylinder drag and bed friction (cases W and W0 in Fig. 4.1a). Flow is considered uniform when the flow parameters (water depth, mean velocity, turbulence) remain constant in the downstream direction. In the case of flow through an emergent cylinder array, uniformity is reached when the flow no longer varies from one elementary pattern to another.

4.3.1 Bed friction

The Manning roughness coefficient of the meadow was evaluated as $n = 0.0166\,\mathrm{s.m}^{-1/3}$ based on uniform test cases M-Q7, M-Q15 and M-Q50. Variation in this n-value for the three M-cases was lower than ± 2.5 %. It should be noted that bed and side walls do not have the same roughness. The heterogeneous roughness along the wetted perimeter can be approximately taken into account using a Manning formula for composite roughness (Yen, 2002). The Manning coefficient of the glass wall was estimated in previous experiments: $n_{glass} = 0.0096\,\mathrm{s.m}^{-1/3}$ with variations lower than 4 % in the range of Reynolds number values considered.

Figure 4.3 shows the vertical profiles of mean longitudinal velocity U for the above three M-cases. Open circles are used for ADV probe measurements and crosses for PIV measurements, which were only available for test cases M-Q7 and M-Q50. ADV and PIV measurements collapse in the upper water column for $z > 20$ mm. Below this level, the ADV probe underestimates the mean velocity. In this region, the ADV measurements are scattered and the signal quality is lower; this was not observed with a smooth glass bed. The plastic grass therefore appears to cause defective behaviour of the ADV in this

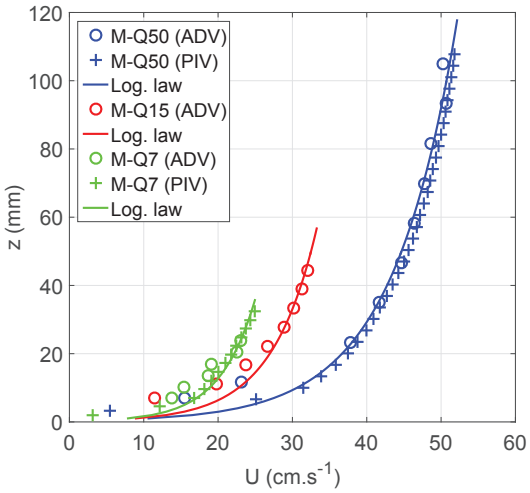

Figure 4.3: Vertical profiles of mean longitudinal velocity for uniform flows over a meadow-type roughness for flow rates $Q = 7$, 15 and 50 L.s^{-1}.

region: it may induce acoustic signal interference or ejection of the tracer from the near-bed region. Measurement difficulties with ADV probes in near-wall regions have been regularly reported (Chanson *et al.*, 2007). The accuracy of the PIV measurements in the near-bed region has been verified by comparing them with a logarithmic law as shown in Fig. 4.3.

The vertical distribution of mean velocity for a turbulent boundary layer over a rough bed is usually described by the logarithmic law of the wall. The domain of validity of the logarithmic law within the water column remains an open issue (George, 2007; Nezu and Rodi, 1986; Nikora *et al.*, 2001; Raupach *et al.*, 1991). The most commonly used formulation of the logarithmic law in hydraulics is based on the equivalent sand grain size k_S and the zero plane displacement d and writes (Raupach *et al.*, 1991):

$$\frac{U}{U^*} = 2.5 \ln\left(\frac{z-d}{k_S}\right) + 8.5 \tag{4.1}$$

where U^* is the friction velocity, defined by $U^* = \sqrt{\tau_b/\rho}$ with τ_b the bed shear stress and ρ the fluid density. In most cases, the length k_S is an abstract length and is not geometrically measurable. The zero plane displacement d allows to shift down the beginning of the logarithmic profile. This is necessary for rough beds with sparse elements for which a flow rate exists below the roughness crest. When $z = 0$ is defined at the roughness crest (like in the present case), d is negative; it is positive when $z = 0$ is defined at the foot of the roughness element.

Equation 4.1 was fitted to the experimental measurements (the ADV measurements below $z = 20$ mm were excluded). The best fit – to be seen in Fig. 4.3 – is obtained for equivalent sand grain sizes of $k_S = 6$, 7 and 9 mm for test cases M-Q7, M-Q15, M-Q50, respectively. The zero-plane displacement is found to be zero for the three cases, which is consistent with the high density of the meadow. The fact that the length k_S varies with water depth for the same bed roughness highlights the limitations of Eq. 4.1. One limitation comes from its domain of validity within the water column. Another limitation comes from the simplicity of this equation, which contains only two parameters for representing a rough bed. Indeed, the length scales characterizing a rough bed are multiple: mean height and mean diameter of the roughness elements, mean lateral and longitudinal spacings, standard deviations of these same variables, etc.

4.3.2 Cylinder drag combined with bed friction

This section considers uniform flows through an array of rigid vertical emergent cylinders (cases W and W0). It is important to note that, compared with previous studies of cylinder arrays (Liu *et al.*, 2008; Martino *et al.*, 2012; Poggi *et al.*, 2004), the characteristic length

of the bed roughness is of the same order of magnitude as the cylinder diameter in this case: $k_S/D \approx 0.7$, where k_S is the equivalent sand grain size of the bed roughness.

4.3.2.1 Relative weights of bed friction and drag

The flow resistance through a cylinder array is caused by the combination of cylinder drag force and bed friction. According to Nepf (1999), the volume force F_{arr} exerted by a cylinder array can be expressed as:

$$F_{arr} = \frac{1}{2}\rho a C_D U_Q^2 \tag{4.2}$$

where a is the frontal area per unit volume of cylinder array ($a = ND$ for circular cylinders; $a = 0.81\text{m}^{-1}$ in the present case), C_D is the drag coefficient of each cylinder and U_Q is the bulk velocity. Neglecting the friction on the glass side walls, a 1D force balance between the driving gravity force, the bed friction force and the drag force leads to:

$$\rho g H S_0 = \tau_b + \frac{1}{2}\rho a C_D H U_Q^2 \tag{4.3}$$

where S_0 is the channel slope, H is the water depth and τ_b is the bed shear stress. It should be noted that the fraction of the volume occupied by the cylinders ($\approx 6.10^{-3}$) is neglected in this equation.

According to Kothyari *et al.* (2009), the drag coefficient of one cylinder in a cylinder array is a function of the area concentration of cylinders aD and of the cylinder Reynolds number $Re_D = U_Q D/\nu$. Using the empirical formula of Kothyari *et al.* (2009) and comparing with the C_D-value recommended by Nepf (1999), we take $C_D = 1.2$ in the present case. Using the Manning roughness coefficient n determined in Section 4.3.1 for the bed roughness, the bed shear stress is:

$$\tau_b = \frac{\rho g n^2 U_Q^2}{H^{1/3}}. \tag{4.4}$$

Combining Eqs. 4.3 and 4.4 gives the stage-discharge relationship:

$$Q = \left(\frac{H^3 B^2 g S_0}{g n^2 H^{-1/3} + \frac{1}{2} a C_D H}\right)^{1/2}. \tag{4.5}$$

Equation 4.5 is based on the assumption that the overall flow resistance is given by simply summing the two contributions, *i.e.* bed shear stress and drag. This is not the case in general: bed shear stress is actually affected by the cylinders (Eq. 4.4 is valid for bed roughness alone) and, conversely, bed friction affects the drag in the near-bed region, resulting in a modified mean drag coefficient. The uniform flow depths predicted by Eq. 4.5 match the experimental data (2.7 % mean relative error), indicating that the previous assumption is consistent in the present case.

The effect of bed friction relative to drag force can be quantified using the ratio between the two terms on the right-hand side of Eq. 4.3:

$$R = \frac{2 g n^2}{a C_D H^{4/3}}. \tag{4.6}$$

The R-ratios for the three test cases are reported in Table 4.1. If ratio R is sufficiently low (*e.g.* $R < 0.1$), the bed friction can be neglected compared with the drag forces.

Drag forces act as a volume force on the fluid and therefore make the velocity field constant in the vertical direction, except in the near-bed region, where bed friction influences the flow and a boundary layer forms (Liu *et al.*, 2008; Martino *et al.*, 2012; Poggi *et al.*, 2004). The water column can thus be divided into two parts: (1) a region of constant velocity in the upper part of the water column, termed the constant-velocity region and (2) a boundary layer, defined as the region in which the velocity is variable. The space-averaged velocity in the constant-velocity region $\langle U \rangle_{drag}$ is obtained by assuming that the bed shear stress is zero in Eq. 4.3:

$$\langle U \rangle_{drag} = \sqrt{\frac{2gS_0}{aC_D}}. \tag{4.7}$$

The velocity $\langle U \rangle_{drag}$ is independent of water depth, according to the fact that the flow is driven by two volume forces only: gravity and drag. In the present case $\langle U \rangle_{drag} = 14.6\,\mathrm{cm.s^{-1}}$. The difference between this value and the bulk velocity (see Table 4.1) also quantifies the influence of the bed friction on the flow.

4.3.2.2 Near-bed region

Figure 4.4a shows vertical profiles of longitudinal mean velocity at Point C (see Fig. 4.1b), *i.e.* 40 mm upstream of a cylinder, for the three test cases with the rough bed (cases W, measurements using PIV) and for the test case with the smooth glass bed (case W0, measurements using ADV probe). The longitudinal velocity is normalised with the velocity $\langle U \rangle_{drag}$. For the highest flow rate (W-Q21), the velocity profile is cut and continues outside the PIV measuring window, but it can be assumed to be constant in the upper water column. Water column separation between the constant-velocity region (CVR) and the boundary layer (BL) is shown in Fig. 4.4. The boundary layer height δ is the same for the four cases ($\delta \approx 40\,\mathrm{mm}$), and appears to be independent of the water depth and the type of bed roughness. Length δ is therefore probably dependent on the geometry of the cylinder array only (cylinder density, cylinder diameter, cylinder arrangement). For test case W-Q7 with a relative high R-ratio, only a very small constant-velocity region can be distinguished and the velocity in this region is smaller than that in other cases. As Point C is aligned with a longitudinal row of cylinders, the local constant velocity is lower than the mean uniform velocity $\langle U \rangle_{drag}$ (spatially averaged over a pattern).

A local velocity increase is observed in the near-bed region. This velocity bulge reaches its maximum at $z/D = 2$ ($z = 20\,\mathrm{mm}$); its position is independent of water depth and of bed roughness (rough or smooth). The intensity of the velocity bulge is higher for the smooth case: it represents about $+35\,\%$ and $+10\,\%$ of the velocity in the constant-velocity region for the smooth and the rough case respectively.

A side view of the velocity bulge phenomenon for test case W0-Q15 is illustrated in Fig. 4.4b. Two lateral velocity profiles in the wake of a cylinder (40 mm downstream of the cylinder centre) are plotted at two different heights: $z/D = 1.9$ (where the maximum velocity bulge is observed) and at $z/D = 4.1$ (corresponding to the constant-velocity region). The velocity bulge is clearly visible in the cylinder alignment ($y = 260\,\mathrm{mm}$) and is associated with a weaker wake at $z/D = 1.9$ compared with the wake in the constant-velocity region. On the other hand, in the free stream region between two longitudinal rows of cylinders ($280 < y < 320\,\mathrm{mm}$), the velocity values at $z/D = 1.9$ and $z/D = 4.1$ are very similar (despite measurement scatter), indicating that the velocity bulge vanishes in this region.

The velocity bulge phenomenon was first reported in the literature by Liu *et al.* (2008) and was reproduced in LES simulations conducted by Stoesser *et al.* (2010). In

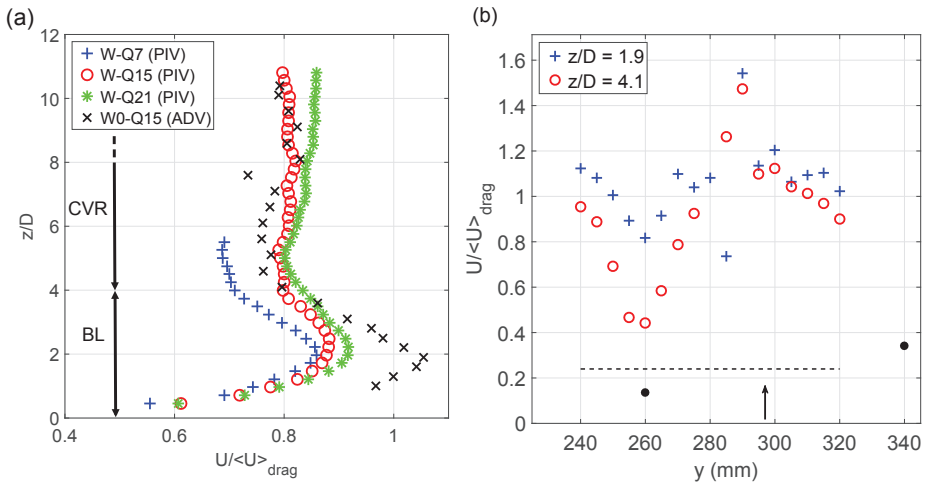

Figure 4.4: (a) Vertical profiles of mean longitudinal velocity U for uniform flows at Point C of the cylinder array, *i.e.* 40 mm upstream of the cylinder axis and at $y = 340$ mm. BL is the boundary layer and CVR the constant-velocity region. (b) Lateral profiles of mean longitudinal velocity U for W0-Q15 at two different heights: near the velocity bulge maximum ($z/D = 1.9$) and in the constant-velocity region ($z/D = 4.1$); black solid circles indicate cylinder positions (not to scale), the dashed line is the measuring position and the arrow shows the flow direction. The velocity is normalised by the spatially averaged velocity $\langle U \rangle_{drag}$ in the constant-velocity region (Eq. 4.7) and the vertical coordinate is normalised by the cylinder diameter.

common with our observations, Liu *et al.* (2008) found the velocity bulge to be clearly pronounced in line with a cylinder row and to disappear in the free stream region between two longitudinal rows of cylinders. However, unlike the present study, they measured the maximum bulge closer to the bed at $z/D \approx 0.5$. Liu *et al.* (2008) explain the velocity bulge by the horseshoe vortex at the foot of the cylinder; the legs of this vortex would transport fast fluid from the free stream region to the wake region. However, for a high bed roughness with a characteristic length of the same order of magnitude as the cylinder diameter, we may ponder whether a horseshoe vortex can in fact develop and whether its formation is not hindered by bed-induced turbulent motion.

Figure 4.5 illustrates the ADV-time series of lateral velocity for test case W0-Q15 at distances of 4 cm upstream of a cylinder (Point C, Fig. 4.5a) and of 4 cm downstream of a cylinder (Point A, Fig. 4.5b) as well as at four different elevations. Lateral velocity is a good indicator of the presence of periodic coherent structures associated with the von Kármán vortex street. The bed is smooth so the ADV probe measurements in test case W0-Q15 are of good quality even close to the bed. Downstream of the cylinder, clear periodic oscillations of almost constant amplitude can be observed in the constant-velocity region ($z/D = 4.1$ and 10.1 in Fig. 4.5b). These periodic oscillations are dampened, when moving downstream, and become less regular, but they are still visible 4 cm upstream of the next cylinder ($z/D = 4.1$ and 10.1 in Fig. 4.5a). These oscillations are less and less coherent, when moving downwards, until they almost vanish close to the bed ($z/D = 1.0$), where random fluctuations of bed-induced turbulence can be observed ($z/D = 1.0$ in Figs. 4.5a and 4.5b).

This analysis infers that the von Kármán vortex street is well developed in the constant-velocity region and is associated with large, high energy vortices, whereas in the boundary layer, the vortex street is unstructured probably by bed-induced turbulence. The drag and energy loss in the cylinder wake are reduced due to the absence of

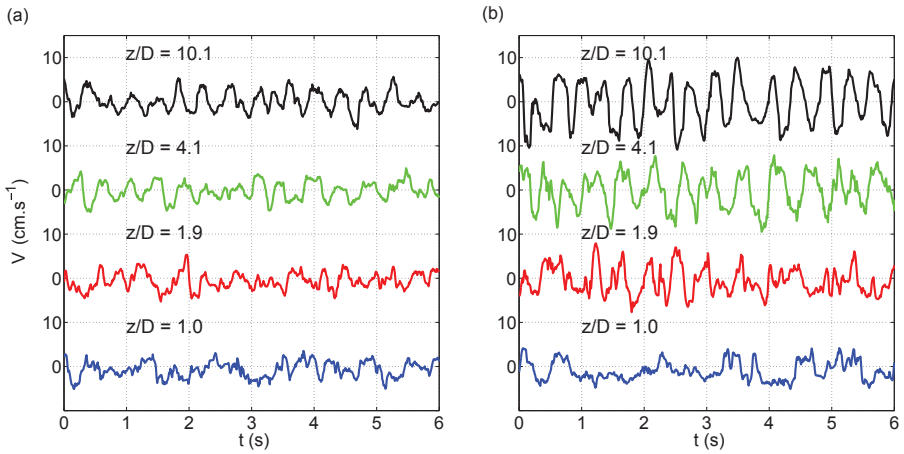

Figure 4.5: Time series of lateral velocity for test case W0-Q15: (a) upstream of a cylinder at Point C and (b) downstream of a cylinder at Point A, and at four different heights. The vertical axis origin is shifted for each elevation.

large vortices, which would explain the velocity bulge.

Bed-induced turbulence disorganizes vortex shedding but also causes additional energy loss. This additional energy loss is smaller for a smooth bed than for a rough bed; this fact could explain the higher velocity bulge for a smooth bed (W0-Q15) than for a rough bed (W-Q15).

4.3.2.3 Free surface oscillations

Flows through cylinder arrays are associated with periodic free surface oscillations as observed by previous authors (Defina and Pradella, 2014; Zhao *et al.*, 2014; Zima and Ackermann, 2002). This physical process has been termed seiching or seiche in analogy with the phenomenon occurring in harbours and lakes, although the mechanism generating such oscillations through cylinder arrays is significantly different. In the latter case, seiching results from lateral lift forces induced by the cylinders. Lift forces induced by the different cylinders enter in phase to produce regular transverse standing waves (Zima and Ackermann, 2002). Seiching in cylinder arrays has been observed for both staggered and in-line cylinder arrangements (Jafari *et al.*, 2010) as well as for randomly distributed cylinders (Sarkar, 2012).

Zima and Ackermann (2002) have provided a physical explanation of the seiche phenomenon: when the vortex shedding frequency f_V of each cylinder is close to the natural frequency of the transverse waves in the channel f_{TW}, then the energy of these transverse waves is amplified. Resonance occurs between the two oscillations and both frequencies become equal (lock-in process). The natural frequency of the transverse waves can be calculated using the equation derived by Zima and Ackermann (2002):

$$f_{TW} = \left(\frac{g n_0}{4\pi B} \tanh \frac{n_0 \pi H}{B} \right)^{1/2} \tag{4.8}$$

where n_0 is the oscillation mode.

Zima and Ackermann (2002) have derived a formula for predicting the maximum seiching amplitude and Defina and Pradella (2014) have rewritten and extended their

Table 4.2: Seiche parameters for the uniform flow cases through the cylinder array: maximum fluctuation amplitude of water depth A, maximum standard deviation σ_{Hmax}, seiche amplitude A_{Zima} derived from Eq. 4.9, cylinder Reynolds number $Re_D = U_Q D/\nu$, peak frequency of water depth spectra f_H, peak frequency of velocity spectra f_V, most appropriate oscillation mode n_0, natural frequency of transverse waves f_{TW}, Strouhal number $St = f_V D/U_Q$; 'N.M.' = 'not measured'.

Test case	Seiche	A (mm)	A/H	σ_{Hmax} (mm)	A_{Zima} (mm)	Re_D	f_H (Hz)	f_V (Hz)	n_0	f_{TW} (Hz)	St
W-Q7	no	0.2	< 0.01	0.2	2.4	1273	-	2.16	7	2.14	0.17
W-Q15	yes	10	0.09	2.5	5.0	1327	2.08	2.08	6	2.13	0.16
W-Q21	yes	7	0.05	1.9	7.3	1382	2.14	N.M.	6	2.16	0.15

formula for any oscillation mode n_0:

$$\frac{A_{Zima}}{H} = 2.255 \frac{D}{B} N D^2 n_0 \frac{1}{St^2} \tag{4.9}$$

where St is the Strouhal number, the normalised form of the vortex-shedding frequency: $St = f_V D/U_Q$.

We also observed free surface oscillations during our experiments. Table 4.2 summarizes these observations: seiching was observed for the two higher flow rates (W-Q15 and W-Q21) but not for the lowest flow rate (W-Q7). Random fluctuations of the free surface only were observed in the latter case.

Seiche frequency f_H was evaluated using the water depth fluctuation spectra, in which a clear peak can be distinguished (not shown). Seiche frequency f_H is almost the same in flows in which seiching occurs (W-Q15 and W-Q21), and $f_H \approx 2.1$ Hz. The vortex shedding frequency can be evaluated using the peak frequency f_V in the velocity spectrum (not shown). This peak frequency is about $f_V \approx 2.1$ Hz for W-Q7 and W-Q15. It was not measured for W-Q21, but it can be assumed to be the same because, according to Section 4.3.2.2, the constant-velocity region is identical in test cases W-Q15 and W-Q21.

Table 4.2 reports the natural frequency of transverse waves f_{TW} using oscillation mode n_0, for which f_{TW} (calculated using Eq. 4.8) is closest to vortex shedding frequency f_V. This oscillation mode is *a priori* the mode most appropriated for seiching. The most appropriated mode appears to be $n_0 = 6$ for W-Q15 and W-Q21 (experimentally confirmed, see below) and $n_0 = 7$ for W-Q7. For these three cases, the corresponding natural transverse wave frequency f_{TW} is very close to the vortex shedding frequency f_V and to the seiche frequency f_H. This confirms the hypothesis of Zima and Ackermann (2002) of a lock-in process between natural transverse waves and vortex shedding. However, this cannot explain why the seiche does not occur for the lowest flow rate W-Q7. In common with the two other cases, frequencies f_{TW} and f_V are very similar for W-Q7 and conditions are favourable to frequency lock-in.

Absence of seiching for the lower flow rate W-Q7 could be explained by the strong three-dimensional nature of the flow in this case. Figure 4.4 shows that for W-Q7, the constant-velocity region, in which the von Kármán vortex street is well developed, occupies a very small part of the water column. Below $z = 40$ mm, the von Kármán vortex street is disorganised due to near-bed turbulence (see Fig. 4.5 in Section 4.3.2.2). The lift forces, which are the seiche driving forces, are therefore smaller and less periodic than in flow cases with a large constant-velocity region. This means that the water depth/boundary layer height ratio (H/δ) is an important parameter for the seiche. No seiche can occur, if

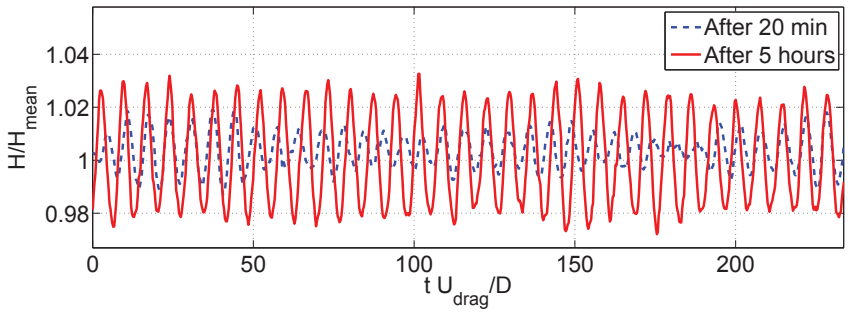

Figure 4.6: Time series of normalised flow depth H/H_{mean} (where H_{mean} is the time-averaged flow depth) for test case W-Q15, 20 minutes ($1.8\,10^4 D/U_{drag}$) and five hours ($2.6\,10^5 D/U_{drag}$) after starting experiment. Measuring position: $x = -2\,\text{m}$, $y = 450\,\text{mm}$.

this ratio is too close to 1. For example, there is a seiche for W-Q15, for which $H/\delta = 2.05$, but there is no seiche for W-Q7, for which $H/\delta = 1.38$.

The seiching in test case W-Q15 was investigated in more detail. The time required to reach a steady state was found to be very long (several hours) as shown in Fig. 4.6. Twenty minutes after starting the experiment ($1.8\,10^4 D/U_{drag}$), the oscillations have a quite constant period but the amplitude fluctuates with time. After five hours ($2.6\,10^5 D/U_{drag}$), the amplitude has increased and remains constant. This observation allows us to deduce that bringing all cylinder wakes into phase is a very slow process.

Figure 4.7 shows two lateral profiles of the flow depth standard deviation, located downstream from an even row (Position 1 in Fig. 4.1b) and an odd row (Position 2), respectively, and after seiching convergence. The standard deviation profile is the same for the two rows, indicating that the seiche is a purely transversal standing wave, the longitudinal heterogeneity of the flow within the cylinder array having no incidence.

Antinodes are the locations with maximum standard deviation. From Fig. 4.7 the distance between two antinodes can be evaluated at 165 mm, corresponding to an estimated wavelength of 330 mm. As antinodes also are the locations where the transverse flow rate is zero, two antinodes are located at each side-wall of the flume (Rabinovich, 2009). Since the channel width is $B = 1000\,\text{mm}$, it can be concluded that the mode of oscillation is $n_0 = 6$, which indeed corresponds to the most appropriate oscillation mode calculated above, and there is exactly three wavelengths across the channel, as sketched in Fig. 4.1b.

The lateral free surface waves induce lateral mass transfers with maximal lateral flow rates located at the nodal points. Figure 4.7 shows that for test case W-Q15, the cylinders of even rows are close to a nodal point. In the wake of these cylinders, the periodic lift forces are thus sustaining the lateral mass transfers that generate the seiching. On the contrary, the cylinders of odd rows are close to an antinode where the transverse flow rate due to the seiche is equal to zero. It can be assumed that in the wake of these cylinders the lift forces do not contribute to the seiche generation. We can wonder if the proximity of a longitudinal row of cylinders to a nodal point is a necessary condition for the seiching. For the test

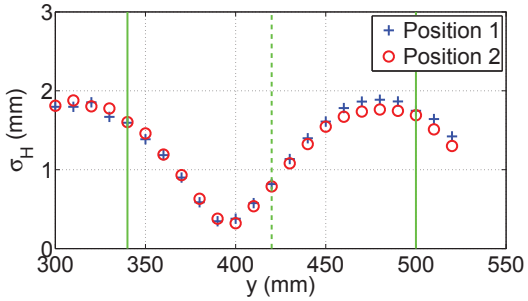

Figure 4.7: Lateral variation in standard deviation of flow depth for the test case W-Q15 downstream of an even and an odd row (Position 1 and 2, respectively, see Fig. 4.1b). Dashed and solid lines represent the lateral positions of the cylinders for an even and an odd row, respectively.

case W-Q7, it has been shown above that the most appropriate oscillation mode is $n_0 = 7$. It appears that with this oscillation mode the nodal points are located nearly in the free stream region, *i.e.* where no lift forces exist. This fact may contribute to the non-existence of the seiche for the test case W-Q7.

Table 4.2 reports the maximum seiche amplitude A, *i.e.* the amplitude at an antinode and at mid-length of the cylinder array (see Section 4.4.3 for the longitudinal variation in seiche amplitude) as well as the seiche amplitude A_{Zima} predicted using Eq. 4.9 for the most appropriated mode n_0. The equation of Zima and Ackermann (2002) provides an excellent estimation of seiching amplitude for W-Q21, but underestimates by a factor 2 the measured seiching amplitudes for W-Q15. It does not predict that the W-Q15 seiche is larger than the W-Q21 seiche nor that no seiching occurs in test case W-Q7.

We end this section with a brief discussion concerning the Strouhal number. The shedding frequency is usually predicted using the Strouhal-Reynolds number relationship $St = f(Re_D)$, Re_D being the cylinder-based Reynolds number $Re_D = U_Q D/\nu$. A critical point in the calculation of the Strouhal number is the choice of the velocity scale. For an isolated cylinder, the velocity scale is the free stream velocity; but in an array of cylinders, the free stream velocity cannot be defined. Here, we chose the bulk velocity of the flow; but in some studies the choice of the velocity scale is not clearly defined. For the present cylinder Reynolds number range ($1273 < Re_D < 1382$), the Strouhal number of the isolated cylinder is invariant and $St \approx 0.21$ (Lienhard, 1966). Within a cylinder array, the Strouhal number is furthermore a function of the distance between the cylinders. Ghomeshi *et al.* (2007) review several formulae for estimating the Strouhal number for cylinders in staggered or in-line arrays as a function of lateral and longitudinal distances between the cylinders. According to these formulae, the array arrangement for the present case does not change the Strouhal number, which is equal to the Strouhal number of the isolated cylinder. However, the Strouhal number calculated for the present flows with f_V and U_Q has a value of $St = 0.16 \pm 0.01$ (the same result is obtained for the non-uniform flows through the cylinder array presented in section 4.4). The formulae reported by Ghomeshi *et al.* (2007) suggest that the Strouhal number can only rise in a cylinder array compared to the isolated cylinder. This low St-value thus remains unexplained. Using the averaged velocity in the free-stream region $< U_{drag} >$ instead of the bulk velocity U_Q in the Strouhal number calculation leads to an even weaker Strouhal number. Therefore the bed friction effect cannot explain the Strouhal number overestimation.

4.4 Longitudinal roughness transitions

In this section, we investigate non-uniform flows associated with a longitudinal transition from bed friction to emergent cylinder drag and *vice versa*. We first analyse the longitudinal variation in water depth, mean velocity and turbulence. The effect of flow non-uniformity on the seiche phenomenon is subsequently considered.

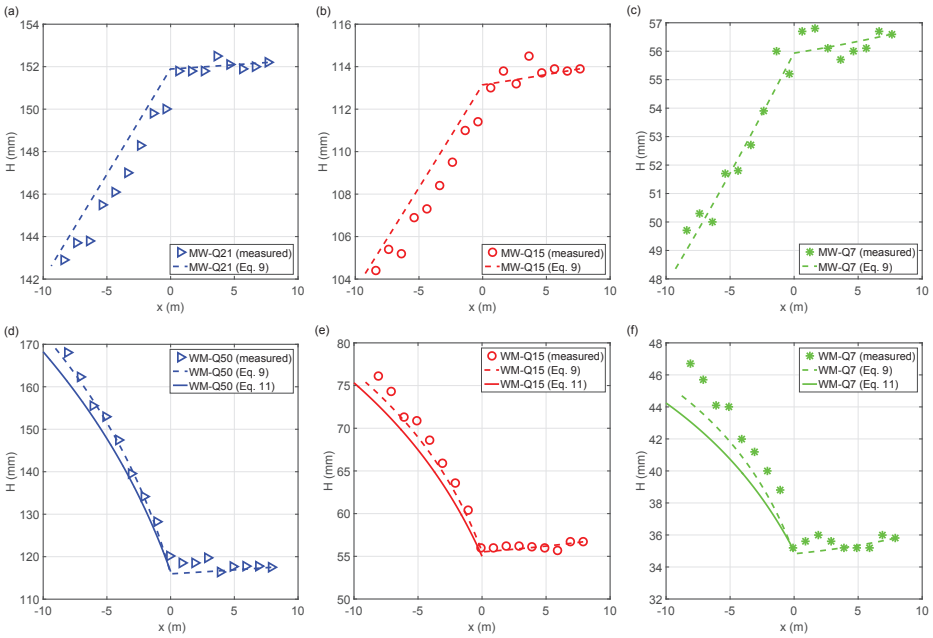

Figure 4.8: Longitudinal profiles of water depth for six test cases involving a roughness transition. Symbols are measuring points, dashed lines are numerical solutions of Eq. 4.10 and solid lines are numerical solutions of Eq. 4.12.

4.4.1 Water depth

Figure 4.8 shows the longitudinal variations in water depth for the six test cases involving a roughness transition (see Table 4.1). The water depth varies only upstream of the transition. Downstream, the uniform water depth related to the downstream roughness is immediately reached (compare with uniform water depth in Table 4.1).

Water depth control by the downstream boundary condition is typical for subcritical flows. The longitudinal water depth profiles upstream of the meadow-to-wood and the wood-to-meadow transitions correspond to M1 and M2-type backwater curves, respectively (following the classification of Graf and Altinakar (1998)).

In the following discussion, a simple 1D-momentum equation is introduced to calculate the water depth in a non-uniform flow subjected to bed friction and emergent cylinder drag. Non-uniform open channel flow over a conventional bed roughness is described by the 1D shallow water equation provided by Graf and Altinakar (1998), for example. To account for the drag forces exerted by the cylinder array, this equation can be modified (see Dupuis *et al.* (2015) for more detail) into:

$$\frac{\partial H}{\partial x}\left(1-\frac{Q^2}{gB^2H^3}\right)=S_0-\frac{n^2Q^2}{H^{10/3}B^2}-\frac{aC_DQ^2}{2gH^2B^2} \tag{4.10}$$

in which the drag force term is the third term on the right-hand side of the equation. The second term on the right-hand side is the bed friction term, expressed using the Manning coefficient n. The values of n and C_D provided by uniform flow cases (see Section 4.3) are used to solve Eq. 4.10. These solutions have been plotted as dotted lines in Fig. 4.8. Computation starts from the most downstream measuring point. This value does not exactly match the uniform water depth, so a slight water depth variation can be sometimes observed in the downstream reach. Moreover, discrepancies between the model and the measurements may be related to the Eq. 4.4 insufficiency for modelling

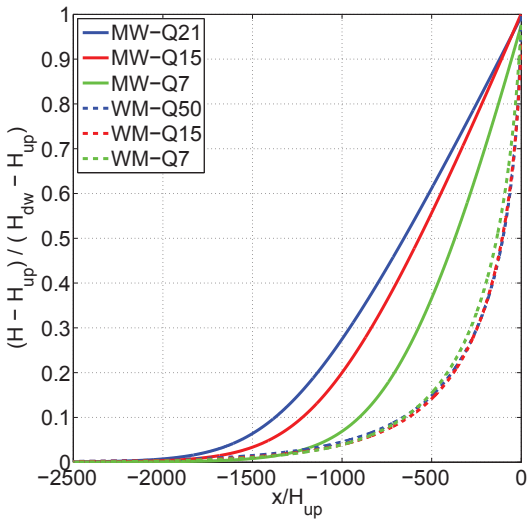

Figure 4.9: Extrapolated backwater curves for the six roughness transitions studied (upstream of roughness transition).

bed shear stress with an emergent cylinder array (second term on the right-hand side of Eq. 4.10). Very satisfactory results are nevertheless obtained: the model reproduces the measuring points with a mean relative error of $\epsilon = 0.9\,\%$ and a maximum relative error of $\epsilon_{max} = 3.8\,\%$.

The 1D-momentum equation was used to extrapolate the longitudinal profiles of water depth further upstream. The results are shown in Fig. 4.9 in non-dimensional form: H_{up} and H_{dw} refer to the uniform water depth associated with the upstream and downstream roughnesses respectively. The distance required to reach equilibrium upstream of the transition L_{up} is defined as the distance, at which the water surface slope is $|dH/dx| = 10^{-6}$. For the six flow cases, $L_{up}/H_{up} = 2580 \pm 15\,\%$ and thus L_{up} approximately scales with H_{up}. This implies that, for a given flow rate, a roughness step change with downstream increasing roughness will reach equilibrium over a shorter distance than a roughness step change with downstream decreasing roughness.

When bed friction is negligible compared to drag forces ($R < 0.1$), the bed friction terms in Eqs. 4.3 and 4.10 can be assumed to be zero. Combining these equations then gives:

$$\frac{\partial \overline{H}}{\partial \overline{x}} \left(1 - Fr^2\right) = S_0 \left(1 - \frac{1}{\overline{H}^2}\right) \tag{4.11}$$

with $\overline{H} = H/H_{up}$ and $\overline{x} = x/H_{up}$. Considering that $(1 - Fr^2) \approx cst \approx 1$, which is a good approximation for flows in cylinder arrays (see Table 4.1), Eq. 4.11 can be solved analytically (but implicitly):

$$\frac{H - H_{dw}}{H_{up}} - \text{atanh}\,\frac{H}{H_{up}} + \text{atanh}\,\frac{H_{dw}}{H_{up}} = S_0 \frac{x}{H_{up}}. \tag{4.12}$$

Equation 4.12 has been plotted for the three wood-to-meadow cases illustrated in Figs. 4.8d, 4.8e and 4.8f as solid lines. Since the analytical equation neglects bed friction, it has been applied only to the wood area ($x < 0$). The analytical solution reproduces the measurements for test cases WM-Q50 and WM-Q15 with mean relative errors of $\epsilon = 2.4\,\%$ and $\epsilon = 3.6\,\%$, respectively. For the test case WM-Q7, the errors are larger ($\epsilon = 5.5\,\%$) since bed roughness has a greater influence ($R \approx 0.4$).

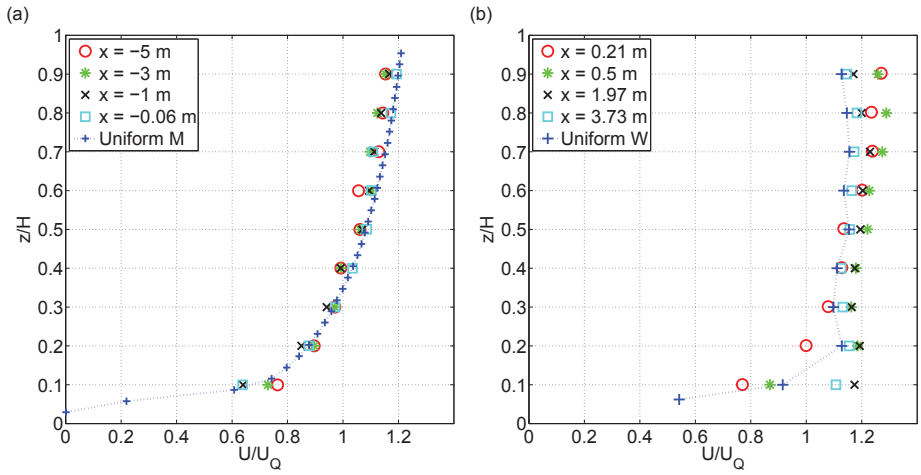

Figure 4.10: Vertical profiles of mean longitudinal velocity normalised by local bulk velocity at various distances x from transition: (a) upstream and (b) downstream of the roughness transition for test case MW-Q15. Blue crosses correspond to uniform flows over the meadow (M-Q50 -PIV) for panel a and in the wood (W-Q15) for panel b.

4.4.2 Mean velocity and turbulence

Figures 4.10a and 4.10b show vertical profiles of mean longitudinal velocity for test case MW-Q15 upstream and downstream of the roughness transition. Measurement was performed at Point B within the cylinder array, *i.e.* in the free stream region between two longitudinal rows of cylinders. Velocity U is normalised by the local bulk velocity U_Q and elevation z by the local water depth H. The collapse of the normalised velocity profiles upstream of the transition (Fig. 4.10a) indicates flow self-similarity. No shape deviation was observed even very close to the roughness step change.

Figure 4.10a also shows the uniform velocity profile over the meadow (taken from test case M-Q50 and measured with PIV). The normalised profiles of test case MW-Q15 collapse with the normalised uniform flow profile. Depth-averaged flow MW-Q15 is decelerating (water depth increasing in the upstream reach when going downstream). Kironoto and Graf (1994) have shown that there is a deviation from the uniform normalised profile, when flows are sufficiently accelerated or decelerated. In this case, flow deceleration upstream of the transition is not large enough for deviation from the uniform distribution.

Kironoto and Graf (1994) show that accelerating and decelerating flows have different velocity and turbulence distributions compared with the uniform flow. The vertical velocity profiles are straighter vertically for accelerating flows and, on the contrary, are more stretched longitudinally for decelerating flows. Kironoto and Graf (1994) characterize the flow non-uniformity with the normalized driving pressure gradient β defined for an open channel flow over a rough bed as:

$$\beta = \frac{H}{\tau_b}\frac{\partial p^*}{\partial x} \tag{4.13}$$

where τ_b is the local bed shear stress and $\partial p^*/\partial x$ is the longitudinal driving pressure gradient defined as:

$$\frac{\partial p^*}{\partial x} = \rho g\left(\frac{\partial H}{\partial x} - S_0\right). \tag{4.14}$$

For an open channel flow subjected to both bed friction and cylinder drag, Eq. 4.13 can be modified into:

$$\beta = \frac{H}{\tau_b + \frac{1}{2}aC_D\rho HU^2}\frac{\partial p^*}{\partial x}. \tag{4.15}$$

The definition of β implies that $\beta = -1$ for a uniform flow, $\beta < -1$ for an accelerating flow and $\beta > -1$ for a decelerating flow. Kironoto and Graf (1994) observed significant deviations from the uniform flow

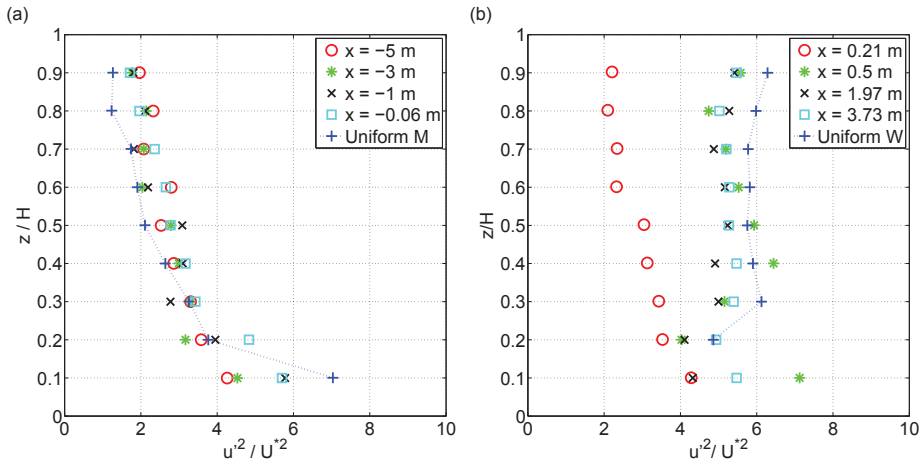

Figure 4.11: Vertical profiles of longitudinal turbulence intensity normalised by local shear velocity at various distances x from the transition: (a) upstream and (b) downstream of the roughness transition for test case MW-Q15. Blue crosses correspond to uniform flows over meadow (M-Q15) for (a) and over wood (W-Q15) for (b).

distribution for $\beta \approx -3$ for accelerating flows and $\beta \approx 4$ for decelerating flows. The parameter β was calculated for the six non-uniform flows investigated (see the values in Table 4.1). The bed friction was estimated using the concept of the equivalent slope: $\tau_b = \rho g H S_f$ where S_f is the equivalent slope determined with the Manning equation $S_f = n^2 U_Q^2 / H^{4/3}$. The longitudinal gradient of the water depth in Eq. 4.14 was taken as the mean value in the upstream reach. For MW-Q7, $\beta < -1$ although it is a decelerating flow; this anomaly can be attributed to the simplistic way of calculating τ_b and dH/dx. It appears that in the present study, the β-values for all flows are in the range $-1.28 < \beta < -0.83$. As a result, the non-uniformity of the flow in the present case is too weak to observe a deviation from the uniform distribution.

Figure 4.10 shows that longitudinal changes in the mean velocity profile are only observed downstream of the transition (Fig. 4.10b), where the logarithmic profile changes gradually into the characteristic constant velocity profile of the wood (blue crosses indicate the uniform flow profile).

Figure 4.11 shows the vertical profiles of longitudinal turbulence intensity at the same x-positions as in Fig. 4.10. The turbulence intensity is normalised by the local shear velocity $U^* = (gHS_f)^{1/2}$, where S_f is the equivalent bed friction slope determined from the Manning equation $S_f = n^2 U_Q^2 / H^{4/3}$. In common with the velocity, normalised turbulence intensity is relatively self-similar upstream of the transition (Fig. 4.11a) and the vertical distribution is close to the uniform one. Downstream of the transition (Fig. 4.11b), the turbulence intensity profile adapts to the downstream roughness: starting with an exponential form characteristic of bed roughness (Nezu and Rodi, 1986), which persists at $x = 0.21\,\mathrm{m}$, the turbulence intensity increases and becomes uniformly distributed along the water column.

Kironoto and Graf (1994) show that the normalized turbulence intensities and Reynolds stresses are weaker for accelerating and stronger for decelerating flows, compared with the uniform flow. Indeed the decelerating flow upstream from the transition (Fig. 4.11a) has a slightly higher normalized turbulence intensity, excepted close to the bed, but since the flow is weakly non-uniform (according to the parameter β), the deviation from the uniform distribution is low.

The above flow dynamics for the meadow-to-wood transition were also observed for the reverse wood-to-meadow transition (not shown here, see Dupuis *et al.* (2015)). The flow is self-similar upstream of the transition, the normalised profiles collapse with the uniform flow profile; downstream of the transition, the vertical profile changes gradually

into the uniform profile of downstream roughness. As observed by Chen and Chiew (2003), the vertical profile downstream of the transition is simultaneously transformed across the entire flow depth and not gradually from the wall to the top of the boundary layer, as is the case for air flows.

In keeping with the self-similarity of the flow upstream of the wood-to-meadow transition, the velocity in the constant velocity region within the cylinder array scales with the local bulk velocity U_Q and is not constant with water depth as in the case of uniform flows. This variation in mean velocity in the cylinder array probably affects the near-bed region (boundary layer height, velocity bulge). Unfortunately, the measurements in the near-bed region were not accurate enough to provide a quantitative description.

For the three transition flows investigated with the ADV probe (MW-Q15,WM-Q15 and WM-Q50), the downstream distance L_{dw} from the transition before reaching the uniform flow (for mean velocity and turbulence) can be estimated as $L_{dw}/H_{dw} \approx$ 35-50. No effect of flow rate and transition type could be established over this distance, but further experiments with more configurations and with a more precise determination of L_{dw} are required to be able to conclude on this issue.

The ratio L_{dw}/H_{dw} is much higher than the one observed by Chen and Chiew (2003), namely $L_{dw}/H_{dw} = 6$, for a bed roughness change with a roughness step of $M_0 = -2.4$. This could be explained by the much higher step change of the present study. For a transition between a bed roughness and an emergent roughness, it is not easy to compute the roughness step, since both roughness types cannot be characterized by a common length scale. The equivalent sand grain size of the meadow was evaluated in section 4.3.1 by $k_S = 7\,\text{mm}$; a length scale of the cylinder array could be the inverse of the frontal area per unit volume $a^{-1} = 1235\,\text{mm}$. With these two length scales, we can estimate a roughness step of $M_0 = -5.2$, which is significantly higher that the roughness step investigated by Chen and Chiew (2003). Compared to roughness transitions in air flows for which $L_{dw}/H \approx 20$, the present adjustment length is approximately twice larger.

Figures 4.12a and 4.12b show lateral profiles of mean longitudinal velocity at mid-depth ($z/H = 0.5$) for various distances x from the transition for the test cases MW-Q15 and WM-Q50, respectively. The profiles are not normalized, contrary to Figs. 4.10 and 4.11. The uniform flow profile in the wood is plotted with blue crosses in Fig. 4.12a: it exhibits a typical wavy shape, with maximal velocity between two longitudinal rows of cylinders ($y = 460\,\text{mm}$, position B) and minimal velocity downstream of a cylinder ($y = 420\,\text{mm}$, position A). Immediately upstream from the meadow-to-wood transition ($x = -0.06\,\text{m}$ in Fig. 4.12a), the longitudinal velocity is still constant across the channel. Downstream from the transition, five meters are required so that the profile develops towards the uniform wavy profile. For the wood-to-meadow transition (Fig. 4.12b), the wavy velocity profile turns into a constant velocity profile from $x = 0.06\,\text{m}$, to $x = 0.6\,\text{m}$. This suggests that the lateral homogenization of the flow for the wood-to-meadow transition occurs more rapidly than the establishing of the wavy profile in the cylinder array for the meadow-to-wood transition.

Summing up the observations on the roughness transition flows, it can be said that the dynamic of the water depth is controlled by the downstream boundary conditions (a classical result for subcritical free surface flows) and that the dynamic of the flow field structure is controlled by the upstream boundary conditions.

4.4.3 Free surface oscillations

The seiche phenomenon (see Section 4.3.2.3) was also observed, when there was a roughness transition. The free surface oscillations in meadow-to-wood transition MW-Q15 were studied in detail to examine how flow non-uniformity affects seiching. Defina and Pradella Defina and Pradella (2014) theoretically showed that a longitudinal water depth gradient should reduce seiching.

Figure 4.13 illustrates the longitudinal variation in flow depth standard deviation along an antinode line for a uniform flow through a cylinder array and for a meadow-to-wood transition under the same flow rate (test cases W-Q15 and MW-Q15). For the uniform flow case, the seiche longitudinal profile is triangular with a maximum intensity

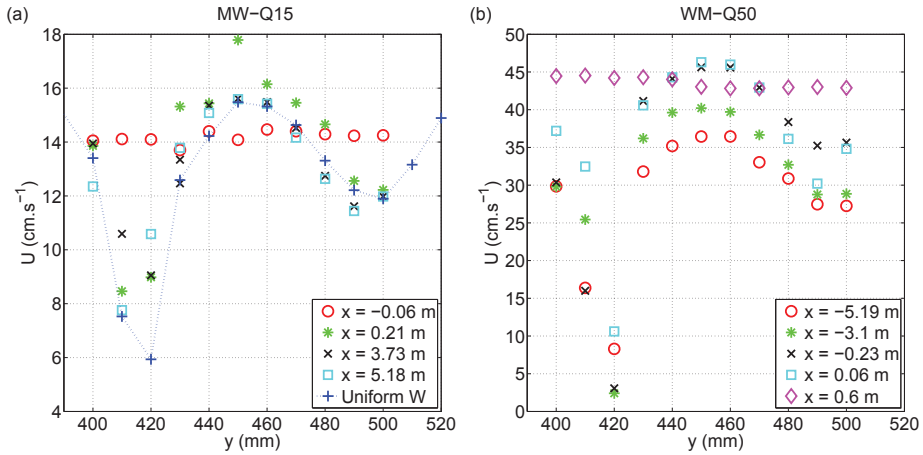

Figure 4.12: Lateral profiles at elevation $z/H = 0.5$ of mean longitudinal velocity for various distances x from the transition for the test cases (a) MW-Q15 and (b) WM-Q50. The blue crosses in (a) correspond to the uniform flow in the wood W-Q15.

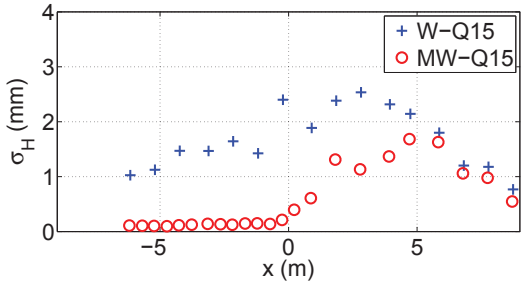

Figure 4.13: Longitudinal variation in flow depth standard deviation σ_H along an antinode line for a uniform flow (W-Q15) and a roughness transition (MW-Q15) under the same flow rate $Q = 15\,L.s^{-1}$.

almost at mid-length of the cylinder array. For MW-Q15 (cylinder array occupying only second half of flume), the seiche intensity decreases dramatically outside the cylinder array. However, the time series of the free surface elevation shows that seiching persists outside the cylinder array. Coherent free surface oscillations with the same frequency were observed as far as the upstream end of the channel, although their amplitudes become very small. Within the cylinder array, the seiche intensity was also triangular with a maximum intensity at mid-length of the cylinder array.

It can be noted that downstream of the maximal-intensity-point of MW-Q15 ($x > 5\,\mathrm{m}$), the seiche intensity seems to be the same in both cases. This could be explained by the influence of the downstream weir, that imposes no oscillations at the flume outlet.

Sarkar (2012) has also noted an almost triangular shape of the seiche amplitude longitudinal profile. However, Sarkar finds the maximum amplitude to be at one-fifth of the total length of the cylinder array, which is different to our finding that the maximum amplitude is at mid-length. This difference could be attributed to non-uniformity of the flow within the cylinder array in Sarkar's experiments.

The peak intensity of the seiche is lower in roughness transition case MW-Q15 than in uniform flow case W-Q15. This may be due to the shorter length of the cylinder array. Flow non-uniformity in the first metres after the meadow-to-wood step change in test case MW-Q15 (see Section 4.4.2) may also contribute to lower peak seiche intensity.

Figure 4.13 indicates that the seiche amplitude is closely dependent on longitudinal position within the array. However, this parameter is never considered in the expressions that can be found in the literature for evaluating seiche amplitude (reviewed by Defina and Pradella, 2014). Figure 4.13 also shows that the length of the cylinder array influences the maximum oscillation amplitude. This differs from the result of Zima and Ackermann (2002) who stated that when the cylinder array is longer than a minimum length of the order of six cylinder rows, the wave amplitude is independent on the cylinder array length. These facts could partly explain the wide variation in seiche amplitude measurements found in the literature. The values presented in Table 4.2 are the maximum seiche amplitudes over the channel length.

The flow accelerates within the cylinder array and the water depth varies in the wood-to-meadow transition. This means that the vortex shedding and the natural frequency of the transverse waves vary in the longitudinal direction. If the vortex shedding frequency varies too much, no resonance can be expected to occur on the array scale. To test this hypothesis (seiching was unfortunately not investigated for the WM cases), we studied two accelerated flows in a cylinder array occupying the whole flume under the same flow rate $Q = 15\,\mathrm{L.s^{-1}}$: a lower acceleration with a water depth gradient of $dH/dx = -0.6\,\mathrm{mm.m^{-1}}$ ($H(x = 0) = 92\,\mathrm{mm}$) and a higher acceleration with a water depth gradient of $dH/dx = -1.3\,\mathrm{mm.m^{-1}}$ ($H(x = 0) = 84\,\mathrm{mm}$). The accelerated flows were obtained by lowering the flume downstream weir. Figure 4.14 illustrates the flow depth standard deviations for these two accelerated flows. The variations in Strouhal frequency, using $f_{St} = 0.2U_Q/D$, for these accelerations are $df_{St}/dx = 0.021\,\mathrm{Hz.m^{-1}}$ and $df_{St}/dx = 0.055\,\mathrm{Hz.m^{-1}}$ respectively.

Periodic free surface oscillations were observed in the water depth time series. However, the fluctuation amplitudes were lower than those in the uniform flow case (W-Q15): the amplitudes are approximately one half and one quarter of those of the uniform flow case for the lower and higher accelerations respectively. The water depth time series show that the frequency along the flume is constant for both flows. It can be concluded that, although the seiche can still be observed when the flow is non-uniform within the cylinder array, its intensity is greatly reduced.

For the lower acceleration the seiche frequency is $f_H \approx 2.7\,\mathrm{Hz}$ and the corresponding most appropriate oscillation mode, using the water depth at mid-length of the cylinder array $H(x = 0)$, is $n_0 = 10$ ($f_{TW} = 2.79\,\mathrm{Hz}$). A lateral water surface profile confirms that the wave length of the seiche for this flow is 200 mm. For the higher acceleration the seiche frequency is $f_H \approx 3.0\,\mathrm{Hz}$ and the corresponding most appropriate oscillation mode is $n_0 = 12$ ($f_{TW} = 3.06\,\mathrm{Hz}$).

The seiche phenomenon was not investigated for the present wood-to-meadow cases. But considering the water depth gradients of these flows ($dH/dx = -1.5, -2.5$ and $-6.0\,\mathrm{mm.m^{-1}}$ for test cases WM-Q7, WM-Q15 and WM-Q50, respectively) it can be assumed that some weak coherent free surface oscillations should occur for WM-Q7 but that no seiche should be present for the two other cases.

4.5 Conclusion

The combined effects of bed friction and cylinder drag were analysed for uniform flows through an array of emergent cylinders installed on a rough bed (dense meadow) or a smooth bed (glass bottom). The water column within a cylinder array could be divided into a constant-velocity region in the upper water column and a boundary layer in the near-bed region. The boundary layer height was found to be independent of the water depth and of the bed surface condition (rough or smooth). Conversely, the shape of the boundary layer was dependent on the bed roughness. A local increase in longitudinal velocity (velocity bulge) was observed near the bed in line with a longitudinal row of

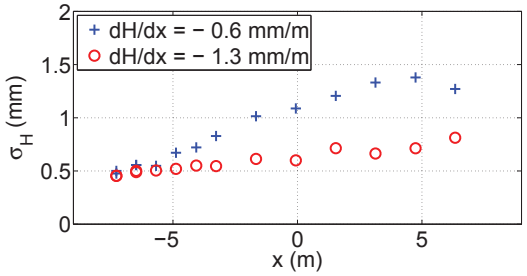

Figure 4.14: Longitudinal variation in flow depth standard deviation σ_H for two accelerated flows with water depth gradients of $dH/dx = -0.6\,\mathrm{mm.m^{-1}}$ and $dH/dx = -1.3\,\mathrm{mm.m^{-1}}$ respectively. Flow rate is $Q = 15\,\mathrm{L.s^{-1}}$. Cylinder array is 18 m long.

cylinders. This velocity bulge may be related to the effect of bed-induced turbulence. The latter disorganizes the von Kármán vortex street, resulting in smaller drag forces and less momentum loss in the cylinder wake. Additional energy loss is due to the bed friction in the near-bed region. Friction is higher for a rough bed than for a smooth bed, so near-bed velocity is lower and velocity bulge is weaker in the case of a rough bed.

Longitudinal roughness transitions between bed friction and emergent cylinder drag, and *vice versa*, were then investigated. Flow depth and velocity responses to roughness transitions were found to oppose each other. The water depth varied upstream of a roughness transition, while the vertical profiles of mean longitudinal velocity and turbulence remained constant and similar to uniform flow profiles, if the former parameters were normalised by the local section-averaged mean velocity and the local shear velocity respectively. The water depth was constant downstream of the transition, while a vertical redistribution of mass and momentum occurred over a longitudinal distance of $L_{dw}/H_{dw} \approx$ 35-50, where H_{dw} is the uniform flow depth of the downstream roughness.

A 1D momentum equation including a volume drag force was used to predict the water depth profile with a mean error of 0.9 %. This equation was also used to calculate the distance upstream of the transition to reach equilibrium L_{up}. This distance scaled approximately with the uniform flow depth of the upstream roughness H_{up} and $L_{up}/H_{up} \approx$ 2580. The momentum equation was analytically solved for zero bed friction.

Free surface oscillations (seiching) were observed through the cylinder array under uniform and non-uniform flow conditions. Several hours were required to achieve constant amplitude oscillations. The amplitude was found to be dependent on the longitudinal position within the array with a peak value at its mid-length. Furthermore, the seiching decreased with a decreasing array length. The seiche driving forces are the periodic lift forces in the cylinder wake. These were found to be only present in the constant-velocity region, whereas they were prevented in the boundary layer because of the disorganization of the von Kármán vortex street. Therefore, if the water depth/boundary layer height ratio was close to unity, no seiche appeared. Finally, the seiching process was found to decrease with increasing flow non-uniformity. This could be associated with the increasing Strouhal frequency gradient along the cylinder array, which curtails synchronization between cylinder wakes.

Chapter 5

Development towards uniformity of a compound channel flow with and without emergent rigid vegetation on the floodplains

Preliminary note

A part of this chapter was submitted to publication to the journal *Experimental in Fluids*.

5.1 Introduction

An overflowing river gives rise to a flow in a compound cross-section, composed of the river main channel and adjacent floodplains. The compound channel mixing layer, generated by the difference in velocity between main channel and floodplain, has three-dimensional features owing to the two-stage geometry and the vertical confinement, which give it a special scientific interest. After a brief review of various types of mixing layers, the compound channel mixing layer specificity will be exposed.

The turbulent plane mixing layer is formed by two parallel streams of different velocities without vertical or lateral confinement. The turbulent plane mixing layer width grows linearly and indefinitely when going downstream. The growth rate is a function of the normalised velocity difference $\lambda = (U_1 - U_2)/(U_1 + U_2)$ where U_1 and U_2 are the velocities outside the mixing layer in the high speed stream and low speed stream, respectively. Several formulations have been proposed to relate the growth rate of the mixing layer width to parameter λ (Brown and Roshko, 1974; Oster and Wygnanski, 1982; Yule, 1972). However, the growth rate appears to significantly vary from one experiment to another. In particular, this growth rate is dependant on the nature of the boundary layer (laminar or turbulent state, boundary layer heigth) at the trailing edge of the initial flow splitter plates (Bell and Mehta, 1990) and can also be influenced by forced periodic excitation in the initial region, for example through resonance phenomenon in the experimental facility (Ho and Huerre, 1984). Except in the wake of the splitter plate, the flow in the turbulent plane mixing layer is self-similar, i.e. the lateral profiles of longitudinal mean velocity and of turbulence quantities are invariant in the longitudinal direction when normalised by the velocity difference $U_1 - U_2$ and the mixing layer width.

Brown and Roshko (1974) showed with flow visualization that the velocity fluctuations of the plane turbulent mixing layer are driven by 2D horizontal coherent structures, whose

shape and dynamics resemble to the Kelvin vortex of the laminar mixing layer. These coherent structures are generated quasi-periodically. According to Ho and Huerre (1984), the coherent structures of the plane mixing layer are generated with a preferred mode, which is characterised by the Strouhal number $St = f\theta/U_0$, where f is the passage frequency of the coherent structures and θ is the momentum thickness of the mixing layer, defined by:

$$\theta = \int_{-\infty}^{+\infty} \left(\frac{1}{4} - \left(\frac{U - U_0}{U_1 - U_2} \right)^2 \right) dy. \tag{5.1}$$

The natural Strouhal number of the plane mixing layer is $St = 0.032$ for sufficiently low free stream velocities. If the free stream velocities are such that the initial boundary layers at the splitter plates are turbulent, the Strouhal number of the plane mixing layer is increased to $St = 0.044$-0.048 (Ho and Huerre, 1984). Brown and Roshko (1974) showed that the mean distance L_{CS} between two successive coherent structures is proportional to the vorticity width of the mixing layer, defined by $\delta_\omega = (U_1 - U_2)/(dU/dy)_{max}$, and they estimated $L_{CS} \approx 2.9\delta_\omega$.

Compared to the plane mixing layer, the shallow mixing layer is a vertically confined flow that is influenced by the bottom and the free surface (Chu and Babarutsi, 1988; Uijttewaal and Booij, 2000). If the influence of the bed is sufficiently important, the mixing layer width converges to a constant at a longitudinal distance of $x^* = xc_f/H \approx 0.6$-1, where H is the water depth and c_f is the averaged bed friction coefficient across the mixing layer ($c_f = 0.5(c_{f1} + c_{f2})$ with $c_{fi} = \tau_b/(0.5\rho U_i^2)$, $i \in \{1, 2\}$ and τ_b the bed shear stress). This convergence is attributed to the stabilizing effect of the small-scale 3D bed-induced turbulence on the 2D horizontal coherent structures.

Mixing layers can also be generated by a lateral change in roughness along a flat channel. Such flows were investigated by Vermaas *et al.* (2011) in the case of a rough bed adjacent to a smooth bed and by White and Nepf (2007) and Zong and Nepf (2010) in the case of an array of emergent cylinders adjacent to a smooth bed. Vermaas *et al.* (2011) showed that in the fully developed flow region, the contribution of the secondary currents to the lateral exchange of longitudinal momentum can exceed that of the lateral Reynolds stresses. This makes an important difference with the plane mixing layer for which longitudinal vorticity, although present (Bernal and Roshko, 1986), plays a rather minor role in the lateral momentum exchange. White and Nepf (2007) showed that, similarly to shallow mixing layers, in the case of emergent roughness elements on one side of the mixing layer, the mixing layer stops growing at a certain distance downstream. This is attributed to the high energy dissipation of the coherent structures in the cylinder array. They found out that the elementary coherent structure is quasi-2D and consists in a Kelvin-type vortex associated with a strong ejection event (transfer of slow-moving fluid into the high speed region) upstream of the vortex and a somewhat weaker aspiration event (transfer of fast-moving fluid into the low speed region) downstream of the vortex. The lateral flux of longitudinal momentum is mostly due to the ejection and aspiration events, while the contribution to this flux by the secondary currents is one order of magnitude lower. White and Nepf (2007) found the passage frequency of the coherent structure to be approximately that of the laminar mixing layer $St = 0.032$.

For practical reasons plane and shallow mixing layers are always laterally confined. This results in a reduction of the velocity $U_1 - U_2$ and in a lateral homogenisation of the flow when going downstream. Wood and Bradshaw (1984) showed furthermore that the presence of a confining side wall influences the turbulence budget within the plane mixing layer, both before and after the mixing layer reaches the wall.

Compared to the previous types of mixing layer, the compound channel mixing layer has specific properties that make the physical processes somewhat different. The pres-

ence of the bed induces a vertical boundary layer that is superimposed to the mixing layer and made it three-dimensional, in common with the shallow mixing layers. The compound channel mixing layer is laterally confined, either by side walls or by the mixing layer of the opposite bank. But contrary to plane and shallow mixing layers, the lateral flow confinement does not induce a reduction of the velocity difference $U_1 - U_2$ when going downstream: the velocity difference is self-sustained by the two-stage geometry. Both subsections, main channel and floodplain, are characterized by different aspect ratios and potentially different hydraulic roughnesses, leading to different flow structures (e.g. secondary currents). As a result, the compound channel mixing layer can be largely asymmetric with respect to the main channel/floodplain interface. The lateral distribution of longitudinal velocity cannot therefore be represented with an antisymmetric function such as the the hyperbolic tangent or the error functions, as is done for plane mixing layers.

According to Knight and Demetriou (1983), Knight and Shiono (1990) and Tominaga and Nezu (1991), the main driving parameters of a straight compound channel flow are: the relative flow depth $D_r = H_f/H_m$ (ratio of floodplain flow depth H_f to main channel flow depth H_m); the aspect ratios of the main channel $\alpha_m = B_m/H_m$ and of the floodplain $\alpha_f = B_f/H_f$ where B_m and B_f are the main channel and floodplain widths respectively; the roughness in each subsection; and, for trapezoidal channels, the main channel and/or floodplain bank slopes. The decrease in relative depth D_r or the increase in the difference in roughness between floodplain and main channel both result in increasing the velocity difference across the mixing layer and therefore in enhancing turbulence production (Fernandes, 2013). Relative depth, aspect ratio and bank slopes of each subsection largely determine the secondary currents (Blanckaert *et al.*, 2010; Tominaga and Nezu, 1991), that in turn play an important role in the momentum distribution across the compound channel section (Kara *et al.*, 2012). For the same aspect ratio α_m, the fact that the compound section is symmetric (two identical floodplains on both sides of the main channel) or asymmetric (one floodplain on one side and a vertical wall on the other side) also influences the flow field (Proust *et al.*, 2013). In symmetrical layout the two opposite mixing layers mostly meet at the main channel centreline. In asymmetrical layout, the mixing layer mostly reaches the lateral boundary layer of the vertical wall.

Compound channel flows were investigated in previous laboratory studies for different types of floodplain roughness: smooth bed (Knight and Shiono, 1990; Peltier, 2011; Stocchino and Brocchini, 2010), rough bed (Fernandes, 2013; Tominaga and Nezu, 1991) and emergent roughness (Kozioł, 2013; Pasche and Rouvé, 1985). The flow is generally analysed at a constant downstream position, where it is considered as fully developed. However, only few studies considered the longitudinal flow development. Proust *et al.* (2016) in the case of a smooth compound channel and Fernandes (2013) in the case of a compound channel with rough floodplains showed that the mixing layer width levels off when going downstream and that the initial growth rate is comparable to that of a plane mixing layer.

The presence of coherent structures in the compound channel flow has been early identified (Sellin, 1964). Stocchino and Brocchini (2010) showed that macro-vortices at the main channel/floodplain interface are only present for sufficiently shallow flows ($D_r < 0.5$). According to Proust *et al.* (2016), coherent structures are only present for $\lambda' > 0.3$, where $\lambda' = (U_{d1} - U_{d2})/(U_{d1} + U_{d2})$ is based on the depth-averaged velocities (subscript d refers to depth-averaging). Tamai *et al.* (1986) showed that despite the complex 3D organisation of the compound channel coherent structures, their periodicity can be predicted by a 2D stability analysis. Nezu and Nakayama (1997) showed that the secondary currents at the main channel/floodplain interface are intermittent phenomena,

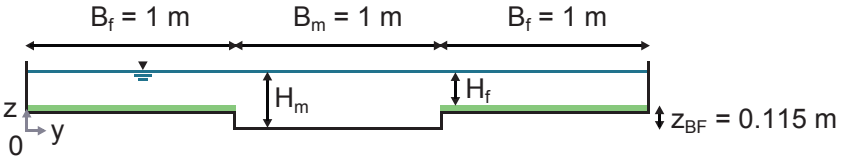

Figure 5.1: Front view of the compound channel flume.

which are coupled with the horizontal coherent structures, both forming a unique vortex structure. Lukowicz (2002) confirmed the coupling between horizontal vortices and time-dependant secondary currents and showed that the vortex structure is preceded by a sweep event and followed by an ejection event. A Lagrangian analysis of the compound channel coherent structures was carried out by Stocchino *et al.* (2011) who showed that the coherent structures are responsible for an intermediate region in the Lagrangian mixing between the initial ballistic regime and the asymptotic Brownian regime.

The present experimental study aims at investigating the longitudinal development and the flow structure of two compound channel mixing layers, with either a bed roughness or an emergent cylinder array on the floodplain. The flow conditions are such that $D_r < 0.5$ and $\lambda' > 0.3$, therefore coherent structures are present in the flows and are investigated.

5.2 Experimental setup and methodology

The experiments were performed in an 18 m long and 3 m wide glassed-wall flume, located in the Hydraulics and Hydromorphology Laboratory of Irstea, Lyon-Villeurbanne, France. The compound channel cross section was symmetrical and composed of a rectangular central main channel of width $B_m = 1$ m and two adjacent floodplains of width $B_f = 1$ m (see Fig. 5.1). The longitudinal bottom slope was $S_0 = 1.05\,\mathrm{mm.m^{-1}}$. Both right and left floodplains were covered by a dense plastic grass, whose blades were 5 mm long and rigid. The bankfull level, measured from the bottom of the main channel to the crest of the grass blades was $z_{BF} = 115$ mm.

The inlet discharges in the three subsections (main channel, right and left floodplains) were regulated independently with control valves and measured by electromagnetic discharge-meters. After leaving the inlet tank, the flows in the right and left floodplains were accelerated along a linear ramp before reaching the bankfull level (see Fig. 5.2). The streams in the three subsections were separated by vertical splitter plates until the ramp end. A 100 mm-thick honeycomb was installed in the inlet tank of the main channel in order to vertically and laterally homogenize the flow (alveolus size 8 mm). At the flume outlet, the flow was controlled by three independent weirs (one per subsection). Downstream splitter plates maintained the flow in the three subsections separated over a distance of 50 cm upstream of the weirs.

The x-, y- and z-axis refer to the longitudinal (along flume bottom), lateral and vertical (normal to flume bottom) directions, respectively. In this coordinate system, the instantaneous velocities, time-averaged velocities and velocity fluctuations are denoted by (u, v, w), (U, V, W) and (u', v', w'). Overline denotes time-averaging (e.g. $\overline{u'v'}$). The origin of the longitudinal coordinate is defined at the trailing edge of the upstream splitter plates[1]. The origin of the lateral axis is located at the side wall of the right floodplain. The origin of the vertical coordinate is defined at the bottom of the main channel. A relative vertical coordinate z_f is additionally defined at the floodplain bottom: $z_f = z - z_{BF}$.

[1]The longitudinal coordinate with origin at the splitter plates is denoted x_a in all other chapters.

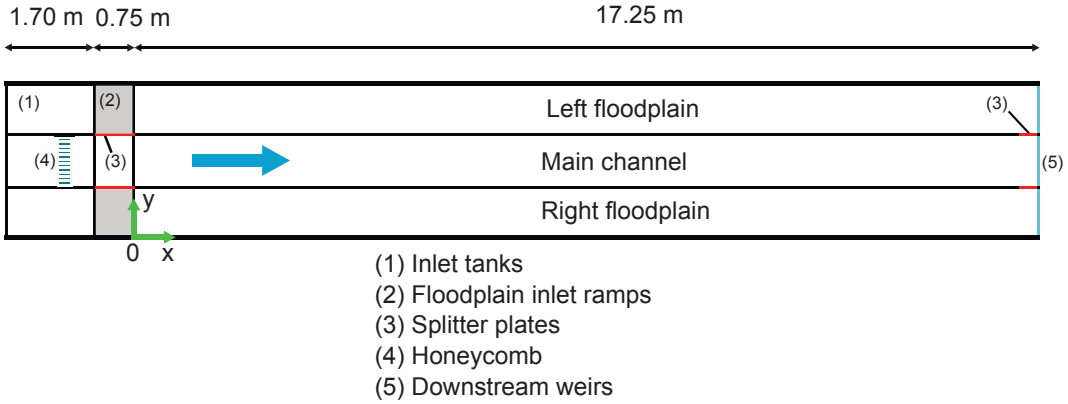

Figure 5.2: Plan view of the compound channel flume.

Two flow test cases were investigated, with floodplains covered either by plastic grass only or by an array of emergent cylinders set on plastic grass. These two roughness types represent a highly submerged meadow and a wood with emergent trees on the floodplain, respectively. In the following, these two test cases are termed CM (for Compound channel flow with Meadow over the floodplains) and CW (for Compound channel flow with Wood on the floodplains). The total discharge was the same for the two test cases ($Q_{tot} = 162\,\mathrm{L.s^{-1}}$). Following Bousmar *et al.* (2005) the upstream discharge distribution and the downstream weir levels were adjusted by an iterative process in order to get a free surface parallel to the channel bed and to minimize the lateral fluid transfers between subsections. The flow conditions are reported in Table 5.1.

Table 5.1: Flow conditions of the test cases: total discharge Q_{tot}, discharge in the main channel Q_m, discharge in each floodplain Q_f, water depth in the main channel H_m, relative flow depth D_r, Reynolds number $Re_i = 4Q_i/(\nu(2H_i + B_i))$ and Froude number $Fr_i = Q_i/(H_i^{3/2} g^{1/2} B_i)$ in each subsection ($i \in \{m, f\}$).

Test case	Q_{tot} ($\mathrm{L.s^{-1}}$)	Q_m ($\mathrm{L.s^{-1}}$)	Q_f ($\mathrm{L.s^{-1}}$)	H_m (mm)	D_r	Re_m $\times 10^{-4}$	Fr_m	Re_f $\times 10^{-4}$	Fr_f
CM	162	126	18	171	0.33	37.6	0.57	6.5	0.42
CW	162	134	14	214	0.46	37.5	0.43	4.7	0.14

The cylinder array for test case CW was made of wooden circular cylinders that were uniformly distributed in staggered rows (see Fig. 5.3b). The cylinder diameter was $D = 10\,\mathrm{mm}$ and the cylinder density $N = 81\,\mathrm{cylinders.m^{-2}}$. They were hold together with an emergent wooden superstructure (see Fig. 5.3a). Cylinder rows in the lateral direction are called even or odd whether they consist in an even or odd number of cylinders. The accuracy of each cylinder position was $\pm 5\,\mathrm{mm}$ in both lateral and longitudinal directions.

The free surface levels were measured with ultrasonic sensors (UNDK20I69, Baumer) with an accuracy of $\pm 0.5\,\mathrm{mm}$. Longitudinal profiles of free surface level with a longitudinal step of 1 m were measured at 7 lateral positions ($y = 300, 700, 1200, 1500, 1800, 2200, 2700\,\mathrm{mm}$). The recording time was 3 min for each measuring point and the sampling rate was 50 Hz. The water depth was found to be constant in the range $2 < x < 17\,\mathrm{m}$ in the three subsections with discrepancies of $\pm 1\,\mathrm{mm}$ around the averaged value for both flows. Two types of velocity measurements were carried out: single point measurements with a unique ADV probe and two-point space-time correlation measurements with two ADV probes. Side-looking ADV probes were used (Vectrino

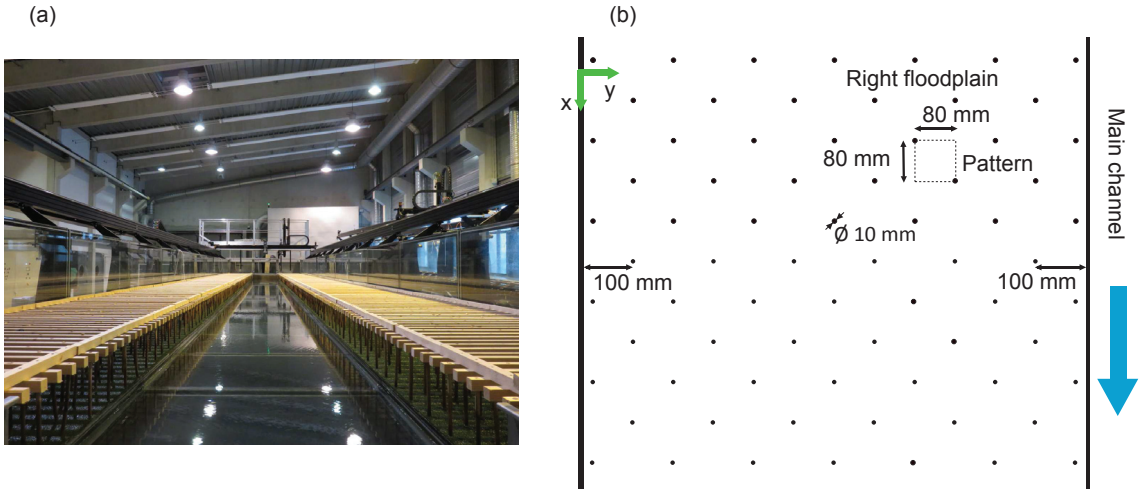

Figure 5.3: (a) Picture from downstream of the compound channel flume located at Irstea, with wooden cylinders set on plastic grass over the floodplain (test case CW). (b) Plan view of the cylinder array arrangement for test case CW.

Plus, Nortek), working with a sampling rate of 100 Hz. A recording time of 120 s was found to be sufficient to obtain converged mean velocities and turbulence quantities. The recording time was increased to 600 s for spectral analysis, autocorrelations and spatial correlation measurements. The ADV raw data were filtered with the software WinADV based on the despiking concept developed by Goring and Nikora (2002).

Velocity fields in the (y, z)-plane were measured across the compound section at five x-stations along the flume for test case CM and at four x-stations, but only in the main channel, for test case CW (owing to the high flow heterogeneity in the wooded floodplain, very refined measuring grid are required). The main channel discharge Q_m was calculated by integrating the velocity field over the main channel cross-section for each x-station. The maximum discrepancy between the inlet main channel discharge (measured with the discharge-meter) and the discharge obtained by velocity integration in the flume was 1.1 % for test case CM and 0.9 % for test case CW. The discharge distribution between subsections was thus considered to be constant along the channel for both test cases.

Owing to the symmetry of the compound cross-section, we mostly present herein measurements across the right-hand half of the flume. The vertical (x, z)-plane at the main channel-floodplain boundary is called the interface ($y = y_{int} = 1000$ mm).

5.3 Longitudinal flow development

5.3.1 Cross-sectional distribution of flow quantities

Figure 5.4 shows the cross-sectional distribution of mean longitudinal velocity U (total cross-section) and lateral turbulence intensity $\rho\overline{v'^2}$ (half cross-section) at different x-stations for test case CM. The flow is fairly symmetrical about the main channel centreline. A marked longitudinal development can be observed for both quantities. The region of maximum velocity U is located beneath the bankfull level in the first measuring station and progressively moves towards the free surface when going downstream. The region of high lateral turbulence intensity expands on both sides of the interface when going downstream. Another source of turbulence is located at the bottom of the main channel and this turbulence diffuses towards the free surface when going downstream.

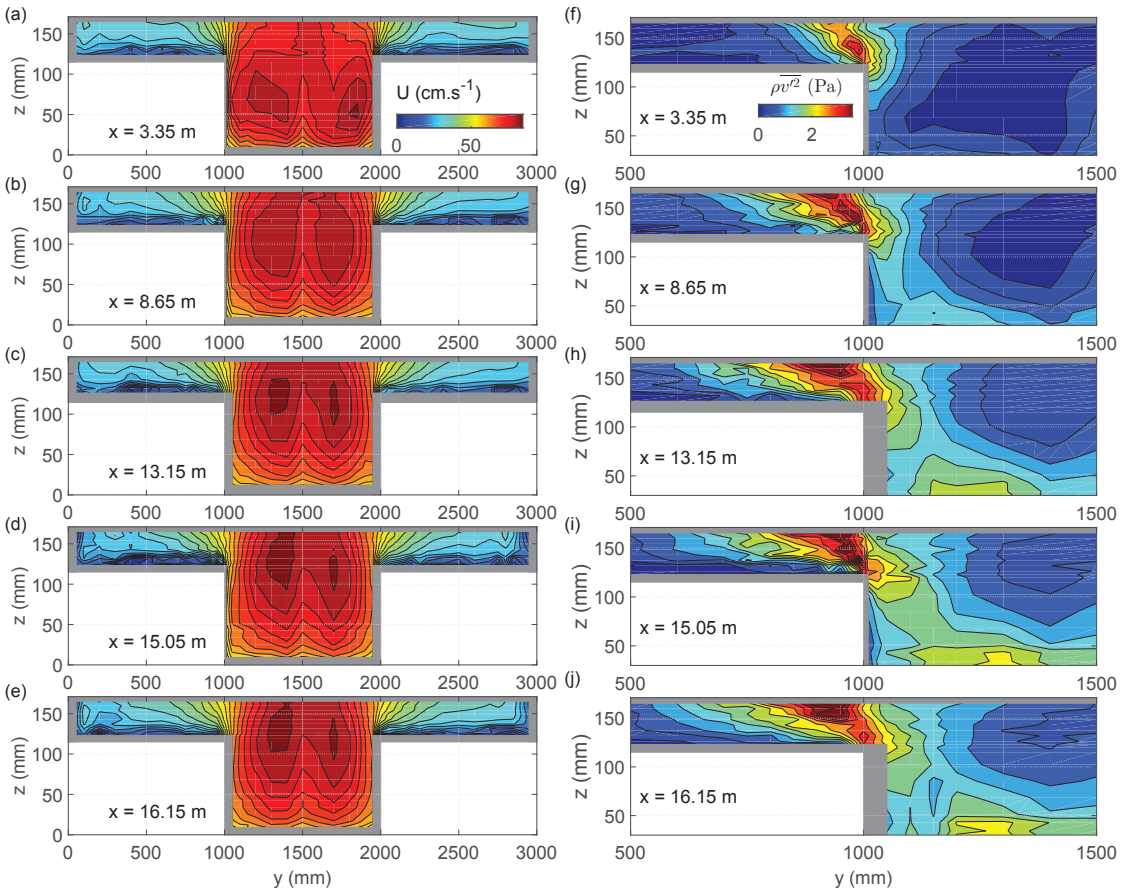

Figure 5.4: Development towards uniformity of a compound channel flow with bed roughness over the floodplains (test case CM).(a-e) Mean longitudinal velocity U in the total compound cross-section and (f-j) lateral turbulence intensity in the right-hand half cross-section at various x-positions. Regions where measurements are unavailable are grey shaded.

Figure 5.5 shows the same quantities for test case CW but in the right-hand half main channel only. The observations are similar to test case CM (rising up of the region of maximum velocity, lateral extension of the turbulence region at the interface, turbulence production at the main channel bottom). The distributions of U and $\rho\overline{v'^2}$ are very similar in the two last stations for both flows (this was also observed for the other turbulence quantities).

5.3.2 Flow quantities at the main channel/floodplain interface

The longitudinal flow development was analysed in detail along the interface. In order to quantify this development, an indicator I_A is defined:

$$I_A(x)[\%] = \frac{100}{n}\sum_{i=1}^{n}\left|\frac{A(x,z_i) - A_c(z_i)}{A_c(z_i)}\right| \tag{5.2}$$

where A is a flow quantity, n is the number of measuring points over the flow depth and $A_c(z_i)$ is an average of the last three vertical profiles, measured in the region $14.5 < x < 16.9$ m. This indicator I_A is an estimate of the discrepancy between the vertical profile $A(x,z_i)$ and the averaged profile in the most downstream part of the channel $A_c(z_i)$. Figure 5.6 shows the longitudinal evolution of the I_A-indicator for $A = U$, $\overline{u'v'}$, $\overline{u'^2}$ and $\overline{v'^2}$ for the two test cases CM and CW. When the indicator I_A does no longer decrease,

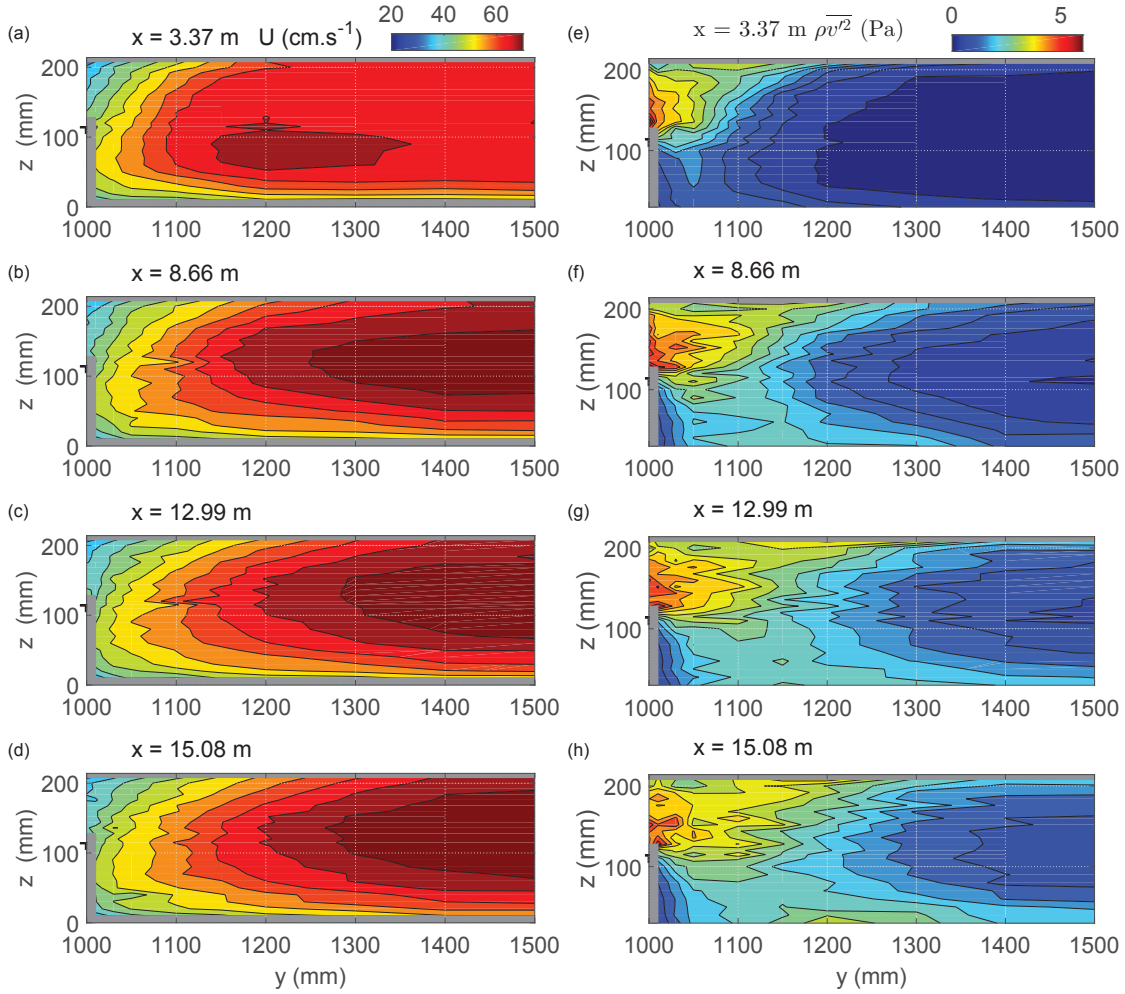

Figure 5.5: Development towards uniformity of a compound channel flow with an emergent cylinder array on the floodplains (test case CW). (a-d) Mean longitudinal velocity and (e-h) lateral turbulence intensity in the right-hand half cross-section of the main channel at various x-positions. Regions where measurements are unavailable are grey shaded. The black edge on the vertical axis indicates bankfull level.

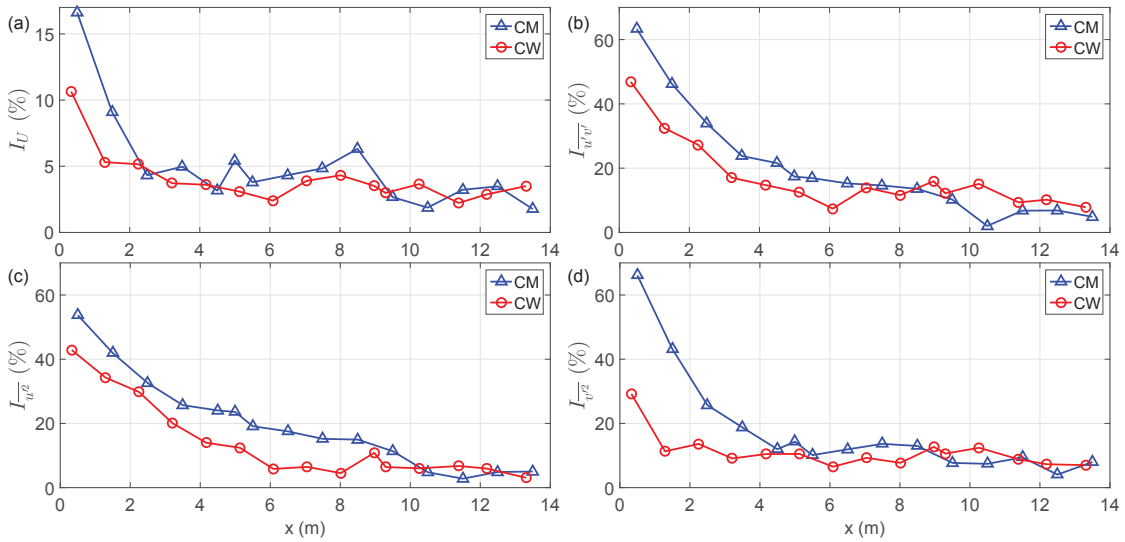

Figure 5.6: Longitudinal development of the vertical profiles of (a) mean longitudinal velocity U and (b) lateral Reynolds stress $-\rho\overline{u'v'}$, (c) longitudinal turbulence intensity $\rho\overline{u'^2}$ and (d) lateral turbulence intensity $\rho\overline{v'^2}$ at the interface between main channel and floodplain ($y = 1000\,\mathrm{mm}$) for test cases CM and CW. Indicator I_A, for any flow variable A, is defined in Eq. 5.2.

the quantity A can be considered as converged. For both flows, first the mean velocity U, then the lateral turbulence intensity $\rho\overline{v'^2}$ and finally the lateral Reynolds stress $\rho\overline{u'v'}$ together with the longitudinal turbulence intensity $\rho\overline{u'^2}$ converge successively. However, the development towards uniformity is faster for test case CW than for test case CM, all flow quantities considered being constant beyond $x \approx 6\,\mathrm{m}$ and $x \approx 11\,\mathrm{m}$, respectively.

5.3.3 Mixing layer

5.3.3.1 Mixing layer centre

For plane mixing layers, because of the symmetry of the lateral velocity profile (hyperbolic tangent), the lateral position y_{U_0} where the mean velocity across the mixing layer $U_0 = (U_1 + U_2)/2$ is reached, and the position of the mean velocity inflexion point y_{IP} collapse. In compound channels, these two positions can differ (Fig. 5.8a). As the inflexion point is the primary source of flow instability (Fjortoft, 1950), we consider the inflexion point position as the centre of the mixing layer. The position of the inflection point y_{IP} (not shown) appears to be constant over the depth and along the flume, with $y_{IP} = 1000 \pm 5\,\mathrm{mm}$ for both test cases CM and CW. The position of the inflection point is thus related to the position of the vertical bank. On the contrary, the position y_{U_0} is not located at the interface, as seen in Fig. 5.7. The y_{U_0}-location is displaced towards the main channel when going downstream (Fig. 5.7a). Positions y_{U_0} is also displaced towards the main channel when going upwards in the water column (Fig. 5.7b). The lateral displacement of y_{U_0} with respect to y_{IP} is sketched in Fig. 5.8a.

5.3.3.2 Mixing layer width

The transverse development of the mixing layer was studied by estimating the mixing layer width at different x-positions and at the constant altitude $z_f = H_f/2$. To take into account the asymmetry of the compound channel mixing layer with respect to the longitudinal interface, two mixing layer widths are defined on either side of the interface:

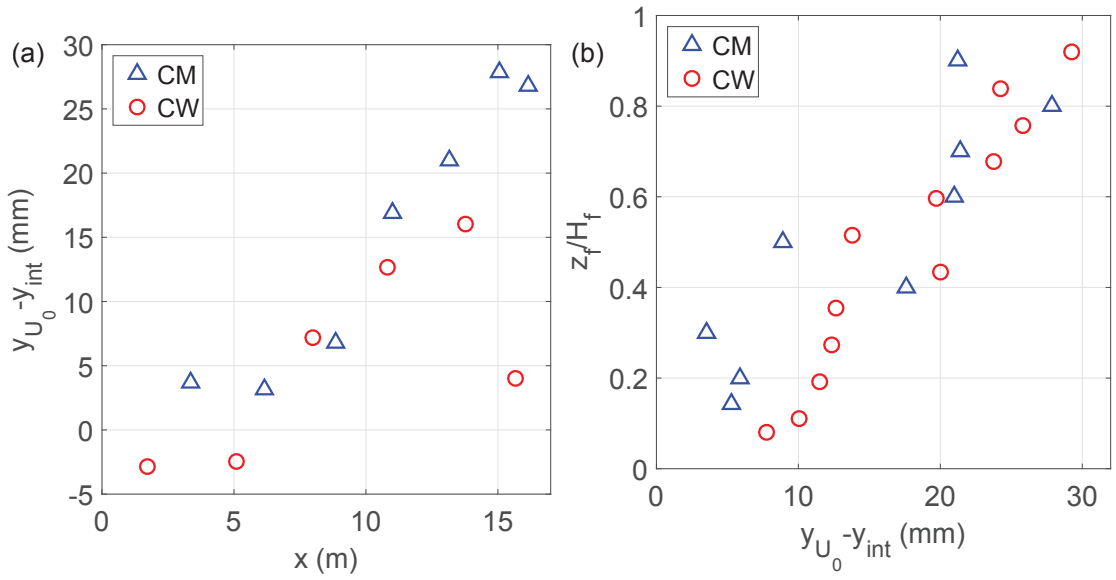

Figure 5.7: (a) Longitudinal variation in position y_{U_0} at constant elevation ($z_f = H_f/2$) and (b) vertical variation in position y_{U_0} (at $x = 15.05\,\mathrm{m}$ for test case CM and at $x = 11.76\,\mathrm{m}$ for test case CW).

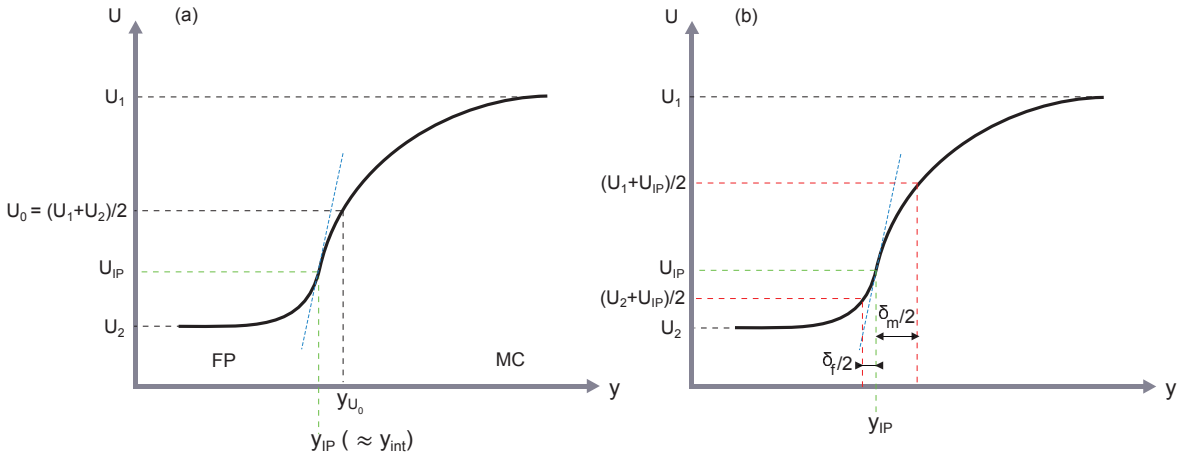

Figure 5.8: (a) Displacement of the lateral position of the mean velocity across the mixing layer y_{U_0} with respect to the position of the inflexion point y_{IP}. (b) Calculation of the main channel and floodplain mixing layer widths, δ_m and δ_f, from the lateral profile of mean longitudinal velocity U.

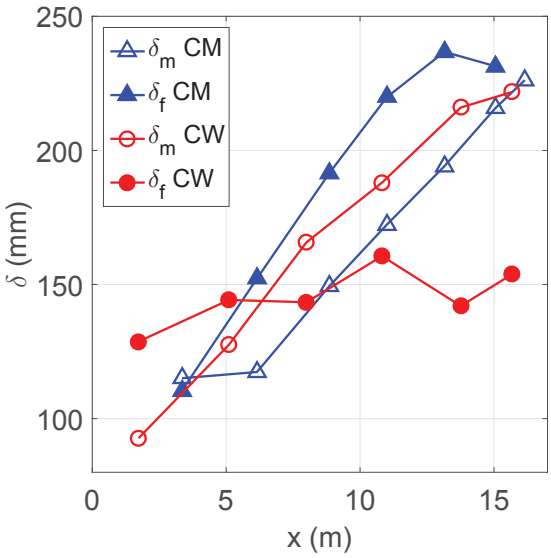

Figure 5.9: Longitudinal variation in main channel and floodplain mixing layer widths. Measurements at $z_f/H_f = 0.5$.

the main channel mixing layer width δ_m and the floodplain mixing layer width δ_f. Widths δ_m and δ_f are calculated from the lateral velocity profile as follows (see sketch in Fig. 5.8b):

$$U(y_{IP} + \delta_m/2) = \frac{U_1 + U_{IP}}{2} \tag{5.3}$$

$$U(y_{IP} - \delta_f/2) = \frac{U_2 + U_{IP}}{2} \tag{5.4}$$

where U_1 is the maximum velocity in the main channel, U_2 is the velocity in the floodplain outside the mixing layer in the plateau region and U_{IP} is the velocity at the inflexion point. These definitions are consistent with the choice of y_{IP} as the mixing layer centre. Note that for an antisymmetric mixing layer ($U_{IP} = U_0$), the total mixing layer width $\delta_{tot} = \delta_m + \delta_f$ is the same as the one defined by Van Prooijen *et al.* (2005).

Figure 5.9 shows the longitudinal evolution of widths δ_m and δ_f. Width δ_m is increasing all along the measuring domain for both flow test cases. Width δ_f levels off at $x \approx 13\,\text{m}$ in the grassed floodplain and at $x \approx 5\,\text{m}$ in the wooded floodplain. The growth rate of the main channel mixing layer width is similar for both test cases with $\partial\delta_m/\partial x \approx 10\,\text{mm.m}^{-1}$. A higher growth rate is observed on the floodplain side for test case CM: $\partial\delta_f/\partial x \approx 14\,\text{mm.m}^{-1}$.

Peltier (2011) found that the mixing layer was no more extending laterally towards the main channel after $x = 6\,\text{m}$ for asymmetric compound channel flows in the range $H_r = 0.2$-0.4 with smooth floodplains. This difference with the present observations could be explained by the much narrower main channel in Peltier's experiment ($B_m = 0.4\,\text{m}$) than in the present experiment ($B_m = 1\,\text{m}$). When the main channel width decreases, the mixing layer is more rapidly constrained by the lateral boundary layer (in the case of an asymmetrical compound channel) or by the opposite mixing layer (in the case of a symmetrical compound channel).

The convergence of the mixing layer width in the grassed floodplain can be explained by the effects of shallowness and bed friction, which stabilise the mixing layer (Chu and Babarutsi, 1988). For the wooded floodplain, the cylinder array is responsible for the rapid convergence of δ_f: as pointed out by White and Nepf (2007), the lateral penetration of

the mixing layer and the associated coherent structures in a cylinder array is limited by the strong energy dissipation related to the cylinder drag.

5.3.3.3 Self-similarity in the longitudinal direction

The theory of plane mixing layer (Yule, 1972) states that lateral profiles of mean velocity and turbulence quantities are self-similar when going downstream, except in the near-field region (wake of the splitter plate). In order to test the self-similarity of the compound channel mixing layer, lateral profiles at $z_f = H_f/2$ of mean longitudinal velocity and of all six components of the Reynolds stress tensor were measured (Figs. 5.10 and 5.11 for test cases CM and CW, respectively). Mean velocity and turbulence quantities are normalised by the velocity difference $U_1 - U_2$, similarly to plane mixing layers. To take into account the asymmetry of the mixing layer, the lateral coordinate y is normalised by width δ_f in the floodplain and by width δ_m in the main channel. The mixing layer is found to be self-similar after $x = 6.1\,\mathrm{m}$ for test case CM and after $x = 1.7\,\mathrm{m}$ for test case CW. For test case CM the self-similarity is less marked on the floodplain side than on the main channel side (especially for $\overline{u'^2}$, $\overline{w'^2}$ and $\overline{u'w'}$). This can be related to shallowness effects on the floodplain side, that influence the flow structure. Note that for test case CW, the lateral profiles of flow quantities on the floodplain side are not only self-similar, they are almost constant after $x = 5\,\mathrm{m}$, as δ_f has stabilised.

Table 5.2 shows a comparison of the normalised peak values of $\sqrt{\overline{u'^2}}$, $\sqrt{\overline{v'^2}}$ and $\sqrt{\overline{u'v'}}$ measured at $z_f = H_f/2$ for test cases CM and CW with typical values for plane mixing layers (Olsen and Dutton, 2002) and with values for shallow mixing layers studied by Uijttewaal and Booij (2000). For test case CW, the peak values are measured 120 mm downstream of the cylinder positioned at $y = 980\,\mathrm{mm}$, such that the peak values are not due to the cylinder wake. Some higher values of $\sqrt{\overline{u'^2}}_{max}/(U_1-U_2)$ and $\sqrt{\overline{u'v'}}_{max}/(U_1-U_2)$ are observed for test case CW but globally the peak turbulence values are of the same order of magnitude for all types of mixing layer.

The lateral Reynolds stress $-\rho\overline{u'v'}$ is related to the lateral exchange of longitudinal momentum across the mixing layer due to turbulent motion, while the vertical Reynolds stress $-\rho\overline{u'w'}$ is related to the vertical exchange of longitudinal momentum across the water column. The value of $-\rho\overline{u'w'}$ is positive on the floodplain side for test case CM (Fig. 5.11b) because of the vertical boundary layer that is of logarithmic type. On the contrary, the value of $-\rho\overline{u'w'}$ is quasi equal to zero for test case CW (Fig. 5.11e), because of the absence of vertical boundary layer in the upper column of a cylinder array (see Chapter 4). Negative values of $-\rho\overline{u'w'}$ are observed for both test cases on the main channel side. This is due to the negative vertical gradient of longitudinal velocity U in this region, that in turn is related to the deceleration of this flow region induced by the floodplain flow. Sign inversion of $-\rho\overline{u'w'}$ at the main channel/floodplain vertical interface was also found in the large-eddy-simulations of Kara *et al.* (2012). Turbulent shear stress $-\rho\overline{v'w'}$ is related to longitudinal vorticity (secondary currents); the second spatial derivative of $\overline{v'w'}$ in the lateral direction is one of the production term in the transport equation of longitudinal vorticity (Bradshaw, 1987; Einstein and Li, 1958). The high gradients of $\overline{v'w'}$ near the interface (Figs. 5.11c and 5.11f) suggest that there is an important production of longitudinal vorticity in this region.

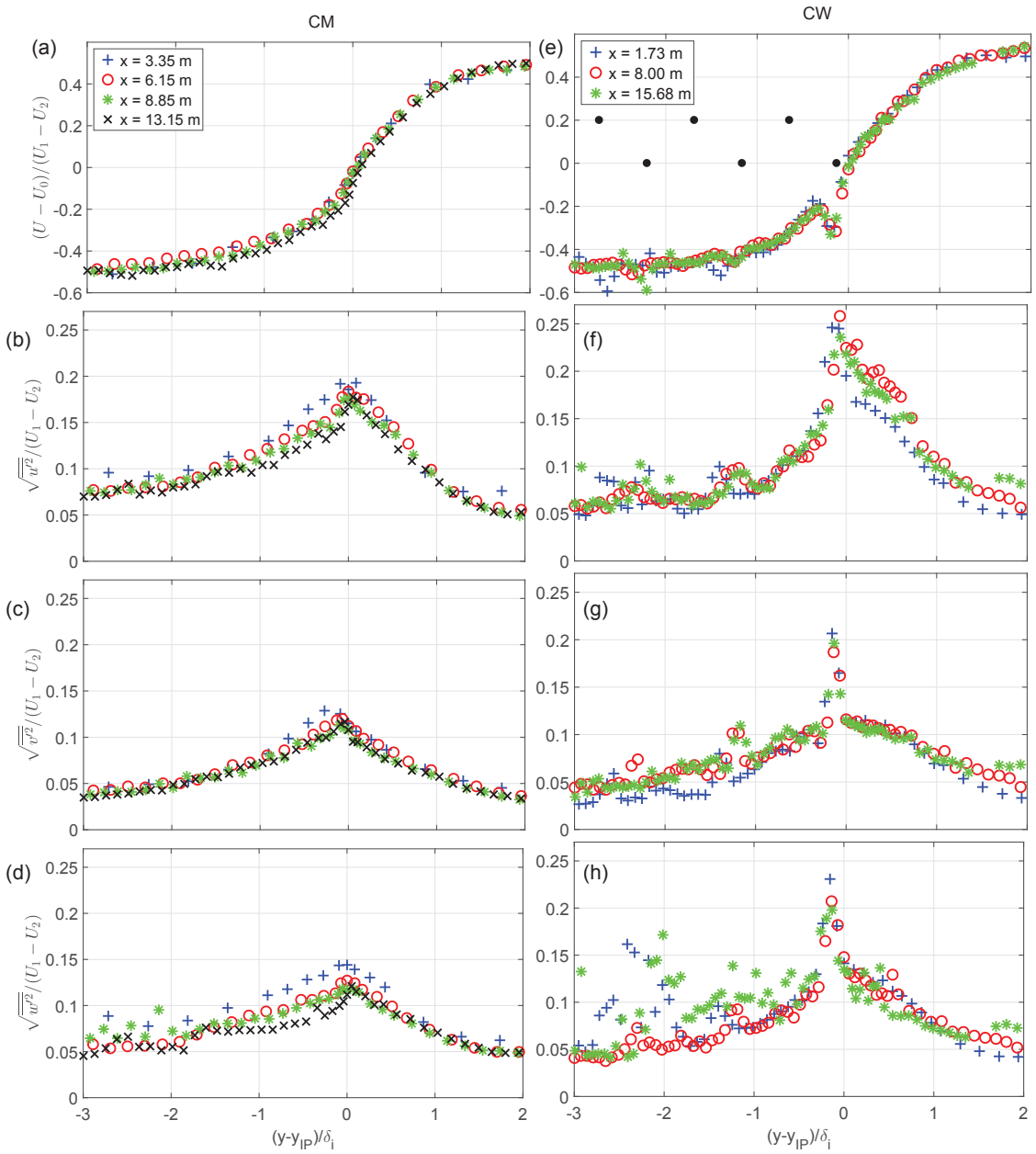

Figure 5.10: Lateral profiles at $z_f = H_f/2$ of normalised longitudinal mean velocity, longitudinal, lateral and vertical turbulence intensities for (a-d) test case CM and (e-h) test case CW. The mixing layer width δ_i is equal to δ_f on the floodplain side and to δ_m on the main channel side.

Table 5.2: Comparison of the normalised peak values of $\sqrt{\overline{u'^2}}$, $\sqrt{\overline{v'^2}}$ and $\sqrt{\overline{u'v'}}$ for the compound channel test cases CM and CW at $z_f = H_f/2$, the plane mixing layer (PML, see Olsen and Dutton, 2002) and the shallow mixing layer (SML, see Uijttewaal and Booij, 2000).

	$\sqrt{\overline{u'^2}}_{max}/(U_1-U_2)$	$\sqrt{\overline{v'^2}}_{max}/(U_1-U_2)$	$\sqrt{\overline{u'v'}}_{max}/(U_1-U_2)$
CM	0.17	0.11	0.10
CW	0.21	0.13	0.13
PML	0.17	0.14	0.10
SML	0.13	0.11	0.09

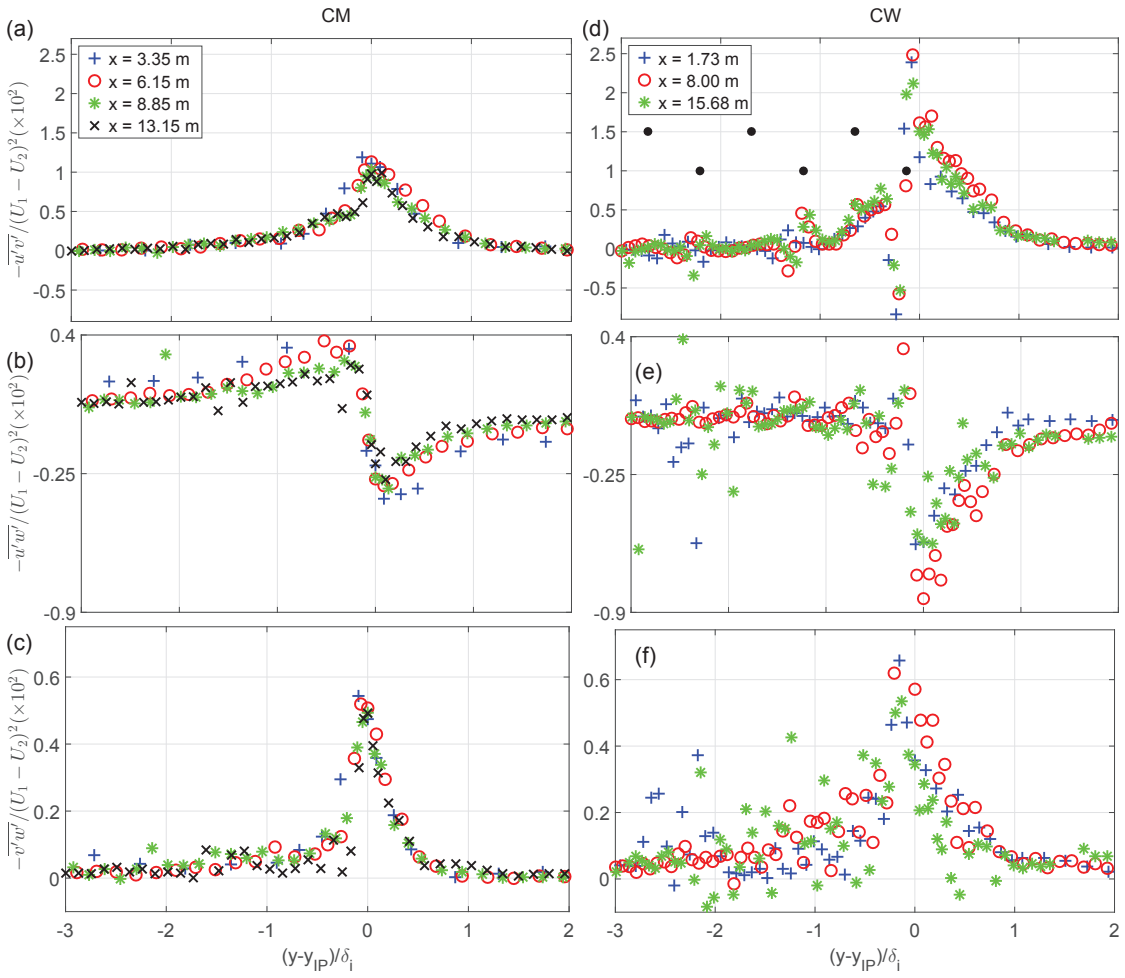

Figure 5.11: Lateral profiles at $z_f = H_f/2$ of the three normalised cross components of the Reynolds stress tensor for (a-d) test case CM and (e-h) test case CW. The mixing layer width δ_i is equal to δ_f on the floodplain side and to δ_m on the main channel side.

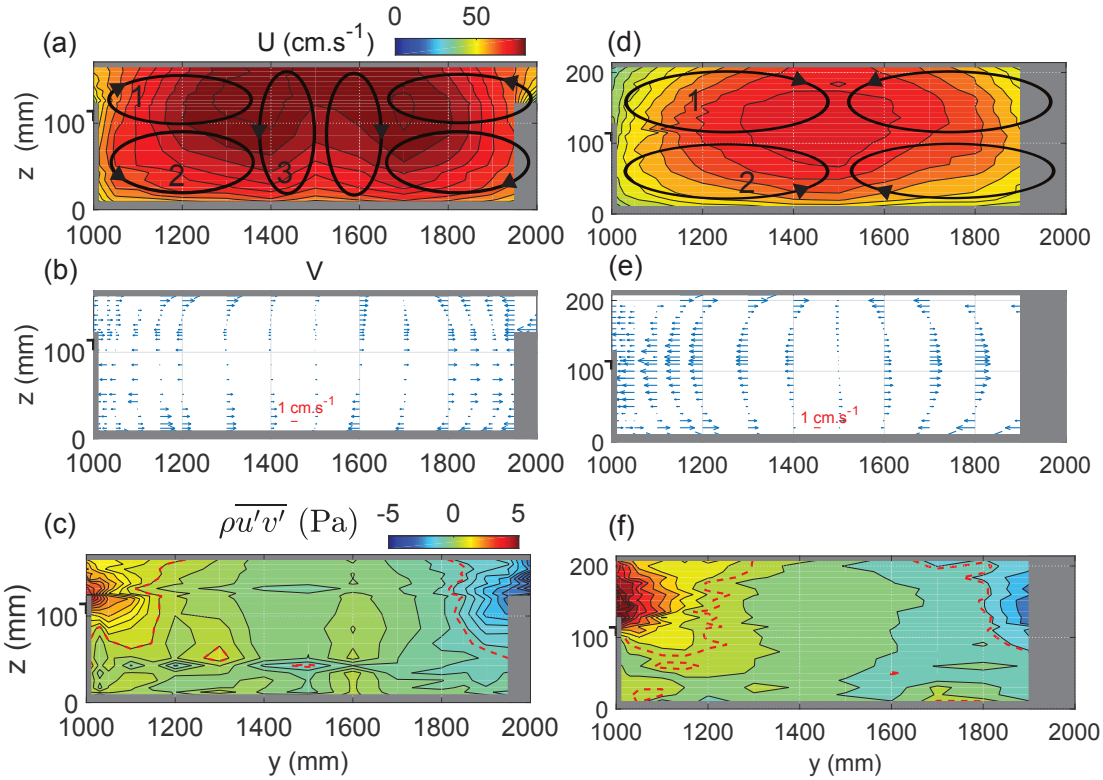

Figure 5.12: Cross-sectional distribution of longitudinal mean velocity U, lateral mean velocity V and lateral Reynolds stress $-\rho\overline{u'v'}$ in the main channel (a-c) for test case CM at $x = 15.05\,\mathrm{m}$ and (d-f) for test case CW at $x = 12.99\,\mathrm{m}$. The red dotted lines in panels c and f are the isolines $\pm 0.7\,\mathrm{Pa}$. Black arrows in panels a and d depict the secondary current cells.

5.4 Flow structure in the main channel

5.4.1 Isovels and secondary currents

Figure 5.12 shows the cross-sectional distribution of mean longitudinal velocity U, mean lateral velocity V and lateral Reynolds stress $-\rho\overline{u'v'}$ in the main channel at $x = 15.05\,\mathrm{m}$ for test case CM and at $x = 12.99\,\mathrm{m}$ for test case CW.

In the presence of grassed floodplains (test case CM), the mean longitudinal velocity field is characterized by two quasi-symmetric high velocity regions, separated by a velocity dip at the centre of the channel (Fig. 5.12a). The two symmetric maximum velocity points are located at $z/H_m \approx 0.73$ ($z_f/H_f \approx 0.18$) and at about $(y - y_{centre})/B_m = \pm 0.15$, where $y_{centre} = 1500\,\mathrm{mm}$. On the contrary, for the flow with wooded floodplains CW (Fig. 5.12d), the isovels (longitudinal velocity contour lines) are radially distributed around a unique maximum velocity point, which is located at the main channel centreline and at $z/H_m \approx 0.54$ ($z_f/H_f \approx 0$).

It should be noted that the vertical mean velocities W could not have been reliably measured with the ADV probe. Nevertheless, from the distribution of the lateral mean velocities V, shown in Figs. 5.12b and 5.12e, we can infer the presence of six secondary current cells for test case CM (depicted in Fig. 5.12a with black arrows) and of four cells for test case CW (Fig. 5.12d).

Focusing on the right-hand half of the main channel, the upper cell close to the interface for test case CM (cell 1) is characteristic of compound channel flows (Tominaga and Nezu, 1991) and is commonly called main channel vortex. This cell is usually associated

with a counter-rotating cell on the floodplain side, the floodplain vortex, which is not observable with the present data. The cell close to the bottom (cell 2) has also been observed by Tominaga and Nezu (1991) for relative depths D_r between 0.25 and 0.5. A third cell (cell 3) is observed near the main channel centreline. This cell is not directly related to the compound channel geometry and is responsible for the velocity dip at the main channel centreline (advection of slow fluid from the bottom region towards the free surface region).

Only cells 1 and 2 are observed for test case CW. They advect slow fluid from the floodplain and from the lower main channel corner towards the main channel centreline and induce the concentric contour lines pattern. The absence of cell 3 is consistent with the absence of velocity dip at the centreline. When comparing the lateral velocity vectors in Figs. 5.12b and 5.12e, it appears that the secondary current magnitude is globally higher with emergent rigid cylinders over the floodplain than with bed roughness only.

Cell 3 for test case CM spans the entire flow depth, which is typical for secondary cells in flat straight channels (Blanckaert *et al.*, 2010). The width-to-height ratio of cells 1 and 2 taken together is 2 for test case CM and 2.3 for test case CW, therefore relatively close. Assuming that the width-to-height ratio of cells 1+2 is a constant and considering that the water depth is higher for test case CW than for test case CM, the absence of cell 3 for test case CW could then be due only to the lack of space, which prevents the development of a couple of two symmetric cells near the channel centreline.

5.4.2 Lateral exchange of momentum

The cross-sectional distribution of longitudinal velocity U in Figs. 5.12a and 5.12d can be related to the lateral exchange of longitudinal momentum. The time averaged and depth-averaged lateral exchange of longitudinal momentum reads (Proust *et al.*, 2013):

$$\rho\overline{(uv)_d} = \rho(\overline{u'v'})_d + \rho(U(V - V_d))_d + \rho U_d V_d \tag{5.5}$$

where subscript d refers to depth-averaging. When the flow is uniform the depth-averaged lateral velocity V_d is equal to zero, such that the lateral exchange of momentum $\rho\overline{(uv)}_d$ is driven by lateral Reynolds stress and secondary currents only (first and second term on the right of Eq. 5.5).

The region of lateral Reynolds stress values higher than 0.7 Pa is depicted in Figs. 5.12c and 5.12f (red dotted line). This region is more extended for test case CW than for test case CM. Therefore the turbulent diffusion of low momentum fluid from the floodplain to the main channel is more significant with emergent cylinders than with bed roughness only and the isovels are more curved towards the main channel centreline for test case CW (Fig.5.12d) than for test case CM (Fig.5.12a).

Figure 5.13 shows the lateral distribution of lateral Reynolds stress $\rho(\overline{u'v'})_d$ and of the secondary currents term $\rho(U(V - V_d))_d$ (first and second terms on the right of Eq. 5.5). The contributions of turbulent mixing and secondary currents to the lateral exchange of momentum are comparable in the region $1200 < y < 1800$ mm. Close to the interface with the floodplain, the secondary currents contribution vanishes. This means that secondary currents only redistribute longitudinal momentum within the main channel, but do not contribute to the momentum exchange with the floodplains. The shape of the lateral profile of $\rho(U(V-V_d))_d$ is similar for both test cases (fit with a polynomial function of fifth order in Fig. 5.13b) although the cross-sectional distribution of secondary currents are very different (Fig.5.12). In particular, the lateral positions of the peak values of $\rho(U(V-V_d))_d$ are the same ($y = 1200$ and 1800 mm). The secondary currents advect momentum in the same direction as the lateral Reynolds stress, i.e. towards the floodplains.

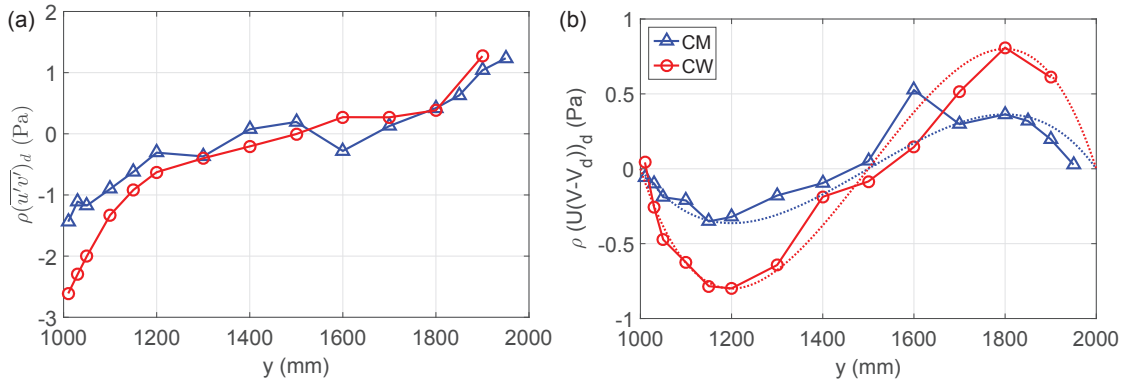

Figure 5.13: Depth-averaged lateral momentum exchange related to (a) lateral Reynolds stress and (b) secondary currents in the main channel for test cases CM and CW. Dotted lines in panel b are polynomial interpolations on the order 5.

Figure 5.13b confirms what was observed in Figs. 5.12b and 5.12e: compared to the case of grassed floodplains, the secondary currents are significantly enhanced in the case of wooded floodplains.

To conclude, secondary currents advect positive longitudinal momentum from the main channel centreline towards the flooplain, this lateral momentum flux being maximum at $y = 1200\,\text{mm}$ (when considering the right-half main channel) and vanishing at the interface with the floodplain. Secondary currents exert a driving force on the fluid (on an infinitesimal volume of width dy) in the region $y < 1200\,\text{mm}$, that is opposite and of the same order of magnitude than the lateral Reynolds stress, and exert a resistance force on the fluid in the region $y > 1200\,\text{mm}$, that is of the same sign and of the same order of magnitude than the lateral Reynolds stress.

5.4.3 Depth-averaged force balance

The depth-averaged momentum equation in the main channel for a uniform flow reads (see Chapter 3, Eq. 3.35):

$$S_0 = \frac{1}{gH_m}\frac{\partial H_m (UV)_d}{\partial y} + \frac{1}{gH_m}\frac{\partial H_m (\overline{u'v'})_d}{\partial y} + \frac{\tau_b}{\rho g H_m} \tag{5.6}$$

where τ_b is the bed shear stress. The three terms on the right-hand side of Eq. 5.6, related to secondary currents, turbulent mixing and bed friction, respectively, have been calculated from the experimental data and are plotted in Fig. 5.14 for both flow cases. Note that the second term on the right-hand side of Eq. 5.6 also takes into account the friction on the side walls. Bed shear stress (and lateral shear on the side walls) was calculated using the logarithmic law applied to the vertical (and horizontal) velocity profiles, assumed to be logarithmic in the near wall region. In Fig. 5.14 the three previously mentioned terms have been normalised by bottom slope S_0 (gravity term).

In the region $y < 1200\,\text{mm}$, the force due to secondary currents tends to accelerate the flow and is therefore opposite to the force due to lateral Reynolds stress (the lateral Reynolds stress is therefore partly counterbalanced by the secondary currents). In the region $y > 1200\,\text{mm}$, both forces are resistant; they are negligible compared to bed friction for test case CM, but not for test case CW.

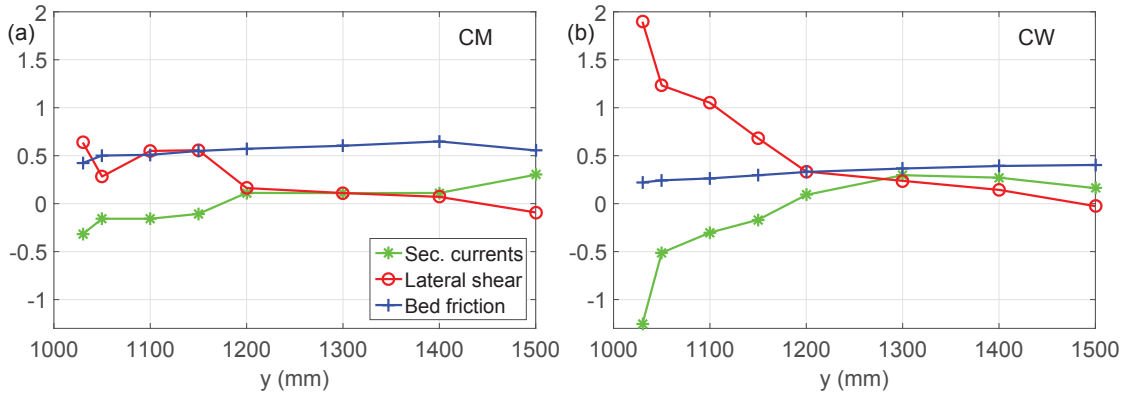

Figure 5.14: Depth-averaged momentum balance in the main channel for (a) test case CM and (b) test case CW. The three terms on the right of Eq. 5.6 have been normalised by bottom slope S_0.

5.5 Flow structure in the interface region

5.5.1 Cross-sectional distribution of flow quantities

Figures 5.15a-d and 5.15e-h show the cross-sectional distributions of longitudinal mean velocity, lateral Reynolds stress and longitudinal and lateral turbulence intensities within the interface region at $x = 15.05\,\mathrm{m}$ for test case CM and at $x = 11.76\,\mathrm{m}$ for test case CW, respectively. The cross section is located downstream of an even row of cylinders for test case CW, i.e. in the near wake of a cylinder at $y = 900\,\mathrm{mm}$ (white dotted line).

For test case CM, the lateral Reynolds stress $-\rho\overline{u'v'}$ (Fig. 5.15b) and the longitudinal turbulence intensity $\rho\overline{u'^2}$ (Fig. 5.15c) are maximum at the bankfull level and decrease when going upwards. The lateral position of the peak value of $\rho\overline{u'v'}$ is increasingly displaced towards the floodplain when going upwards. Contrary to the two previous turbulence quantities, the maximum value of the lateral turbulence intensity $\rho\overline{v'^2}$ (Fig. 5.15d) is quasi constant over the depth. Similarly to the lateral Reynolds stress, the location of maximum $\rho\overline{v'^2}$ follows an inclined straight line having an angle of about 50 ° towards the floodplain with respect to the vertical direction.

For test case CW, turbulence is produced by three sources: bed friction, mixing layer and cylinder wakes. At the downstream position of the cross-section shown in Figs. 5.15e-h, the wake turbulence of the upstream cylinder located near the interface ($y = 980\,\mathrm{mm}$) is nearly completely dissipated (this can be checked by considering cylinders outside the mixing layer, not shown), such that turbulence at the interface is mostly due to the mixing layer and not to the cylinder wake. On the other hand, the turbulence related to the cylinder wake at $y = 900\,\mathrm{mm}$ can be clearly seen. The cross-sectional distribution of lateral Reynolds stress (Fig. 5.15f) and longitudinal turbulence intensity (Fig. 5.15g) at the interface are very similar. The maximums are located nearly at the interface ($y = 1000\,\mathrm{mm}$), but the high intensity regions extend more towards the main channel than towards the floodplain. The opposite is observed for the lateral turbulence intensity (Fig. 5.15h), for which the high intensity region extends more towards the floodplain and follows an inclined orientation, although less pronounced than it is for test case CM.

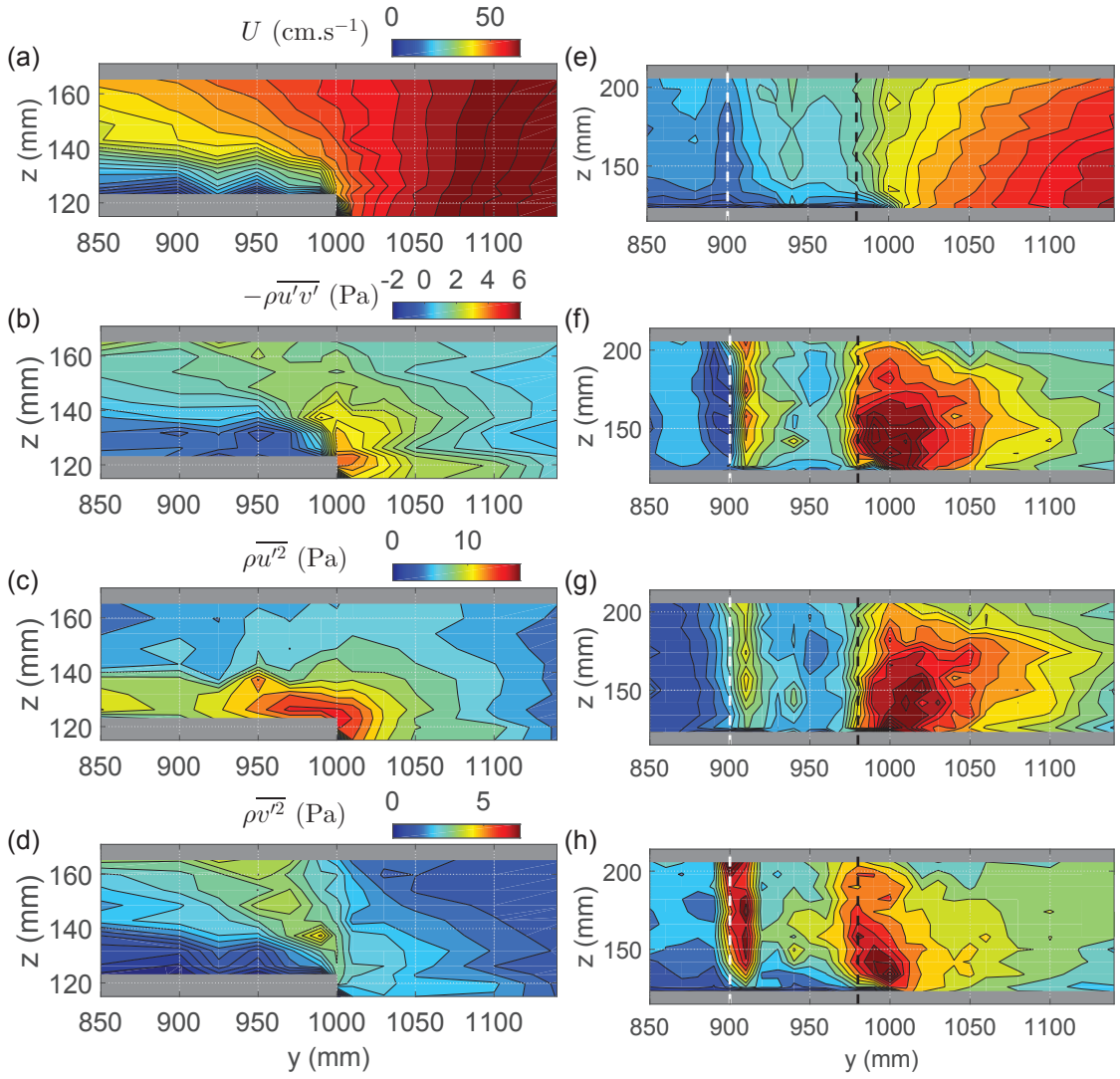

Figure 5.15: Cross-sectional distribution of longitudinal mean velocity U, lateral Reynolds stress $-\rho\overline{u'v'}$, longitudinal turbulence intensity $\rho\overline{u'^2}$ and lateral turbulence intensity $\rho\overline{v'^2}$ in the interface region (a-d) for test case CM at $x = 15.05\,\mathrm{m}$ and (e-h) for test case CW at $x = 11.76\,\mathrm{m}$, downstream of an even cylinder row. In panels e-h, the white dotted line is the cylinder position for an even row (cylinder located 4 cm upstream, $y = 900\,\mathrm{mm}$) and the black dotted line is the cylinder position for an odd row (cylinder located 4 cm downstream, $y = 980\,\mathrm{mm}$).

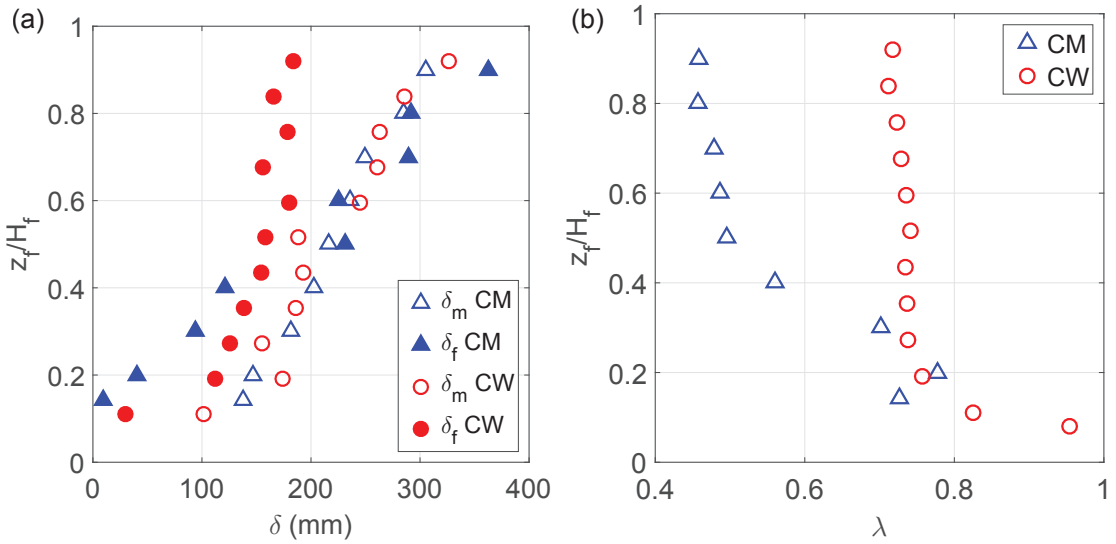

Figure 5.16: Vertical variation in (a) main channel and floodplain mixing layer width and (b) λ-ratio for test case CM (at $x = 15.05\,\mathrm{m}$) and test case CW (at $x = 11.76\,\mathrm{m}$).

5.5.2 Mixing layer width

Figures 5.16a shows the vertical variation in main channel and floodplain mixing layer width δ_m and δ_f for the two test cases CM and CW. Both widths δ_m and δ_f increase when going towards the free surface. However, the increase in δ_f is less significant in the case of a wooded floodplain, as expected since the velocity distribution is constant over the water column, outside the near bed region (Fig. 5.15e).

Figure 5.16b shows the vertical variation in the normalised velocity difference $\lambda = (U_1 - U_2)/(U_1 + U_2)$. For both cases, a strong increase is observed near the floodplain bottom, which is due to the decrease of U_2 near the bed. For comparison, at constant elevation $z_f/H_f = 0.5$, the normalised velocity difference λ is increasing from 0.40 to 0.50 for test CM and from 0.70 to 0.74 for test case CW along the flume (not shown). This longitudinal increase of λ is due to the increase of the maximum velocity in the main channel U_1, whereas U_2 keeps nearly constant at fixed elevation. Note that as δ_f, ratio λ is more constant over the depth for test case CW.

As a result, the compound channel mixing layer is very heterogeneous in the vertical direction, with important variations in mixing layer widths and λ-value. However, the presence of an emergent cylinder array makes the mixing layer more two-dimensional.

5.5.3 Lateral profiles of velocity and turbulence at different elevations

Figure 5.17 shows the lateral profiles of normalised longitudinal velocity and turbulence quantities at three different elevations, at a given x-station for test case CM (study not performed for test case CW). The lateral profiles have been normalised in the same way as in Figs. 5.10 and 5.11, widths δ_i and velocities U_1 and U_2 being calculated at the considered elevation. The profiles do not coincide over the depth, particularly on the floodplain side. The magnitude and the position of the peaks of turbulence quantities vary across the water column, as shown in Section 5.5.1. The absence of superposing of the lateral profiles at different elevations can be attributed to the shallowness effect in the floodplain: due to bed-induced turbulence production, turbulence budget and flow equilibrium are necessarily different in the near bed region and in the free-surface region.

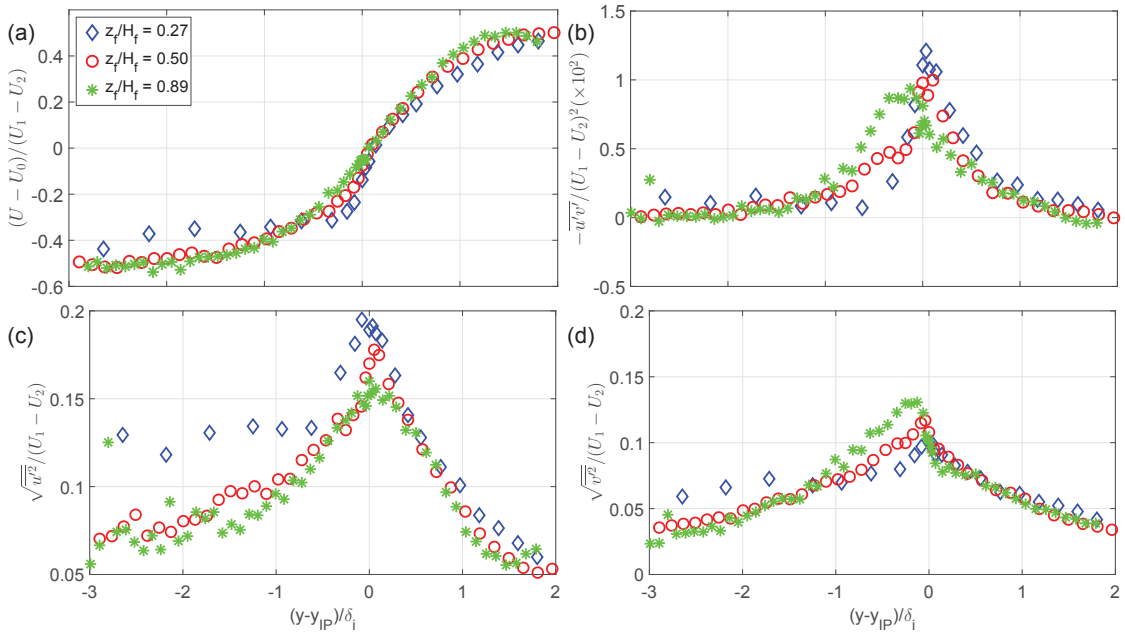

Figure 5.17: Lateral profiles at $x = 13.15$ m and at three different elevations of normalised (a) mean longitudinal velocity, (b) lateral Reynolds stress, (c) longitudinal turbulence intensity and (d) lateral turbulence intensity for test case CM. $\delta_i = \delta_f$ in the floodplain side and $\delta_i = \delta_m$ in the main channel side.

On the main channel side, where shallowness effects are lower, the differences between the normalised profiles are less important.

On the floodplain side, the normalised turbulence quantities $\sqrt{\overline{v'^2}}/(U_1 - U_2)$ and $\sqrt{\overline{u'v'}}/(U_1 - U_2)$ decrease when approaching the bed, probably because the small-scale 3D bed turbulence tends to disorganize the large 2D turbulent coherent structures, compared to the upper water column. In the near-bed region, the overall turbulence is due both to bed turbulence and mixing layer turbulence. The bed do not induce lateral shear stress but induces turbulence intensities: according to Nezu and Nakagawa (1993) the normalised longitudinal and lateral turbulence intensities induced by bed friction are $\sqrt{\overline{u'^2}}/U^* = 2.30$ and $\sqrt{\overline{v'^2}}/U^* = 1.63$ at the bed level, where U^* is the shear velocity. The bed therefore induces more longitudinal than lateral turbulence intensity, which could explain that, contrary to $\sqrt{\overline{v'^2}}/(U_1 - U_2)$, $\sqrt{\overline{u'^2}}/(U_1 - U_2)$ increases when approaching the bed on the floodplain side. Besides, we can note that when going away from the interface towards the floodplain, the levels of $\sqrt{\overline{u'^2}}/(U_1 - U_2)$ and $\sqrt{\overline{v'^2}}/(U_1 - U_2)$ remains high at $z_f/H_f = 0.27$, compared to the profiles in the upper water column, which is due to the contribution of bed turbulence in the overall turbulence. The ratio $\sqrt{\overline{u'^2}}/\sqrt{\overline{v'^2}}$ is about 2, which is higher but on the same order of magnitude than that given by Nezu and Nakagawa (1993), i.e. 1.4.

5.6 Coherent structures

5.6.1 Definitions and procedure

The longitudinal and lateral velocity time series feature large quasi periodic oscillations in the interface region, as illustrated in Fig. 5.18a. These oscillations are the signature of

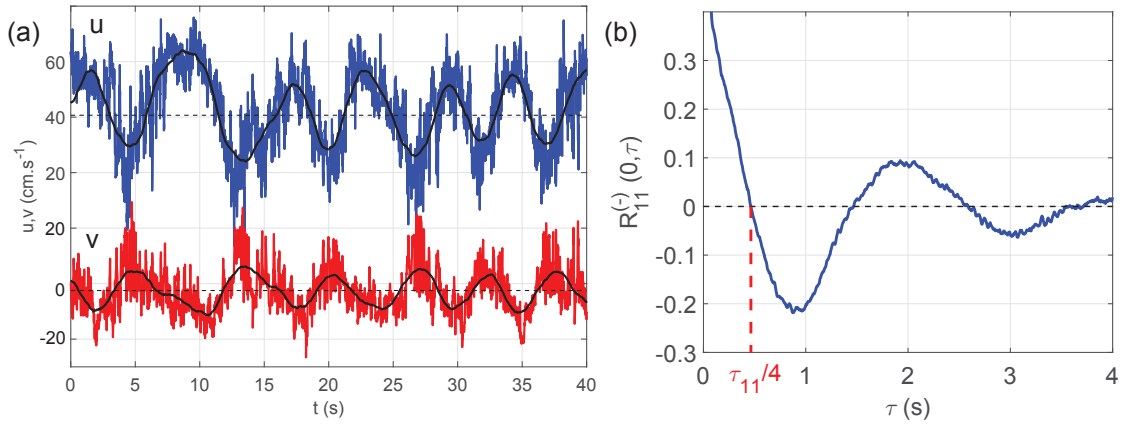

Figure 5.18: (a) Time series of longitudinal and lateral velocities for test case CW (measurement at $x = 15.68\,\mathrm{m}$, $y = 1000\,\mathrm{mm}$, $z_f/H_f = 0.52$). The red and blue lines are the raw signals, the black lines are the low-pass-filtered signals and the dashed lines are the mean value of the raw signal. Vertical axis differs for u and v. (b) Autocorrelation function of longitudinal velocity fluctuations for test case CW (measurement at $x = 11.12\,\mathrm{m}$, $y = 1000\,\mathrm{mm}$ and $z_f/H_f = 0.78$) and definition of the integral time scale τ_{11}.

coherent structures that are generated by the mixing layer. The longitudinal and lateral velocities are in opposite phase, such that these coherent events can be considered as an alternate succession of large sweeps ($u' > 0$, $v' < 0$, when considering the right-bank mixing layer) and ejections ($u' < 0$, $v' > 0$).

In order to investigate the spatial extent of the coherent structures, two-point space-time correlations were carried out in the longitudinal, lateral and vertical directions. The reference probe was kept constant at position (x^r, y^r, z^r) and the moving probe was moved in one direction, the other coordinates being the same as the reference probe. The two-point space-time correlation function is defined by:

$$R_{ik}^{(j)}(\xi_j, \tau) = \frac{\overline{u_i'(x_j, t) u_k'(x_j + \xi_j, t + \tau)}}{\left(\overline{u_i'^2}(x_j, t)\overline{u_k'^2}(x_j + \xi_j, t)\right)^{1/2}} \tag{5.7}$$

where ξ_j and τ are the spatial and time lags, $i, j, k \in \{1, 2, 3\}$, $(x_1, x_2, x_3) = (x, y, z)$ and $(u_1, u_2, u_3) = (u, v, w)$. In the present report, only inter-correlations of the longitudinal and lateral velocities are considered, i.e. $R_{11}^{(j)}$ and $R_{22}^{(j)}$; the behaviour of the cross-correlation $R_{12}^{(j)}$ was found to represent an average of the behaviours of the two previous ones.

The Eulerian integral time scales of the longitudinal and lateral velocity fluctuations τ_{11} and τ_{22} are calculated from the autocorrelation functions $R_{11}^{(-)}(0, \tau)$ and $R_{22}^{(-)}(0, \tau)$, respectively, and taken as four times the first zero-crossing, as sketched in Fig. 5.18b. Indeed, the first zero crossing corresponds to the quarter of period for a periodic signal.

For a given space lag ξ_j, the maximum correlation time lag $\tau_{ii,max}^{(j)}$ is defined as the time lag such that the correlation function is maximum:

$$R_{ii}^{(j)}(\xi_j, -\tau_{ii,max}^{(j)}) = \max_{\tau} R_{ii}^{(j)}(\xi_j, \tau) = R_{ii,max}^{(j)}(\xi_j) \tag{5.8}$$

where $R_{ii,max}^{(j)}$ is called the maximum of correlation. The maximum correlation time lag is defined such that $\tau_{ii,max}^{(j)}$ is positive when the moving probe receives the signal in advance

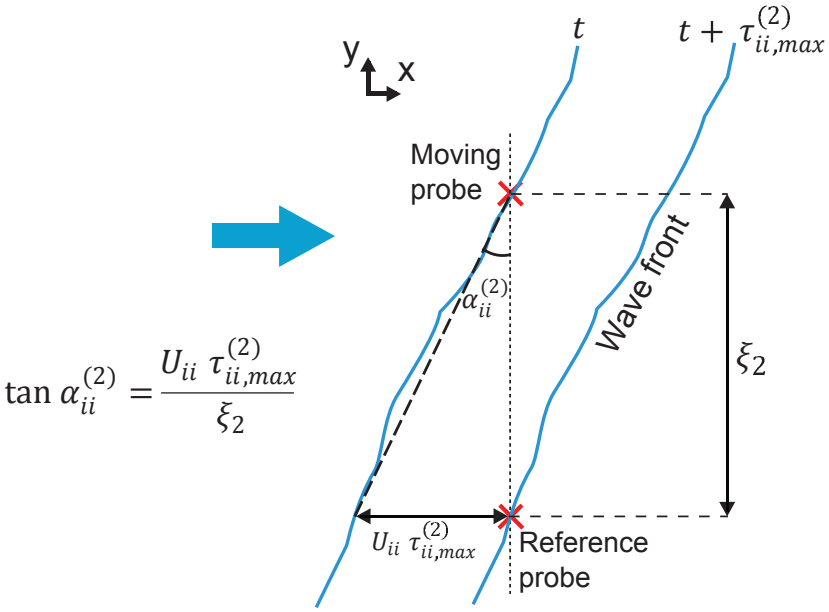

Figure 5.19: Calculation of the inclination of the wave front from the two-point space-time correlation measurements. Correlation in the lateral direction.

with respect to the reference probe (which explains the minus sign in Eq. 5.8).

Consider a space-time correlation in the lateral direction. Let U_{ii} be the longitudinal phase velocity of the fluctuations of velocity u_i. Then the inclination $\alpha^{(2)}_{ii}$ of the u_i-fluctuations wave front, relative to the y-axis, can be expressed as a function of U_{ii}, $\tau^{(2)}_{ii,max}$ and ξ_2, as sketched in Fig. 5.19. The longitudinal space lag with which the two probes receive the coherent signal is calculated using the Taylor hypothesis (see Section 5.6.2) and is equal to $U_{ii}\,\tau^{(2)}_{ii,max}$. The same reasoning can be made for a correlation measurement in the vertical direction, such that the inclination $\alpha^{(j)}_{ii}$ of the wave front in the lateral ($j = 2$) or vertical ($j = 3$) direction is:

$$\alpha^{(j)}_{ii} = \text{atan}\,\frac{U_{ii}\,\tau^{(j)}_{ii,max}}{\xi_j}. \tag{5.9}$$

The autocorrelation functions were calculated with the raw time series. In order to remove the influence of the small scale fluctuations, which are uncorrelated even for small spatial lags, the two-point space-time correlations were calculated with low-pass filtered signals, using a Savitzky-Golay smoothing filter (Matlab function 'sgolayfilt'). The window size of the filter was chosen iteratively in order to minimise the dispersion of the time intervals between zero-crossings in the filtered velocity signal. The optimal window size, using a second order polynomial, was found to be about 75 % of the mean period of the coherent events. Low-pass-filtered velocity signals are shown in Fig. 5.18a for test case CW (black lines).

5.6.2 Phase velocity

If the coherent velocity fluctuations are considered as waves that propagate downstream, we can define the phase velocity of the coherent fluctuations of the longitudinal and lateral velocity, U_{11} and U_{22}. Using the Taylor hypothesis, the Eulerian integral time

scales can then be converted into longitudinal Eulerian integral length scales with the equation $L_{ii}^{(1)} = U_{ii}\tau_{ii}$.

The experimental determination of phase velocity U_{ii} is often a difficult task. Zaman and Hussain (1981) tested different assumptions for approximating the phase velocity (local instantaneous velocity, local mean velocity, etc.) and found that the best results were obtained by taking a constant velocity across the entire coherent structure, equal to the mean velocity at the centre of the structure. Shaw *et al.* (1995) showed for a vertical mixing layer above a canopy that taking the local mean velocity in the Taylor hypothesis led to erroneous results (the phase velocity can exceed the local mean velocity by a factor of three).

In the present experiments, direct estimation of the phase velocities was undertaken at some locations, in order to assess the best choice for approximating U_{ii}. Phase velocity was evaluated by tracking the coherent events between two points separated by a longitudinal spatial lag (space-time correlation in the longitudinal direction). The coherent events were detected using the local velocity maximum in the low-pass filtered time series; only coherent events that could be clearly recognized were selected (see note below). Phase velocities were obtained by averaging about 100 selected coherent events.

Phase velocities U_{11} and U_{22} at the interface ($y = 1000\,\text{mm}$) and at $z_f = H_f/2$ for both test cases CM and CW are presented in Table 5.3 and are compared with the local mean longitudinal velocity and with the depth averaged mean longitudinal velocity. Phase velocities U_{11} and U_{22} are nearly identical for test case CM. Velocity U_{22} is about 8 % lower than U_{11} for test case CW in average, although they are equal within the measurement uncertainty. The depth-averaged velocity at the interface seems to give a rather good estimate of the phase velocities. The local mean velocity is not adapted, especially for test case CM, for which it would overestimate by 15% the measured phase velocity. In the following, when using the Taylor hypothesis, the phase velocity is taken as the depth-averaged longitudinal velocity at the interface and is assumed to be constant over the depth and across the lateral extent of the coherent structure, following the recommendations of Zaman and Hussain (1981). Although the above results suggest that U_{11} *a priori* differs from U_{22}, for sake of simplicity no distinction is made between the phase velocity of longitudinal and lateral velocity fluctuations.

Table 5.3: Estimation of the phase velocities of longitudinal and lateral velocity fluctuations U_{11} and U_{22} at the interface ($y = 1000\,\text{mm}$) and at $z_f = H_f/2$ for test cases CM ($x = 14.80\,\text{m}$) and CW ($x = 14.55\,\text{m}$). Comparison with depth averaged mean velocity U_d and the local mean velocity U_{local}.

Test case	U_{11}	U_{22}	U_d	U_{local}
CM	45.5 ± 3	46.5 ± 3	48 ± 1	53 ± 1
CW	39 ± 3	36 ± 3	40.5 ± 1	39 ± 1

Note

The above described procedure for estimating experimentally the phase velocity gives only rough estimates. For small spatial lags, the dispersion in the detected time lag between the coherent events is important. For large spatial lags, the velocity signal of the coherent event is distorted from one probe to the other and the recognition is difficult.

Phase velocities U_{11} and U_{22} were also estimated at another vertical position ($z_f/H_f = 0.78$) and at two other lateral positions ($y = 1050$ and $1100\,\text{mm}$) for test case CW. It could be observed (not shown) that the phase velocities remain in the velocity range given in Table 5.3. The spatial variation in the phase velocities was not tested for test case CM.

It was observed that the phase velocities greatly vary from one structure to the other. It is therefore to be remembered that U_{11} and U_{22} are averaged values and that each structure has its own phase velocity (evolving with time).

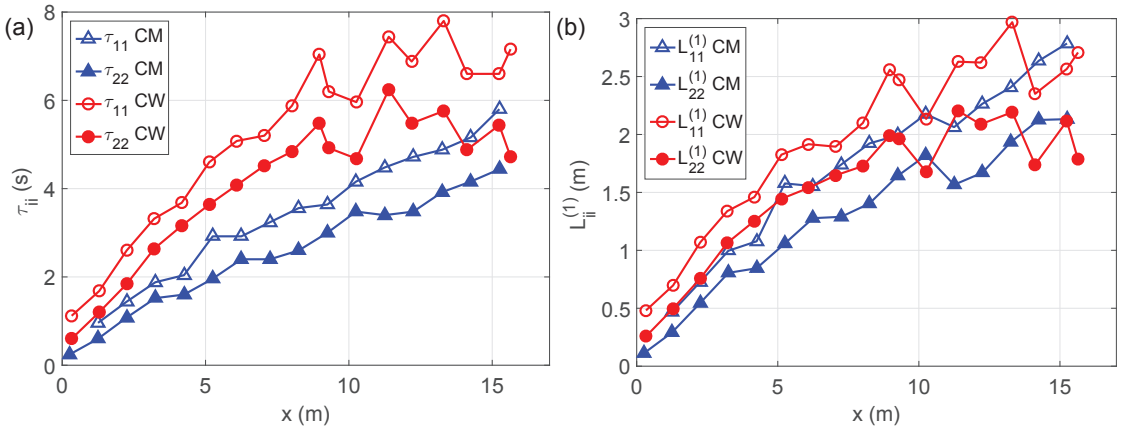

Figure 5.20: Longitudinal evolution along the interface ($y = 1000\,\text{mm}$) of (a) the integral time scales τ_{11} and τ_{22} and (b) the integral length scales $L_{11}^{(1)}$ and $L_{22}^{(1)}$ for test cases CM (at $z_f/H_f = 0.20$) and CW (at $z_f/H_f = 0.60$).

The phase velocity of the coherent velocity fluctuations can also theoretically be calculated from the longitudinal two-point space-time correlation with $\xi_1/\tau_{ii,max}^{(1)}$. However, the so-obtained phase velocities were too dispersive and unreliable.

5.6.3 Longitudinal evolution

Figure 5.20a shows the longitudinal evolution of the integral time scales τ_{11} and τ_{22} of the longitudinal and lateral coherent velocity fluctuations, respectively, for test cases CM and CW along the interface. The integral length scales $L_{11}^{(1)}$ and $L_{22}^{(1)}$ of the coherent structures, calculated from the integral time scales using Taylor hypothesis, are then shown in Fig. 5.20b.

The coherent structures are growing approximately linearly until the channel end for test case CM. The coherent structure size stabilises for test case CW after $x \approx 10\,\text{m}$. These trends can be related to the evolution of the total mixing layer width $\delta_m + \delta_f$ (see Chapter 6 for more details). For both flows the integral time scale is higher for the longitudinal velocity than for the lateral velocity. The ratio τ_{11}/τ_{22} is about 1.4 for CM and 1.25 for CW.

5.6.4 Vertical extension

Figure 5.21 shows the vertical variation in the integral time scales τ_{11} and τ_{22} for test cases CM and CW. Time scales τ_{11} and τ_{22} are rather constant across the water column (a decrease of about 10% is observed from the bankfull level to the free surface). Assuming a constant phase velocity over the depth, as stated in Section 5.6.2, it follows that the integral length scales $L_{11}^{(1)}$ and $L_{22}^{(1)}$, and therefore the longitudinal size of the coherent structures, are also constant across the water column. The coherent structures related to the longitudinal velocity are longer than those related to the lateral velocity; the ratio τ_{11}/τ_{22} is the same for both test cases CM and CW and is about 1.3.

Figures 5.22a and 5.22b show the maximum correlation time lags $\tau_{11,max}^{(3)}$ and $\tau_{22,max}^{(3)}$ in the vertical direction and the corresponding maximum of correlation $R_{11,max}^{(3)}$ and $R_{22,max}^{(3)}$. The reference probe is located near the free surface (horizontal dotted lines in the figures). A slight loss of correlation is observed when the two probes move away, mainly for test

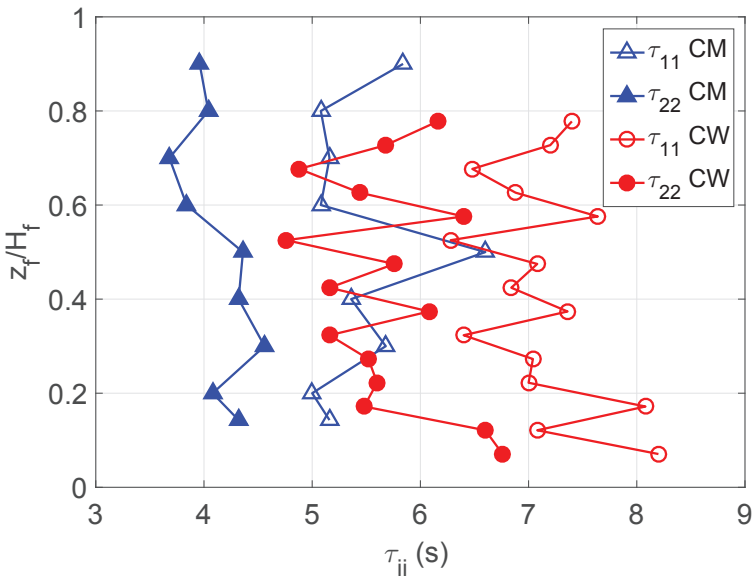

Figure 5.21: Vertical variation in the integral time scales τ_{ii} of the longitudinal and lateral velocity fluctuations for test cases CM (at $x = 15.05\,\mathrm{m}$) and CW (at $x = 13.76\,\mathrm{m}$) at the interface ($y = 1000\,\mathrm{mm}$).

case CM, but the maximums of correlation for the two velocity components remain high (> 0.8). Therefore, the coherent structures can be considered as a unique entity that spans the entire water column. Time lags $\tau^{(3)}_{11,max}$ and $\tau^{(3)}_{22,max}$ are nearly equal to zero across the water column for test case CW, indicating that the front of the coherent waves of the u- and v-fluctuations is vertical ($\alpha^{(3)}_{11} = \alpha^{(3)}_{22} = 0$). On the contrary, significant time lags $\tau^{(3)}_{11,max}$ and $\tau^{(3)}_{22,max}$ are observed between the upper and lower water column for test case CM, the velocity signal at the free surface being ahead. The corresponding inclinations of the u- and v-wave fronts relative to the vertical direction are $\alpha^{(3)}_{11} \approx 81^{\circ}$ and $\alpha^{(3)}_{22} \approx 67^{\circ}$ (see sketch in Fig. 5.23).

5.6.5 Lateral extension

Figures 5.24c and 5.24d show the maximum of correlation $R^{(2)}_{11,max}$ and $R^{(2)}_{22,max}$ on either side of the interface, the reference probe being at the interface. For a better understanding, the lateral profiles of mean longitudinal velocity at the same measurement location are plotted in Figs. 5.24a and 5.24b. The fluctuations of the lateral velocity remain highly correlated on both sides of the mixing layer (see $R^{(2)}_{22,max}$). The correlation of the longitudinal velocity fluctuations decreases much more rapidly when going away from the reference probe (see $R^{(2)}_{11,max}$) and this decrease is higher for test case CM than for test case CW.

The correlation of the lateral velocity fluctuations $R^{(2)}_{22,max}$ is quasi unaffected by the presence of the cylinders on the wooded floodplains, whereas $R^{(2)}_{11}$ decreases drastically in the cylinder wakes. This local loss of correlation is followed by a new increase of the correlation outside the cylinder wake. This indicates that points on either side of the cylinder wake keep correlated, the wake does not enhance the lateral loss of correlation.

Figures 5.24e and 5.24f show the maximum correlation time lags $\tau^{(2)}_{11,max}$ and $\tau^{(2)}_{22,max}$ in the floodplain and in the main channel, respectively. Important positive time lags are

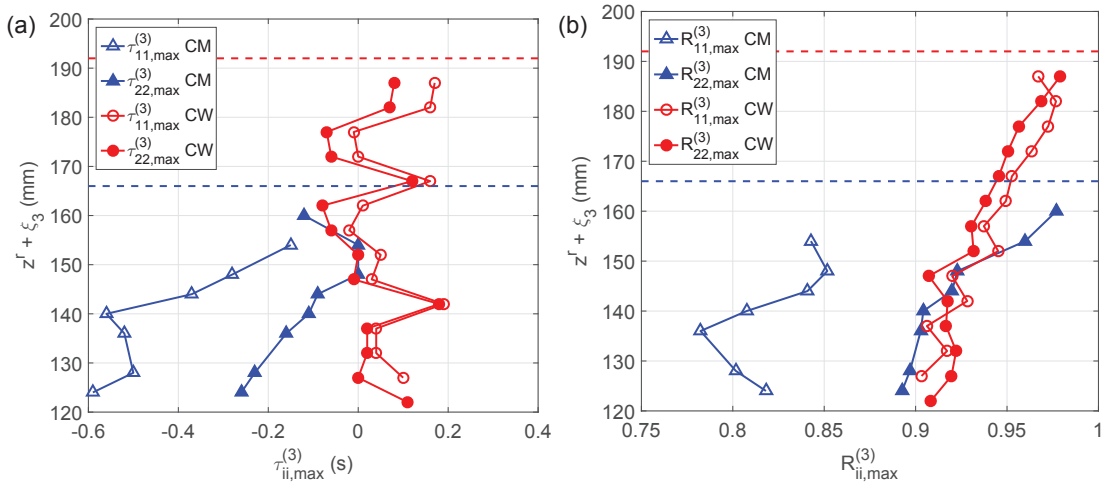

Figure 5.22: (a) Maximum correlation time lag $\tau^{(3)}_{ii,max}$ and (b) maximum of correlation $R^{(3)}_{ii,max}$ in the vertical direction for test case CM with reference probe at ($x^r = 13.82\,\text{m}$, $y^r = y_{int}$, $z^r = 166\,\text{mm}$) and for test case CW with reference probe at ($x^r = 13.76\,\text{m}$, $y^r = y_{int}$, $z^r = 192\,\text{mm}$). The vertical position of the reference probe is marked with dotted lines.

observed for the longitudinal velocity fluctuations ($\tau^{(2)}_{11,max}$). Towards the main channel, $\tau^{(2)}_{11,max}$ is similar for both flows until $y = 1200\,\text{mm}$ and varies approximatively linearly. The corresponding inclination of the u-wave front relative to the lateral direction is $\alpha^{(2)}_{11} \approx 72^o$ for test case CM and $\alpha^{(2)}_{11} \approx 69^o$ for test case CW, the fluctuation being ahead in the main channel (Fig. 5.23).

Time lag $\tau^{(2)}_{11,max}$ decreases after $y = 1200\,\text{mm}$ for test case CW, until becoming negative. This negative values are associated with an increase of the correlation (see Fig. 5.24d). For the moment this fact remains unexplained. It suggests the existence of a second line of coherent structures, parallel and anti-correlated with the first one. Such a pattern could be expected for test case CM, for which a secondary mixing layer exists at $y \approx 1450\,\text{mm}$, associated with the velocity dip caused by secondary currents (see Fig. 5.24b), but not for test case CW for which the velocity profile remains convex across the main channel.

Positive time lags $\tau^{(2)}_{11,max}$ are also observed in the floodplain (Fig. 5.24e). Time lag $\tau^{(2)}_{11,max}$ varies approximatively linearly until $y = 720\,\text{mm}$ for test case CM and the corresponding inclination of the u-wave front relative to the lateral direction is $\alpha^{(2)}_{11} \approx 55^o$, the fluctuation being ahead in the floodplain. It can be observed that time lag $\tau^{(2)}_{11,max}$ increases drastically in the cylinder wake for test case CW. The wave front of the longitudinal velocity fluctuations in the wooded floodplain has therefore a sawtooth-shape, with the "teeth" located in the alignment of the cylinders (Fig. 5.23).

The time lags relative to the lateral velocity fluctuations $\tau^{(2)}_{22,max}$ are quasi equal to zero in the main channel for both flows, such that the v-front wave is straight ($\alpha^{(2)}_{22} = 0$). However, positive time lags $\tau^{(2)}_{22,max}$ are observed in the floodplain for both flows, and the corresponding inclination of the the v-front wave is $\alpha^{(2)}_{22} \approx 30^o$ for test case CM and $\alpha^{(2)}_{22} \approx 24^o$ for test case CW, the fluctuation being ahead in the floodplain.

Figure 5.23 summarizes the vertical and lateral shapes of the u- and v-wave fronts for both test cases. A physical understanding of the mechanisms responsible for the inclination of the velocity wave fronts is needed. It may be related to the time evolution

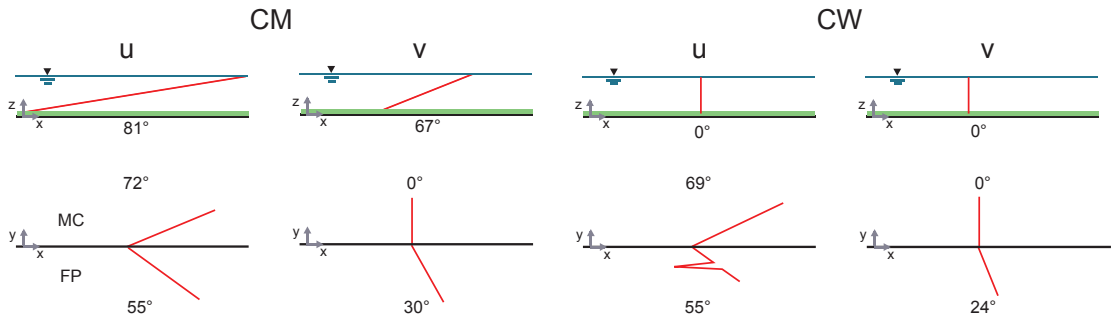

Figure 5.23: Vertical and lateral shapes of the u- and v-wave fronts for test cases CM and CW. Red lines depict the wave front. Numbers are the angle of inclination of the wave front relative to the vertical or lateral axis.

of the sweep and ejection events, that may start outside the interface and rather near the free surface, and then propagate towards the interface and towards the bankfull level.

Note

Zong and Nepf (2010) showed that in a single channel with a cylinder array occupying a portion of the channel width, the penetration of the coherent structures into the cylinder array is given by $\delta = 0.5(C_D a)^{-1}$ where C_D is the drag coefficient of the cylinder and a is the frontal area per unit volume of the cylinder array. With $C_D = 1.2$ and $a = 0.81\,\mathrm{m}^{-1}$, we obtain $\delta = 0.51\,\mathrm{m}$ in the present case. Therefore, it is not surprising that the velocity fluctuations remain correlated until $y = 680\,\mathrm{mm}$ (Fig. 5.24c). Unfortunately, no spatial correlation measurements were undertaken in the region $y < 680\,\mathrm{mm}$.

5.6.6 Interaction between cylinder wake and mixing layer

The cylinder wake located at $y = 980\,\mathrm{mm}$ generates a local velocity dip in the lateral profile of mean longitudinal velocity (see Fig. 5.24a). The cylinder wake can be viewed as two local mixing layers, the one on the main channel side having the same velocity gradient sign as the large scale mixing layer and the other on the floodplain side having an opposite sign (U increases locally towards the floodplain). This latter mixing layer is enclosed in a larger scale mixing layer for which the direction of the lateral exchange of longitudinal momentum is of opposite sign.

Figure 5.25 shows the time series of the lateral velocity in the cylinder wake at $y = 980\,\mathrm{mm}$. Compared to the velocity in the interface region but outside the cylinder wake (see Fig. 5.18), small scale coherent oscillations with high amplitudes are observed. These velocity oscillations are related to the coherent structures generated by the cylinder wake (von Kármán vortex street). In Fig. 5.25 the low-pass filtered signal, corresponding to the coherent structures of the large scale mixing layer, is superposed to the raw signal. It can be observed that the coherent structures of the cylinder wake are mostly generated when the low-pass filtered lateral velocity is negative, i.e. during sweep events of the large scale mixing layer. Therefore a coupling exists between the large scale mixing layer and the cylinder vortex street.

Figure 5.26 shows the power spectral density of the lateral velocity fluctuations in the wake of the cylinder at $y = 980\,\mathrm{mm}$ and outside the cylinder wake at $y = 920\,\mathrm{mm}$. At both locations, the spectral peak corresponding to the large quasi-2D coherent structures of the compound channel mixing layer is clearly visible (at $f \approx 0.13\,\mathrm{Hz}$). The associated decaying slope is close to $-3\,\mathrm{dB}$, which is characteristic for 2D structures (Batchelor, 1969). In the cylinder wake, an additional spectral peak is present around $f \approx 7.2\,\mathrm{Hz}$ and corresponds to the coherent structures formed in the cylinder wake. Using the Strouhal

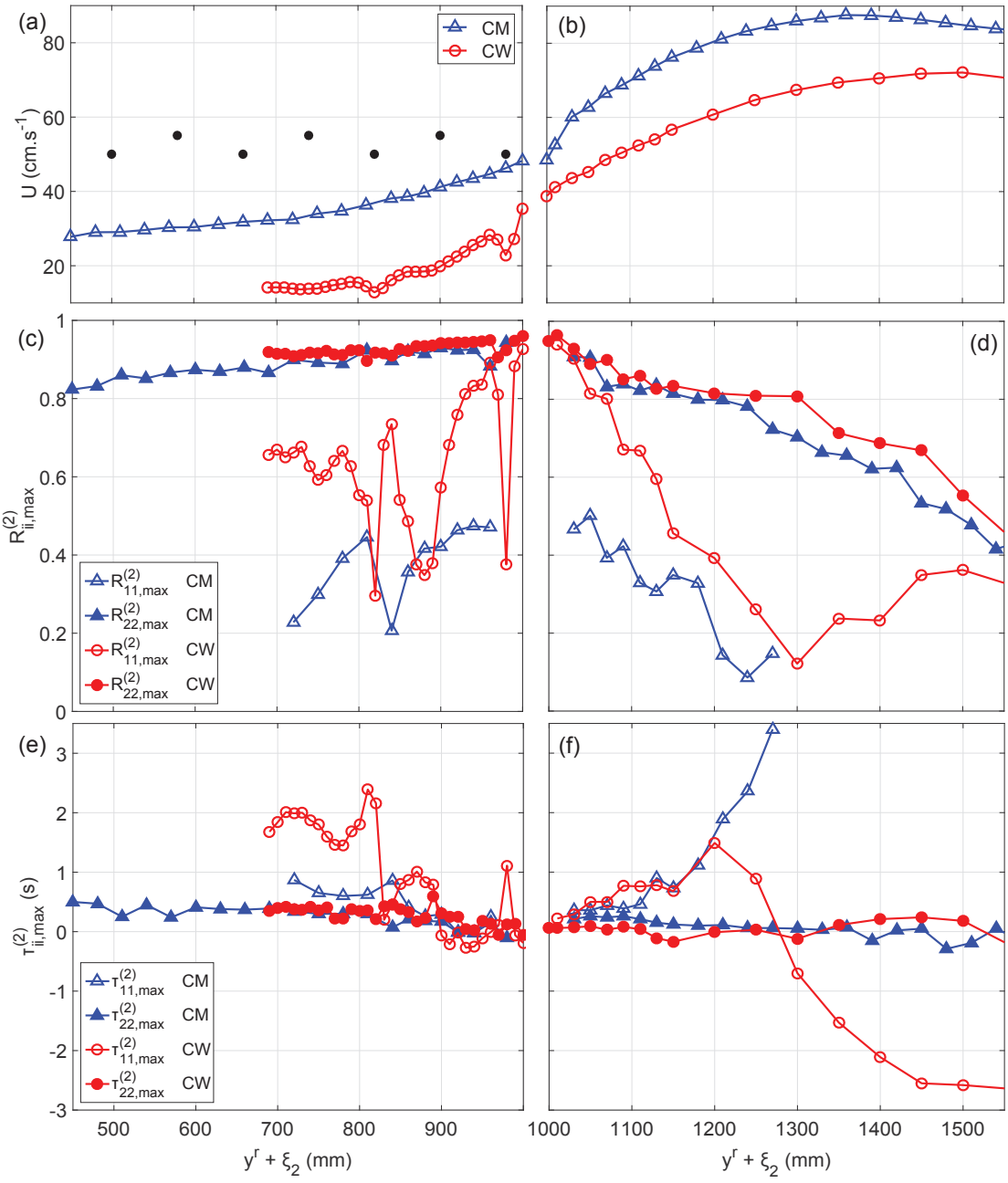

Figure 5.24: Lateral profiles of mean longitudinal velocity U (a) in the floodplain and (b) in the main channel. Maximum of correlations $R^{(2)}_{11,max}$ and $R^{(2)}_{22,max}$ (c) in the floodplain and (d) in the main channel. Maximum correlation time lags $\tau^{(2)}_{11,max}$ and $\tau^{(2)}_{22,max}$ (e) in the floodplain and (f) in the main channel for test cases CM and CW. For test case CM the reference probe is located at ($x^r = 13.82\,\text{m}$, $y^r = y_{int} = 1000\,\text{mm}$, $z^r = 143\,\text{mm}$) for measurements in the floodplain and in the main channel. For test case CW the reference probe is located at ($x^r = 13.76\,\text{m}$, $y^r = y_{int}$, $z^r = 166\,\text{mm}$) for measurements in the floodplain and at ($x^r = 13.76\,\text{m}$, $y^r = y_{int}$, $z^r = 192\,\text{mm}$) for measurements in the main channel. Spatial lag ξ_2 is the distance of the moving probe from the reference probe.

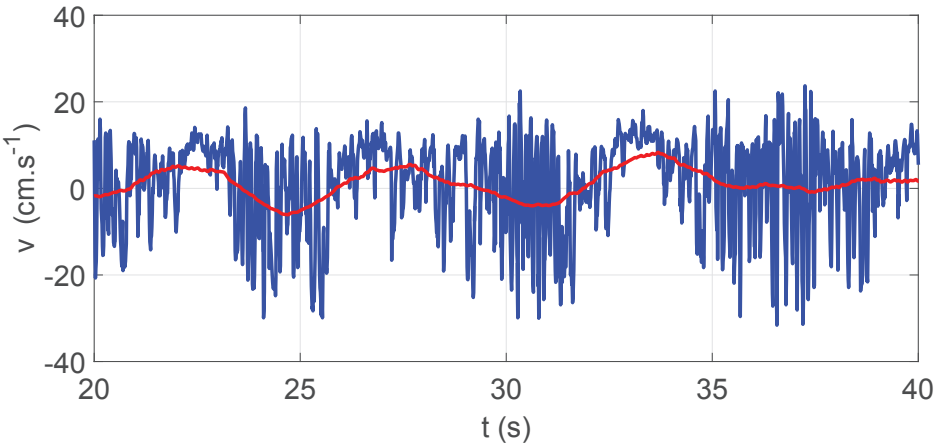

Figure 5.25: Time series of the raw and low-pass filtered lateral velocity in the wake of the cylinder at $y = 980\,\text{mm}$. $x = 13.76\,\text{m}$ and $z_f/H_f = 0.5$.

number of the isolated cylinder $St = f_{St}D/U_{cyl} = 0.21$ and using as velocity scale U_{cyl} the mean velocities upstream of the cylinder, the frequency of the vortex street in the cylinder wake can be estimated to $f_{St} = 6.3\,\text{Hz}$, which is not so far from the observed spectral peak.

5.7 Comparison with the isolated floodplain

Open-channel flows over the same floodplain roughnesses as in the present chapter were investigated in a single channel, i.e. in the case of a floodplain isolated from the main channel, in Chapter 4. In this section a comparison is made between the main-channel-influenced-floodplain (configurations CM and CW) and the isolated floodplain (configurations M and W, see Fig. 2.5 and Table 2.1 in Section 2).

5.7.1 Longitudinal flow development

In single channel, the longitudinal flow development is only due to the boundary layer development. For configurations M (meadow) and W (wood) the mean velocity and the turbulence fields were found to be fully developed about 5 m downstream of the channel inlet for all flow test cases (not shown). The development length in the main-channel-influenced-floodplains was much longer, due to the lateral extension of the mixing layer when going downstream. With the cylinder array, the flow development is accelerated and the development length on the floodplain side is comparable to that in single channel (about 5 m).

5.7.2 Acceleration by the main channel flow

In comparison with an isolated floodplain, the conveyance (discharge per cross-sectional area) of the main-channel-influenced-floodplain is modified by the momentum exchange with the main channel. The flow rate in the main-channel-influenced-floodplain is increased by 12.5 % for the grassed floodplains (CM) and by only 2.9 % for the wooded floodplains (CW), compared with the flow rate with the same floodplain water depth in the isolated floodplain (that can be calculated with the stage-discharge relationship introduced in Chapter 4, see Eq. 4.5). The acceleration of the floodplain flow by the main

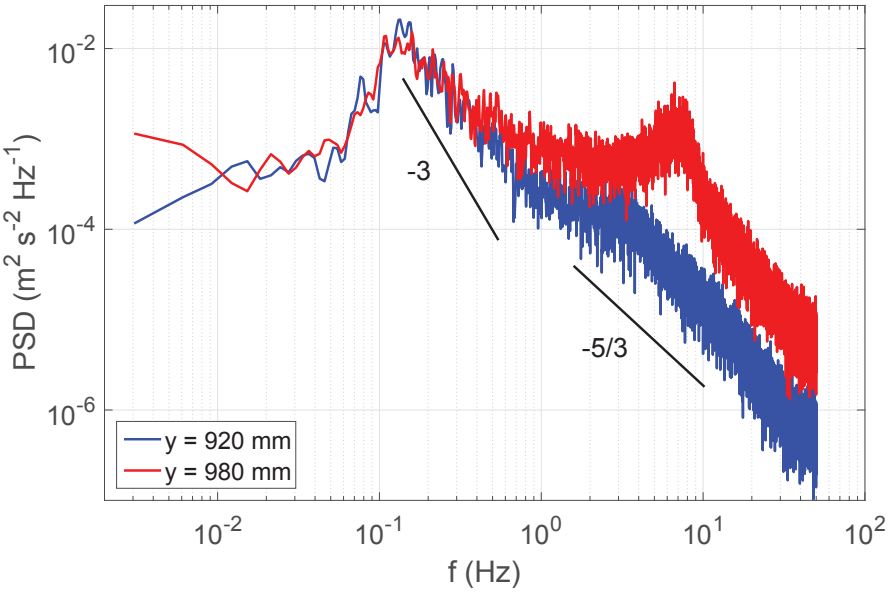

Figure 5.26: Power spectral density of the lateral velocity fluctuations in the wake of the cylinder at $y = 980$ mm and outside the cylinder wake at $y = 920$ mm. Downstream position $x = 13.76$ m and elevation $z_f/H_f = 0.5$.

channel flow is therefore much more reduced for the wooded floodplain, compared to the grassed floodplain.

The region in the floodplain that is accelerated by the main channel flow is depicted in Fig. 5.27, which shows the lateral profiles of mean longitudinal velocity and turbulence quantities at $z_f = H_f/2$ for test cases CM and CW. For each quantity, a plateau is observed between the lateral boundary layer caused by the side wall and the interface region. It can be observed that the influence region of the main channel flow is quantity-dependant. For longitudinal mean velocity, lateral Reynolds stress and longitudinal turbulence intensity, lateral gradients are observed over a width of about 450 mm and 270 mm from the interface for the grassed and the wooded floodplain, respectively. These widths are larger when considering the lateral turbulence intensity (620 mm and 470 mm for the grassed and the wooded floodplain, respectively).

5.7.3 Flow within the cylinder array

Figure 5.28 shows a comparison of the cross-sectional distribution of mean longitudinal velocity and turbulence intensities across a cylinder array elementary pattern, between the wooded isolated floodplain (test case WQ15) and the wooded main-channel-influenced-floodplain (test case CW). For test case CW, the measurement is carried out within the plateau region of the flow quantities (see Section 5.7.2). Some discrepancies can be observed between the distribution of the mean longitudinal velocity. For the main-channel-influenced-floodplain, the lateral variations are more important, as well as the extreme values. A surprising observation is that the velocity is higher at $y = 340$ mm (i.e. 4 cm downstream of a cylinder) than at $y = 420$ mm (i.e. 12 cm downstream of a cylinder) for test case CW. This fact remains unexplained.

The mean velocity averaged over a lateral pattern of the cylinder array (in the range $340 < y < 420$ mm) is equal to 12.7 cm.s^{-1} for test case WQ15 and to 9.8 cm.s^{-1} for test case CW (-23 %), the floodplain flow depth being $H_f = 113$ mm and $H_f = 99$ mm, respectively. It has been shown in Chapter 4 that in single channel the spatially averaged

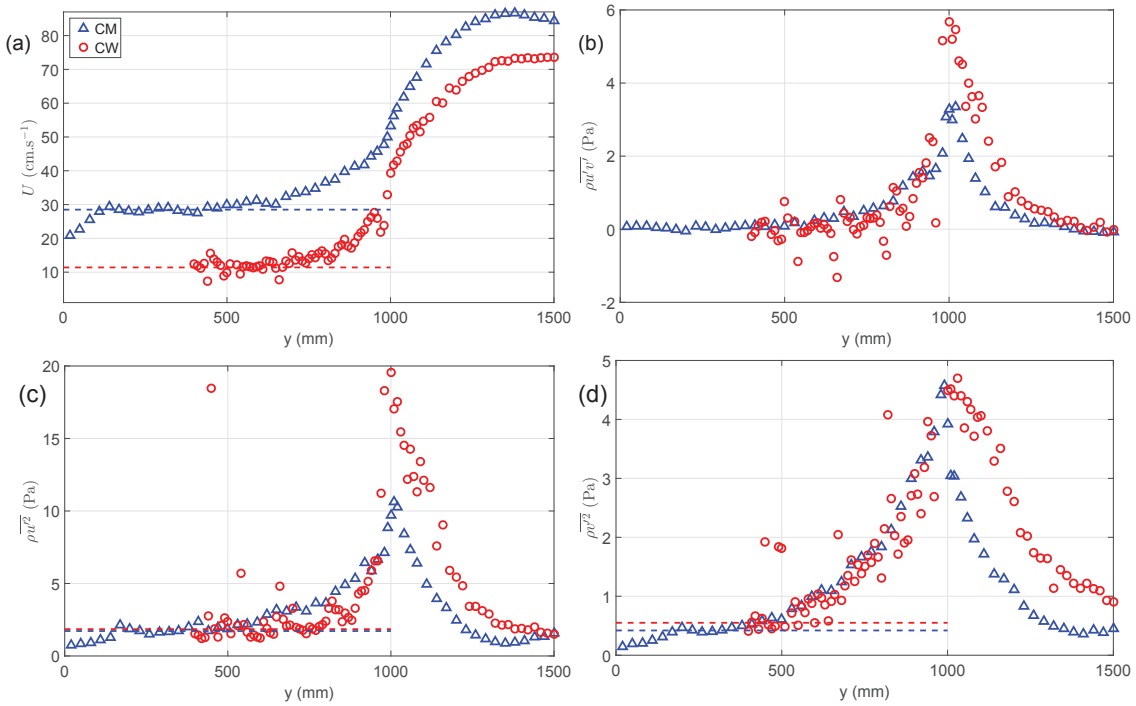

Figure 5.27: Lateral profiles of (a) mean longitudinal velocity, (b) lateral Reynolds stress, (c) longitudinal turbulence intensity and (d) lateral turbulence intensity at $z_f = H_f/2$ for test cases CM ($x = 13.15\,\mathrm{m}$) and CW ($x = 13.76\,\mathrm{m}$).

velocity (over a pattern) within the cylinder array under uniform flow conditions is quite independent of flow depth. It can thus be induced that the pattern-averaged velocity is lower in the plateau region of the main-channel-influenced-floodplain than in the isolated floodplain. This fact explains the reason why the conveyance of the wooded main-channel-influenced-floodplain is not increased a lot compared to the wooded isolated floodplain: the flow acceleration in the interface region is counterbalanced by a decreased pattern-averaged velocity outside the interface region.

This lower pattern-averaged velocity for the wooded main-channel-influenced-floodplain can be explained by the long-living sweep and ejection events that introduce a periodic lateral flow within the cylinder array. Close to the interface, the lateral velocity amplitudes associated with this periodic flow are of the same order of magnitude than the longitudinal mean velocity. This periodic flow is still present in the plateau region and the periodic lateral velocities are 15 % of the mean longitudinal velocity in the region $340 < y < 420\,\mathrm{mm}$. This lateral velocity increases the drag forces and therefore the energy losses in the cylinder wakes, compared to the case of a purely longitudinal flow as in single channel.

The periodic lateral flow in the wooded main-channel-influenced-floodplain can also probably explain the reason why the turbulence production in the cylinder wakes is higher than it is for the isolated floodplain, as can be observed in Fig. 5.28c-f with the longitudinal and lateral turbulence intensities.

As a conclusion, even in the plateau region, the flow in the main-channel-influenced-floodplain cannot be considered as an isolated floodplain flow.

In Chapter 4 we investigated in detail the near-bed region of the flow through a cylinder array in single channel configuration, focusing in particular on the velocity bulge phenomenon. The near-bed region was not investigated in detail for the compound chan-

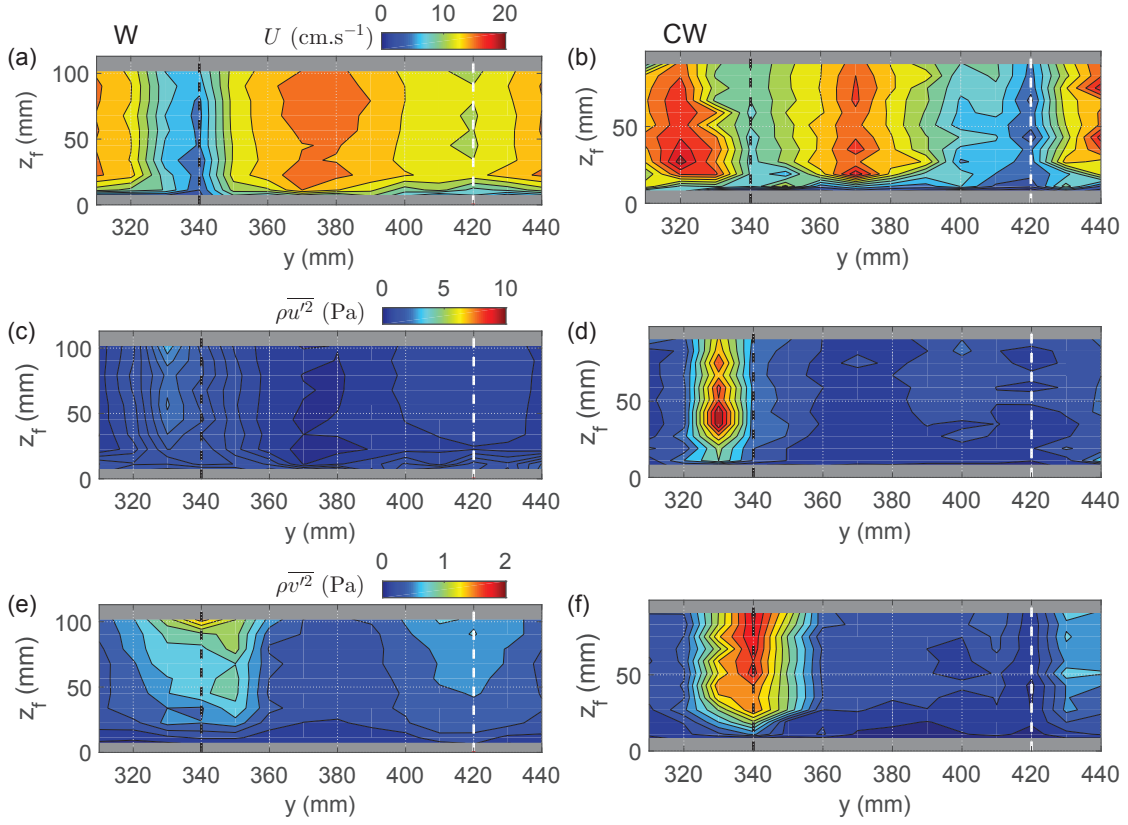

Figure 5.28: Cross-sectional distribution of (a-b) mean longitudinal velocity U, (c-d) longitudinal turbulence intensity $\rho\overline{u'^2}$ and (e-f) lateral turbulence intensity $\rho\overline{v'^2}$ within an elementary pattern of the cylinder array for test case WQ15 at $x = 13.15\,\mathrm{m}$ (left panels) and for test case CW in the plateau region of U and at $x = 11.83\,\mathrm{m}$ (right panels). Measurement downstream of an odd lateral row of cylinders, at mid-distance between two lateral rows of cylinders. Black and white dotted lines indicate the position of the cylinders located at 4 cm upstream and 4 cm downstream of the measurement, respectively.

nel experiments. As the ADV measurements are less accurate in the vicinity of the grass blades, it should have required the use of the PIV system, but for practical reasons this was not easy to set up (laser access through the floodplain bank). However, the presence of the constant-velocity region was also observed in compound channel (flow case CW, see Figs. 5.15 and 5.28).

The flow through a cylinder array in single channel generated free surface oscillations, called seiching, as shown in Chapter 4. Seiching was not present in the compound channel experiments. The free surface oscillations were probably absorbed by the main channel flow. Therefore lateral flow confinement appeared to be a necessary condition for seiching.

5.8 Conclusion

Two compound channel flows with floodplains covered either by a bed roughness (meadow-type vegetation) or an emergent cylinder array installed on a bed roughness (wood-type vegetation) were experimentally investigated. The main results are summarized below:

- The growth rate of the mixing layer and the stabilisation of its width both differed on the main channel side and on the floodplain side. The mixing layer width stabilised earlier in the floodplain, under the effect of shallowness. The presence of emergent roughness in the floodplain also accelerated the convergence towards a constant mixing layer width. Due to the wide main channel of the present study, convergence of the mixing layer width on the main channel side was never observed.

- The compound channel mixing layer was self-similar at a given elevation in the longitudinal direction, when the flow quantities were normalised by the velocity difference across the mixing layer and the lateral coordinate was normalised by the mixing layer width in the floodplain and in the main channel on either side of the interface.

- The compound channel mixing layer was highly heterogeneous in the vertical direction, in particular the mixing layer width increased and the dimensionless velocity difference λ decreased from the bankfull level to the free surface. The presence of emergent roughness in the floodplain tended to homogenize the mixing layer on the vertical direction. Floodplain shallowness prevented the normalised lateral profiles of velocity and turbulence to coincide at different elevations.

- Turbulent coherent structures in the form of a succession of large sweep and ejection events were present in the compound channel mixing layer. The phase velocity of the coherent structures could be fairly approximated by the depth-averaged longitudinal velocity at the main channel/floodplain interface.

- The coherent structures spanned the entire floodplain flow depth. Important differences were observed concerning the spatial organisation of the longitudinal and the lateral coherent velocity fluctuations. The lateral extent of the coherent fluctuations was much higher for the lateral than for the longitudinal velocity. The wave front of the coherent fluctuations propagated with a phase advance in the upper water column relative to the lower water column. This phase lag in the vertical direction disappeared with the presence of a cylinder array on the floodplains. A phase lag was also observed laterally, with a phase advance on both sides of the mixing layer, relative to the main channel/floodplain interface. Further studies are needed to better understand the spatial organisation and the physical processes that drive the coherent structures in the compound channel flow.

- Compared to the isolated floodplain, the conveyance capacity of the main-channel-influenced-floodplain was much more increased in the case of a grassed floodplain (+12.5 %) than in the case of a wooded floodplain (+2.9 %). For the wooded floodplain, the flow acceleration by the main channel in the interface region was counterbalanced by a higher energy loss in the cylinder array due to important lateral velocity components (related to the mixing layer coherent structures) that were not present in the isolated floodplain.

Chapter 6

Compound channel flow with a longitudinal transition in hydraulic roughness on the floodplains

Preliminary note

A part of this chapter was submitted to publication to the journal *Environmental Fluid Mechanics*.

6.1 Introduction

Compound open channel flows have been widely investigated under uniform flow conditions. However, compound channel flows are often subjected to different sources of flow non-uniformity in the field. A first source is the longitudinal variation in cross-sectional shape, that was studied in the case of skewed floodplains (Elliott and Sellin, 1990), of narrowing or enlarging floodplains (Bousmar *et al.*, 2004; Proust *et al.*, 2006), of local obstacles like groynes set on the floodplain (Peltier *et al.*, 2013). These studies showed that the lateral momentum exchange between main channel and floodplain is driven both by the turbulent diffusion related to the mixing layer that forms at the main channel/floodplain interface and by the net lateral mass transfers between main channel and floodplain. Proust *et al.* (2013) investigated the relaxation of flows in a straight smooth compound channel in which the upstream discharge distribution has been destabilized with regards to the uniform discharge distribution. It appears that the relaxation to uniformity is a relatively slow process: for an excess or a deficit in floodplain discharge of $\pm 19\%$ at flume inlet, the uniform discharge distribution is not reached 10 m downstream. Bousmar *et al.* (2005) pointed out that the longitudinal development of a compound channel mixing layer is longer than a boundary layer development.

Longitudinal changes in floodplain roughness are also an important source of non-uniformity in the field. This subject was scarcely investigated so far. Jahra *et al.* (2011) investigated short patches of emergent rigid vegetation on the floodplain and compared their experiments with a 3D numerical model. Compound channel flows with a longitudinal change in roughness can be compared to flows in a single channel where a longitudinal and a lateral transition in roughness are combined. In the latter case, the lateral change in roughness also induces a mixing layer. Such flows were investigated by Vermaas *et al.* (2011) in the case of a rough bed parallel to a smooth bed, by Rominger and Nepf (2011) in the case of a parcel of emergent cylinders of finite width in the middle of a flat channel and by Zong and Nepf (2010) in the case of an emergent cylinder array occupying the

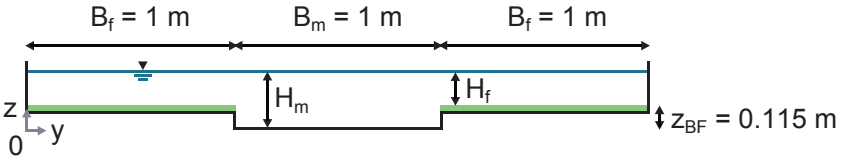

Figure 6.1: Front view of the compound channel flume.

right third of the channel width. Vermaas *et al.* (2011) showed that the lateral exchange of momentum between the two beds due to secondary currents can be of the same order of magnitude than the momentum exchange due to net mass transfers and to turbulent diffusion. Rominger and Nepf (2011) showed that the parcel influences the flow upstream of the leading edge over a length of $L_{up} \approx 4b$, where b is the half-width of the parcel. Downstream of the leading edge, they defined an interior adjustment region, associated with net lateral mass transfers, of length $L_{dw} \approx 6(1+(C_D ab)^2)/(C_D a)$, a being the frontal area per unit volume and C_D the cylinder drag coefficient. This adjustment region is followed by a region of vortex (shear layer) growth, before the flow gets fully developed (constant vortex size).

The present study investigates compound channel flows subjected to a longitudinal transition in roughness on the floodplains. The transition occurs between a rough bed, representing a highly submerged meadow, and an array of emergent cylinders, representing a woodland with emergent trees. The first objective is to study the compound channel mixing layer properties under non-uniform flow conditions. In particular, the mixing layer width, the lateral profiles of mean velocity and turbulence quantities and the coherent structures dynamics are experimentally analysed. The second objective is to investigate the main forces that drive the flow dynamics.

The experimental setup is described in Section 6.2. The compound channel flows with a change in roughness are first investigated in terms of longitudinal variations in water depth (Section 6.3), longitudinal variations in discharge distribution between main channel and floodplain (Section 6.4) and secondary currents (Section 6.5). Then the dynamics of the mixing layer is analysed (Section 6.6); in particular, mixing layer width, lateral velocity profiles and coherent structures are considered. An analysis of the flow in the wooded floodplain is carried out in Section 6.7. Finally a force analysis is undertaken in Section 6.8, where the relative weights of the different forces are assessed.

6.2 Experimental setup and methodology

The experiments were performed in an 18 m long and 3 m wide glassed-wall flume, located in the Hydraulics and Hydromorphology Laboratory of Irstea, Lyon-Villeurbanne, France. The compound channel cross section was symmetrical and composed of a rectangular central main channel of width $B_m = 1$ m and two adjacent floodplains of width $B_f = 1$ m (see Fig. 5.1). The longitudinal bottom slope was $S_0 = 1.05\,\mathrm{mm.m^{-1}}$. Both right and left floodplains were covered by a dense plastic grass, whose blades were 5 mm long and rigid. The bankfull level, measured from the bottom of the main channel to the crest of the grass blades was $z_{BF} = 115$ mm.

The inlet discharges in the three subsections (main channel, right and left floodplains) were regulated independently with control valves and measured by electromagnetic discharge-meters. After leaving the inlet tank, the flows in the right and left floodplains were accelerated along a linear ramp before reaching the bankfull level (see Fig. 5.2). The

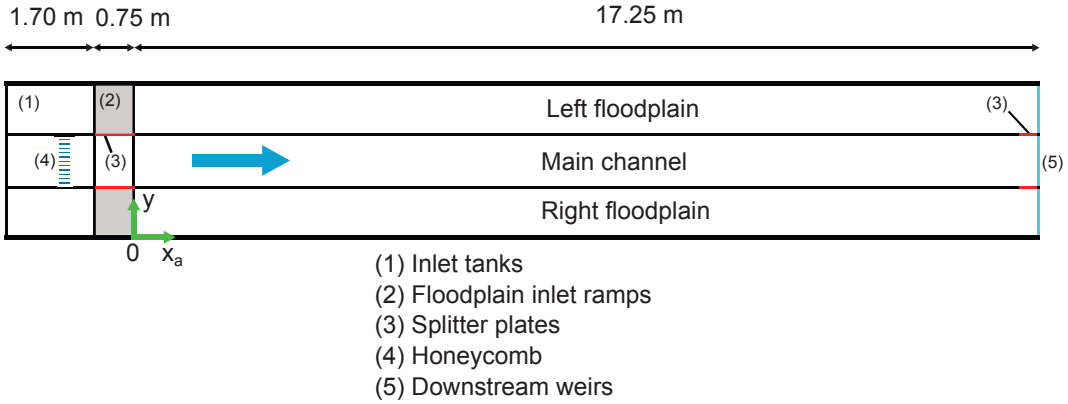

Figure 6.2: Plan view of the compound channel flume.

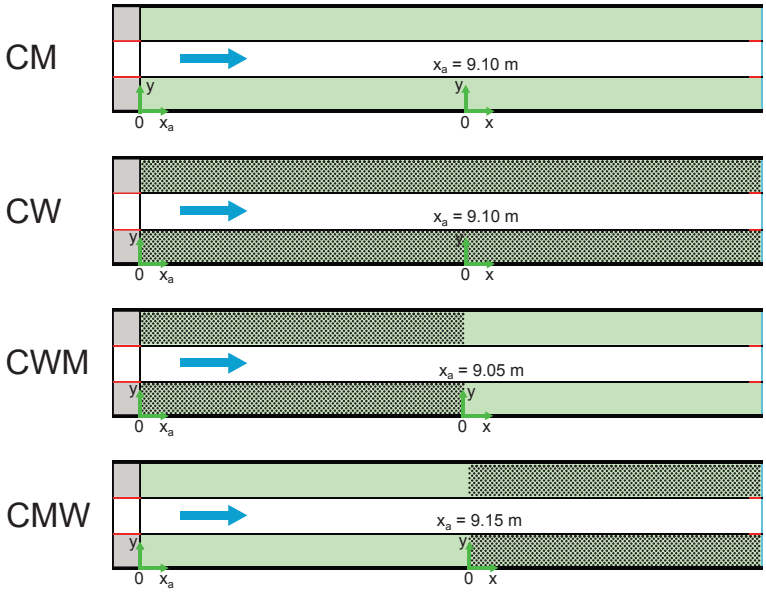

Figure 6.3: Plan view of the four flow configurations.

streams in the three subsections were separated by vertical splitter plates until the ramp end. A 100 mm-thick honeycomb was installed in the inlet tank of the main channel in order to vertically and laterally homogenize the flow (alveolus size 8 mm). At the flume outlet, the flow was controlled by three independent weirs (one per subsection). Downstream splitter plates maintained the flow in the three subsections separated over a distance of 50 cm upstream of the weirs.

The floodplains were covered either by plastic grass alone or by an array of emergent cylinders set on the plastic grass. Four flow configurations were investigated (see Fig. 6.3), corresponding to different floodplain occupations: (1) floodplains covered by plastic grass only (CM: Compound channel with Meadow), (2) floodplains covered by a cylinder array along the whole flume length (CW: Compound channel with Wood), (3) floodplains covered by a cylinder array in the upstream half of the flume and by plastic grass in the downstream half (CWM: Compound channel with a longitudinal transition from Wood to Meadow) and (4) floodplains covered by plastic grass in the upstream half and by a cylinder array in the downstream half (CMW: Compound channel with a longitudinal transition from Meadow to Wood). Figure 6.4a shows a picture of configuration CWM.

The longitudinal axis (x-axis) is defined along the flume bottom, the vertical axis (z-axis) is normal to the bed and the lateral axis (y-axis) is oriented from the right to the left bank. In this coordinate system, the instantaneous velocities, time-averaged velocities and velocity fluctuations are denoted (u, v, w), (U, V, W) and (u', v', w'), respectively. Overline denotes time-averaging (e.g. $\overline{u'v'}$). Two longitudinal coordinates x and x_a are defined (see Fig. 6.3). The x_a-origin is defined at the trailing edge of the upstream splitter plates. The x-origin is located at the roughness transition for the flows with a roughness transition and at $x_a = 9.10\,\mathrm{m}$ for the two uniform flows. In the following, all results are presented using the relative coordinate x. The origin of the lateral coordinate y is located at the side wall of the right floodplain. The origin of the vertical coordinate z is defined at the bottom of the main channel. A relative vertical coordinate z_f is additionally defined with origin at bankfull level: $z_f = z - z_{BF}$. Subscripts m and f refer to main channel and floodplain, respectively.

The total discharge was the same for all flow configurations ($Q_{tot} = 162\,\mathrm{L.s^{-1}}$). For the two uniform test cases (CM and CW), the upstream discharge distribution and the downstream weirs were adjusted iteratively (Bousmar *et al.*, 2005) in order to get a free surface parallel to the bed and to minimize the net mass exchange between subsections. Two different upstream discharge distributions were investigated for each roughness transition configuration: floodplain discharges of $Q_f = 18$ and 12 $\mathrm{L.s^{-1}}$ for configuration CWM and $Q_f = 18$ and 26 $\mathrm{L.s^{-1}}$ for configuration CMW. The levels of the downstream weirs were the same as those for the uniform flows over the downstream roughness (e.g. for configuration CMW the downstream weir levels are those of test case CW). The flow conditions of the six flows investigated are reported in Table 6.1.

Table 6.1: Flow conditions of the six test cases: discharge in each floodplain Q_f, water depth in the floodplain H_f, relative flow depth D_r, Reynolds number $Re_i = 4Q_i/(\nu(2H_i + B_i))$, Froude number $Fr_i = Q_i/(H_i^{3/2} g^{1/2} B_i)$ and bulk velocity $U_i = Q_i/(H_i B_i)$ in each subsection ($i \in \{m, f\}$). For roughness transition test cases, measurements at the most upstream position ($x \approx -8\,\mathrm{m}$), at the roughness transition ($x \approx 0\,\mathrm{m}$) and at the most downstream position ($x \approx 7\,\mathrm{m}$) are indicated.

Test case	Q_f (L.s^{-1})			H_f (mm)			D_r			Re_f $\times 10^{-4}$			Fr_f			U_f (cm.s^{-1})			Re_m $\times 10^{-4}$			Fr_m			U_m (cm.s^{-1})		
	$x(m)$ = - 8	0	7	-8	0	7	-8	0	7	-8	0	7	-8	0	7	-8	0	7	-8	0	7	-8	0	7	-8	0	7
CM		18			56			0.33			6.5			0.43			32.1			37.6			0.57			73.7	
CW		14			99			0.46			4.7			0.14			14.1			37.5			0.43			62.6	
CWMQ18	17.5	12.1	16	67	51	55	0.37	0.31	0.32	6.2	4.4	5.8	0.32	0.34	0.40	26.1	23.7	29.1	37.2	41.4	38.8	0.52	0.65	0.6	69.8	83.0	76.5
CWMQ12	11	10.9	14.7	62	50	54	0.35	0.30	0.32	3.9	4.0	5.3	0.23	0.31	0.37	17.7	21.8	27.2	41.4	42.2	39.6	0.60	0.67	0.6	79.1	85.0	78.5
CMWQ18	19.2	23.7	17.4	96	105	100	0.45	0.48	0.47	6.4	7.8	5.8	0.21	0.22	0.18	20.0	22.6	17.4	34.8	31.8	35.6	0.41	0.35	0.4	58.6	52.1	59.2
CMWQ26	27.1	27.2	17.3	100	107	100	0.47	0.48	0.47	9.0	9.0	5.8	0.27	0.25	0.17	27.1	25.4	17.3	30.2	29.8	35.6	0.35	0.33	0.4	50.1	48.5	59.3

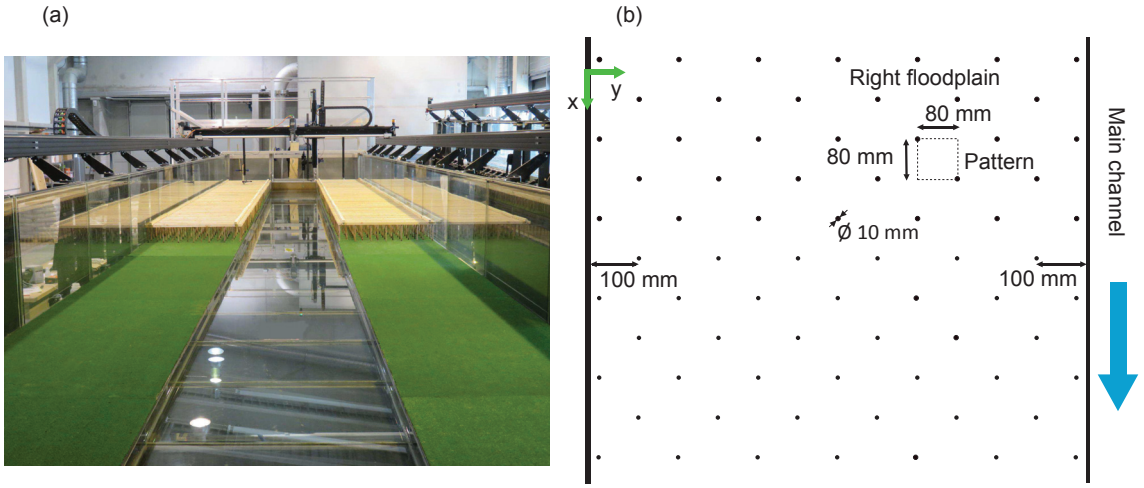

Figure 6.4: (a) Compound channel flume at Irstea, longitudinal transition from wood to meadow (configuration CWM, picture viewed from downstream). (b) Plan view of the cylinder array.

The cylinder array was made of wooden circular cylinders that were uniformly distributed in staggered rows (see Fig. 6.4b). The cylinder diameter was $D = 10\,\text{mm}$ and the cylinder density $N = 81\,\text{cylinders.m}^{-2}$. Cylinders were hold together with an emergent wooden superstructure (see Fig. 6.4a). The accuracy of the cylinder position was $\pm 5\,\text{mm}$ in both lateral and longitudinal directions.

The free surface elevation was measured with ultrasonic sensors (UNDK20I69, Baumer) with an accuracy of $\pm 0.5\,\text{mm}$. Recording time was 3 minutes at a 50 Hz sampling rate. For the two uniform flows (test cases CM and CW), the water depth was constant for $2 < x_a < 17\,\text{m}$ in the three subsections with a scatter of $\pm 1\,\text{mm}$. For all test cases, no significant lateral gradient of free surface level was observed. Velocity was measured by means of a side-looking ADV probe (Vectrino Plus, Nortek) with a sampling rate of 100 Hz. The sampling volume was a 7 mm long circular cylinder with a 6 mm diameter. A recording time of 120 s was sufficient to get converged values of turbulence statistics of first and second orders. For the computation of autocorrelation functions, the recording time was set to 600 s in order to increase measurement quality. The ADV raw data were filtered with the free software WinADV, which uses the despiking concept developed by Goring and Nikora (2002).

Owing to cross-section symmetry, we present herein measurements in the right half of the compound section. The vertical plane (x, z) at the main channel/floodplain boundary is called interface and is denoted y_{int} ($y_{int} = 1000\,\text{mm}$ for the right-hand interface). In the following, the analysis focused on the flows subject to a roughness transition (configurations CWM and CMW), using the uniform flows (configurations CM and CW) as references.

6.3 Water depth

Figure 6.5a shows the longitudinal profiles of floodplain water depth for the roughness transition test cases, along with the uniform water depths (test cases CM and CW). As the flow is subcritical along the whole flume length, the water depth profile is primarily controlled by the downstream weir levels, which are those of the uniform flow over the downstream roughness. For all test cases, an inversion of the free surface slope is observed at the transition. Although the uniform water depth of the downstream roughness is

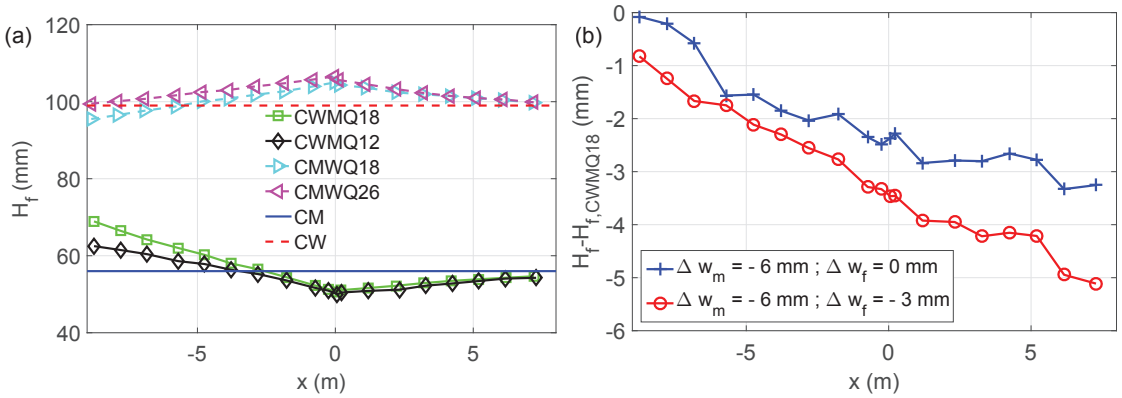

Figure 6.5: (a) Longitudinal profiles of floodplain water depth for the roughness transition test cases. The uniform water depths (test cases CM and CW) are reminded. Dotted lines denote test cases ending with wooded floodplains. (b) Longitudinal profiles of floodplain water depth relatively to the water depth profile of test case CWMQ18 ($H_{f,CWMQ18}$) after dropping the main channel w_m and/or the floodplain downstream weir height w_f.

reached at the downstream end of the flume ($x = 8\,\mathrm{m}$), no plateau is observed, indicating that flow uniformity is not achieved.

In order to check the influence of the downstream boundary condition on the longitudinal water depth profile, tests were carried out with different downstream weir levels in the main channel w_m or in the floodplain w_f for test case CWMQ18. The resulting water depth profiles, relative to the water depth profile of test case CWMQ18, are shown in Fig. 6.5b. A weir level decrease in the main channel or in the floodplain induces a water level drop and this drop decreases gradually when going upstream. The increasing water depth downstream of the roughness transition for test case CWMQ18 (Fig. 6.5a) remains after weir dropping. Thus it is not induced by the downstream boundary conditions but is intrinsic to the flow dynamics.

Figure 6.6 shows a comparison of longitudinal water depth profiles between roughness transitions in a compound channel (test cases CWMQ12 and CMWQ18) and the same roughness transitions in a single channel, i.e. in the case of an isolated floodplain, for close discharge values (12 and $7\,\mathrm{L.s^{-1}}$ for the wood-to-meadow transition and 18 and $21\,\mathrm{L.s^{-1}}$ for the meadow-to-wood transition). The single channel experiments are taken from Chapter 4 (test cases WMQ7 and MWQ21). In Fig. 6.6 the most downstream water depth value has been subtracted to the water depth profile, in order to better compare the different flow test cases. Whereas the roughness transitions in a single channel are characterized by water depth gradient only upstream of the transition (backwater effect), water depth variations are present both upstream and downstream of the transition for the main-channel-influenced-floodplain. This is related to the double influence of the upstream and downstream boundary conditions, typical for compound channel flows (Proust *et al.*, 2013), and especially to the lateral net mass exchanges that occur between main channel and floodplain downstream of the roughness transition (see Section 6.4). Upstream of the transition, the free surface slope is similar for both the isolated and main-channel-influenced-floodplain.

In order to see the influence of the upstream discharge distribution on the water depth, test case CWMQ18 is first taken as reference and the floodplain discharge is either decreased or increased, the total discharge being kept constant. The variation in water level compared with test case CWMQ18 is shown in Fig. 6.7a. The same tests

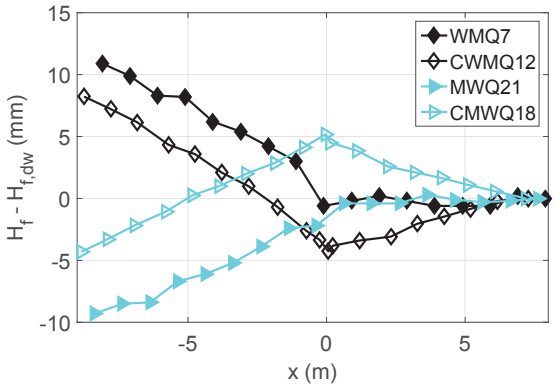

Figure 6.6: Longitudinal water depth profile for isolated floodplains (test cases WMQ7 and MWQ21) and main-channel-influenced-floodplains (test cases CWMQ21 and CMWQ18) with a longitudinal change in roughness. The most downstream water depth value $H_{f,dw}$ has been subtracted.

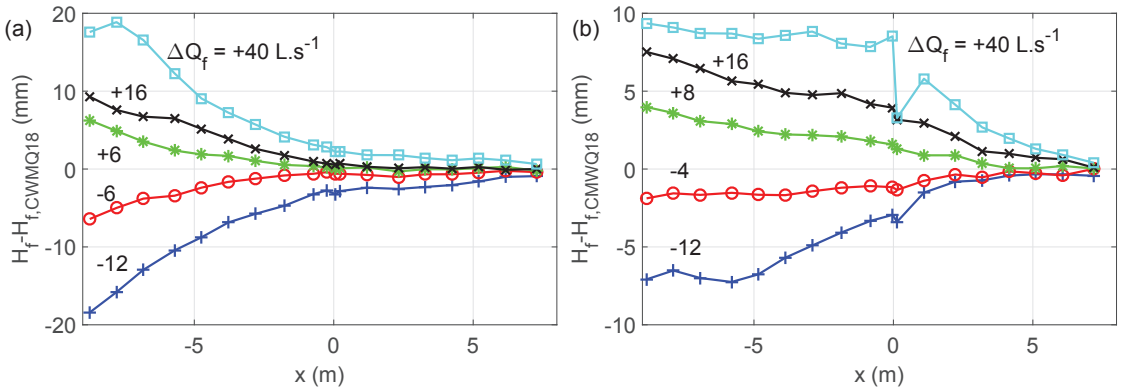

Figure 6.7: (a) Longitudinal profiles of floodplain water depth relative to the water depth profile of test case CWMQ18 ($H_{f,CWMQ18}$) for the wood-to-meadow transition for different upstream discharge distributions. (b) Longitudinal profiles of floodplain water depth relative to the water depth profile of test case CMWQ18 ($H_{f,CMWQ18}$) for the meadow-to-wood transition for different upstream discharge distributions. Numbers on the figure indicate the variation in floodplain discharge relative to the reference test case ($Q_f = 18\,\mathrm{L.s^{-1}}$).

were carried out with test case CMWQ18 as reference (Fig. 6.7b). For both kinds of transition, an increase in floodplain discharge induces an increase in water level. For the wood-to-meadow transition (Fig. 6.7a), the upstream discharge distribution has an effect mainly upstream of the transition, whereas the variation in H_f with Q_f downstream of the transition is rather small. For the meadow-to-wood transition (Fig. 6.7b), the discrepancy of H_f with the reference flow is nearly proportional to the downstream distance. Note that for the meadow-to-wood transition, a local unevenness of water surface is observed at the transition (Fig. 6.7b), which is due to a stationary wave at this location.

6.4 Subsection discharge distribution

The velocity field was measured in the right-hand half main channel cross-section at nine x-stations for each roughness transition test case. Assuming symmetry of the flow, the discharge distribution between subsections was then calculated by integration of the

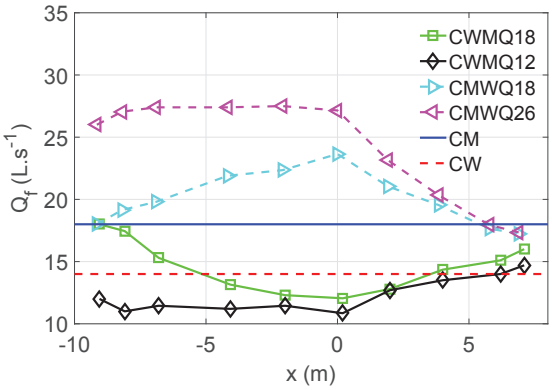

Figure 6.8: Longitudinal variation in floodplain discharge for the four transitions investigated; the floodplain discharge of the uniform meadow and uniform wood flows are reminded with blue and red horizontal lines, respectively. Dotted lines refer to test cases ending with wooded floodplains.

velocity field. The longitudinal variation in floodplain discharge is shown in Fig. 6.8. For each transition type, two cases are observed: a case with a change in the direction of the net mass exchange between main channel and floodplain (CWMQ18 and CMWQ18) and a case without mass exchange upstream of the transition (CWMQ12 and CMWQ26). The direction of the mass transfers between main channel and floodplain is reported in Table 6.2.

Table 6.2: Directions of lateral mass transfers upstream ($x < 0$) and downstream ($x > 0$) of the roughness transition. MC = main channel. FP = floodplain. $\varnothing$ = no transfers.

	CWMQ18	CWMQ12	CMWQ18	CMWQ26
$x < 0$	FP $\rightarrow$ MC	$\varnothing$	MC $\rightarrow$ FP	$\varnothing$
$x > 0$	MC $\rightarrow$ FP	MC $\rightarrow$ FP	FP $\rightarrow$ MC	FP $\rightarrow$ MC

Downstream of the transition, the discharge distribution tends towards the distribution of the uniform flow on the downstream roughness, but for none of the cases the uniform distribution is reached (horizontal lines). Rominger and Nepf (2011) estimated the distance over which lateral mass transfer occurs downstream of the leading edge of a cylinder array set in the middle of a flat channel by $L_{dw} \approx 6(1+(C_D ab)^2)/(C_D a)$, where b is the half cylinder array width. Applied to the present meadow-to-wood transition, with b the floodplain width, this formula gives $L_{dw} = 3.2\,\mathrm{m}$. For configuration CMW, mass transfers are still present 7 m downstream of the roughness change. Thus, mass exchanges appeared to be slower in a compound channel than in a flat channel. This fact can be explained by considering the vertical surface available for the lateral mass exchange, that spans the whole water column for the flat channel, but is reduced to the floodplain flow depth for the compound channel flow.

6.5 Secondary currents

The depth-averaged lateral transfer of longitudinal momentum due to secondary currents is given by $\rho(U(V - V_d))_d$, where subscript d stands for depth-averaging (Vermaas *et al.*, 2011). Figure 6.9 shows the lateral distribution of this quantity in the main channel. Profiles upstream and downstream of the transition are shown for test cases CWMQ18

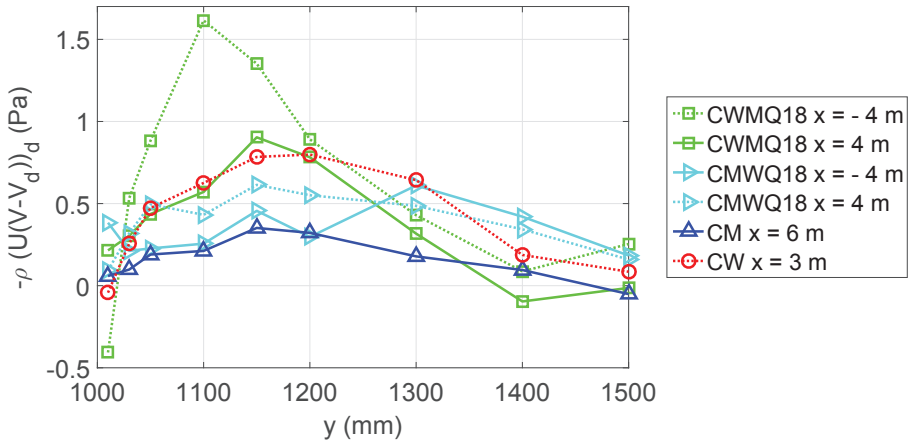

Figure 6.9: Lateral distribution of the depth-averaged lateral transfer of longitudinal momentum due to secondary currents in the main channel. Dotted lines denote profiles in reaches with wooded floodplains.

and CMWQ18, along with the uniform flow test cases CM and CW. Momentum transfers due to secondary currents are more important in reaches with wooded floodplains (dotted lines) than in reaches with grassed floodplains. The lateral exchange of momentum by secondary currents is equal to zero at the main channel centreline, which is expected owing to flow symmetry. The quantity $\rho(U(V-V_d))_d$ also tends to vanish at the interface with the floodplain. Secondary currents thus generate a redistribution of momentum inside the main channel (momentum is transferred positively in the direction of the floodplain), but the exchange with the floodplains seems to be negligible for all test cases.

Figure 6.10a shows the longitudinal evolution of quantity $\rho(U(V-V_d))_d$ along the position $y = 1150\,\text{mm}$, i.e. where the lateral exchange is nearly maximum (see Fig. 6.9). Over uniform roughness (test cases CM and CW), the quantity $\rho(U(V-V_d))_d$ is fully developed after an adjustment length. The plateau value is higher for the wooded floodplain than for the grassed floodplain.

Figure 6.10b shows the same quantity as in Fig. 6.10a normalised by the depth-averaged longitudinal velocity at the interface $U^2_{d,int}$. Quantity $(U(V-V_d))_d/U^2_{d,int}$ is quasi invariant for a given floodplain roughness, irrespective of flow conditions. The value is nearly fourth times higher for the wooded floodplain than for the floodplain covered by a meadow. At the channel inlet and after the roughness transition, an adjustment length is necessary before the fully-developed state is reached.

The transport equation of longitudinal vorticity states that the main production term of longitudinal vorticity (secondary currents) is (Einstein and Li, 1958; Kara *et al.*, 2012):

$$\frac{\partial^2\left(\overline{v'^2}-\overline{w'^2}\right)}{\partial y \partial z}. \tag{6.1}$$

The secondary current generation is therefore mainly related to the cross-sectional distribution of the turbulence anisotropy $\overline{v'^2}-\overline{w'^2}$. It will be shown in Section 6.6.4 that the turbulence intensities scale with $U^2_{d,int}$ for a given floodplain roughness type. It is thus coherent that the secondary currents intensity also scales with $U^2_{d,int}$.

The vertical turbulence intensity $\overline{w'^2}$ could not be reliably measured, which makes not possible the estimate of the turbulence anisotropy. Figure 6.11 shows the cross-sectional distribution of lateral turbulence intensity $\rho\overline{v'^2}$, together with the quantity $V-V_d$, which is the lateral component of the secondary currents, for test case CWMQ12 in the wooded

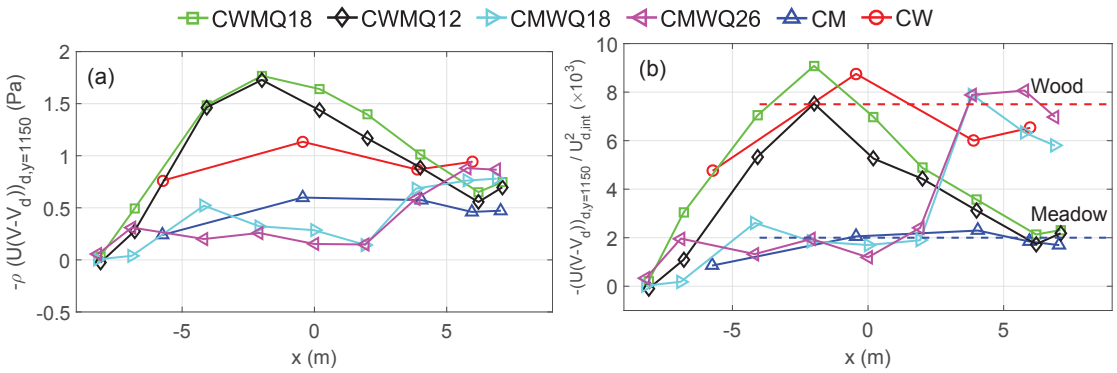

Figure 6.10: Longitudinal variation in the depth-averaged lateral transfer of longitudinal momentum due to secondary currents at $y = 1150\,\text{mm}$ (a) in Pascal and (b) after normalisation by $U_{d,int}$.

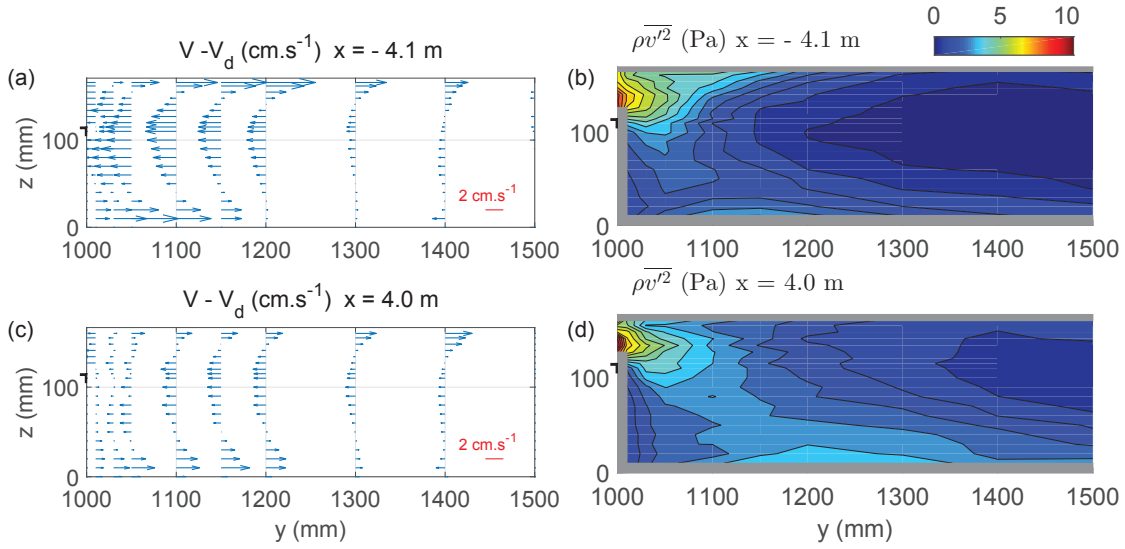

Figure 6.11: Cross-sectional distribution of the quantity $V - V_d$ and of lateral turbulence intensity (a-b) at $x = -4.1\,\text{m}$ and (c-d) at $x = 4.0\,\text{m}$ for test case CWMQ12.

reach ($x = -4.1\,\text{m}$) and in the grassed reach ($x = 4.0\,\text{m}$). At these two stations the value of $U^2_{d,int}$ is comparable ($U^2_{d,int} = 52.4\,\text{cm.s}^{-1}$ at $x = -4.1\,\text{m}$ and $U^2_{d,int} = 53.3\,\text{cm.s}^{-1}$ at $x = 4.0\,\text{m}$). The section-averaged value of $\rho\overline{v'^2}$ in the half main channel (Figs. 6.11b and 6.11d) is lower at station $x = -4.1\,\text{m}$ with a wooded floodplain (1.40 Pa) than at station $x = 4.0\,\text{m}$ with a grassed floodplain (2.20 Pa), while the secondary currents are more intensive at the first station (Figs. 6.11a and 6.11c). The difference in secondary currents intensity between the cases with grassed floodplains and with wooded floodplains is therefore related only to the different cross-sectional distribution of turbulence intensity and not to the value of the turbulence intensity.

6.6 Mixing layer dynamics

In this section the mixing layer of the compound channel flow is investigated at the constant altitude $z_f = H_f/2$. Lateral profiles of mean velocities and turbulence quantities have been measured at different x-stations for each transition. As seen in Chapter 5, the

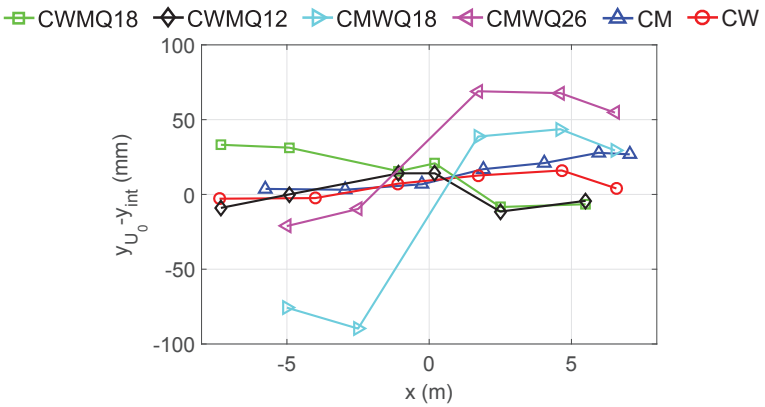

Figure 6.12: Longitudinal evolution of the lateral position y_{U_0} where the velocity U_0 is reached at $z_f = H_f/2$.

properties of the compound channel mixing layer (width, dimensionless velocity difference λ, position of y_{U_0}, see below) change across the water column. The vertical position of the measurements varies only between ± 3 mm ($\pm 5\,\%$ of H_f) along the flume for a given test case. Therefore, the longitudinal variations that are observed for a given test case can be attributed to the longitudinal flow development and not to the effect of vertical variations due to the measuring position.

6.6.1 Mixing layer centre

As stated in Chapter 5, we define the inflexion point in the lateral profile of mean velocity as the centre of the mixing layer, since it is the primary source of flow instability (Fjortoft, 1950). The position of the inflexion point (not shown) is quasi invariant in the longitudinal direction for all uniform and non-uniform flow test cases and $y_{IP} = y_{int} \pm 10$ mm. The position of y_{IP} is therefore forced by the bathymetry. Unlike Proust *et al.* (2013) and Peltier *et al.* (2013), we do not detect a lateral displacement of the inflection point position y_{IP} when mass is transferred from the floodplain to the main channel. This may be due to weaker mass transfers as those in the experiments of Proust *et al.* (2013) and Peltier *et al.* (2013).

For an antisymmetric mixing layer, the position of the inflexion point y_{IP} collapses with the lateral position y_{U_0} where the velocity $U_0 = 0.5(U_1 + U_2)$ is reached, with U_1 the maximum velocity in the main channel and U_2 the velocity in the floodplain outside the mixing layer in the plateau region. Figure 6.12 shows that in the present experiments the position of y_{U_0} is controlled by the lateral mass exchange between floodplain and main channel: when mass is transferred from the floodplain to the main channel (upstream of the transition for CWMQ18 and downstream of the transition for CMWQ18 and CMWQ26), y_{U_0} is displaced towards the main channel. On the contrary, when mass is transferred from the main channel to the floodplain (downstream of the transition for CWMQ18 and CWMQ12 and upstream of the transition for CMWQ18), y_{U_0} is displaced towards the floodplain. For the flows without mass transfers (CM, CW and CWMQ12 and CMWQ26 upstream of the transition), y_{U_0} is close to the interface, although it moves slightly towards the main channel when going downstream (see Section 5.3.3.1).

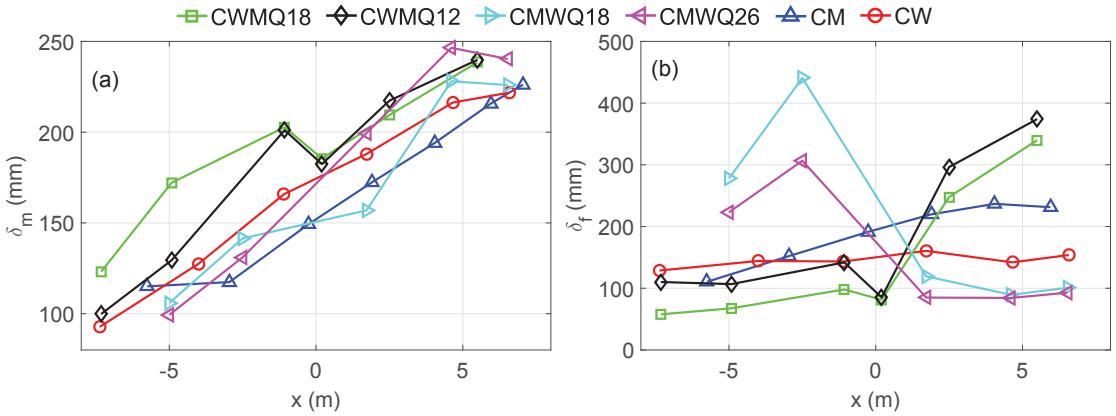

Figure 6.13: Longitudinal evolution of (a) main channel mixing layer width and (b) floodplain mixing layer width at $z_f = H_f/2$.

6.6.2 Mixing layer width

As in Chapter 5, we define the main channel and the floodplain mixing layer widths, δ_m and δ_f, as follows:

$$U(y_{IP} + \delta_m/2) = \frac{U_1 + U_{IP}}{2} \tag{6.2}$$

$$U(y_{IP} - \delta_f/2) = \frac{U_2 + U_{IP}}{2} \tag{6.3}$$

where U_{IP} is the velocity at the inflexion point.

Figure 6.13 shows the main channel and floodplain mixing layer widths for the different flow test cases. As shown in Chapter 5, for the two uniform test cases (CM and CW) δ_m grows until the channel outlet and δ_f levels off at $x \approx 4\,\mathrm{m}$ and $x \approx -4\,\mathrm{m}$ for test cases CM and CW, respectively. With a roughness transition, width δ_f undergoes an important change in trend at the transition: the floodplain-side of the mixing layer is widening downstream of the wood-to-meadow transition and is narrowing downstream of the meadow-to-wood transition. Width δ_m is less affected by the longitudinal change in roughness.

It is known from plane mixing layers that the mixing layer width increases with increasing normalised velocity difference λ (Brown and Roshko, 1974). It is also known from shallow mixing layers that flow confinement and bed roughness tend to constraint the lateral extend of the mixing layer (a decrease in H or an increase in bed roughness lead to a decrease in δ). Chu and Babarutsi (1988) suggested to normalise the shallow mixing layer width δ in the form $\delta^* = \delta c_f/(H\lambda)$ where c_f is the averaged bed friction coefficient across the mixing layer ($c_f = 0.5(c_{f1} + c_{f2})$ with $c_{fi} = \tau_b/(0.5\rho U_i^2)$, $i \in \{1, 2\}$ and τ_b the bed shear stress) and showed that for flows that are shallow enough the quantity δ^* converges towards a constant value when going downstream ($\delta^*_{max} \approx 0.13$). In the following a similar normalisation of the mixing layer width as done by Chu and Babarutsi (1988) is carried out.

To take into account the asymmetrical character of the compound channel mixing layer width, specific λ-values are defined in the main channel and in the floodplain:

$$\lambda_m = \frac{U_1 - U_{IP}}{U_{IP}} \tag{6.4}$$

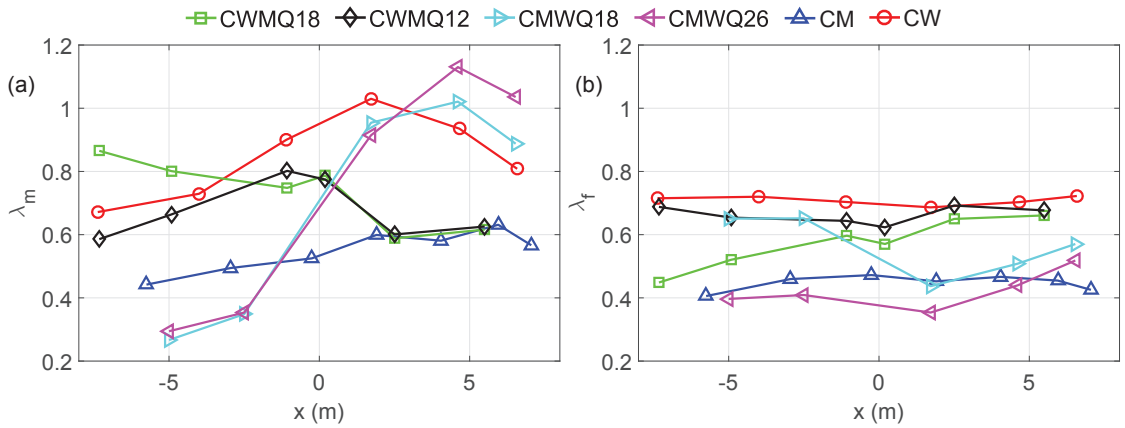

Figure 6.14: Longitudinal evolution of the dimensionless velocity difference (a) on the main channel side λ_m and (b) on the floodplain side λ_f.

$$\lambda_f = \frac{U_{IP} - U_2}{U_{IP}}. \tag{6.5}$$

For an antisymmetric mixing layer $\lambda_m = \lambda_f = \lambda$. The values λ_i represent the λ-value of an equivalent antisymmetric mixing layer with $U_0' = U_{IP}$. The longitudinal evolutions of λ_m and λ_f are shown in Fig. 6.14. The λ_i-values are directly related to the direction of the lateral mass transfers between subsections (see Table 6.2): mass transfers from the floodplain to the main channel increases λ_m and decreases λ_f compared to the uniform flow value, and conversely mass transfers from the main channel to the floodplain decreases λ_m and increases λ_f. This can also be related to the lateral displacement of position y_{U_0} with the lateral mass transfers (Fig. 6.12).

The main channel and floodplain mixing layer widths are normalised in the following way:

$$\delta_m^+ = \frac{\delta_m}{\lambda_m H_f} \tag{6.6}$$

$$\delta_f^+ = \frac{\delta_f}{\lambda_f H_f}. \tag{6.7}$$

Note that for δ_m^+ not H_m but H_f is used since the latter is the vertical extension of the mixing layer. From the definition of δ^* of Chu and Babarutsi (1988) emerges that δ_m^+ and δ_f^+ should only depend on the bed friction coefficient ($\delta^+ = \delta^* c_f$). In the present experiments, the bed friction coefficient c_f is not adapted for describing emergent roughness elements. The substitution of c_f by $c_f + aC_D H_f$, as an analysis of forces should suggest, does not give convincing results.

Figure 6.15 shows the longitudinal evolution of δ_m^+ and δ_f^+. Both normalised widths δ_m^+ and δ_f^+ are equal and rather constant along the channel for test case CW with a mean value of 2. For test case CM, δ_m^+ increases all along the flume and δ_f^+ levels off at $x \approx 4\,\mathrm{m}$, the values being higher than for test case CW, i.e. between 4 and 9. For the test cases with a roughness transition, we observe that δ_m^+ and δ_f^+ approximately follow the trend of the uniform flow test cases (CM or CW) corresponding to the floodplain roughness in the reach considered. One exception is the upstream reach of the wood-to-meadow transitions (test cases CWMQ18 and CWMQ12), where δ_m^+ is about twice higher than the value related to the uniform flow test case CW (Fig. 6.15a).

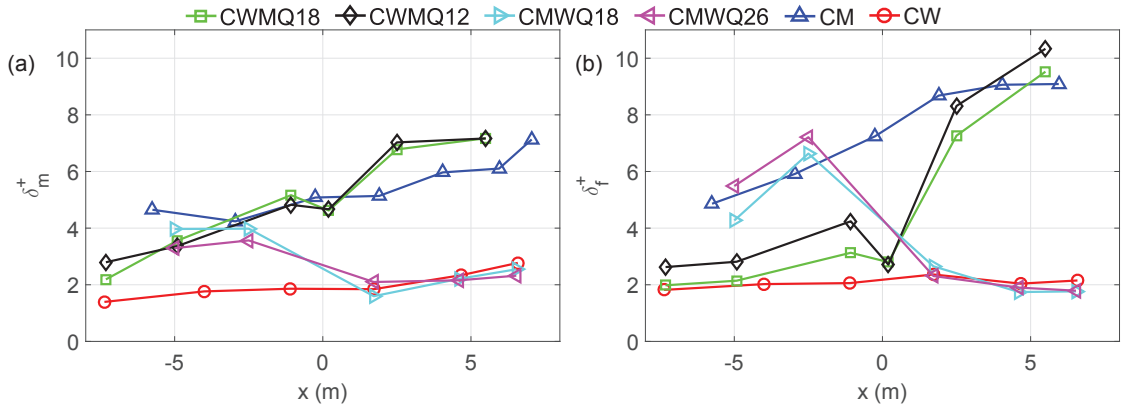

Figure 6.15: (a) Main channel and (b) floodplain mixing layer widths at $z_f = H_f/2$, normalised by λ_i and floodplain water depth.

The larger normalised mixing layer widths for reaches with grassed floodplains than with wooded floodplains (about three times higher) can be related to the obstruction caused by the cylinder array, which limits the penetration of the coherent structures into the floodplain (White and Nepf, 2007).

6.6.3 Normalised lateral profiles

Figures 6.16 and 6.17 show the longitudinal development of the longitudinal velocity at $z_f = H_f/2$ within the mixing layer for the wood-to-meadow and the meadow-to-wood transitions, respectively. The velocity is normalised in the form $(U - U_0)/(U_1 - U_2)$ and the lateral coordinate is normalised by the subsection mixing layer width, in the same way as in Chapter 5. The self-similar profiles of the uniform flows for each roughness type is also plotted (see Chapter 5 for the self-similarity of test cases CM and CW).

The longitudinal development of the mean longitudinal velocity for the wood-to-meadow transition (Fig. 6.16) is quite self-similar at $z_f = H_f/2$. The difference in the cylinder wake location (particularly in Fig. 6.16a) is due to the scaling of the lateral coordinate by δ_f. On the other hand, self-similarity is not observed for the meadow-to-wood transition (Fig. 6.17). This absence of self-similarity seems to be related to the lateral mass transfers: mass transfers from the main channel to the floodplain bring high-speed fluid into the interface region and tend to increase the normalised velocity in the interface region, compared to the uniform flow test case (Fig. 6.17a). Reversely, mass transfers from the floodplain to the main channel bring low-speed fluid into the interface region and tend to decrease the normalised velocity (Figs. 6.17b and 6.17d). These trends can also be observed for the wood-to-meadow transition (Fig. 6.16), but the effect is much weaker.

The lateral profiles of lateral shear stress, normalised by the velocity difference $U_1 - U_2$, are shown in Figs. 6.18 and 6.19 at the same x-stations as in Figs. 6.16 and 6.17. The longitudinal development of the lateral shear stress is not self-similar for both transitions, especially in the reaches with grassed floodplains (Figs. 6.18b, 6.18d, 6.19a and 6.19c). In the reaches with wooded floodplains, the lateral distribution is not so far from that of the uniform flow test case. Lateral mass transfers may contribute to the absence of self-similarity of the lateral shear stress but is not the single cause since important deviations from the uniform flow distribution are observed in the upstream reach for test case CMWQ26 (Fig. 6.19c), where no lateral mass transfer occurs.

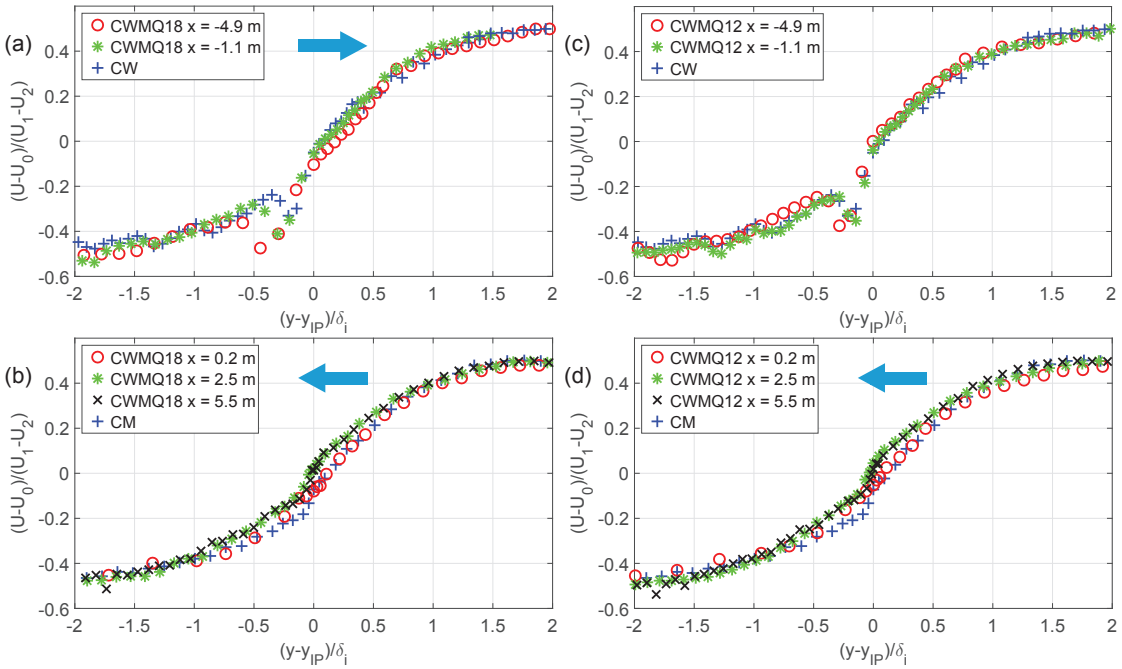

Figure 6.16: Lateral profiles at different x-stations and at $z_f = H_f/2$ of the normalised longitudinal mean velocity (a-b) for the CWMQ18 test case and (c-d) for the CWMQ12 test case. The self-similar profiles of the uniform cases are also plotted (blue crosses). Arrows indicate the direction of mass transfers. $\delta_i = \delta_f$ on the floodplain side and $\delta_i = \delta_m$ on the main channel side.

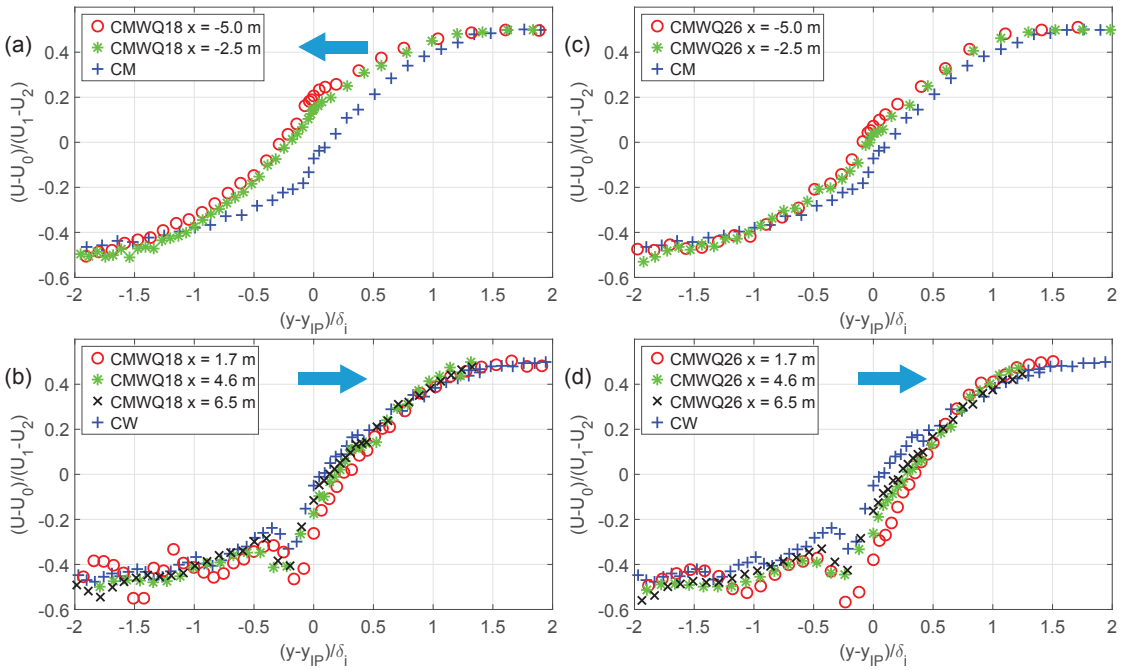

Figure 6.17: Lateral profiles at different x-stations and at $z_f = H_f/2$ of the normalised longitudinal mean velocity (a-b) for the CMWQ18 test case and (c-d) for the CMWQ26 test case. The self-similar profiles of the uniform cases are also plotted (blue crosses). Arrows indicate the direction of mass transfers. $\delta_i = \delta_f$ on the floodplain side and $\delta_i = \delta_m$ on the main channel side.

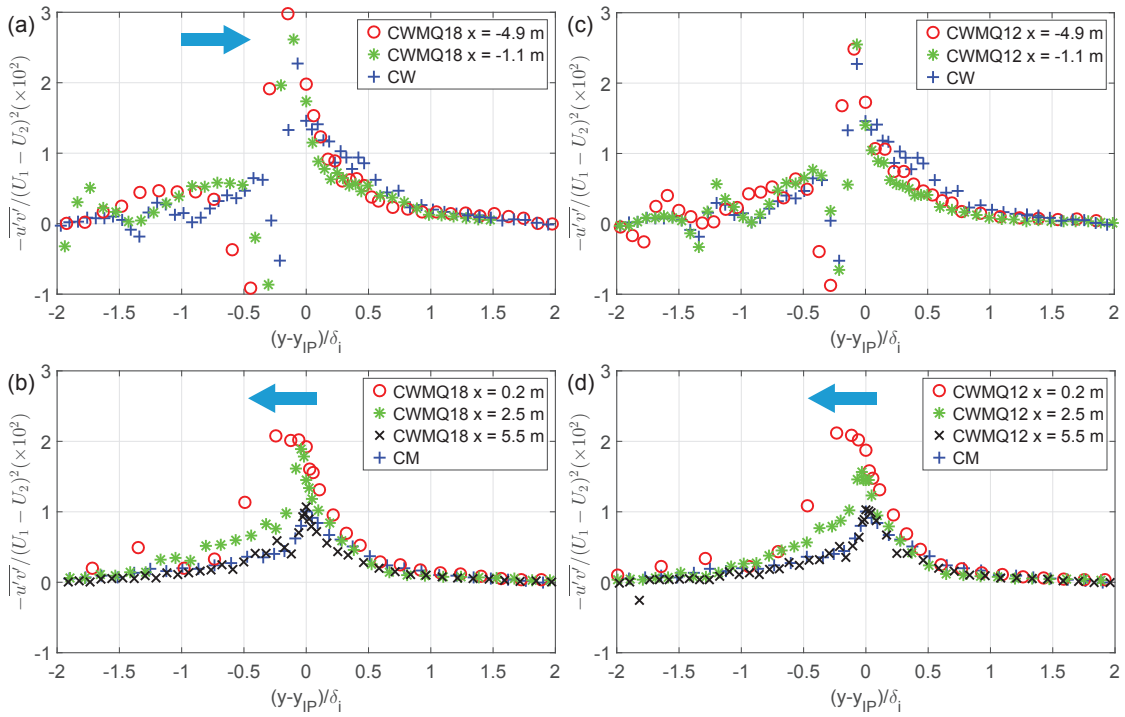

Figure 6.18: Lateral profiles at different x-stations and at $z_f = H_f/2$ of the normalised lateral shear stress (a-b) for the CWMQ18 test case and (c-d) for the CWMQ12 test case. The self-similar profiles of the uniform cases are also plotted (blue crosses). Arrows indicate the direction of mass transfers. $\delta_i = \delta_f$ on the floodplain side and $\delta_i = \delta_m$ on the main channel side.

Self-similarity of the distributions of velocity and turbulence quantities is a sign of flow equilibrium, i.e. when the turbulence budget reduces to a balance between production and dissipation of turbulent energy (Townsend, 1961). Deviation of self-similarity therefore indicates flow disequilibrium. Whereas in a single channel a longitudinal change in roughness leads to flow disequilibrium only downstream of the change in roughness (see Chapter 4 and Antonia and Luxton, 1971), in compound channel configuration the flow is outer equilibrium both upstream and downstream of the change in roughness.

6.6.4 Coherent structures

The longitudinal and lateral velocity time series feature large quasi periodic oscillations in the interface region. These oscillations are the signature of coherent structures that are generated by the mixing layer. The Eulerian integral time scale τ_{ii} of the longitudinal ($i = 1$) or lateral ($i = 2$) velocity fluctuations can be calculated as four times the first zero-crossing of the autocorrelation function of the velocity signal (see Section 5.6.1). The longitudinal Eulerian integral length scales $L_{ii}^{(1)}$ can then be calculated with the Taylor hypothesis using the relation $L_{ii}^{(1)} = U_{d,int}\tau_{ii}$, where $U_{d,int}$ is the depth-averaged mean longitudinal velocity at the interface, considered as the coherent structure convection velocity, see Section 5.6.2. Length scales $L_{11}^{(1)}$ and $L_{22}^{(1)}$ characterise the longitudinal size of the coherent structures considering the longitudinal and lateral velocity fluctuations.

Figure 6.20 shows the longitudinal evolution of length scales $L_{11}^{(1)}$ and $L_{22}^{(1)}$ at the interface and at $z_f = H_f/2$. The coherent structures grow continuously when going downstream for the uniform test case with grassed floodplains CM. By contrast, the coherent structure size levels off at $x \approx 2\,\mathrm{m}$ for the uniform test case with wooded floodplains

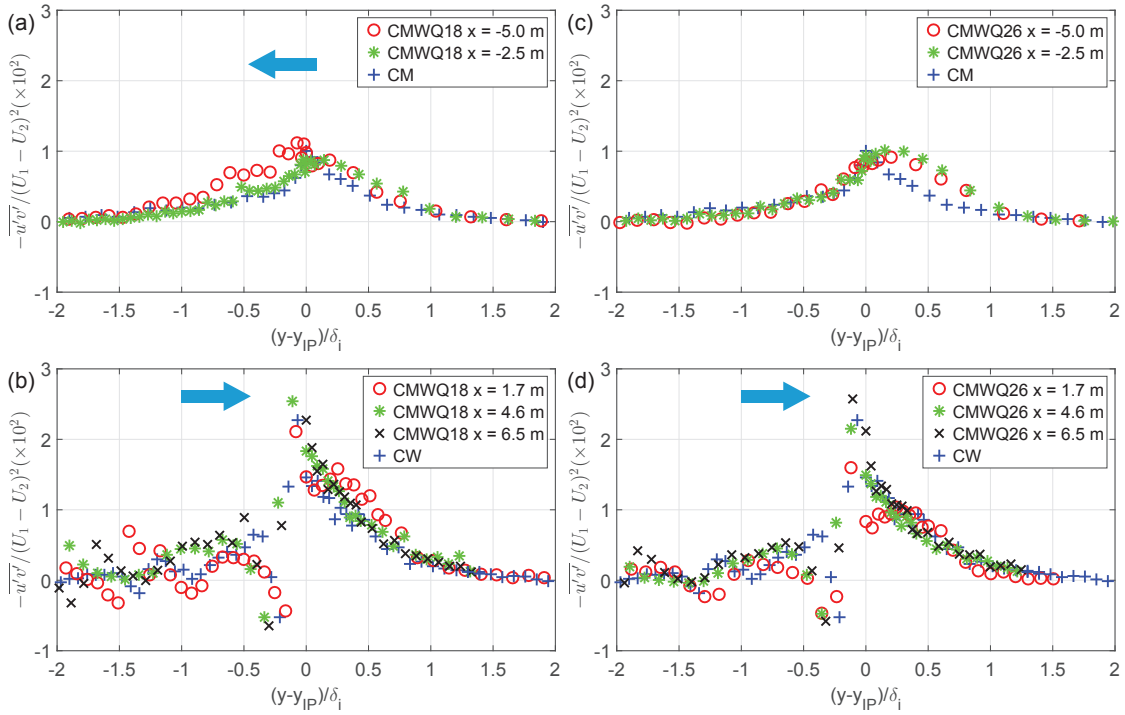

Figure 6.19: Lateral profiles at different x-stations and at $z_f = H_f/2$ of the normalised lateral shear stress (a-b) for the CMWQ18 test case and (c-d) for the CMWQ26 test case. The self-similar profiles of the uniform cases are also plotted (blue crosses). Arrows indicate the direction of mass transfers. $\delta_i = \delta_f$ on the floodplain side and $\delta_i = \delta_m$ on the main channel side.

CW. A change in trend is observed downstream of the roughness transition for test cases with change in roughness. An increase of the growth rate is observed downstream of the wood-to-meadow transition. On the other hand, the meadow-to-wood transition is characterised by a decrease of the coherent structure size, followed by a new increase at $x \approx$ 2-3 m. Reduction of coherent structure size is not a common observation in fluid mechanics, since coherent structures are often associated with an inverse energy cascade and commonly grow with time (see discussion below).

Figure 6.21 shows the ratios $L_{ii}^{(1)}/\delta_{tot}$, where $\delta_{tot} = \delta_m + \delta_f$ is the total mixing layer width. Only x-stations where δ_{tot} is available are plotted. Although an important scatter is observed between the different flow cases, it appears that the length scales $L_{ii}^{(1)}$ approximately scale with δ_{tot}. Moreover, the ratios $L_{ii}^{(1)}/\delta_{tot}$ do not seem to be specific to a roughness type (meadow or wood). The mean values for all flow cases together are $L_{11}^{(1)}/\delta_{tot} = 5.5$ and $L_{22}^{(1)}/\delta_{tot} = 4.2$. Knowing that $L_{ii}^{(1)}$ is proportional to δ_{tot}, we can relate the decrease of $L_{ii}^{(1)}$ immediately downstream of the meadow-to-wood transition to the decrease of δ_f in this region (Fig. 6.13b) and the following increase of $L_{ii}^{(1)}$ at $x \approx$ 2-3 m to the increase of δ_m (Fig. 6.13a).

The velocity fluctuations at the interface are primarily due to the coherent structures. Assuming a sinusoidal shape of the fluctuations $u' = C\sin(2\pi ft)$, f being the passage frequency of the coherent structures, the amplitude C can be computed by $C = \sqrt{2}\sqrt{\overline{u'^2}}$. Figure 6.23 shows the depth-averaged quantities $\sqrt{2}\sqrt{\overline{u'^2}}_{d,int}$ and $\sqrt{2}\sqrt{\overline{v'^2}}_{d,int}$. For all roughness transition test cases, the amplitude of the coherent oscillations is either constant (CMW) or increasing (CWM) upstream of the transition, while the coherent structures are growing (Fig. 6.20). By contrast, amplitude of the oscillations and coherent structure

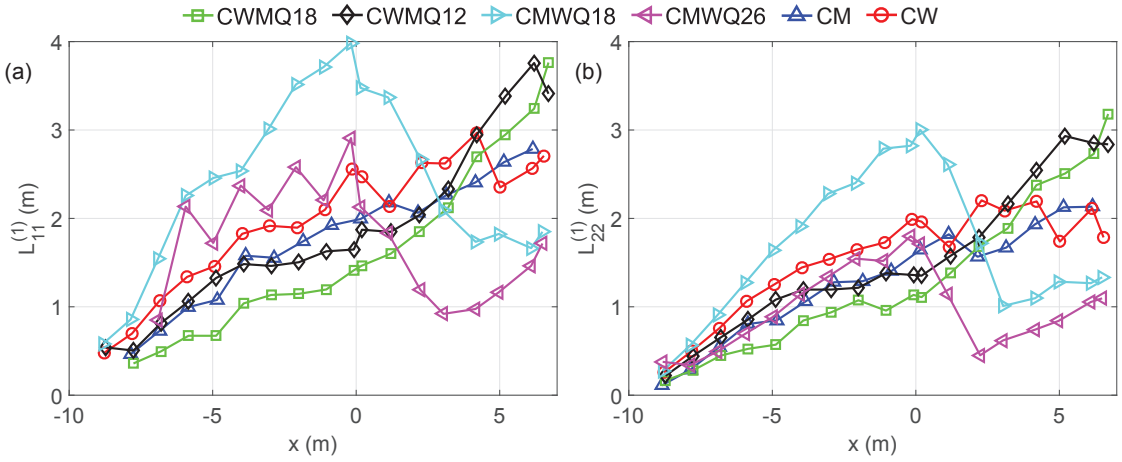

Figure 6.20: Longitudinal evolution of the longitudinal integral length scales of (a) the longitudinal velocity and (b) the lateral velocity at the interface and at $z_f = H_f/2$.

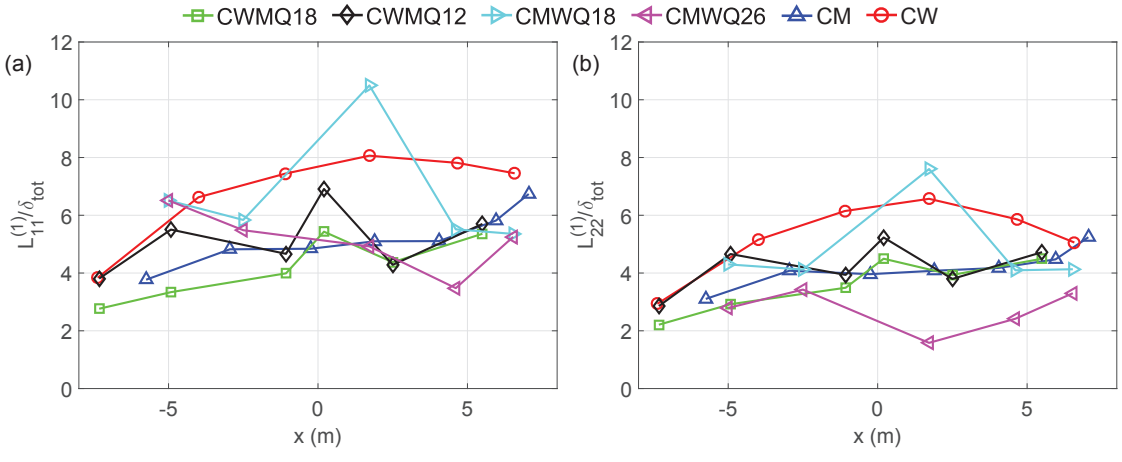

Figure 6.21: Longitudinal evolution of (a) ratio $L_{11}^{(1)}/\delta_{tot}$ and (b) ratio $L_{22}^{(1)}/\delta_{tot}$.

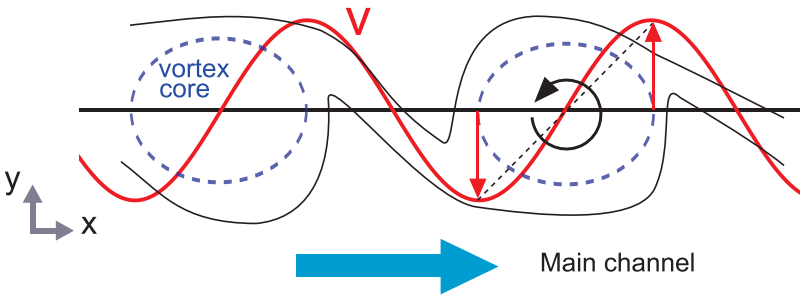

Figure 6.22: Conceptual model of the compound channel mixing layer, composed of series of vortex cores in rigid-body rotation, connected by braids.

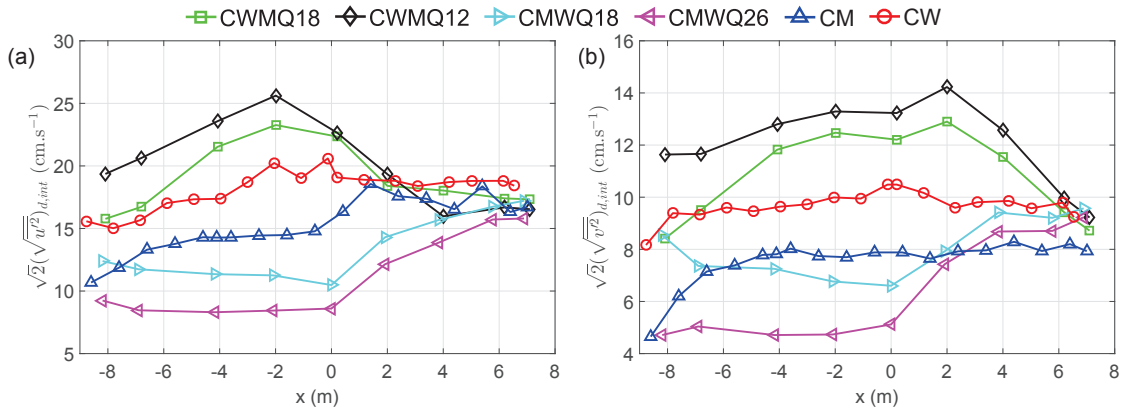

Figure 6.23: Longitudinal evolution of the amplitude of the (a) longitudinal and (b) lateral velocity fluctuations at the interface, averaged over the depth.

size evolve in an opposite way downstream of the transition, e.g. for the meadow-to-wood transition, the amplitude of the oscillations increases while the coherent structures are shrinking. These observations can be explained by the following qualitative reasoning.

Consider a vortex model with a core in rigid-body rotation, as sketched in Fig. 6.22. If R_c is the typical radius of the vortex core and ω its rotation speed, the vortex structure angular momentum is proportional to ωR_c^2. Qualitatively we can assume the scaling relations $R_c \sim L_{22}^{(1)}$ and $\omega R_c \sim \sqrt{\overline{v'^2}}$, and therefore that angular momentum is proportional to $L_{22}^{(1)}\sqrt{\overline{v'^2}}$. For the two uniform flows CM and CW and in the region upstream of the transition for the change in roughness cases, $L_{22}^{(1)}$ continuously increases while $\sqrt{\overline{v'^2}}$ is constant or increases too. Therefore angular momentum is not conserved and the coherent structure growth is associated with structure interaction (vortex merging) and/or fluid entrainment (Moore and Saffman, 1975; Winant and Browand, 1974). Downstream of the change in roughness, the variations in $L_{22}^{(1)}$ and $\sqrt{\overline{v'^2}}$ are opposite, such that the variation of $L_{22}^{(1)}\sqrt{\overline{v'^2}}$ is limited. This let think that in these regions the coherent structures are driven by a different process, which conserves angular momentum, for example vortex stretching.

Figure 6.24 shows the same quantities as in Fig. 6.23, normalised by the depth-averaged longitudinal mean velocity at the interface $U_{d,int}$. The amplitude of the coherent oscillations scales with $U_{d,int}$, which is considered as the convection velocity of the coher-

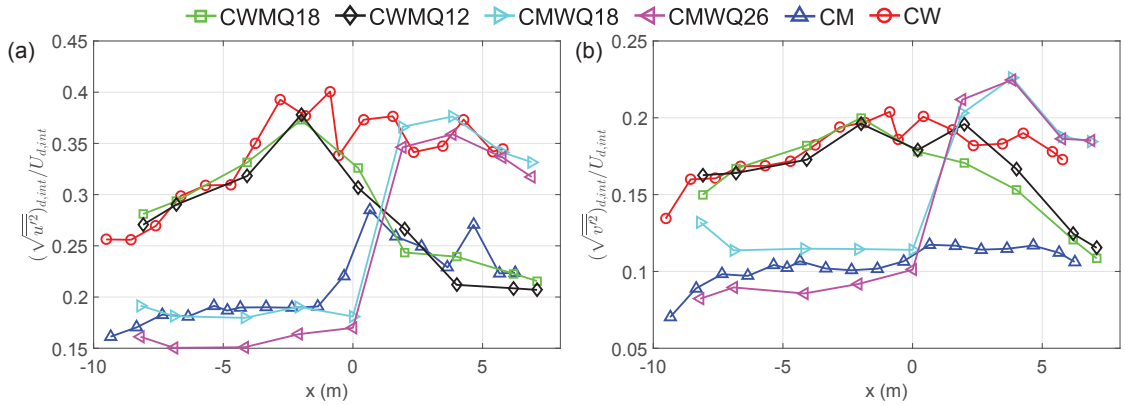

Figure 6.24: Longitudinal evolution of (a) the longitudinal and (b) the lateral depth-averaged turbulence intensities at the interface.

ent structures, see Section 5.6.2. It appears that the amplitude of the coherent oscillations scales with $U_{d,int}$ for a given floodplain roughness. The normalised turbulence intensities are higher for the wooded floodplain: $(\sqrt{\overline{u'^2}})_{d,int}/U_{d,int} \approx 0.23$ and $(\sqrt{\overline{v'^2}})_{d,int}/U_{d,int} \approx 0.11$ for grassed floodplains; $(\sqrt{\overline{u'^2}})_{d,int}/U_{d,int} \approx 0.35$ and $(\sqrt{\overline{v'^2}})_{d,int}/U_{d,int} \approx 0.18$ for wooded floodplains. These values are independent of water depth, of flow non-uniformity and of the presence of lateral mass transfer. Figure 6.24 therefore suggests that there exists an equilibrium between convection velocity of the structure and amplitude of the velocity fluctuations within the structure. In the region downstream of the transition, an adjustment length is observed before the equilibrium related to the new roughness is reached. This adjustment length is higher for the wood-to-meadow ($\approx 5\,\mathrm{m}$) than for the meadow-to-wood transition ($\approx 3\,\mathrm{m}$).

We suggest the following process for explaining the mixing layer dynamics at the roughness transition. When the ratio $(\sqrt{\overline{u'^2}})_{d,int}/U_{d,int}$ (or $(\sqrt{\overline{v'^2}})_{d,int}/U_{d,int}$) is outer equilibrium, the value of $(\sqrt{\overline{u'^2}})_{d,int}$ is varying in order to tend to equilibrium (the value of $U_{d,int}$ being determined macroscopically). This in turn induces a change of the coherent structure size according to conservation of angular momentum and therefore a change in mixing layer width.

Although some scatter is observed, particularly for the longitudinal component, the normalised turbulence intensities are specific for each roughness type, being higher for the wooded floodplain: $(\sqrt{\overline{u'^2}})_{d,int}/U_{d,int} \approx 0.23$ and $(\sqrt{\overline{v'^2}})_{d,int}/U_{d,int} \approx 0.11$ for grassed floodplains; $(\sqrt{\overline{u'^2}})_{d,int}/U_{d,int} \approx 0.35$ and $(\sqrt{\overline{v'^2}})_{d,int}/U_{d,int} \approx 0.18$ for wooded floodplains. These values are independent of water depth, of flow non-uniformity and of the presence of lateral mass transfer. However, in the region downstream of the transition, an adjustment length is observed until the value relative to the new roughness is obtained. This adjustment length is higher for the wood-to-meadow ($\approx 5\,\mathrm{m}$) than for the meadow-to-wood transition ($\approx 3\,\mathrm{m}$).

6.7 Flow in the wooded floodplain

Figure 6.25 shows lateral profiles at $z_f = H_f/2$ of mean longitudinal velocity and turbulence quantities for the uniform flow test case CW, for test case CWMQ18 at $x = -4.92\,\mathrm{m}$ and for test case CMWQ26 at $x = 4.61\,\mathrm{m}$. Similarly to White and Nepf (2007), the floodplain can be separated into two regions: a mixing layer region ($700 < y < 1000\,\mathrm{mm}$), where

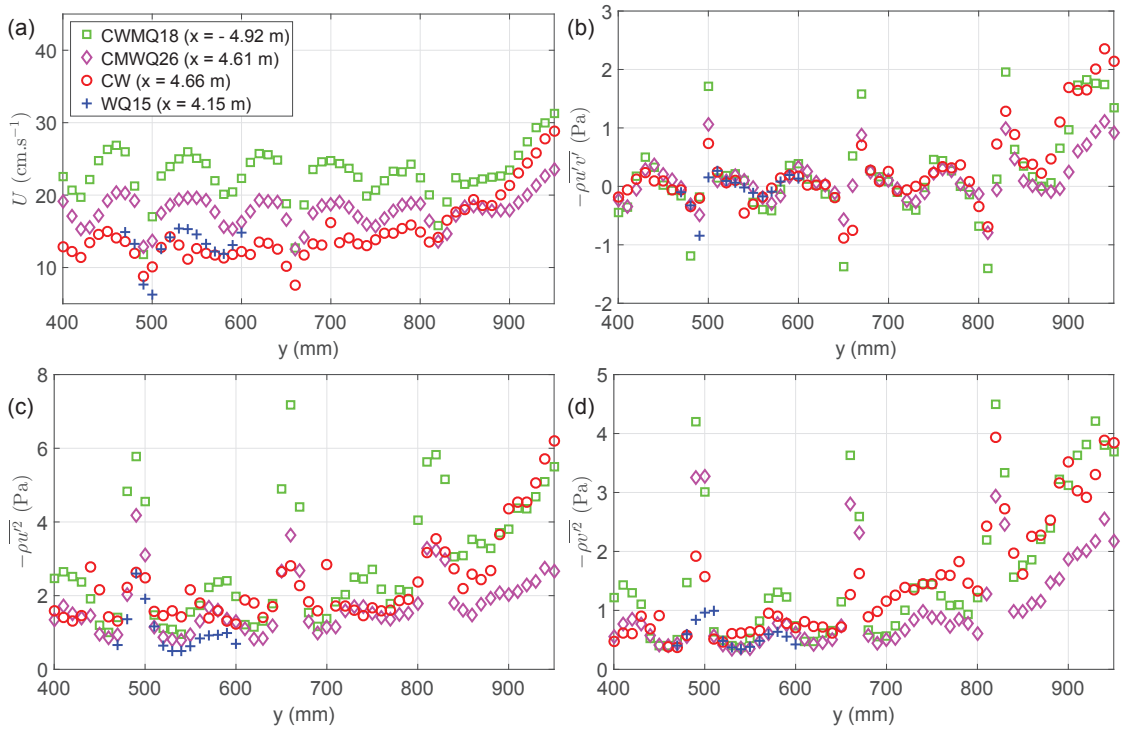

Figure 6.25: Lateral profiles at $z_f = H_f/2$ of (a) mean longitudinal velocity, (b) lateral Reynolds stress, (c) longitudinal turbulence intensity and (d) lateral turbulence intensity in the wooded floodplain for experiments CW ($x = 4.66\,\mathrm{m}$), a reference flow WQ15 in single channel with discharge $Q_f = 15\,\mathrm{L.s^{-1}}$ ($x = 4.15\,\mathrm{m}$), CWMQ18 ($x = -4.92\,\mathrm{m}$) and CMWQ26 ($x = 4.61\,\mathrm{m}$).

the flow is dominated by the transverse exchange of momentum with the main channel and an outer region ($y < 700\,\mathrm{mm}$), where the flow becomes periodic laterally (following the periodicity of the cylinder array). In addition, the lateral profile at $z_f = H_f/2$ of a flow in an isolated wooded floodplain (i.e. in a single channel) with discharge $Q_f = 15\,\mathrm{L.s^{-1}}$ is plotted in Fig. 6.25 (test case WQ15 from Chapter 4).

In the outer region, the longitudinal mean velocity (Fig. 6.25a) for the uniform compound channel CW is slightly smaller but comparable with that of the isolated floodplain WQ15. For test case CWMQ18, the floodplain discharge in the wooded reach is close to that of the uniform case CW but the water depth is lower ($H_f \approx 60\,\mathrm{mm}$ for CWMQ18 and $H_f = 99\,\mathrm{mm}$ for CW); this results in increased velocities compared to the uniform case. For test case CMWQ26, the water depth in the wooded reach is close to the uniform case CW but the discharge is higher ($Q_f \approx 19\,\mathrm{L.s^{-1}}$ for CWMQ18 and $Q_f = 14\,\mathrm{L.s^{-1}}$ for CW); this also results in increased velocities.

The lateral shear stress in the outer region (Fig. 6.25b) is similar for the different cases, except in the alignment of cylinder rows where peak shear stresses are higher for the cases with higher velocities.

Concerning the turbulence intensities (Figs. 6.25c and 6.25d), differences can be observed in the outer region, especially for the longitudinal component; these differences are not correlated with the mean longitudinal velocity but with the turbulence intensity within the mixing layer: for the isolated floodplain (test case WQ15) for which no mixing layer exists and for test case CMWQ26 where the turbulence production in the mixing layer is quite below the other cases, the turbulence intensities are lower. This indicates that the turbulence level in the outer region is still influenced by the mixing layer.

6.8 Force analysis

6.8.1 Equation of momentum

As shown in Chapter 3 the section-averaged momentum equation of the non-uniform compound channel flow in the main channel reads:

$$S_0 = \frac{1}{gH_m}\frac{\partial H_m U_m^2}{\partial x} - \frac{U_{d,int}}{gH_m}\frac{\partial H_m U_m}{\partial x} + \frac{\partial H_m}{\partial x} + \frac{2H_f(\tau_{xy})_{y=y_{int},z>z_{BF},d}}{\rho g H_m B_m} + \frac{(\tau_{xz})_{z=0,w}}{\rho g H_m} + \frac{2z_{BF}(\tau_{xy})_{y=y_{int},z<z_{BF},d}}{\rho g H_m B_m} \tag{6.8}$$

with $\tau_{xy} = -\rho\overline{u'v'}$, $\tau_{xz} = -\rho\overline{u'w'}$ and $U_{d,int} = U_{y=y_{int},d,z>z_{BF}}$.

In Eq. 6.8, the gravitational force (bottom slope) is balanced by (in the order of the terms on the right-hand side of the equation): (1) the longitudinal flux of momentum, (2) the lateral net mass exchange with the floodplains, (3) the longitudinal pressure gradient, (4) the turbulent exchange at the interface, (5) the bed friction, (6) the friction on the lateral walls (beneath the bankfull level).

Similarly, the section-averaged momentum equation in the right-hand floodplain reads (see Chapter 3):

$$S_0 = \frac{1}{gH_f}\frac{\partial H_f U_f^2}{\partial x} - \frac{U_{d,int}}{gH_f}\frac{\partial H_f U_f}{\partial x} + \frac{\partial H_f}{\partial x} - \frac{(\tau_{xy})_{d,y=y_{int},z>z_{BF}}}{\rho g B_f} + \frac{(\tau_{xz})_{z=z_{BF},w}}{\rho g H_f} + \frac{aC_D U_f^2}{2g}. \tag{6.9}$$

The last term on the right-hand side stands for the drag forces of the cylinder array, where a is the frontal area per unit volume ($a = ND$) and C_D is the cylinder drag coefficient.

The longitudinal flux of momentum in Eq. 6.8 or 6.9 can be split into two terms:

$$\frac{1}{gH_i}\frac{\partial H_i U_i^2}{\partial x} = \frac{2U_i}{gH_i}\frac{\partial H_i U_i}{\partial x} - \frac{U_i^2}{gH_i}\frac{\partial H_i}{\partial x} \tag{6.10}$$

with $i \in \{m, f\}$. The first term is the acceleration/deceleration due to positive/negative lateral mass exchange and the second term is the acceleration/deceleration due to the contraction/expansion of the flow through water depth variation. The factor 2 before the first term can be interpreted as follows. Consider a lateral mass transfer without water depth variation: on the one hand the flow has to be "compressed" by the arriving lateral flow, i.e. accelerated in order to let place for the arriving flow; on the other hand, the arriving flow has to be accelerated until the subsection velocity. A similar reasoning can be made for flow leaving the subsection.

When the first term on the right of Eq. 6.10 is combined with the mass exchange term of Eq. 6.8 or 6.9 (first term on the right), the total normalised force exerted by the lateral mass exchange is obtained:

$$A_i = \frac{2U_i - U_{d,int}}{gH_i}\frac{\partial H_i U_i}{\partial x}. \tag{6.11}$$

Term A_i can be split up into two contributions: (1) the acceleration due to flow contraction when fluid enters the subsection (or the deceleration due to flow expansion when fluid

leaves the subsection):

$$A_{c,i} = \frac{U_i}{gH_i}\frac{\partial H_i U_i}{\partial x} \tag{6.12}$$

and (2) the acceleration/deceleration due to the difference between the velocity of the entering/leaving fluid and the subsection-averaged velocity:

$$A_{a,i} = \frac{U_i - U_{d,int}}{gH_i}\frac{\partial H_i U_i}{\partial x}. \tag{6.13}$$

When the velocity of the entering flow $U_{d,int}$ is equal to the mean velocity in the subsection U_i, then $A_i = A_{c,i}$.

As $U_m \geq U_{d,int}$, we have always $2U_m - U_{d,int} \geq 0$. Therefore a mass gain ($\frac{\partial H_m U_m}{\partial x} > 0$) induces a resistance force in the main channel ($A_m > 0$) and a mass loss ($\frac{\partial H_m U_m}{\partial x} < 0$) induces a driving force ($A_m < 0$). For a given fluid transfer direction, the two contributions $A_{c,m}$ and $A_{a,m}$ are of the same sign.

In the floodplain, two cases have to be distinguished: (1) if $2U_f - U_{d,int} \geq 0$, then the mass transfer effect is the same as discussed above for the main channel; (2) If $2U_f - U_{d,int} < 0$, a mass gain induces a driving force ($A_f < 0$) and a mass loss induces a resistance force ($A_f > 0$). As we have $U_f \leq U_{d,int}$, $A_{c,f}$ and $A_{a,f}$ are of opposite sign and the two contributions partly cancel each other.

The second term on the right-hand side of Eq. 6.10 can be combined with the pressure term of Eqs. 6.8 and 6.9:

$$D_i = \left(1 - \frac{U_i^2}{gH_i}\right)\frac{\partial H_i}{\partial x} \tag{6.14}$$

Term D_i has two contributions: the longitudinal pressure gradient:

$$D_{p,i} = \frac{\partial H_i}{\partial x} \tag{6.15}$$

and the vertical flow contraction due to water depth variation:

$$D_{c,i} = -\frac{U_i^2}{gH_i}\frac{\partial H_i}{\partial x}. \tag{6.16}$$

The latter is related to the subsection Froude number: $D_{c,i} = -Fr_i^2 D_{p,i}$.

Equations 6.8 and 6.9 can then be rewritten:

$$S_0 = A_i + D_i + E_i + F_i + G_i \tag{6.17}$$

where term A_i is the total force due to mass exchange defined by Eq. 6.11, term D_i is the total force due to water depth gradient defined by Eq. 6.14, term E_i is the turbulent exchange at the interface, defined by:

$$E_m = \frac{2H_f(\tau_{xy})_{y=y_{int},z>z_{BF},d}}{\rho g H_m B_m} \tag{6.18}$$

$$E_f = -\frac{(\tau_{xy})_{d,y=y_{int},z>z_{BF}}}{\rho g B_f}, \tag{6.19}$$

term F_i is the bed and wall friction, defined by:

$$F_m = \frac{(\tau_{xz})_{z=0,w}}{\rho g H_m} + \frac{2z_{BF}(\tau_{xy})_{y=y_{int},z<z_{BF},d}}{\rho g H_m B_m} \tag{6.20}$$

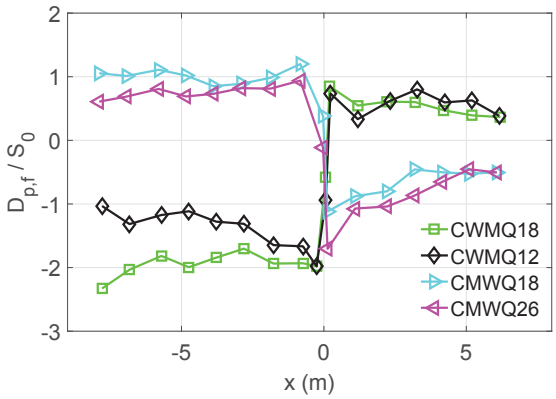

Figure 6.26: Longitudinal variation in longitudinal pressure gradient (Eq. 6.15), normalised by bottom slope.

$$F_f = \frac{(\tau_{xz})_{z=z_{BF},w}}{\rho g H_f} \tag{6.21}$$

and term G_i is the cylinder drag force, defined by:

$$G_m = 0 \tag{6.22}$$

$$G_f = \frac{aC_D U_f^2}{2g}. \tag{6.23}$$

Thereafter the terms D_i, A_i and E_i are analysed separately. Finally, the different terms in Eq. 6.17 are compared together in a force balance. The terms are normalised by the bottom slope S_0 in order to assess their relative weights compared to the gravitational force.

All terms in Eq. 6.17 could be directly measured, except the bed friction $(\tau_{xz})_{w,z=0}$ that was calculated using the logarithmic law in the main channel and using a Manning formula in the floodplain.

6.8.2 Effect of water depth variations

The two forces induced by water depth variations, the pressure forces $D_{p,i}/S_0$ and the vertical compression force $D_{c,i}/S_0$ are shown in Figs. 6.26 and 6.27 respectively. As no lateral gradient of free surface elevation are detected, the pressure forces are the same in main channel and floodplain ($D_{p,m} = D_{p,f}$). The pressure forces are up to two times greater than the gravitational force.

The vertical compression force $D_{c,i}$ is important only for sufficiently high values of subsection Froude numbers ($Fr_i > 0.3$, see Table 6.1). This force is important for the wood-to-meadow transition in the main channel and is otherwise rather small.

6.8.3 Effect of mass exchange

Figure 6.28 shows the two forces induced by mass exchange, the acceleration due to flow contraction $A_{c,i}/S_0$ and the acceleration due to the difference between the velocity of the entering/leaving fluid and the subsection-averaged velocity $A_{a,i}/S_0$, together with the sum of these two forces A_i/S_0, in the main channel and in the floodplain.

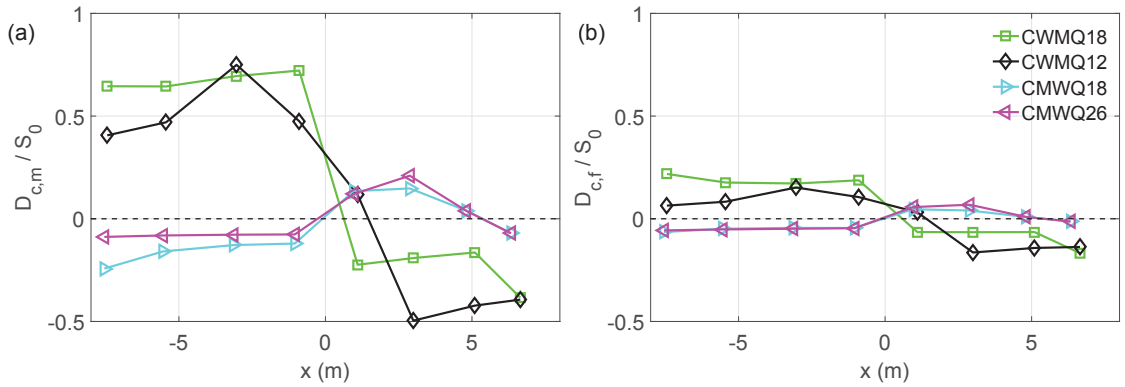

Figure 6.27: Compression force due to water depth variation (Eq. 6.15), (a) in the main channel and (b) in the floodplain.

The two forces $A_{c,i}$ and $A_{a,i}$ are on the same order of magnitude. As stated in Section 6.8.1 they are of the same sign in the main channel and of opposite sign in the floodplain. As a result, they add each other in the main channel, which results in an important total force A_m that is up to twice the gravitational force; and they cancel each other in the floodplain, resulting in a very small force A_f. Force A_f is resistant when mass enters in the floodplain, as we are in the case $2U_f - U_{d,int} \geq 0$ (see Section 6.8.1).

6.8.4 Turbulent exchange

Figure 6.29a shows the normalised turbulent exchange term in the floodplain $E_f/S_0 = -\overline{u'v'}_{d,int}/(gB_fS_0)$. The shear force at the interface is 10 to 100 % of the bottom slope, depending on flow conditions.

The modelling of the turbulent exchange is one of the most difficult issue in compound channel numerical models. Figure 6.29b shows the lateral Reynolds stresses at the interface normalised by the depth-averaged velocity at the interface $U_{d,int}$. The ratio $\overline{u'v'}_{d,int}/U^2_{d,int}$ appears to be rather constant and little dependent on flow conditions for a given roughness type. This ratio is much higher for the wooded floodplain ($\overline{u'v'}_{d,int}/U^2_{d,int}$ = 0.040-0.050) than for the grassed floodplain ($\overline{u'v'}_{d,int}/U^2_{d,int}$ = 0.005-0.015). An adjustment length downstream of the transition is necessary to reach the level related to the downstream roughness. Similarly to the normalised turbulence intensities (Fig. 6.24), this adjustment length is higher for the wood-to-meadow ($\approx$ 6 m) than for the meadow-to-wood transition ($\approx$ 4 m).

In several 1D numerical models (Bousmar and Zech, 1999; Proust *et al.*, 2009) the lateral shear stresses at the interface are modelled with $\overline{u'v'}_{d,int} = \Psi_t(U_m - U_f)^2$, where Ψ_t is a calibrating parameter that is assumed to be constant. Figure 6.30 shows the ratio $\overline{u'v'}_{d,int}/(U_m - U_f)^2$ for the different test cases. If the upstream flow development of test case CM is not taken into account, the ratio varies between 0.013 and 0.034 for all flow cases. The mean value is close to that used by Proust *et al.* (2009), i.e. $\Psi_t = 0.020$. However, similarly to ratio $\overline{u'v'}_{d,int}/U^2_{d,int}$, ratio Ψ_t seems to be specific for a roughness type: $\Psi_t \approx 0.017$ for grassed floodplains and $\Psi_t \approx 0.025$ for wooded floodplains.

6.8.5 Force balance

Figure 6.31 shows the different terms on the right-hand side of Eq. 6.17, which represents the force balance in the main channel or in the floodplain, for all roughness transition

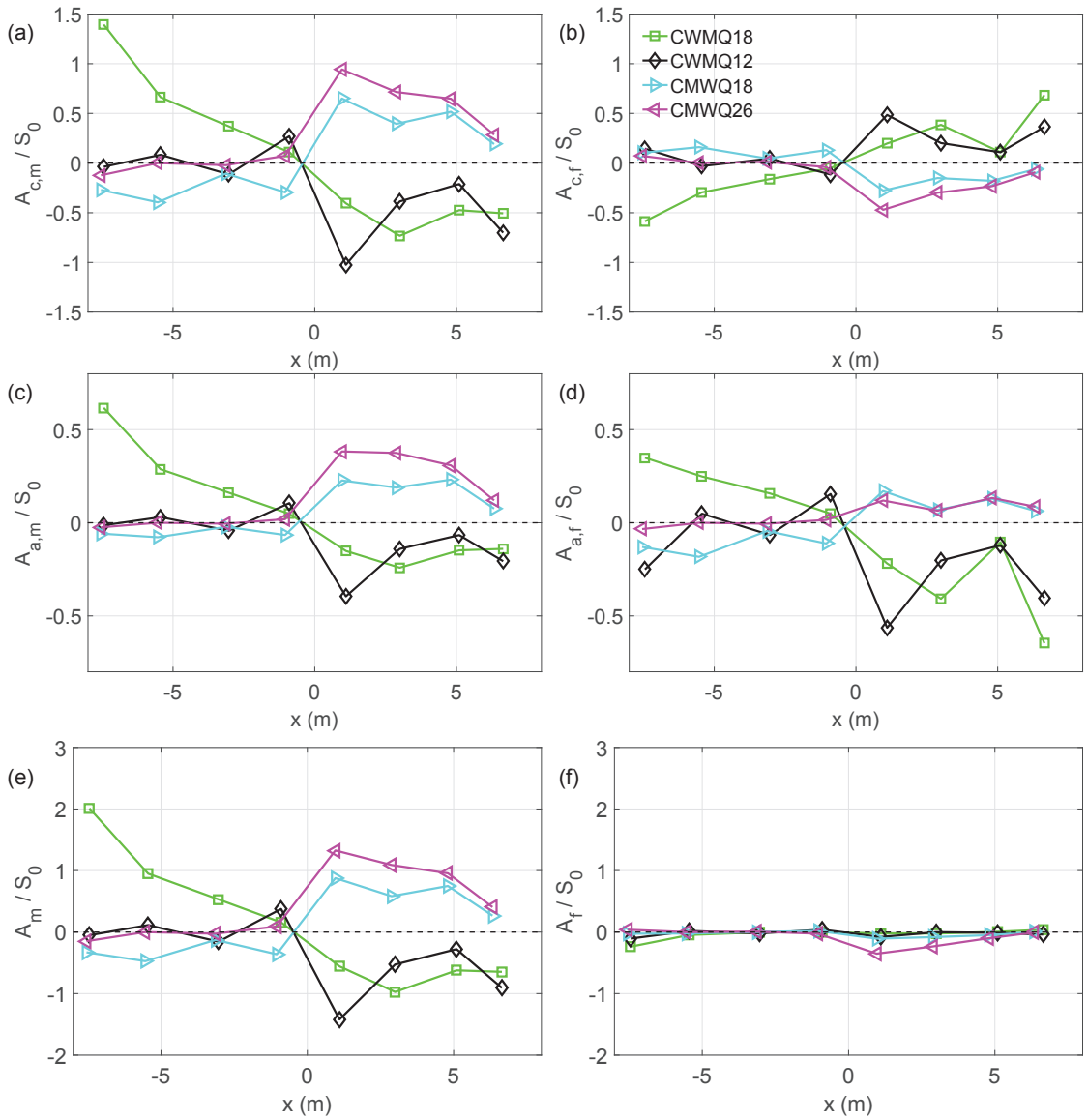

Figure 6.28: (a-b) Compression force due to mass exchange (Eq. 6.12), (c-d) acceleration due to mass exchange (Eq. 6.13), (e-f) total force due to mass exchange (Eq. 6.11) in the main channel (left panels) and in the floodplain (right panels).

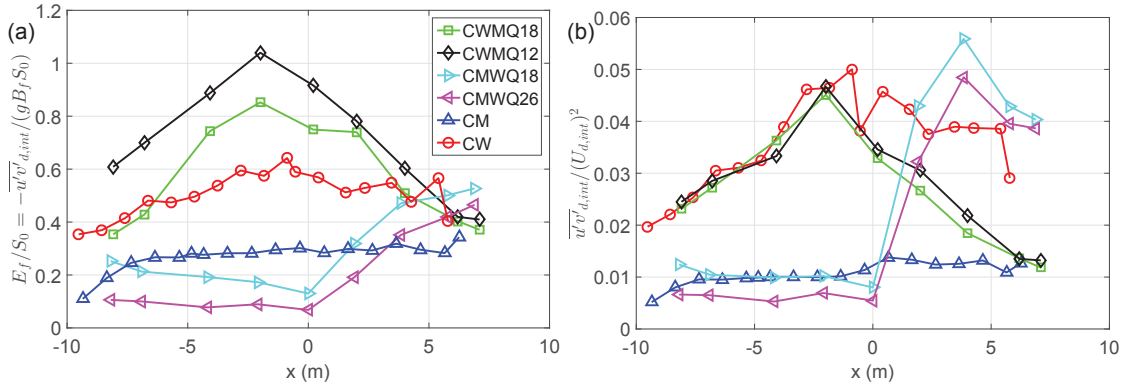

Figure 6.29: (a) Normalised lateral shear forces at the interface (Eq. 6.19). (b) Depth-averaged lateral Reynolds stresses at the interface normalised by $U_{d,int}$.

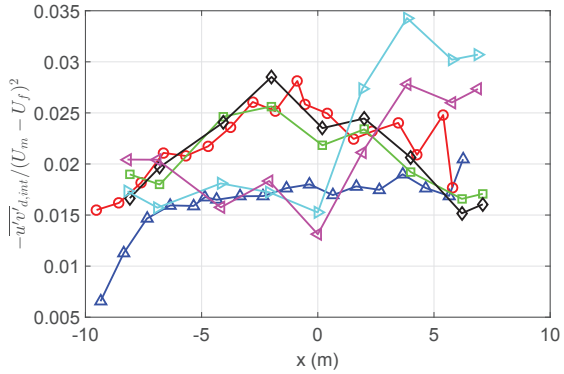

Figure 6.30: Lateral Reynolds stresses at the interface normalised by the bulk velocity difference between subsections $U_m - U_f$. Same legend as is Fig. 6.29.

test cases. The different terms are normalised by the bottom slope. Resistance forces are positive and driving forces are negative in the diagrams. Also shown is the unbalanced rest of the equation (thus, the sum of the contributions including the rest is equal to 1). Although the rest is not always negligible, it remains small for all cases. The rest is due partly to the assumptions made for Eqs. 6.8 and 6.9 and partly to experimental inaccuracies.

The force due to mass exchange A_m and the force due to water depth gradient D_m partly compensate each other in the main channel. This is not the case in the floodplain, where A_f and D_f are of the same sign and contribute to counterbalance the drag forces. The drag forces for the roughness transition test cases are indeed much higher than for the uniform test case CW (for the latter the cylinder drag term is close to the bottom slope).

6.8.6 Comparison with the isolated floodplain

Figure 6.32 shows the force balance in the floodplain (Eq. 6.17) for the wood-to-meadow test case CWMQ12 and the meadow-to-wood test case CMWQ18, along with the force balance for the same roughness transitions in an isolated floodplain, i.e. in single channel, for close discharge values. The single channel experiments are taken from Chapter 4 (test cases WMQ7 and MWQ21). For the isolated floodplain, we have $A_f = 0$ and $E_f = 0$.

Due to the absence of water depth variation, term D_f is nearly zero downstream of the transition for the isolated floodplain, whereas for the main-channel-influenced-floodplain, term D_f is one of the most dominant term downstream of the transition.

The drag forces are much higher for the main-channel-influenced-floodplain than for the isolated floodplain (about two times higher) for the meadow-to-wood transition. Indeed, although the discharge are similar for test cases MWQ21 and CMWQ18 in the wooded area (downstream of the transition), water depths are very different ($\approx 152\,$mm for MWQ21 and $\approx 102\,$mm for CMWQ18). This results in higher bulk velocities in the cylinder array ($\approx 13.8\,\mathrm{cm.s^{-1}}$ for MWQ21 and $\approx 20\,\mathrm{cm.s^{-1}}$ for CMWQ18) and therefore higher drag forces for test case CMWQ18.

For the wood-to-meadow transition, water depth and bulk velocities in the cylinder array are similar for the main-channel-influenced and the isolated floodplains. Therefore drag forces are comparable (the difference in drag forces between WMQ7 and CWMQ12 can be mostly attributed to the difference in discharge value).

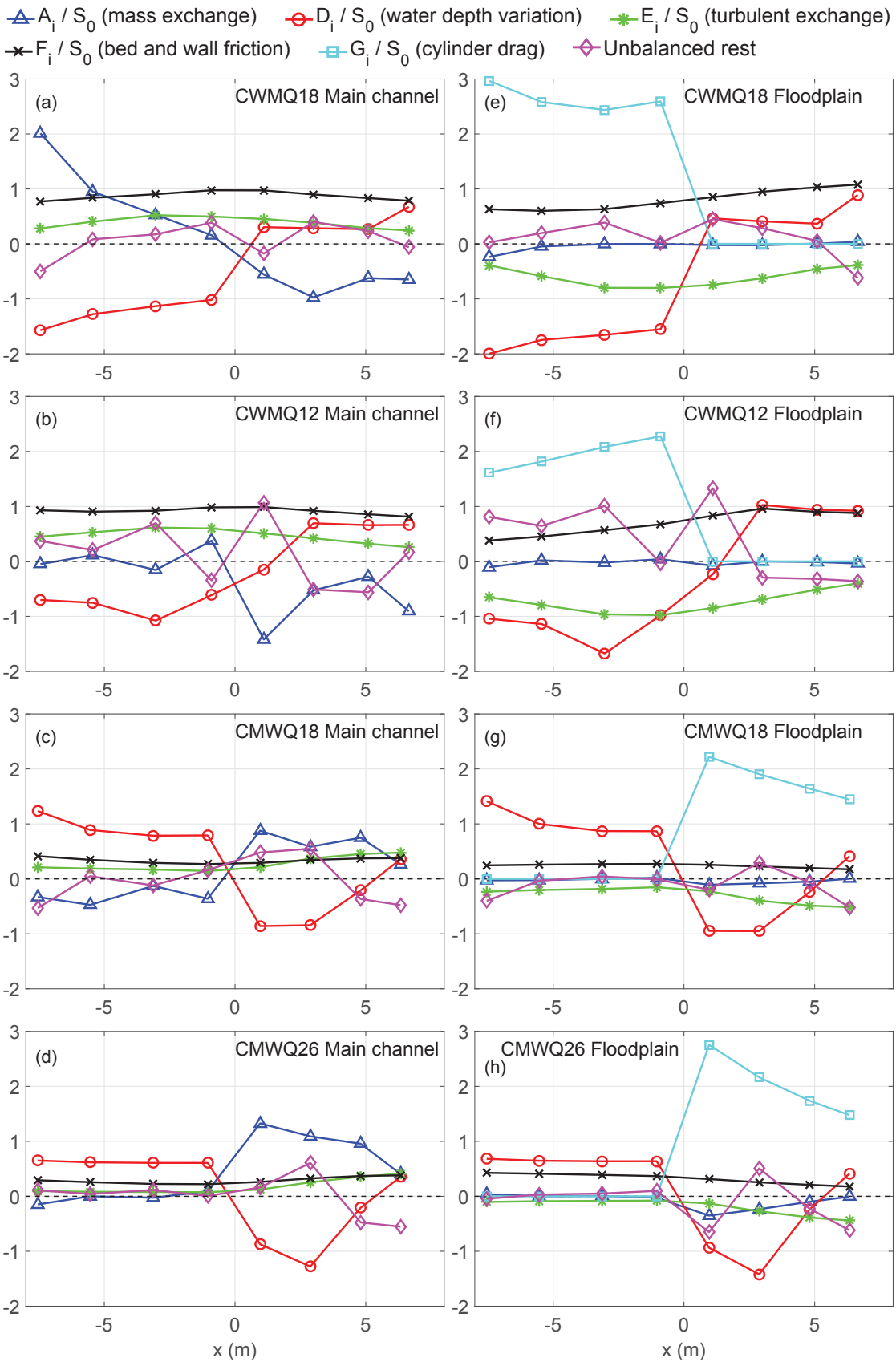

Figure 6.31: Longitudinal evolution of the different terms of Eq. 6.17, normalised by the bottom slope (a-d) in the main channel and (e-h) in the floodplain, for the different roughness transition test cases.

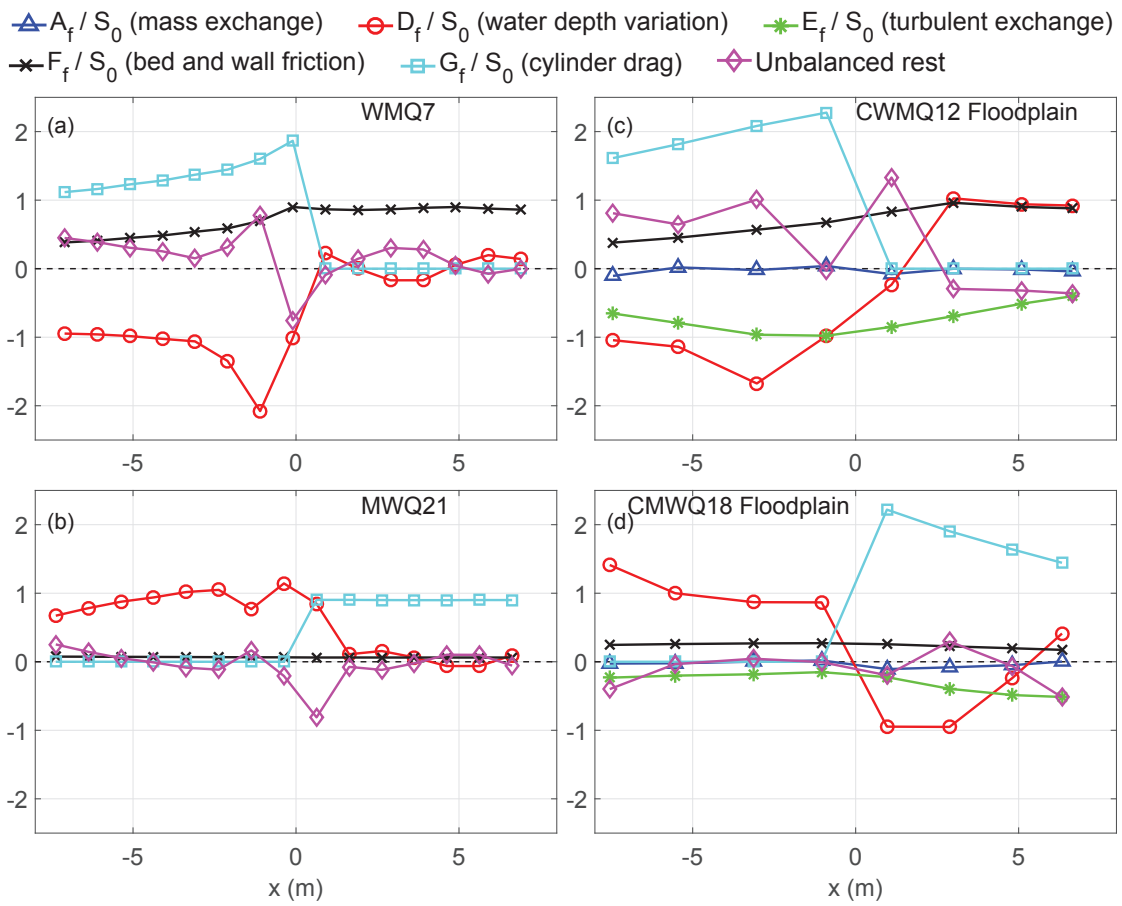

Figure 6.32: Comparison of force balance between (a-b) isolated floodplains and (c-d) main-channel-influenced-floodplains.

6.9 Conclusion

Compound channel flows were experimentally investigated with a longitudinal roughness transition on the floodplains between a bed roughness, modelled by a plastic grass (meadow), and emergent macro-roughnesses, modelled by an array of emergent cylinders installed on a rough bed (wooded area), and *vice versa*. The flows with a transition in roughness were compared to uniform compound channel flows with only grassed or only wooded floodplains.

Unlike flows in single channel, the longitudinal transition in roughness in compound channel induced water depth gradients both upstream and downstream of the change in roughness. Moreover, an inversion of water depth gradient was observed at the transition.

The mixing layer was not self-similar at constant elevation, indicating that the roughness transition induced a flow disequilibrium both downstream and upstream of the change in roughness. Lateral mass transfers seemed to be partly responsible for the absence of self-similarity.

The longitudinal length scale of the coherent structures scaled with the total mixing layer width. Two different processes were identified in the coherent structure dynamics: vortex merging and/or fluid entrainment was responsible for the overall growth of the structures all along the flume and a process conserving angular momentum (vortex stretching), was additionally involved downstream of the transition in order to adapt (increase or decrease) the structure size to the new flow conditions.

The total force induced by the mass transfers was important in the main channel but negligible in the floodplain. In the latter, the two contributions of the mass transfers in the force balance, i.e. flow contraction and the effect of the difference between the velocity of the entering/leaving fluid and the subsection-averaged velocity, cancelled each other.

Compound channel flows with either grassed or wooded floodplains featured specific flow structures:

- The mixing layer widths on the main channel and on the floodplain side were normalised by the floodplain water depth and by the normalised velocity difference. The normalised widths on both sides of the mixing layer were about three times higher for reaches with grassed floodplains than with wooded floodplains. This could be related to the obstruction caused by the cylinder array.

- The normalised shear stress at the interface was about three times higher for the wooded floodplain than for the grassed floodplain.

- The secondary currents in the main channel were more intense with wooded floodplains than with grassed floodplains. This could be related to the different cross-sectional distribution of the turbulence anisotropy.

Downstream of the roughness transition, an adjustment length was required before the flow features related to the new roughness were observed. This adjustment length was larger for the wood-to-meadow than for the meadow-to-wood transition.

Chapter 7

Conclusion

The present work experimentally investigated the effects of a longitudinal change in floodplain vegetation on overflooding river flows. Two types of vegetation were chosen: a highly submerged dense meadow, modelled by a plastic grass and hydraulically equivalent to a bed roughness, and a woodland, represented by an array of emergent cylinders and corresponding to emergent macro-roughnesses. The flows were investigated either in a single channel, i.e. in the case of a floodplain isolated from the main channel, or in a compound channel configuration, for which the floodplains were interacting with the main channel. For each channel geometry (single or compound section), the flows were first investigated over each roughness type uniformly distributed along the channel. Then, the longitudinal transitions from meadow to wood and from wood to meadow were studied.

7.1 Flows with uniformly distributed roughness

7.1.1 Longitudinal flow development

The floodplain flow development was found to be significantly longer in a compound channel configuration than in an isolated floodplain. This was due to the slow lateral development of the mixing layer when going downstream. The compound channel mixing layer extended asymmetrically towards the main channel and towards the floodplain. We therefore separated the mixing layer width on the main channel side and on the floodplain side. The mixing layer width stabilised earlier in the floodplain than in the main channel because of shallowness effects, or because of the presence of the cylinder array that constrained the lateral penetration of the mixing layer.

The development towards uniformity of the compound channel mixing layer was characterised by self-similarity of the mean longitudinal velocity and of the turbulence quantities at a constant elevation, when the lateral coordinate was scaled by the mixing layer widths in the main channel or in the floodplain on either side of the interface.

7.1.2 Flow through a cylinder array

The flow through an array of emergent cylinders was investigated in detail in the case of a single channel. The water column could be divided into a constant-velocity region and a boundary layer in the near-bed region. In-line with a cylinder row, the boundary layer height was independent of water depth and of bed surface condition (rough or smooth). A local increase in the longitudinal velocity within the boundary layer (resulting in a velocity bulge in the vertical profile) was observed. This velocity bulge has been related to the effect of bed-induced turbulence. The latter disorganizes the von Kármán vortex street, resulting in a smaller drag force and less momentum loss in the cylinder wake.

A constant-velocity region was also observed within the cylinder array in compound channel configuration. However, the near-bed region was not investigated in detail. Similarly to the single channel case, the cylinder array homogenised the flow in the vertical direction.

Coherent free surface oscillations (seiching) were observed through the cylinder array in single channel configuration. Several hours were required to achieve constant amplitude oscillations. The amplitude was found to be dependent on the longitudinal position within the array with a peak value at its mid-length. Furthermore, the seiching decreased with a decreasing array length. The seiche driving forces, i.e. the periodic lift forces associated to the vortex street, were found to be only acting in the constant-velocity region, whereas they were prevented in the boundary layer because of the disorganization of the von Kármán vortex street. Therefore, if the water depth/boundary layer height ratio was close to unity, no seiche appeared. The absence of seiching in the compound channel experiments pointed out that lateral confinement of the flow is a necessary condition for seiching.

7.1.3 Interaction between main channel flow and floodplain flow

The momentum exchange between main channel and floodplain under uniform flow conditions was only attributed to the mixing layer turbulence, whereas the contribution of the secondary currents appeared to be negligible. The secondary currents merely redistributed mass and momentum within each subsection. The contour lines of the longitudinal velocity were directly linked to the secondary currents pattern and to the cross-sectional distribution of the lateral Reynolds stresses. The secondary currents in the main channel and the lateral shear stresses at the main channel/floodplain interface were enhanced in the case of wooded floodplains compared to grassed floodplains.

Turbulent coherent structures in the form of a succession of large sweep and ejection events were observed in the compound channel mixing layer. The phase velocity of the coherent structures could be fairly approximated by the depth-averaged longitudinal velocity at the main channel/floodplain interface. The coherent structures spanned the entire floodplain flow depth. Important differences were observed between the coherent fluctuations of the longitudinal and the lateral velocities, particularly in terms of longitudinal size, of lateral extend and of shape of the propagating wave front. The wave front of the coherent fluctuations globally propagated with a phase advance in the upper water column relative to the lower water column. A phase lag was also observed laterally, with a phase advance on both sides of the mixing layer, relative to the main channel/floodplain interface.

Compared to the isolated floodplain, the conveyance capacity of the main-channel-influenced-floodplain was much more increased in the case of a grassed floodplain (+12.5 %) than for a wooded floodplain (+2.9 %). For the wooded floodplain, the flow acceleration by the main channel in the interface region was counterbalanced by higher drag forces in the cylinder array due to important lateral velocity components (related to the mixing layer coherent structures) that were not present in the isolated floodplain.

7.2 Flows with a longitudinal transition in roughness

7.2.1 Variation in water depth

According to the backwater effect for subcritical 1D flows, water depth varied only upstream of the change in roughness in single channel (isolated floodplain). A 1D momentum

equation including a volume drag force was used to predict the water depth profile with a mean error of 0.9 %. This equation was also used to calculate the distance upstream of the transition to reach equilibrium. This distance was three orders of magnitude higher than the uniform flow depth of the upstream roughness. The momentum equation was analytically solved for zero bed friction.

According to the double influence of the downstream and upstream boundary conditions for compound channel flows, water depth variations were observed both upstream and downstream of the change in roughness. An inversion of longitudinal water depth gradient occurred at the roughness transition. The longitudinal water depth profile was sensitive to the upstream discharge distribution between subsections, an increase in floodplain discharge increasing the free-surface level, for a fixed total discharge.

7.2.2 Mean velocity and turbulence field

In single channel configuration, the vertical distribution of mean velocity and turbulence quantities was found to be self-similar upstream of the change in roughness. Downstream of the change in roughness, mass and momentum were redistributed across the water column within an adjustment length of the order of 35-50 times the water depth, such that the flow field adapted to the new roughness. In compound channel configuration, no flow self-similarity was observed, indicating that the roughness transition led to flow disequilibrium both upstream and downstream of the change in roughness. The absence of self-similarity was partly related to the effect of the lateral mass transfers.

Secondary currents and normalised turbulence quantities appeared to be specific for a given floodplain roughness. In particular, the normalised lateral shear stresses at the main channel/floodplain interface were about three times higher for the wooded floodplain than for the grassed floodplain. As in single channel configuration, an adjustment length was required downstream of the roughness transition before the flow features related to the new roughness were observed. This adjustment length was larger for the wood-to-meadow than for the meadow-to-wood transition.

7.2.3 Mixing layer dynamics

Mixing layer widths were normalised by the floodplain water depth and by the dimensionless velocity difference. The normalised values of mixing layer widths on both main channel side and floodplain side appeared to be specific to a given floodplain roughness, with value three times larger for the grassed floodplain than for the wooded floodplain. This difference was attributed to the obstruction effect of the cylinder array.

The longitudinal length scale of the coherent structures scaled with the total mixing layer width. Two different processes were identified in the coherent structure dynamics: a process for which angular momentum increases when going downstream (vortex merging, fluid entrainment) drove structure dynamics upstream of the roughness transition and a process conserving angular momentum (e.g. vortex stretching) drove structure dynamics downstream of the transition.

7.2.4 Force balance

The equation of momentum was rewritten in order to isolate the effect of the lateral mass exchange between subsections, the effect of variations in water depth and the effect of turbulent exchange between subsections. The total force exerted by mass transfers was important in the main channel but negligible in the floodplain. In the latter, the two contributions of the mass transfers in the force balance, i.e. flow contraction and the effect

of the difference between the velocity of the entering/leaving fluid and the subsection-averaged velocity, cancelled each other.

7.3 Perspectives for future research

The present study brought to light some characteristics of the compound channel mixing layer development, like the self-similarity property, but failed to observe a fully uniform flow in the main channel. The development towards uniformity of the compound channel flow might have been faster if the main channel was narrower. A narrower main channel would also enable an interaction between the two opposite right-bank and left-bank mixing layers, particularly a synchronisation of the coherent fluctuations. In the present experiments the two opposite mixing layers were fully decorrelated.

The secondary currents appeared to largely determine the cross-sectional distribution of momentum. A better comprehension of the secondary current generation mechanisms requires the knowledge of the fine-scale spatial distribution of the turbulence intensities, which is experimentally difficult to obtain. A numerical approach would probably be helpful, but it requires numerical models that allow at least turbulence anisotropy (e.g. LES, DNS).

We showed in the present study that the coherent structures associated with the compound channel mixing layer propagate with phase lags in the vertical and lateral directions. However, we do not give the origin and the physical mechanisms that are responsible for these phase lags. Another surprising result was the important differences that were observed between the coherent fluctuations associated with the longitudinal and the lateral velocities. In the same way, a physical explanation of this fact must be found. Coherent structures, that are mainly considered as a material entity, appeared to have important wave-like properties. Fine resolved space-time measurements, like those provided by a PIV system, could help to better understand the spatial organisation and the mechanisms that drive the coherent structures.

The present study only considered a cylinder array with a regular arrangement. It would be useful to investigate the effect of a randomly distributed cylinder array, in particular on the velocity bulge phenomenon and on the mixing layer dynamics. In particular, we can wonder if the mixing layer coherent structures are sensitive to the cylinder array arrangement.

Bibliography

Antonia RA and Luxton RE. The response of a turbulent boundary layer to a step change in surface roughness Part 1. Smooth to rough. *Journal of Fluid Mechanics*, 48 (04):721–761, 1971.

Batchelor George K. Computation of the energy spectrum in homogeneous two-dimensional turbulence. *Physics of Fluids (1958-1988)*, 12(12):II–233, 1969.

Bell James H and Mehta Rabindra D. Development of a two-stream mixing layer from tripped and untripped boundary layers. *AIAA journal*, 28(12):2034–2042, 1990.

Bernal LP and Roshko A. Streamwise vortex structure in plane mixing layers. *Journal of Fluid Mechanics*, 170:499–525, 1986.

Blanckaert Koen, Duarte A, and Schleiss AJ. Influence of shallowness, bank inclination and bank roughness on the variability of flow patterns and boundary shear stress due to secondary currents in straight open-channels. *Advances in Water Resources*, 33(9): 1062–1074, 2010.

Bousmar D, Proust S, and Zech Y. Experiments on the flow in a enlarging compound channel. Dans *River Flow 2006: Proceedings of the International Conference on Fluvial Hydraulics, Lisbon, Portugal, 6–8 September 2006*, pages 323–332, 2006.

Bousmar Didier and Zech Yves. Momentum transfer for practical flow computation in compound channels. *Journal of hydraulic engineering*, 125(7):696–706, 1999.

Bousmar Didier, Wilkin N, Jacquemart J-H, and Zech Yves. Overbank flow in symmetrically narrowing floodplains. *Journal of hydraulic engineering*, 130(4):305–312, 2004.

Bousmar Didier, Riviere N, Proust S, Paquier A, Morel R, and Zech Yves. Upstream discharge distribution in compound-channel flumes. *Journal of Hydraulic Engineering*, 131(5):408–412, 2005.

Bradshaw Peter. Turbulent secondary flows. *Annual review of fluid mechanics*, 19(1): 53–74, 1987.

Brown Garry L and Roshko Anatol. On density effects and large structure in turbulent mixing layers. *Journal of Fluid Mechanics*, 64(04):775–816, 1974.

Carravetta A and Della Morte R. Response of velocity to a sudden change of bed roughness in sub critical open channel flow. Dans *River Flow 2004: Proceedings of the Second International Conference on Fluvial Hydraulics, 23-25 June 2004, Napoli, Italy, Two Volme Set*, page 389. CRC Press, 2004.

Chanson Hubert, Trevethan Mark, and Koch Christian. Discussion of "Turbulence measurements with acoustic Doppler velocimeters" by C. M. García, M. I. Cantero, Y. Niño, and M. H. García. *Journal of Hydraulic Engineering*, 133(11):1283–1286, 2007.

Chen Xingwei and Chiew Yee-Meng. Response of velocity and turbulence to sudden change of bed roughness in open-channel flow. *Journal of Hydraulic Engineering*, 129 (1):35–43, 2003.

Chen Xingwei and Chiew Yee-Meng. Closure to "response of velocity and turbulence to sudden change of bed roughness in open-channel flow" by xingwei chen and yee-meng chiew. *Journal of Hydraulic Engineering*, 130(6):589–590, 2004.

Cheng H and Castro Ian P. Near-wall flow development after a step change in surface roughness. *Boundary-Layer Meteorology*, 105(3):411–432, 2002.

Chu Vincent H and Babarutsi Sofia. Confinement and bed-friction effects in shallow turbulent mixing layers. *Journal of hydraulic engineering*, 114(10):1257–1274, 1988.

Defina Andrea and Pradella Irene. Vortex-induced cross-flow seiching in cylinder arrays. *Advances in Water Resources*, 71:140–148, 2014.

Dupuis Victor, Proust Sébastien, Berni Céline, Paquier André, and Thollet Fabien. Open-channel flow over longitudinal roughness transition from highly-submerged to emergent vegetation. *36th IAHR World Congress, The Hague*, 2015.

Dupuis Victor, Proust Sébastien, Berni Céline, and Paquier André. Combined effects of bed friction and emergent cylinder drag in open channel flow. *Environmental Fluid Mechanics*, pages 1–21, 2016.

Einstein HoA and Li Huon. Secondary currents in straight channels. *Eos, Transactions American Geophysical Union*, 39(6):1085–1088, 1958.

Elliott SCA and Sellin RHJ. Serc flood channel facility: skewed flow experiments. *Journal of Hydraulic Research*, 28(2):197–214, 1990.

Fernandes JN. *Compound Channel Uniform and Non-Uniform Flows With and Without Vegetation in the Floodplain*. PhD thesis, Ph. D. thesis Departamento de Engenharia Civil. Instituto Superior Técnico da Universidade Técnica de Lisboa, 2013.

Fjortoft Ragnar. Application of integral theorems in deriving criteria of stability for laminar flows and for the baroclinic circular vortex. *Geofys. Publ*, 17(6):1–52, 1950.

George William K. Is there a universal log law for turbulent wall-bounded flows? *Philosophical Transactions of the Royal Society of London A: Mathematical, Physical and Engineering Sciences*, 365(1852):789–806, 2007.

Ghomeshi Mehdi, Mortazavi-Dorcheh Saied Ahmad, and Falconer Roger. Amplitude of wave formation by vortex shedding in open channels. *Journal of Applied Sciences*, 7: 3927–3934, 2007.

Goring Derek G and Nikora Vladimir I. Despiking acoustic Doppler velocimeter data. *Journal of Hydraulic Engineering*, 128(1):117–126, 2002.

Graf Walter H and Altinakar Mustafa S. *Fluvial hydraulics*. Wiley, 1998.

Gray William G and Lee PCY. On the theorems for local volume averaging of multiphase systems. *International Journal of Multiphase Flow*, 3(4):333–340, 1977.

Ho Chih-Ming and Huerre Patrick. Perturbed free shear layers. *Annual Review of Fluid Mechanics*, 16(1):365–422, 1984.

Jafari Ahmad, Ghomeshi Mehdi, Bina Mahmood, and Kashefipour Seyed Mahmood. Experimental study on ten modes of transverse waves due to vertical cylinders in open channels. *Journal of Food, Agriculture & Environment*, 8(2):949–955, 2010.

Jahra Fatima, Kawahara Yoshihisa, Hasegawa Fumiaki, and Yamamoto Hiroyuki. Flow–vegetation interaction in a compound open channel with emergent vegetation. *International journal of river basin management*, 9(3-4):247–256, 2011.

Kara Sibel, Stoesser Thorsten, and Sturm Terry W. Turbulence statistics in compound channels with deep and shallow overbank flows. *Journal of Hydraulic Research*, 50(5): 482–493, 2012.

Kironoto BA and Graf Walter Hans. Turbulence characteristics in rough uniform open-channel flow. *Proceedings of the ICE-Water Maritime and Energy*, 106(4):333–344, 1994.

Knight Donald W and Demetriou John D. Flood plain and main channel flow interaction. *Journal of Hydraulic Engineering*, 109(8):1073–1092, 1983.

Knight DW and Shiono K. Turbulence measurements in a shear layer region of a compound channel. *Journal of hydraulic research*, 28(2):175–196, 1990.

Kothyari Umesh C, Hayashi Kenjirou, and Hashimoto Haruyuki. Drag coefficient of unsubmerged rigid vegetation stems in open channel flows. *Journal of Hydraulic Research*, 47(6):691–699, 2009.

Kozioł AP. Three-dimensional turbulence intensity in a compound channel. *Journal of Hydraulic Engineering*, 139(8):852–864, 2013.

Lienhard John H. *Synopsis of lift, drag, and vortex frequency data for rigid circular cylinders*. Technical Extension Service, Washington State University, 1966.

Liu D, Diplas P, Fairbanks JD, and Hodges CC. An experimental study of flow through rigid vegetation. *Journal of Geophysical Research: Earth Surface (2003–2012)*, 113(F4), 2008.

Lukowicz Joachim von. *Zu kohärenten Turbulenzstrukturen in der Strömung gegliederter Gerinne*. PhD thesis, RWTH Aachen, 2002.

Martino R, Paterson A, and Piva M. Double-average mean flow and local turbulence intensity profiles from PIV measurements for an open channel flow with rigid vegetation. *Environmental Fluid Mechanics*, 12(1):45–62, 2012.

Moore DW and Saffman PG. The density of organized vortices in a turbulent mixing layer. *Journal of Fluid Mechanics*, 69(03):465–473, 1975.

Nepf HM. Drag, turbulence, and diffusion in flow through emergent vegetation. *Water Resources Research*, 35(2):479–489, 1999.

Nezu I and Nakagawa H1. Turbulence in open channels. *IAHR/AIRH Monograph. Balkema, Rotterdam, The Netherlands*, 1993.

Nezu Iehisa and Nakayama Tadanobu. Space-time correlation structures of horizontal coherent vortices in compound open-channel flows by using particle-tracking velocimetry. *Journal of Hydraulic Research*, 35(2):191–208, 1997.

Nezu Iehisa and Rodi Wolfgang. Open-channel flow measurements with a laser Doppler anemometer. *Journal of Hydraulic Engineering*, 112(5):335–355, 1986.

Nikora Vladimir, Goring Derek, McEwan Ian, and Griffiths George. Spatially averaged open-channel flow over rough bed. *Journal of Hydraulic Engineering*, 127(2):123–133, 2001.

Nikora Vladimir, McEwan Ian, McLean Stephen, Coleman Stephen, Pokrajac Dubravka, and Walters Roy. Double-averaging concept for rough-bed open-channel and overland flows: Theoretical background. *Journal of Hydraulic Engineering*, 133(8):873–883, 2007.

Nikora Vladimir, Ballio Francesco, Coleman Stephen, and Pokrajac Dubravka. Spatially averaged flows over mobile rough beds: Definitions, averaging theorems, and conservation equations. *Journal of Hydraulic Engineering*, 139(8):803–811, 2013.

Olsen Michael G and Dutton J Craig. Stochastic estimation of large structures in an incompressible mixing layer. *AIAA journal*, 40(12):2431–2438, 2002.

Oster D and Wygnanski I. The forced mixing layer between parallel streams. *Journal of Fluid Mechanics*, 123:91–130, 1982.

Pasche Erik and Rouvé G1. Overbank flow with vegetatively roughened flood plains. *Journal of Hydraulic Engineering*, 111(9):1262–1278, 1985.

Peltier Yann. *Physical modelling of overbank flows with a groyne set on the floodplain.* PhD thesis, Université de Lyon, 2011.

Peltier Yann, Proust Sebastien, Riviere Nicolas, Paquier Andre, and Shiono Koji. Turbulent flows in straight compound open-channel with a transverse embankment on the floodplain. *Journal of Hydraulic Research*, 51(4):446–458, 2013.

Pendergrass William and Arya SPS. Dispersion in neutral boundary layer over a step change in surface roughness—I. Mean flow and turbulence structure. *Atmospheric Environment (1967)*, 18(7):1267–1279, 1984.

Poggi Davide, Porporato Amilcare, Ridolfi Luca, Albertson JD, and Katul GG. The effect of vegetation density on canopy sub-layer turbulence. *Boundary-Layer Meteorology*, 111 (3):565–587, 2004.

Proust S, Rivière Nicolas, Bousmar Didier, Paquier A, Zech Yves, and Morel R. Flow in compound channel with abrupt floodplain contraction. *Journal of hydraulic engineering*, 132(9):958–970, 2006.

Proust Sébastien, Bousmar Didier, Riviere Nicolas, Paquier André, and Zech Yves. Nonuniform flow in compound channel: A 1-d method for assessing water level and discharge distribution. *Water resources research*, 45(12), 2009.

Proust Sebastien, Fernandes Joao N, Peltier Yann, Leal Joao B, Riviere Nicolas, and Cardoso Antonio H. Turbulent non-uniform flows in straight compound open-channels. *Journal of Hydraulic Research*, 51(6):656–667, 2013.

Proust Sebastien, Fernandes Joao N, Leal Joao B, Riviere Nicolas, and Peltier Yann. Mixing layer and coherent structures in compound channel flows: effects of velocity ratio, streamwise non-uniformity and shallowness. *Submitted to publication*, 2016.

Rabinovich Alexander B. Seiches and harbor oscillations. *Handbook of Coastal and Ocean Engineering*, pages 193–236, 2009.

Raupach MR, Antonia RA, and Rajagopalan S. Rough-wall turbulent boundary layers. *Applied Mechanics Reviews*, 44(1):1–25, 1991.

Ricardo Ana M, Koll Katinka, Franca Mário J, Schleiss Anton J, and Ferreira Rui ML. The terms of turbulent kinetic energy budget within random arrays of emergent cylinders. *Water Resources Research*, 50(5):4131–4148, 2014.

Robert Andre, Roy Andre G, and de Serres Bernard. Changes in velocity profiles at roughness transitions in coarse grained channels. *Sedimentology*, 39(5):725–735, 1992.

Rominger Jeffrey T and Nepf Heidi M. Flow adjustment and interior flow associated with a rectangular porous obstruction. *Journal of Fluid Mechanics*, 680:636–659, 2011.

Sarkar Arindam. Vortex-excited transverse surface waves in an array of randomly placed circular cylinders. *Journal of Hydraulic Engineering*, 138(7):610–618, 2012.

Sellin Robert H J. A laboratory investigation into the interaction between the flow in the channel of a river and that over its flood plain. *La Houille Blanche*, (7):793–802, 1964.

Shaw RH, Brunet Y, Finnigan JJ, and Raupach MR. A wind tunnel study of air flow in waving wheat: two-point velocity statistics. *Boundary-Layer Meteorology*, 76(4): 349–376, 1995.

Siuru WD and Logan E. Response of a turbulent pipe flow to a change in roughness. *Journal of Fluids Engineering*, 99(3):548–553, 1977.

Stocchino Alessandro and Brocchini Maurizio. Horizontal mixing of quasi-uniform straight compound channel flows. *Journal of Fluid Mechanics*, 643:425–435, 2010.

Stocchino Alessandro, Besio Giovanni, Angiolani Sonia, and Brocchini Maurizio. Lagrangian mixing in straight compound channels. *Journal of Fluid Mechanics*, 675: 168–198, 2011.

Stoesser Thorsten, Kim SJ, and Diplas P. Turbulent flow through idealized emergent vegetation. *Journal of Hydraulic Engineering*, 2010.

Tamai Nobuyuki, Asaeda Takashi, and Ikeda Hirokazu. Study on generation of periodical large surface eddies in a composite channel flow. *Water Resources Research*, 22(7): 1129–1138, 1986.

Terrier Benoit. *Flow characteristics in straight compound channels with vegetation along the main channel*. PhD thesis, Loughborough University, 2010.

Tominaga Akihiro and Nezu Iehisa. Turbulent structure in compound open-channel flows. *Journal of Hydraulic Engineering*, 117(1):21–41, 1991.

Townsend AA. Equilibrium layers and wall turbulence. *Journal of Fluid Mechanics*, 11 (01):97–120, 1961.

Uijttewaal WSJ and Booij R. Effects of shallowness on the development of free-surface mixing layers. *Physics of Fluids (1994-present)*, 12(2):392–402, 2000.

Van Prooijen Bram C, Battjes Jurjen A, and Uijttewaal Wim SJ. Momentum exchange in straight uniform compound channel flow. *Journal of hydraulic engineering*, 131(3): 175–183, 2005.

Vermaas DA, Uijttewaal WSJ, and Hoitink AJF. Lateral transfer of streamwise momentum caused by a roughness transition across a shallow channel. *Water resources research*, 47(2), 2011.

White Brian L and Nepf Heidi M. Shear instability and coherent structures in shallow flow adjacent to a porous layer. *Journal of Fluid Mechanics*, 593:1–32, 2007.

Winant CD and Browand FK. Vortex pairing: the mechanism of turbulent mixing-layer growth at moderate reynolds number. *Journal of Fluid Mechanics*, 63(02):237–255, 1974.

Wood DH and Bradshaw P. A turbulent mixing layer constrained by a solid surface. part 2. measurements in the wall-bounded flow. *Journal of fluid mechanics*, 139:347–361, 1984.

Yen Ben Chie. Open channel flow resistance. *Journal of Hydraulic Engineering*, 128(1): 20–39, 2002.

Yule Andrew J. Two-dimensional self-preserving turbulent mixing layers at different free stream velocity ratios. *Aeronautical Research Council*, 3683, 1972.

Zaman KBMQ and Hussain AKMF. Taylor hypothesis and large-scale coherent structures. *J. Fluid Mech*, 112(2):379–396, 1981.

Zhao Kuifeng, Cheng Nian-Sheng, and Huang Zhenhua. Experimental study of free-surface fluctuations in open-channel flow in the presence of periodic cylinder arrays. *Journal of Hydraulic Research*, 52(4):465–475, 2014.

Zima Laura and Ackermann Norbert L. Wave generation in open channels by vortex shedding from channel obstructions. *Journal of Hydraulic Engineering*, 128(6):596–603, 2002.

Zong Lijun and Nepf Heidi. Flow and deposition in and around a finite patch of vegetation. *Geomorphology*, 116(3):363–372, 2010.